



Mechanics of Railway Ballast Behaviour

by

Wee Loon Lim, BEng (Hons)

*Thesis submitted to The University of Nottingham
for the degree of Doctor of Philosophy*

May 2004

To my father

TABLE OF CONTENTS

| | |
|---|--------------|
| TABLE OF CONTENTS..... | I |
| ABSTRACT..... | V |
| ACKNOWLEDGEMENTS..... | VII |
| LIST OF FIGURES | VIII |
| LIST OF TABLES | XVI |
| NOTATION..... | XVIII |
| | |
| CHAPTER 1 INTRODUCTION..... | 1 |
| 1.1 BACKGROUND AND PROBLEM DEFINITION..... | 1 |
| 1.2 AIMS AND OBJECTIVES | 3 |
| 1.3 THESIS OUTLINE..... | 5 |
| | |
| CHAPTER 2 LITERATURE REVIEW..... | 7 |
| 2.1 INTRODUCTION | 7 |
| 2.2 BALLAST..... | 7 |
| 2.2.1 <i>Track components and functions</i> | 8 |
| 2.2.2 <i>Forces exerted on ballast</i> | 10 |
| 2.2.3 <i>Ballast specifications</i> | 14 |
| 2.2.4 <i>Resilient behaviour of granular material</i> | 20 |

| | | |
|-------|---|----|
| 2.2.5 | <i>Permanent deformation of granular material</i> | 23 |
| 2.2.6 | <i>Sources of fouling material in ballast</i> | 27 |
| 2.2.7 | <i>Effect of fouling material on ballast behaviour</i> | 29 |
| 2.2.8 | <i>Effect of fouling on drainage</i> | 30 |
| 2.3 | MICROMECHANICS OF CRUSHABLE AGGREGATES | 32 |
| 2.3.1 | <i>Fracture mechanics</i> | 32 |
| 2.3.2 | <i>Compression of a single particle</i> | 35 |
| 2.3.3 | <i>Weibull statistics applied to soil particle strength</i> | 37 |
| 2.3.4 | <i>Particle survival in aggregates</i> | 40 |
| 2.3.5 | <i>Yielding of granular materials</i> | 43 |
| 2.4 | DISCRETE ELEMENT MODELLING USING PFC ^{3D} | 47 |
| 2.4.1 | <i>Discrete element method and PFC^{3D}</i> | 47 |
| 2.4.2 | <i>Calculation cycle</i> | 49 |
| 2.4.3 | <i>Contact constitutive models</i> | 53 |
| 2.4.4 | <i>Wall control</i> | 55 |
| 2.4.5 | <i>Modelling soil particle fracture</i> | 56 |
| 2.4.6 | <i>Compression tests on an assembly of agglomerates</i> | 61 |
| 2.5 | SUMMARY | 64 |

CHAPTER 3 SINGLE PARTICLE CRUSHING TESTS.....66

| | | |
|-------|-------------------------------------|----|
| 3.1 | INTRODUCTION | 66 |
| 3.2 | TEST PROCEDURES | 67 |
| 3.3 | RESULTS | 69 |
| 3.3.1 | <i>Computation of results</i> | 69 |
| 3.3.2 | <i>Summary of results</i> | 71 |
| 3.4 | DISCUSSION | 73 |
| 3.5 | CONCLUSIONS..... | 76 |

| | | |
|------------------|---|------------|
| CHAPTER 4 | LARGE OEDOMETER TESTS..... | 78 |
| 4.1 | INTRODUCTION | 78 |
| 4.2 | TEST PROCEDURES | 79 |
| 4.3 | RESULTS | 81 |
| 4.3.1 | <i>Computation of results</i> | 81 |
| 4.3.2 | <i>Large oedometer test on 10-14mm ballast</i> | 83 |
| 4.3.3 | <i>Large oedometer test on 37.5-50mm ballast</i> | 86 |
| 4.3.4 | <i>Large oedometer test on specification ballast</i> | 90 |
| 4.3.5 | <i>Summary of results</i> | 94 |
| 4.3.6 | <i>Additional tests</i> | 95 |
| 4.4 | DISCUSSION | 97 |
| 4.5 | CONCLUSIONS..... | 101 |
| | | |
| CHAPTER 5 | BOX TESTS..... | 103 |
| 5.1 | INTRODUCTION | 103 |
| 5.2 | TEST PROCEDURES | 104 |
| 5.3 | RESULTS | 108 |
| 5.3.1 | <i>Box test on ballast A</i> | 108 |
| 5.3.2 | <i>Controlled box tests on ballast A</i> | 114 |
| 5.3.3 | <i>Box test on 10-14mm Ballast A</i> | 118 |
| 5.3.4 | <i>Box tests on ballasts B, C and D</i> | 120 |
| 5.3.5 | <i>Summary and correlation of results with ballast index tests, single particle crushing tests, and large oedometer tests</i> | 123 |
| 5.4 | DISCUSSION | 128 |
| 5.5 | CONCLUSIONS..... | 132 |
| | | |
| CHAPTER 6 | NUMERICAL MODELLING | 136 |
| 6.1 | INTRODUCTION | 136 |
| 6.2 | PRELIMINARY OEDOMETER TEST SIMULATIONS..... | 138 |
| 6.2.1 | <i>Test description</i> | 138 |

| | | |
|-------|---|-----|
| 6.2.2 | <i>One-dimensional compression of agglomerates</i> | 142 |
| 6.2.3 | <i>One-dimensional compression of spherical balls</i> | 145 |
| 6.2.4 | <i>Discussion</i> | 146 |
| 6.3 | SINGLE PARTICLE CRUSHING TEST SIMULATIONS | 146 |
| 6.3.1 | <i>Test description</i> | 147 |
| 6.3.2 | <i>Results</i> | 149 |
| 6.3.3 | <i>Discussion</i> | 152 |
| 6.4 | OEDOMETER TEST SIMULATIONS | 154 |
| 6.4.1 | <i>Test description</i> | 154 |
| 6.4.2 | <i>Results</i> | 156 |
| 6.4.3 | <i>Discussion</i> | 159 |
| 6.5 | BOX TEST SIMULATIONS | 162 |
| 6.5.1 | <i>Test description</i> | 162 |
| 6.5.2 | <i>Results</i> | 164 |
| 6.5.3 | <i>Discussion</i> | 165 |
| 6.6 | CONCLUSIONS | 167 |

**CHAPTER 7 IMPLICATIONS OF THIS RESEARCH FOR
ENGINEERING PRACTICE.....169**

**CHAPTER 8 CONCLUSIONS AND SUGGESTIONS FOR FURTHER
RESEARCH.....175**

| | | |
|-----|--|-----|
| 8.1 | CONCLUSIONS | 175 |
| 8.2 | SUGGESTIONS FOR FURTHER RESEARCH | 180 |

REFERENCES.....182

APPENDIX.....189

ABSTRACT

It is important to have consistent ballast testing methods that provide results reflecting the performance of different ballast materials in the railway trackbed. In this research, extensive laboratory tests were conducted to investigate the correlation between simple ballast index tests, and box tests simulating ballast field loading conditions in a simplified and controlled manner. In the box test, a sleeper load of 40kN was applied to a simulated sleeper on the top of a sample of ballast in a box of dimensions 700×300×450mm. The ballast was tamped using a Kango hammer which caused particles to rearrange as the level of the sleeper was raised.

The ballast tests investigated in this project are those ballast tests specified in the Railtrack Line Specification (RT/CE/S/006 Issue 3, 2000), in addition to single particle crushing tests, oedometer tests, petrographic analysis, and box tests. It was found that there was some correlation between the single particle crushing tests, oedometer tests, box tests and petrographic analysis. One of the current ballast tests, namely the Aggregate Crushing Value (ACV) test, which is analogous to the oedometer test, is not appropriate because the ACV test uses 10-14mm ballast particles, and there is a size effect on the strength of ballast and different ballasts have different size effects. However, if an oedometer test is used on track ballast, the results correlate better with ballast field performance as simulated in the box tests.

Six ballasts were tested: A, B, C, D, E and F (mineralogy of these ballasts can be found in the appendix). The aim was to examine the relative performance of these ballasts and to establish which index tests were most indicative of performance in the box test. Simple index tests were performed on each of the ballasts, whilst box tests were only performed on ballasts A, B, C and D. The box tests were generally performed wet by adding a known volume of water at each tamp. For ballast A, controlled tests were also performed on dry ballast, and tests involving traffic loading only and tamping only were also conducted. A box test on 10-14mm ballast A was also conducted to investigate the size effect on ballast behaviour in the box. The Wet Attrition Value (WAV), Los Angeles Abrasion (LAA), and Micro-Deval

Attrition (MDA) seem to be suitable parameters to indicate ballast performance in the box test. However, this is considered to be due to the rearrangement of particles in the box test caused by the simulated tamping.

In addition to the laboratory tests, the application of discrete element program PFC^{3D} (Itasca Consulting Group, Inc., 1999) in simulating ballast behaviour was also investigated. Single particle crushing test was simulated to produce crushable agglomerates with a distribution of strengths of ballast A. These agglomerates were then used to simulate the oedometer test. The resulting normal compression line was compared with that for real oedometer tests: discrepancies can be attributed to the simplified geometry of the agglomerates. Due to the high computational time in simulating a box test with crushable agglomerates, uncrushable spherical balls and uncrushable angular agglomerates were used to represent individual ballast particles in the box. Important aspects of ballast behaviour under repeated loading, namely resilient and permanent deformation, were studied. It was found that the box test on uncrushable angular agglomerates give less permanent deformation compared with the test on spherical balls, because of the additional resistance provided by the irregular shape of the agglomerates.

ACKNOWLEDGEMENTS

I would like to thank my supervisor, Dr. Glenn McDowell, for his excellent guidance and supervision throughout this research project; without his support, this thesis would not have been possible.

I would also like to express my gratitude to the following people for their advise and help:

Professor Andy Collop and Professor Stephen Brown, co-supervisors, for their invaluable advice.

Dr. Nick Thom from the University of Nottingham, Mr. Robert Armitage from Scott Wilson Pavement Engineering Limited, and Mr. John Harris from Lafarge Aggregates Limited for their technical support.

All the technicians in the School of Civil Engineering for their help with the experimentation, in particular Barry Brodrick, Bal Loyla and Michael Langford.

Dr. Ouahid Harireche for his help with the discrete element program PFC^{3D}.

Dr. David Large for conducting the petrographic analysis.

All colleagues in the School of Civil Engineering for their friendship, in particular Steve Hau and Cuong Doan Khong.

The University of Nottingham, Lafarge Aggregates Limited, and Groundwork Hertfordshire for funding this research project.

Finally, my greatest gratitude goes to my parents, uncle Yuen Hin, brothers, sister and Yuek-Luh Lim for their constant support, belief and encouragement.

LIST OF FIGURES

| | |
|---|-----------|
| Figure 1.1. Substructure contributions to settlement (Selig & Waters, 1994). | 2 |
| Figure 2.1. Track layout of a typical ballasted track- side view (Selig & Waters, 1994). | 8 |
| Figure 2.2. Track layout of a typical ballasted track- cross section (Selig & Waters, 1994). | 9 |
| Figure 2.3. Static and dynamic wheel loads for (a) Colorado test track and (b) mainline track between New York and Washington (Selig & Waters, 1994). | 11 |
| Figure 2.4. Uplift of rails (Selig & Waters, 1994). | 12 |
| Figure 2.5. Tamping action (Selig & Waters, 1994). | 13 |
| Figure 2.6. Effect of slurry on ballast in WAV test (Selig & Waters, 1994). | 16 |
| Figure 2.7. Los Angeles Abrasion (LAA) values and Aggregate Crushing Values (ACV) in different mixtures of flaky and non-flaky materials (Gur et al., 1967). | 17 |
| Figure 2.8. Strains in granular materials during one cycle of load application (Lekarp et al., 2000a). | 20 |
| Figure 2.9. Behaviour of ballast under cyclic triaxial test (Selig & Waters, 1994). | 21 |
| Figure 2.10. Resilient modulus against bulk stress (Alva-Hurtado, 1980). | 22 |
| Figure 2.11. Effect of stress ratio on permanent strain (Knutson, 1976). | 23 |
| Figure 2.12. Effect of difference in sequence of loading on permanent strain (Selig & Waters, 1994). | 24 |
| Figure 2.13. Loading sequences (Shenton, 1974). | 25 |
| Figure 2.14. Contribution of second block of loading to total deformation (Shenton, 1974). | 25 |
| Figure 2.15. Effect of number of repeated load applications on settlement (Shenton, 1974). | 26 |
| Figure 2.16. Effect of frequency on permanent strain (Shenton, 1974). | 27 |

| | |
|--|----|
| Figure 2.17. Sources of ballast fouling (Selig & Waters, 1994)..... | 27 |
| Figure 2.18. Effect of particle rearrangement on particle breakage (Selig & Waters, 1994)..... | 28 |
| Figure 2.19. Effect of degree of fouling and type of fouling material on ballast settlement (Han & Selig, 1997). | 30 |
| Figure 2.20. Effect of water content on ballast settlement for different degrees of fouling and fouling materials (Han & Selig, 1997). | 30 |
| Figure 2.21. Weibull distribution of strengths. | 34 |
| Figure 2.22. Single particle crushing test (Lee, 1992). | 36 |
| Figure 2.23. Typical plot of force against deformation for a typical particle (Lee, 1992)..... | 36 |
| Figure 2.24. Results of single particle crushing tests (Lee, 1992). | 37 |
| Figure 2.25. 37% strength as a function of average particle size at failure (McDowell & Amon, 2000)..... | 39 |
| Figure 2.26. Average force at failure as a function of average size at failure (McDowell & Amon, 2000)..... | 40 |
| Figure 2.27. Large co-ordination numbers are less helpful for more angular particles (McDowell et al., 1996). | 41 |
| Figure 2.28. Evolving particle size distribution curves for one-dimensionally compressed Ottawa sand (Fukumoto, 1992)..... | 42 |
| Figure 2.29. Relation between mean coordination number and voids ratio (Oda, 1977)..... | 43 |
| Figure 2.30. Discrete element simulation of array of photoelastic discs $F_H / F_V = 0.43$ (Cundall & Strack, 1979)..... | 44 |
| Figure 2.31. Compression plots for different uniform gradings of sand (McDowell, 2002)..... | 45 |
| Figure 2.32. Yield stress predicted from single particle crushing tests, assuming yield stress=(37% tensile strength)/4 (McDowell, 2002). | 45 |
| Figure 2.33. Effect of initial voids ratio on one-dimensional compression curve (Nakata et al., 2001)..... | 46 |
| Figure 2.34. Calculation cycle use in PFC ^{3D} (Itasca Consulting Group, Inc., 1999). | 49 |
| Figure 2.35. Crushing test on agglomerate (Robertson, 2000)..... | 57 |

| | |
|---|-----------|
| Figure 2.36. Typical result of a crushing test on an agglomerate (Robertson, 2000). | 58 |
| Figure 2.37. Weibull probability plot for (a) 0.5mm and (b) 1mm diameter agglomerates (McDowell & Harireche, 2002a). | 59 |
| Figure 2.38. Force-strain plots for different platen velocities (McDowell & Harireche, 2002a). | 60 |
| Figure 2.39. Typical contours of equal percentages of bonds breaking in deviatoric stress-mean stress space (Robertson, 2000). | 62 |
| Figure 2.40. Compression curve (McDowell & Harireche, 2002b). | 62 |
| Figure 2.41. Number of intact bonds as a function of strain (McDowell & Harireche, 2002b). | 63 |
| Figure 2.42. (a) Effect of scaling bond strength on the compression curve; and (b) compression curve with stress normalised by 37% agglomerate tensile strength σ_o (McDowell & Harireche, 2002b). | 63 |
| Figure 3.1. Single particle crushing test set-up. | 68 |
| Figure 3.2. Weibull survival probability plots. | 71 |
| Figure 3.3. 37% tensile strength against average particle size at failure plot. | 73 |
| Figure 3.4. Variation of the normalised maximum tensile stress on the axis and on the surface with a_c/R (Shipway & Hutchings, 1993). | 75 |
| Figure 4.1. Oedometer test set-up. | 80 |
| Figure 4.2. Breakage potential, B_p. | 82 |
| Figure 4.3. Total breakage, B_t. | 82 |
| Figure 4.4. One-dimensional compression plot for large oedometer tests on 10-14mm ballast. | 83 |
| Figure 4.5. Particle size distributions for large oedometer tests on 10-14mm ballast. | 84 |
| Figure 4.6. B_t against ACV for oedometer test on 10-14mm ballast. | 85 |

| | |
|--|-----|
| Figure 4.7. ACV for oedometer test on 10-14mm ballast against σ_o (10-14mm)..... | 85 |
| Figure 4.8. B_t for oedometer test on 10-14mm ballast against σ_o (10-14mm)..... | 85 |
| Figure 4.9. One-dimensional compression plot for large oedometer tests on 37.5-50mm ballast..... | 86 |
| Figure 4.10. Particle size distributions for large oedometer tests on 37.5-50mm ballast..... | 87 |
| Figure 4.11. B_t against ACV for oedometer test on 37.5-50mm ballast. | 88 |
| Figure 4.12. ACV for oedometer test on 37.5-50mm ballast against σ_o (37.5-50mm)..... | 88 |
| Figure 4.13. B_t for oedometer test on 37.5-50mm ballast against σ_o (37.5-50mm)..... | 88 |
| Figure 4.14. Particle size distributions for large oedometer tests on 37.5-50mm ballasts A and E..... | 90 |
| Figure 4.15. One-dimensional compression plot for large oedometer tests on specification ballast..... | 91 |
| Figure 4.16. Particle size distributions for large oedometer tests on specification ballast..... | 91 |
| Figure 4.17. B_t against ACV for oedometer test on specification ballast. | 92 |
| Figure 4.18. ACV for oedometer test on specification ballast against σ_{ow} | 93 |
| Figure 4.19. B_t for oedometer test on specification ballast against σ_{ow} | 93 |
| Figure 4.20. Particle size distributions for large oedometer tests on specification ballasts A and E. | 93 |
| Figure 4.21. One-dimensional compression plot for large oedometer tests on dry and wet specification ballasts B and D..... | 96 |
| Figure 4.22. Particle size distributions for large oedometer tests on dry and wet specification ballasts B and D. | 97 |
| Figure 4.23. ACV_d against σ_o | 99 |
| Figure 4.24. B_t against σ_o | 99 |
| Figure 4.25. ACV_d against R_s | 101 |
| Figure 4.26. B_t against R_s | 101 |

| | | |
|---------------------|--|------------|
| Figure 5.1. | Plan of rail and sleepers showing section represented by the box test. | 104 |
| Figure 5.2. | Box test set-up (from the top of the box)..... | 105 |
| Figure 5.3. | Box test set-up (front view). | 106 |
| Figure 5.4. | Kango hammer with one inch wide chisel. | 107 |
| Figure 5.5. | Elevation showing different sections for removal of ballast from the box..... | 107 |
| Figure 5.6. | Sleeper level against number of cycles for ballast A(1). | 109 |
| Figure 5.7. | Sleeper level against number of cycles for ballast A(2). | 109 |
| Figure 5.8. | Settlement against number of cycles for ballast A. | 109 |
| Figure 5.9. | Stiffness against number of cycles for ballast A. | 111 |
| Figure 5.10. | Particle size distributions for box tests on ballast A. | 112 |
| Figure 5.11. | Increase in percentage passing the 37.5mm sieve at different locations (see Figure 5.5) within the box for ballast A(1). | 113 |
| Figure 5.12. | Increase in percentage passing the 37.5mm sieve at different locations within the box for ballast A(2). | 113 |
| Figure 5.13. | Particle size distributions for ballast underneath the sleeper for box tests on ballast A. | 113 |
| Figure 5.14. | Settlement against number of cycles for box tests on dry and wet ballast A. | 115 |
| Figure 5.15. | Stiffness against number of cycles for box tests on dry and wet ballast A. | 115 |
| Figure 5.16. | Particle size distributions for box tests on dry and wet ballast A. | 115 |
| Figure 5.17. | Settlement against number of cycles for traffic-only box tests and standard box test on wet ballast A. | 116 |
| Figure 5.18. | Stiffness against number of cycles for traffic-only box tests and standard box test on wet ballast A. | 117 |
| Figure 5.19. | Sleeper level against number of cycles for box test on 10-14mm ballast A(7). | 119 |
| Figure 5.20. | Settlement against number of cycles for box tests on 10-14mm and track ballast sized ballast A. | 119 |
| Figure 5.21. | Stiffness against number of cycles for box tests on 10-14mm and track ballast sized ballast A. | 119 |

| | |
|---|-----|
| Figure 5.22. Sleeper level against number of cycles for box test on ballast B..... | 120 |
| Figure 5.23. Sleeper level against number of cycles for box test on ballast C..... | 121 |
| Figure 5.24. Sleeper level against number of cycles for box test on ballast D..... | 121 |
| Figure 5.25. Settlement against number of cycles for box tests on different ballasts..... | 122 |
| Figure 5.26. Stiffness against number of cycles for box tests on different ballasts..... | 122 |
| Figure 5.27. Particle size distributions for ballast underneath the sleeper for box tests on different ballasts..... | 123 |
| Figure 5.28. B_t (Box Test) for ballast underneath the sleeper against WAV... | 125 |
| Figure 5.29. B_t (Box Test) for ballast underneath the sleeper against ACV for oedometer test (10-14mm)..... | 126 |
| Figure 5.30. B_t (Box Test) for ballast underneath the sleeper against LAA. ... | 126 |
| Figure 5.31. B_t (Box Test) for ballast underneath the sleeper against MDA... | 126 |
| Figure 5.32. B_t (Box Test) for ballast underneath the sleeper against ACV for oedometer test (specification). | 127 |
| Figure 5.33. B_t (Box Test) for ballast underneath the sleeper against B_t for oedometer test (specification)..... | 127 |
| Figure 5.34. B_t (Box Test) for ballast underneath the sleeper against σ_{ov} (specification)..... | 127 |
| Figure 5.35. B_t (Box Test) for ballast underneath the sleeper against relative strength index R_s | 128 |
| Figure 5.36. Sleeper level against number of cycles for the 2 ballast A samples..... | 129 |
| Figure 5.37. Tamping effect on ballast settlement (Selig & Waters, 1994)..... | 129 |
| Figure 5.38. Sleeper settlement as a function of tamping lift (Selig & Waters, 1994)..... | 131 |

| | | |
|---------------------|---|------------|
| Figure 6.1. | Effect of repeated load on horizontal stress (Norman & Selig, 1983). | 137 |
| Figure 6.2. | A hexagonal closed packed agglomerate with 13 balls. | 139 |
| Figure 6.3. | Oedometer test on 13-ball agglomerates prior to loading. | 141 |
| Figure 6.4. | Oedometer test on spherical balls prior to loading. | 142 |
| Figure 6.5. | V/V_0 against logarithm of vertical stress on the top wall for oedometer test using agglomerates (each agglomerate represent a soil particle). | 143 |
| Figure 6.6. | V/V_0 against logarithm of mean vertical stress for oedometer test using agglomerates. | 143 |
| Figure 6.7. | Average vertical stress on the top and the bottom walls for different displacement rates. | 144 |
| Figure 6.8. | Total number of bonds against logarithm of mean vertical stress for sample loaded with a displacement rate of 0.2ms^{-1}. | 144 |
| Figure 6.9. | V/V_0 against logarithm of mean vertical stress for oedometer test using balls (each ball represents a soil particle). | 145 |
| Figure 6.10. | Typical force-strain plot for 48mm diameter agglomerate initially containing 1477 balls for different platen velocities. | 149 |
| Figure 6.11. | Weibull probability plot for 24 mm diameter agglomerate initially containing 135 balls with stiffnesses and bond strength: (a) unscaled, $f=1$; (b) scaled $f=2.96$. | 150 |
| Figure 6.12. | Weibull probability plot for 48 mm diameter agglomerate initially containing 1477 balls ($f=2.96$). | 151 |
| Figure 6.13. | Weibull probability plot for 48 mm diameter agglomerate initially containing 135 balls with stiffnesses and bond strength: (a) unscaled, $f=1$; (b) scaled $f=2.01$. | 152 |
| Figure 6.14. | Force-strain plot for a 24mm diameter agglomerate initially containing 135 balls for different damping coefficients. | 153 |
| Figure 6.15. | Number of broken bonds against strain for the compression of a 24mm diameter agglomerate initially containing 135 balls with different damping coefficients. | 154 |
| Figure 6.16. | Oedometer test on 48 mm agglomerates initially containing 135 balls prior to loading. | 156 |

| | | |
|---------------------|--|------------|
| Figure 6.17. | V/V_o against logarithm of vertical stress for oedometer test using 135-ball agglomerates of 48mm diameter and the laboratory oedometer test on 37.5-50mm ballast A..... | 157 |
| Figure 6.18. | Total number of bonds against logarithm of mean vertical stress σ_{mean} for the oedometer test simulation on 135-ball agglomerates of 48mm diameter..... | 157 |
| Figure 6.19. | Mean K_o against vertical strain for oedometer test on 135-ball agglomerates of 48 mm diameter..... | 158 |
| Figure 6.20. | K_o against OCR for oedometer test on 135-ball agglomerates of 48 mm diameter..... | 158 |
| Figure 6.21. | Mean vertical stress σ_{mean} against number of timesteps..... | 159 |
| Figure 6.22. | Number of broken bonds against number of timesteps. | 160 |
| Figure 6.23. | K_o against OCR for the sample unloaded by maintaining $R_{mean} \approx 0.001$. | 161 |
| Figure 6.24. | Rolling without slip at a contact bond (Itasca Consulting Group, Inc., 1999). | 161 |
| Figure 6.25. | Constraint provided by surrounding balls which prevent rolling at a contact bond (Itasca Consulting Group, Inc., 1999). | 161 |
| Figure 6.26. | An 8-ball cubic clump..... | 163 |
| Figure 6.27. | Box test on spherical balls prior to loading. | 164 |
| Figure 6.28. | Box test on 8-ball cubic clumps prior to loading..... | 164 |
| Figure 6.29. | Load against deformation for the box test on spherical balls and 8-ball cubic clumps. | 165 |
| Figure 6.30. | Non-uniform distribution of contact forces in the assembly in the box (contact forces are shown as lines with thickness proportional to the magnitude of the contact force)..... | 166 |

LIST OF TABLES

| | | |
|--------------------|---|-----------|
| Table 2.1. | The original (2000) specification for ballast particle size distributions (RT/CE/S/006 Issue 3, 2000). | 15 |
| Table 2.2. | The new (2005) specification for ballast particle size distributions (RT/CE/S/006 Issue 3, 2000). | 18 |
| Table 2.3. | Hydraulic conductivity values for ballast (Selig et al., 1993). | 31 |
| Table 2.4. | Weibull modulus and 37% strength for a wide range of particle sizes of Calcareous Quiou sand (McDowell & Amon, 2000). | 39 |
| Table 3.1. | Summary of single particle crushing test results..... | 72 |
| Table 3.2. | Comparison of theoretical prediction of size effect with the actual size effect for different ballast materials..... | 75 |
| Table 4.1. | Summary of voids ratios and coefficient of compressibility for large oedometer tests on 10-14mm ballast. | 83 |
| Table 4.2. | ACV and B_t values for large oedometer tests on 10-14mm ballast and σ_o of 10-14mm ballast particles. | 84 |
| Table 4.3. | Summary of voids ratios and coefficient of compressibility for large oedometer tests on 37.5-50mm ballast. | 86 |
| Table 4.4. | ACV and B_t values for large oedometer tests on 37.5-50mm ballast and σ_o of 37.5-50mm ballast particles. | 87 |
| Table 4.5. | Flakiness indices (according to BS812 Section 105.1, 1989). | 89 |
| Table 4.6. | Summary of voids ratios and coefficient of compressibility for large oedometer tests on specification ballast. | 91 |
| Table 4.7. | ACV and B_t values for large oedometer tests on specification ballast and σ_{ov} of specification ballast particles. | 92 |
| Table 4.8. | Summary of ACV values for large oedometer tests. | 94 |
| Table 4.9. | Summary of B_t values for large oedometer tests. | 94 |
| Table 4.10. | WAV, LAA, and MDA values. | 95 |
| Table 4.11. | Water absorption values. | 95 |

| | |
|--|------------|
| Table 4.12. Summary of voids ratios and coefficient of compressibility for large oedometer tests on dry and wet specification ballasts B and D..... | 96 |
| Table 4.13. ACV and B_t values for large oedometer tests on dry and wet specification ballasts B and D..... | 97 |
| Table 4.14. Summary of ACV_d values for large oedometer tests..... | 98 |
| Table 4.15. ACV_d, B_t, σ_o and e_i for 10-14mm ballast B and 37.5-50mm ballast C..... | 100 |
| | |
| Table 5.1. B_t values for box tests on ballast A..... | 112 |
| Table 5.2. B_t for ballast underneath the sleeper for box tests on ballast A.... | 114 |
| Table 5.3. Total breakage B_t for controlled box tests on ballast A..... | 117 |
| Table 5.4. B_t for ballast underneath the sleeper for box tests on 10-14mm and track ballast sized ballast A. | 120 |
| Table 5.5. B_t for ballast underneath the sleeper for box tests on different ballasts..... | 123 |
| Table 5.6. Summary of all box test results..... | 124 |
| | |
| Table 6.1. Single particle crushing tests result for ballast A..... | 147 |
| | |
| Table 7.1. WAV and degradation under tamping for different ballasts (Wright, 1983)..... | 170 |

NOTATION

| | |
|--------------------------|---|
| θ | Sum of principal stresses or bulk stress |
| ACV | Aggregate Crushing Value |
| ACV_d | Scaled ACV |
| b | Slope of the line of best fit on a plot of $\text{Log}(\sigma_o)$ against $\text{Log}(d_f)$ |
| B_p | Breakage potential |
| B_t | Total breakage factor |
| C_c | Coefficient of compressibility |
| d | Particle size or average particle size |
| DEM | Discrete Element Method |
| d_f | Particle size at failure |
| e_f | Final voids ratio |
| e_i | Initial voids ratio |
| $e_{i,\max}, e_{i,\min}$ | Maximum and minimum initial voids ratio e_i respectively |
| f | Scaling factor for bond strength, and ball and platen stiffnesses |
| F_c^n, F_c^s | Normal and shear bond strengths respectively |
| F_f | Diametral fracture force |
| K^n, K^s | Normal and shear contact stiffnesses |
| k_n, k_s | Normal and shear stiffnesses |
| K_o | Ratio of mean horizontal effective stress to mean vertical effective stress |
| LAA | Los Angeles Abrasion |
| m | Weibull modulus |
| MDA | Micro-Deval Attrition |
| M_r | Resilient modulus |
| OCR | Overconsolidation ratio |
| p' | mean effective stress |
| P_s | Survival probability |
| q | Deviatoric stress |
| R_e | Relative voids ratio |
| R_{mean} | Ratio of mean unbalanced force to mean contact force |

| | |
|----------------------------------|--|
| R_s | Relative strength index |
| R_σ | Relative tensile strength |
| WAV | Wet Attrition Value |
| σ_3 | Confining stress |
| σ_{av} | Average stress at failure |
| σ_f | Tensile stress at failure |
| σ_o | 37% tensile strength |
| $\sigma_{o,d}$ | Stress for particles of size d such that 37% of tested particles survive |
| $\sigma_{o,max}, \sigma_{o,min}$ | Maximum and minimum 37% tensile strengths for tested ballasts |
| σ_{ow} | Weighted tensile strength |

Chapter 1

Introduction

1.1 Background and problem definition

The railway track system plays an important role in providing a good transportation system in a country. A very large portion of the annual budget to sustain the railway track system goes into track maintenance. In the past, most attention has been given to the track superstructure consisting of the rails, the fasteners and the sleepers, and less attention has been given to the substructure consisting of the ballast, the subballast and the subgrade. Even though the substructure components have a major influence on the cost of track maintenance, less attention has been given to the substructure because the properties of the substructure are more variable and difficult to define than those of the superstructure (Selig & Waters, 1994).

Deterioration of the track geometry has been recognised to be the main source of the need for track maintenance. This deterioration is mainly caused by the settlement of the substructure, which tends to depend on the site conditions. Ballast is the most important component of the substructure because it is the only external constraint applied to the track in order to restrain it. Ballast is also important for providing the fastest and most economical method of restoring track geometry, especially at a subgrade failure situation. However, ballast is also one of the main sources of track geometry deterioration. Figure 1.1 shows a typical profile of the relative contributions of the substructure components on track settlement, assuming a good

subgrade soil foundation (Selig & Waters, 1994). This figure shows that ballast contributes the most to track settlement, compared to subballast and subgrade.

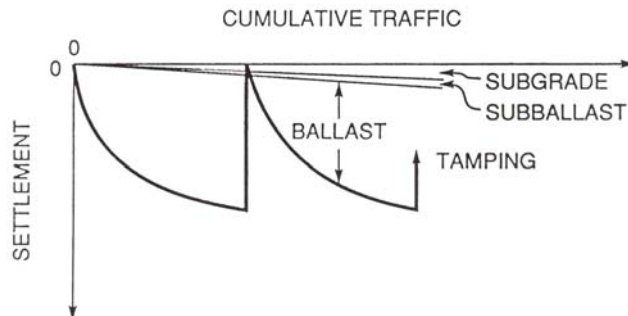


Figure 1.1. Substructure contributions to settlement (Selig & Waters, 1994).

Under traffic loading, the stresses in the ballast are sufficient to cause significant strain in the ballast and ballast particle breakage. This effect causes track settlement and therefore the track geometry will need to be restored by tamping. However, tamping causes further ballast breakdown. This maintenance cycle will eventually lead to loss of strength and stiffness in the ballast when fine material generated from ballast breakdown reaches a critical level and when the water fails to drain from the ballast properly. At this stage, the track needs to be maintained either by ballast cleaning or ballast renewal. Thus, it is important to use good quality ballast material in order to increase ballast life on the track and reduce waste ballast generated from ballast cleaning or ballast renewal.

Researchers (e.g. Wright, 1983; Selig & Boucher, 1990) have shown that conventional ballast abrasion tests, such as the wet attrition value (WAV), Los Angeles abrasion (LAA), and micro-Deval attrition (MDA), give conflicting results and often fail to represent actual field performance. Furthermore, these tests involve revolving particles in a cylinder or drum to measure degradation. The particle mechanics here would not appear to be the same as those beneath the railway track during traffic loading. Despite these shortcomings, abrasion tests are still considered as the best and most important indicators of ballast performance in service. The Aggregate Crushing Value (ACV) test, which is another standard ballast test, might also be considered to be inappropriate, because it involves testing of the small ballast

particles (10-14mm), instead of the normal sizes used in the trackbed (28-50mm). Research has shown that the strength of soil particles varies with size, and larger soil particles tend to have a lower average tensile strength compared to smaller particles because they contain more and larger flaws (McDowell & Amon, 2000). The size effect on average strength varies between materials. Thus, ACV only gives information about the average strength of 10-14mm particles, but does not give information about the average strength of larger ballast particles used in the trackbed. There is therefore a need for better and more consistent ballast testing methods that provide results reflecting the quality of different ballast materials used in the trackbed.

The discrete element program PFC^{3D} (Itasca Consulting Group, Inc., 1999) is believed to be the most suitable numerical model for investigating the micro mechanical behaviour of ballast. PFC^{3D} applies Discrete Element Method (DEM) to model the movement and interaction of stressed assemblies of spherical balls, which can overlap, and displace independently from one another and interact only at contacts or interfaces between the balls. This program applies a contact constitutive law to each particle contact, such that the contact force is related to the amount of overlap, and accelerations are calculated from the contact forces via Newton's second law. These accelerations are integrated to give velocities and displacements via a time-stepping scheme, and the resulting displacements are used to calculate the new contact forces via the contact constitutive law. The material constants for the contact constitutive law have explicit physical meanings. A crushable particle can also be modelled in PFC^{3D} as an agglomerate of balls bonded together. Thus, PFC^{3D} can be used to investigate the heterogeneous stresses in ballast in a way that cannot be achieved using continuum approaches.

1.2 Aims and objectives

The ultimate goal of this project is to produce a methodology to identify good quality ballast and to provide an understanding of the micromechanics of ballast degradation. The aims of this research can be stated as:

- To identify ballast testing methods which provide results reflecting the field performance of different ballast materials.
- To apply the mechanics of crushable soils to ballast in order to gain an understanding of ballast degradation.
- To use the discrete element program PFC^{3D} (Itasca Consulting Group, Inc., 1999) to simulate ballast as an aggregate of crushable or uncrushable balls, in order to study stresses in ballast and the micro mechanics of degradation.

The following specific objectives are required to achieve these aims:

- 1) A literature review on the behaviour of ballast, ballast testing methods, mechanics of crushable soils, concepts and functions of PFC^{3D}, and recent application of PFC^{3D} to simulate soil behavior.
- 2) Selection of six types of ballast that are widely used in the United Kingdom and represent a range of physical properties, and meet the Railtrack Line Specification (RT/CE/S/006 Issue 3, 2000).
- 3) Ballast tests as specified in the Railtrack Line Specification (RT/CE/S/006 Issue 3, 2000).
- 4) Modify a particle crusher, which can measure force as a function of displacement for a ballast particle compressed diametrically between flat loading platens.
- 5) Crushing of single particles of ballast between flat platens to measure, indirectly, the tensile strength, and calculation of the Weibull modulus and tensile strength as a function of size for six types of ballast.
- 6) Design and manufacture of a large oedometer for testing ballast particles of the size used in the trackbed.
- 7) Oedometer tests on ballast to determine ballast degradation upon loading to a stress level equivalent to that of the ACV test, for six types of ballast.
- 8) Design and manufacture of a box test apparatus to simulate ballast field loading conditions in a simplified and controlled manner.
- 9) Box tests on ballast to determine ballast behaviour and degradation under stresses typical in real trackbeds, for four types of ballast.

- 10) Petrographic analysis to give a qualitative assessment of ballast performance and provide rational explanations of the laboratory test results.
- 11) Correlation of test results and proposal of good ballast testing methods and engineering practice.
- 12) Simulations using PFC^{3D} of single particle crushing tests, oedometer tests, and box tests.

1.3 Thesis outline

This thesis is divided into eight chapters. A brief outline of this thesis is given below.

Following the introductory chapter, Chapter 2 contains a literature review consisting of three parts: ballast, micromechanics of crushable aggregates and discrete element modelling using PFC^{3D}. Part one briefly describes the track components and their functions, followed by ballast loading conditions and ballast requirements. Current ballast testing methods and their deficiencies are studied, and the behaviour of ballast under repeated loading and the behaviour of fouled ballast are discussed. Part two examines the strengths of individual soil particles, and the criteria for soil grains to survive during one-dimensional compression of aggregates. The concepts and functions of PFC^{3D} are described in part three followed by a discussion of recent applications of PFC^{3D} in simulating soil behaviour.

Chapter 3 describes the apparatus and the test procedure for the single particle crushing test. The assumptions made and the analysis of the experimental results are also presented and discussed in this chapter. The large oedometer test apparatus and the adopted test procedure are described in Chapter 4. The analysis of the experimental results is presented, together with a discussion of the correlation of the experimental results with the single particle crushing test results. Chapter 5 describes the box test apparatus and test procedure in detail, together with a presentation of the results. The correlations of the performance of ballast in the box test with the current ballast index tests, single particle crushing tests and the large oedometer tests are also presented.

Chapter 6 presents simulations of single particle crushing tests, oedometer tests and the box tests using PFC^{3D}. Each simulation is described, together with the presentation and the discussion of the results. The implications of this research for engineering practice are discussed in Chapter 7. Finally, Chapter 8 presents the conclusions of this research and gives suggestions for future work.

Chapter 2

Literature Review

2.1 Introduction

This chapter is divided into three sections: section 2.2 presents a general review of ballast behaviour, section 2.3 examines the micromechanics of crushable aggregates and in section 2.4 numerical modelling using PFC^{3D} is discussed. Section 2.2 presents a general literature review on ballast requirements, functions, loading conditions, behaviour under repeated loads and behaviour of fouled ballast. A brief description of the track components and their functions, and the current ballast testing methods and their associated inconsistencies will also be presented. Section 2.3 presents a literature review on recent understanding of crushable soils, with particular emphasis given to the quantification of the strength of soil particles. Section 2.4 presents the application of the discrete element program PFC^{3D} to simulate the behaviour of granular materials. This section mainly presents the concepts and the functions of the program. Recent applications of PFC^{3D} in simulating soil behaviour are also presented.

2.2 Ballast

Ballast has many functions. The most important functions are to retain track position, reduce the sleeper bearing pressure for the underlying materials, store fouling materials, provide drainage for water falling onto the track, and rearrange

during maintenance to restore track geometry. Thus, ballast materials are required to be hard, durable, angular, free from dust and dirt, and have relatively large voids. Since ballast is a type of granular material, behaviour of such a material is well documented in granular materials literature. Past experience of ballast field performance has shown that the progressive breakdown of ballast materials, such as that caused by traffic load and maintenance tamping, and the intrusion of external materials, such as wagon spillage and infiltration of underlying materials into the ballast results in major track deterioration. The response of fouled ballast is highly dependent on the types of fouling materials, the quantity of fouling materials and water content.

2.2.1 Track components and functions

Track components are grouped into two main components: the superstructure and substructure. The superstructure refers to the top part of the track that is the rails, the fastening system and the sleepers, while the substructure refers to the lower part of the track: that is the ballast, the subballast and the subgrade. Figures 2.1 and 2.2 show the components of a typical ballasted track.

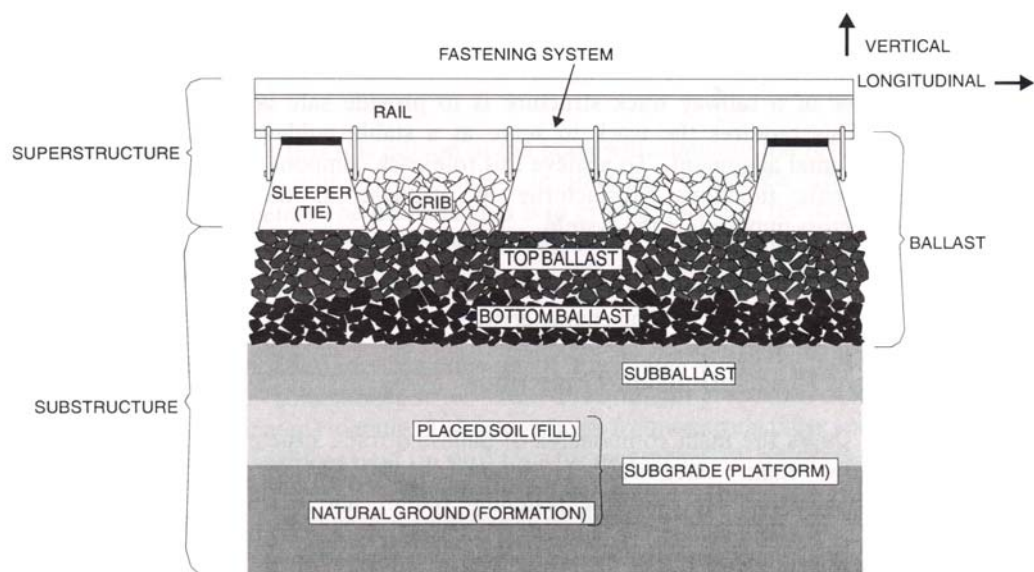


Figure 2.1. Track layout of a typical ballasted track- side view (Selig & Waters, 1994).

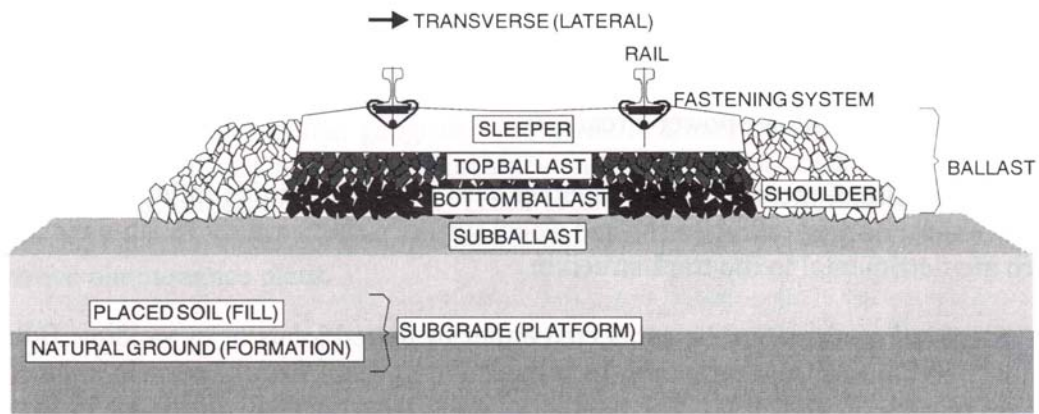


Figure 2.2. Track layout of a typical ballasted track- cross section (Selig & Waters, 1994).

Rails are the longitudinal steel members which are in contact with the train wheels. The function of the rails is to guide the train and transfer concentrated wheel loads to the sleepers. Thus, rails must have sufficient stiffness to distribute wheel loads over sleepers and limit deflection between the supports. Rail defects and discontinuities, such as joints, can cause large impact loads, which have detrimental effects on the track components below.

The fastening system retains the rails against the sleepers and resists vertical, lateral, longitudinal, and overturning movements of the rails. Wooden sleepers require steel plates in their fastening system to distribute the rail force over the wood surface. Concrete sleepers require resilient pads in the fastening system to provide resiliency and damping for the superstructure.

The main functions of sleepers are to distribute the wheel loads transferred by the rails and fastening system to the supporting ballast and restrain rail movement by anchorage of the superstructure in the ballast.

Ballast is the crushed granular material placed as the top layer of the substructure, in the cribs between the sleepers, and in the shoulders beyond the sleeper ends down to the bottom of the ballast layer. Traditionally, good ballast materials are angular, crushed, hard stones and rocks, uniformly graded, free of dust and dirt, not prone to cementing action. However, due to the lack of universal agreement on the specifications for ballast materials, availability and economic considerations have

been the main factors considered in the selection of ballast materials. Thus, a wide range of ballast materials can be found, such as granite, basalt, limestone, slag and gravel. One of the main functions of ballast is to retain track position by resisting vertical, lateral and longitudinal forces applied to the sleepers. Ballast also provides resiliency and energy absorption for the track, which in turn reduces the stresses in the underlying materials to acceptable levels. Large voids are required in the ballast for storage of fouling materials and drainage of water falling onto the track. Ballast also needs to have the ability to rearrange during maintenance level correction and alignment operations.

Subballast is the layer separating the ballast and the subgrade. It reduces the stress levels further to the subgrade, offering a cheaper option to the otherwise thicker ballast. However, the most important function of the subballast is to prevent interpenetration between the subgrade and the ballast. Thus, subballast materials are broadly-graded sand-gravel mixtures, which must fulfil the filter requirements for the ballast and the subgrade.

Subgrade is the foundation for the track structure. It can be existing natural soil or placed soil. The main function of the subgrade is to provide a stable foundation for the track structure. Thus, excessive settlement in the subgrade should be avoided.

2.2.2 Forces exerted on ballast

There are two main forces which act on ballast. These are the vertical force of the moving train and the “squeezing” force of maintenance tamping. The vertical force is a combination of a static load and a dynamic component superimposed on the static load. The static load is the dead weight of the train and superstructure, while the dynamic component, which is known as the dynamic increment, depends on the train speed and the track condition. The high squeezing force of maintenance tamping has been found to cause significant damage to ballast (Selig & Waters, 1994). Besides these two main forces, ballast is also subjected to lateral and longitudinal forces which are much harder to predict than vertical forces (Selig & Waters, 1994).

The dead wheel load can be taken as the vehicle weight divided by the number of wheels. The static load from the dead weight of the train often ranges from about 53kN for light rail passenger services to as high as 174kN for heavy haul trains in North America (Selig & Waters, 1994). The dynamic increment varies with train section as it depends on track condition, such as rail defects and track irregularity. Figures 2.3 (a) and (b) show the static and dynamic wheel loads plotted as cumulative frequency distribution curves for the Colorado test track and the mainline track between New York and Washington respectively (Selig & Waters, 1994). The static wheel load distribution was obtained by dividing known individual gross car weights by the corresponding number of wheels, and the dynamic wheel load distribution was measured by strain gauges attached to the rail. The vertical axes of the two figures give the percentage of total number of wheel loads out of 20,000 axles which exceed the load on the horizontal axis. Clearly, the dynamic increment is more noticeable for high vertical wheel loads and is more significant for the mainline track between New York and Washington than the Colorado test track. This is due to the almost perfect track condition for the Colorado test track. It was also noticed that the high dynamic load for the mainline track between New York and Washington occurred at high speeds (Selig & Waters, 1994).

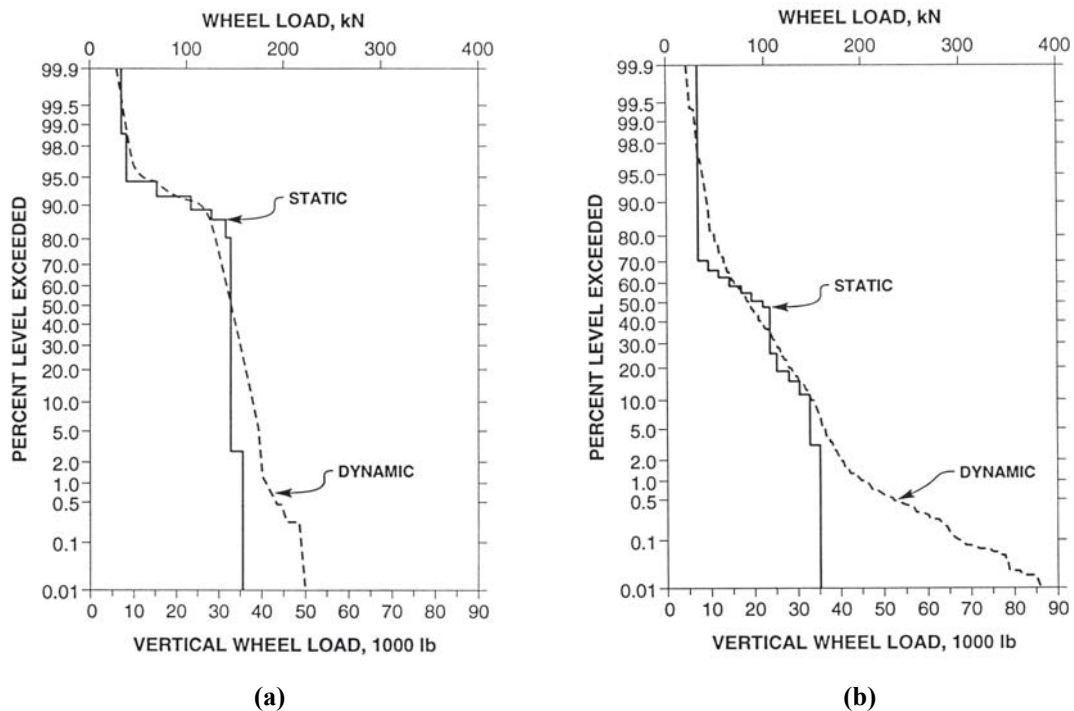


Figure 2.3. Static and dynamic wheel loads for (a) Colorado test track and (b) mainline track between New York and Washington (Selig & Waters, 1994).

The vertical wheel force is distributed through a number of sleepers. The number of sleepers involved is highly dependent on the sleeper spacing and the rail moment of inertia. Selig & Waters (1994) conducted a parametric study using the GEOTRACK computer program, which is a three-dimensional, multi-layer model for determining the elastic response of the track structure. They found that as the sleeper spacing increased from 250mm to 910mm, the load applied to the sleeper beneath the wheel increased by a factor of about 4. They also found that for an increase of rail moment of inertia from 1610cm^4 to 6240cm^4 , the load applied to the sleeper beneath the wheel decreased by 40%. The vertical downwards force at the rail-wheel contact points tends to lift up the rail and sleeper some distance away from the contact point, as shown in Figure 2.4 (Selig & Waters, 1994). The uplift force depends on the wheel loads and self-weight of the superstructure. As the wheel advances, the lifted sleeper is forced downwards causing an impact load, which increases with increasing train speed. This movement causes a pumping action in the ballast, which increases the ballast settlement by exerting a higher force on the ballast and causing “pumping up” of fouling materials from the underlying materials in the presence of water (Selig & Waters, 1994). It is also noted that the impact load increases with the increase in track irregularity or differential settlement (i.e. impact load increases with the increase in the size of the gap underneath the sleeper). The increase of impact load would then lead to an increase in ballast settlement and lead to a larger gap underneath the sleeper. Thus, track geometry tends to degrade in an accelerating manner.

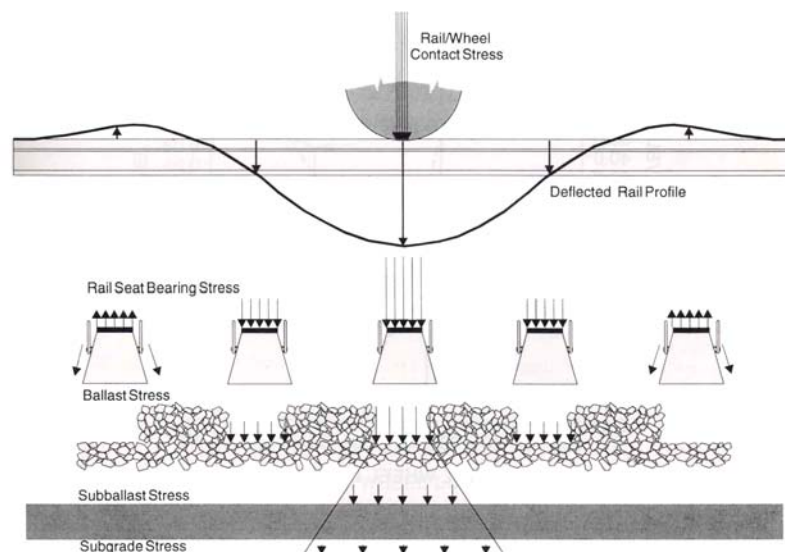


Figure 2.4. Uplift of rails (Selig & Waters, 1994).

Maintenance tamping is the most effective way of restoring track geometry especially where a high lift is required. The process involves lifting the sleeper to a desired level and inserting tamping tines into the ballast with the lifted sleeper between each pair of tines. The tamping tines then squeeze ballast to fill the void underneath the lifted sleeper. This process is shown in Figure 2.5. The impact from the insertion of the tamping tines into the ballast and the high squeezing force have been found to cause particle breakage (Wright, 1983).

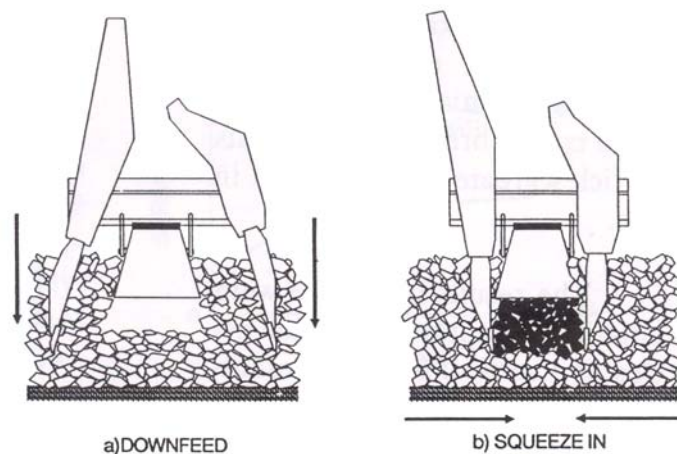


Figure 2.5. Tamping action (Selig & Waters, 1994).

The lateral force is the force that acts parallel to the long axis of the sleepers. The principal sources of this type of force are lateral wheel force and buckling reaction force (Selig & Waters, 1994). The lateral wheel force arises from the train reaction to geometry deviations in self-excited hunting motions which result from bogie instability at high speeds, and centrifugal forces in curved tracks. These type of forces are very complex and much harder to predict than vertical forces (Selig & Waters, 1994). The buckling reaction force arises from buckling of rails due to the high longitudinal rail compressive stress which results from rail temperature increase. The longitudinal force is the force that acts parallel to the rails. The sources of this force are locomotive traction force including force required to accelerate the train, braking force from the locomotive cars, thermal expansion and contraction of rails, and rail wave action (Selig & Waters, 1994).

2.2.3 Ballast specifications

Ballast materials in the United Kingdom are selected based on the specification provided by Railtrack Line Specification (RT/CE/S/006 Issue 3, 2000), which specifies the required grading, properties and shape of track ballast. Appendix E of this specification states that from April 2005, new values of these parameters should be adopted, so as to follow the European specification (BS EN 13450, 2002). Network Rail Limited, which is the company responsible for maintaining the railway infrastructure in the United Kingdom, has already adopted this (2005) specification. Consequently, this section examines the original (2000) specification, in addition to the 2005 specification which is now already in use. Hereafter, the two specifications will be referred to as the original (2000) specification and the new (2005) specification respectively. Both the original (2000) specification and the new (2005) specification require ballast to consist of “uniformly graded crushed hard stones, durable, angular and equidimensional in shape, and free from dust, chemical contamination and cohesive particles”.

The original (2000) specification

The original (2000) specification is the Railtrack Line Specification (RT/CE/S/006 Issue 3, 2000). This specification required the uniformity of the ballast grading to comply with a specified size distribution, where the sieve analysis is conducted according to BS812 Section 103.1 (1985). This specification also requires two ballast testing methods to evaluate the hardness and durability of ballast materials. These are the Wet Attrition Value (WAV) test and Aggregate Crushing Value (ACV) test. The shape of the ballast has to conform to a specified flakiness index and elongation index, which limit the amount of flaky and elongated particles in a ballast sample.

The original (2000) specification requires ballast to conform to the particle size distributions shown in Table 2.1.

| Square Mesh Sieve (mm) | Cumulative % by mass passing BS sieve |
|------------------------|---------------------------------------|
| 63 | 100 |
| 50 | 100-97 |
| 37.5 | 65-35 |
| 28 | 20-0 |
| 14 | 2-0 |
| 1.18 | 0.8-0 |

Table 2.1. The original (2000) specification for ballast particle size distributions (RT/CE/S/006 Issue 3, 2000).

The WAV test procedure is specified in BS812 (1951), Clause 27. The WAV test involves rotating 5kg of wet ballast of particle sizes 37.5-50mm in a cylinder mounted on a shaft with the axis inclined at 30 degrees to the axis of rotation of the shaft. The test sample must not have ballast particles with worn edges or faces, and that are flaky or flat. The test sample in the cylinder is rotated 10,000 times at a rate of 30-33 rpm with an equal mass of clean water. The WAV is expressed as the percentage by weight of ballast particles passing the 2.36mm test sieve and is limited to 4% by the original (2000) specification. Wright (1983) investigated the effect of mechanical maintenance techniques on ballast and found that the WAV test gave an opposite indication of ballast behaviour. He found that both maintenance techniques: tamping and stoneblowing, which are used to maintain long and short wavelength faults respectively, produced a greater amount of fines passing the 14mm sieve in granite than in limestone or quartzite, whilst granite produced fewer fines than limestone or quartzite in the WAV test. Selig & Boucher (1990) summarized an investigation conducted by British Rail on the effect of particle size, particle condition and presence of slurry on the results of the WAV test. It was found that the percentage of fines generated increased with increasing particle size. Freshly crushed particles were also found to generate more fines than used particles. Conflicting results were found for the effect of slurry, as shown in Figure 2.6. The tests with washed particles were tests with ballast particles removed from the cylinders every 10,000 revolutions, and the ballast particles washed and returned to the cylinder. The tests with fines retained were tests with fine particles retained in

the cylinder after each 10,000 revolutions. This figure shows that the percentage of fines generated was greater for granite and less for limestone when slurry was retained during the test. This observation has not been explained (Selig & Boucher, 1990).

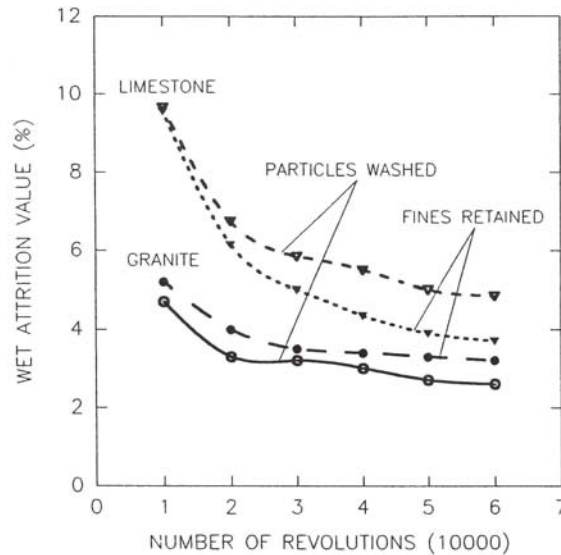


Figure 2.6. Effect of slurry on ballast in WAV test (Selig & Waters, 1994).

The Aggregate Crushing Value (ACV) test gives a relative measure of the resistance of an aggregate to crushing under a gradually applied compressive load (BS 812 Part 110, 1990). This test involves compacting a prepared test portion of dry ballast of particle size 10-14mm with a tamping rod in a 150mm diameter cylindrical steel mould. The depth of the compacted test specimen is approximately 100mm. The compacted specimen in the steel mould is then compressed at a uniform rate to 400kN in approximately 10min. The tested specimen is sieved with a 2.36mm test sieve and the ACV is expressed as the percentage by weight of ballast particles passing the 2.36mm test sieve. The original (2000) specification requires the ACV to be less than or equal to 22%. According to the original (2000) specification, not more than 2 percent by weight of the new ballast shall pass the 14mm test sieve. Thus, the ballast particles used in the ACV test only represent less than 2 percent by weight of the ballast used on the track. In addition, the average strength of the 10-14mm ballast particles will be different from the average strength of the larger ballast particles (e.g. 28-50mm), because there is a size effect on particle strength. The size effect on particle strength will be discussed later in section 2.3.1.

The flakiness index test is specified in BS812 Section 105.1 (1989). The definition of a flaky particle is one having a thickness, which is the smallest dimension, of less than 0.6 of the mean sieve size. The flakiness index test involves sieving a prepared test portion with special sieves having elongated apertures. Each aggregate size fraction is sieved with an elongated aperture having a width of 0.6 times the mean sieve size fraction. The flakiness index is expressed as the percentage by weight of ballast particles passing the special sieves and the original (2000) specification limits the flakiness index to 40%. Flaky particles were limited in this specification because increasing the amount of flaky particles in a ballast sample increases breakage. For example, Gur et al. (1967) shows that increasing the proportion of flaky material increases the ACV and the Los Angeles Abrasion (LAA) values, as shown in Figure 2.7. This figure also shows that the increase in LAA values is more extensive than the increase in ACV. Gur et al. (1967) explains this behaviour as the fracture of one particle in the ACV test would increase the number of contact points and reduce the stress concentration of another particle in the sample, whilst the fracture of one particle in the LAA test does not affect another particle in the sample.

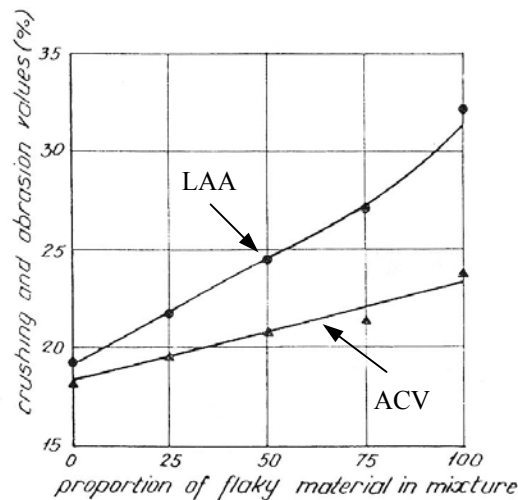


Figure 2.7. Los Angeles Abrasion (LAA) values and Aggregate Crushing Values (ACV) in different mixtures of flaky and non-flaky materials (Gur et al., 1967).

The elongation index test is specified in BS812 Section 105.2 (1990). The definition of an elongated particle is one having a length, which is the greatest dimension, of more than 1.8 times the mean sieve size. The elongated index test involves gauging by hand a prepared test portion with a metal length gauge, which has slots for

different sieve size fractions. Each aggregate size fraction is gauged by hand according to a slot that has a length of 1.8 times the mean sieve size fraction. The elongation index is expressed as the percentage by weight of ballast particles whose greatest dimension prevents them from passing through the designated slot. The original (2000) specification limits the elongation index to 50%.

The new (2005) specification

The new (2005) specification follows the European railway ballast specification BS EN 13450 (2002). This standard recommends a range of tests to define ballast properties. It also provides a range of categories or classes for ballast properties to enable users to select the appropriate limiting values for railway ballast. The new (2005) specification selects five ballast properties to define the specification for track ballast: ballast grading, Los Angeles Abrasion (LAA), micro-Deval attrition (MDA), flakiness index, and particle length.

The new (2005) specification requires track ballast to conform to the particle size distributions shown in Table 2.2. The sieving and analysis must follow EN 933-1 (1997).

| Square Mesh Sieve (mm) | Cumulative % by mass passing BS sieve |
|------------------------|---------------------------------------|
| 63 | 100 |
| 50 | 70-100 |
| 40 | 30-65 |
| 31.5 | 0-25 |
| 22.4 | 0-3 |
| 32-50 | ≥ 50 |

Table 2.2. The new (2005) specification for ballast particle size distributions (RT/CE/S/006 Issue 3, 2000).

The Los Angeles test for railway ballast is carried out as specified in EN 1097-2 (1998) with modifications specified in BS EN 13450 (2002). This test measures the resistance of ballast to fragmentation by providing a Los Angeles Abrasion (LAA) coefficient. The definition of the LAA is the percentage of the test portion passing a 1.6mm sieve after the completion of the test. So, ballast specimens with high values of LAA are more susceptible to fragmentation. The LAA test involves rotating 5 kilograms of 31.5-40mm and 5 kilograms of 40-50mm dry ballast with 12 spherical steel balls weighing approximately 5.2 kilograms in a steel drum. The steel drum is rotated on a horizontal axis for 1000 revolutions with a rotational speed of 31-33 rotations per minute. The tested ballast materials are sieved using a 1.6mm sieve to compute the LAA. The new (2005) specification limits the LAA value to 20.

The micro-Deval test is carried out as specified in EN 1097-1 (1996) with modifications specified in BS EN 13450 (2002). This test measures the resistance of ballast to wear by providing a Micro-Deval Attrition (MDA) coefficient to the ballast tested. The definition of the MDA is the percentage of the test portion passing a 1.6mm sieve after the completion of the test. So, ballast specimens with high values of MDA are more susceptible to wear. The micro-Deval test involves rotating two specimens of dry ballast materials in two separate steel drums. Each specimen consists of 5 kilograms of 31.5-40mm and 5 kilograms of 40-50mm particles. Two litres of water are added into each steel drum and the ballast specimen is rotated on a horizontal axis for 14,000 revolutions with a rotational speed of approximately 100 rotations per minute. The tested ballast specimens are sieved using a 1.6mm sieve to compute the MDA. The new (2005) specification requires the mean value of the MDA for the two specimens to be less than or equal to 7.

The flakiness index test is specified in EN 933-3 (1997). The definition of a flaky particle is one having a thickness, which is the smallest dimension, of less than 0.5 times the larger sieve size fraction. The flakiness index test consists of two sieving operations, the first of which involves using test sieves to separate ballast samples into various particle size fractions. The second is to sieve each size fraction using bar sieves, which have parallel slots of width 0.5 times the larger sieve size. The flakiness index is expressed as the percentage by weight of ballast particles passing

the bar sieves. The new (2005) specification requires the flakiness index to be less than or equal to 35.

The particle length index is defined as the percentage by mass of ballast particles with length larger than or equal to 100mm in a ballast sample of mass exceeding 40kg. This test is conducted by measuring each ballast particle with a gauge or callipers. The new (2005) specification requires the particle length index to be less than or equal to 4.

2.2.4 Resilient behaviour of granular material

Hveem & Carmany (1948) and Hveem (1955) introduced the concept of resilient behaviour and highlighted the importance of resilient behaviour in pavements, particularly in understanding the fatigue cracking of asphalt surfaces. The resilient modulus of a material is defined as the repeated deviator stress divided by the recoverable (resilient) axial strain during unloading in the triaxial test (Seed et al., 1962), as shown in Figure 2.8. Resilient behaviour of railway trackbed is also important; for example, the resilient properties of the subgrade have been shown to affect the degradation and rate of settlement of ballast (Raymond & Bathurst, 1987). The resilient behaviour of the ballast itself will also contribute to the recoverable deformations of the trackbed.

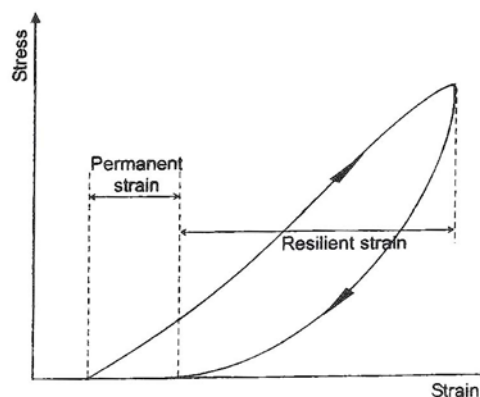


Figure 2.8. Strains in granular materials during one cycle of load application (Lekarp et al., 2000a).

The resilient modulus generally increases gradually with the number of repeated load applications as the material stiffens. The resilient modulus eventually comes to an approximately constant value after a certain number of repeated load applications and the material behaves in an almost purely resilient manner, as shown in Figure 2.9.

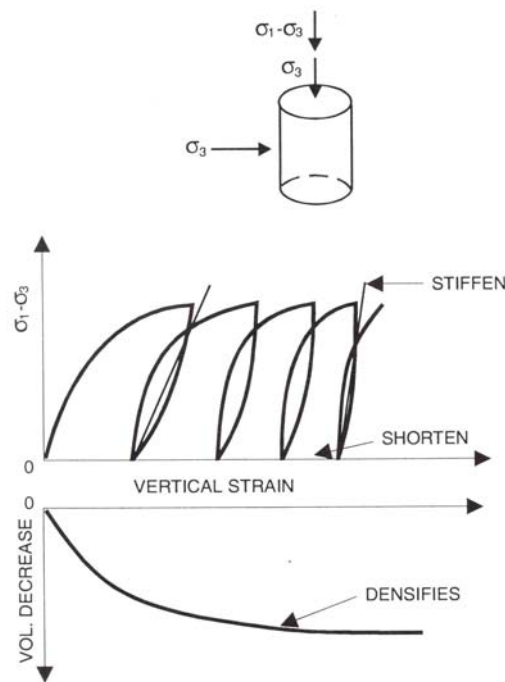


Figure 2.9. Behaviour of ballast under cyclic triaxial test (Selig & Waters, 1994).

The resilient modulus is affected by many factors, such as stress level, density, grading, fines content, maximum grain size, aggregate type, particle shape, moisture content, stress history and number of load applications. However, only the influence of stress and moisture content are consistent (Lekarp et al., 2000a). Researchers agree that the resilient modulus increases considerably with an increase in confining pressure and sum of principal stresses (Lekarp et al., 2000a). The effect of moisture on resilient modulus depends on the degree of saturation. At low degrees of saturation, the moisture content has negligible effect on resilient modulus. However, the resilient modulus decreases considerably for high degrees of saturation, especially as the aggregate approaches complete saturation (Lekarp et al., 2000a).

The effect of stress on the resilient modulus can be described by a widely used $K-\theta$ model (Hicks & Monismith, 1971), which expresses the resilient modulus M_r as a function of the sum of principal stresses or bulk stress θ in the loaded state:

$$M_r = k_1 \theta^{k_2} \quad (2.1)$$

where k_1 and k_2 are constants. Figure 2.10 shows repeated load triaxial test results on a crushed granite ballast which can be described by equation 2.1.

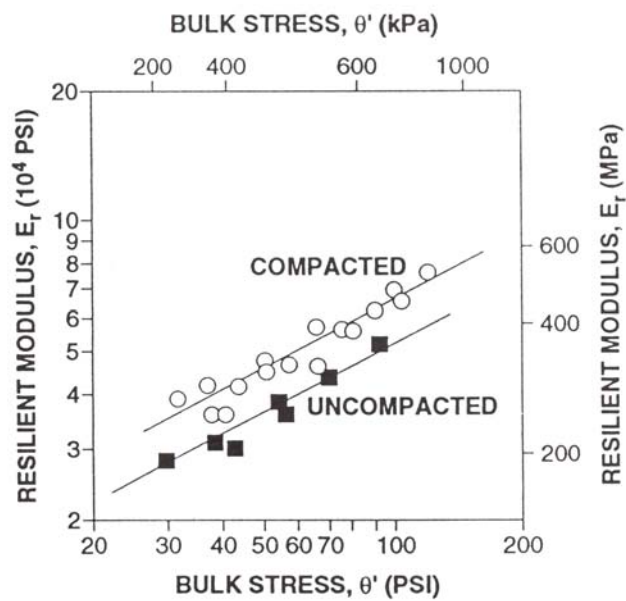


Figure 2.10. Resilient modulus against bulk stress (Alva-Hurtado, 1980).

It should be noted that the $K-\theta$ model has several drawbacks, such as assuming a constant Poisson's ratio to model radial strain of the material, and it does not include the effect of the deviator stress. Many modifications of the model can be found in the pavement soil mechanics literature. However, it was noted that a better description of the resilient behaviour of granular materials can be obtained by decomposing both stresses and strains into volumetric and shear components (Brown & Hyde, 1975). For example, the contour model by Pappin & Brown (1980) treats volumetric and shear strains separately and gives stress-dependent bulk and shear moduli.

2.2.5 Permanent deformation of granular material

The irrecoverable strain of granular material during unloading, or permanent strain, is defined in Figure 2.8. Possible micro mechanisms for the accumulation of permanent strain which occurs under repeated loading are particle rearrangement and particle breakage.

The influence of stress level on permanent strain is very significant. Knutson (1976) concluded that the permanent strain accumulated after a certain number of repeated loads is directly related to the ratio of deviatoric stress q to confining stress σ_3 , which might be called a stress ratio, but is not the conventional stress ratio q / p' , where p' is the mean effective stress. Increasing the stress ratio q / σ_3 (with either σ_3 or q held constant) increases the permanent strain accumulated after a certain number of repeated loads, as shown in Figure 2.11, which shows the increase in permanent strain with number of repeated loads for different values of q and σ_3 for the triaxial test on limestone ballast (Knutson, 1976). This figure also shows that, for the same stress ratio (i.e. 20/5 and 60/15 both correspond to $q / \sigma_3 = 4$), increasing the stress path length increases the amount of permanent strain accumulated. This is consistent with Lekarp et al. (2000b).

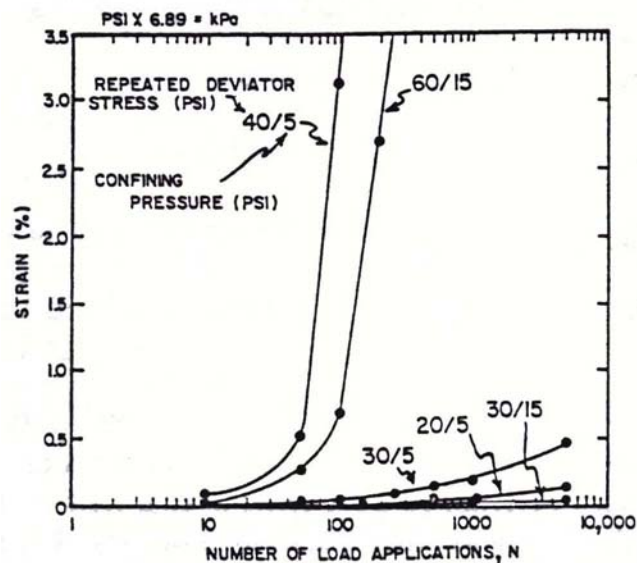


Figure 2.11. Effect of stress ratio on permanent strain (Knutson, 1976).

The sequence of loading does not affect permanent strain accumulation (Selig & Waters, 1994). Figure 2.12 shows a typical result of permanent strain accumulation for different loading sequences, where the deviator stress was changed after every 1000 load applications. Clearly, the final permanent strains for all the different loading sequences are approximately equal. Shenton (1974) investigated a large triaxial test with a two-block loading sequence, as shown in Figure 2.13. He found that the contribution of the second block of loading to the total deformation depended on the ratio of the stress in the second block to the stress in the first block, as shown in Figure 2.14. The contribution of the second block of loading to the total deformation was found to increase with increasing ratio. It is interesting to note that if the ratio of the stress in the second block to the stress in the first block was less than 0.5, some recovery was observed on application of the smaller stresses - in other words, the sample was found to get longer (Shenton, 1974).

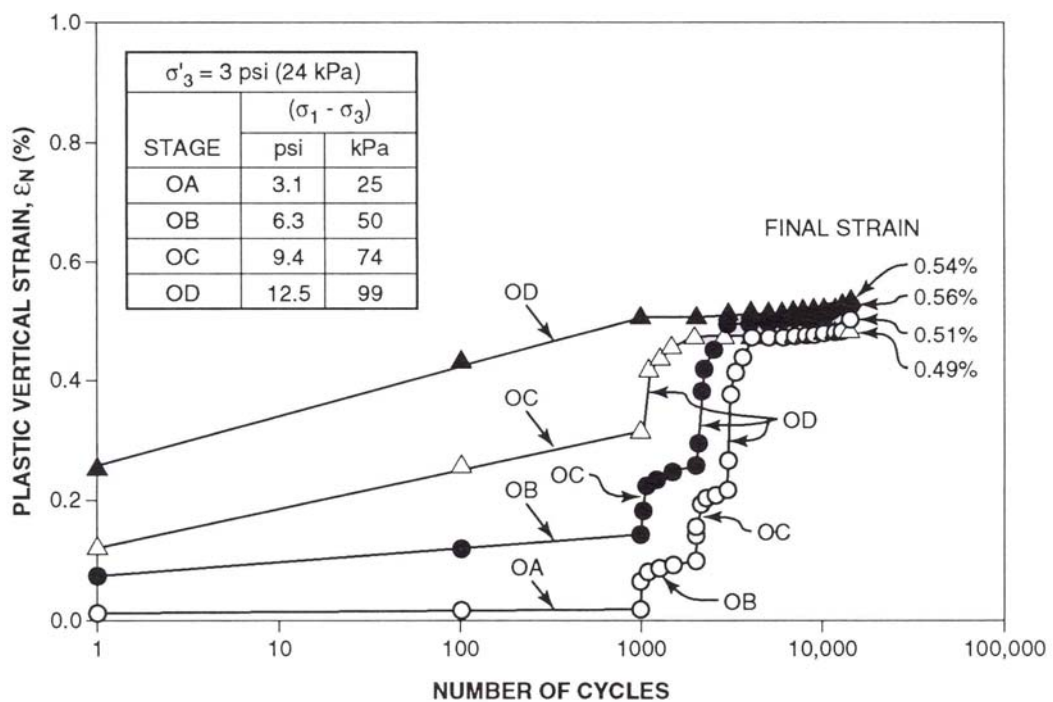


Figure 2.12. Effect of difference in sequence of loading on permanent strain (Selig & Waters, 1994).

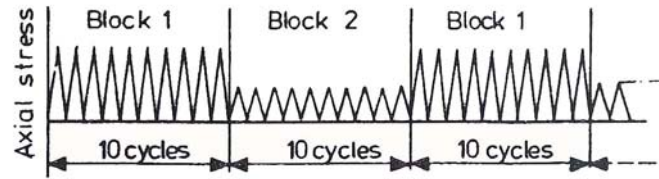


Figure 2.13. Loading sequences (Shenton, 1974).

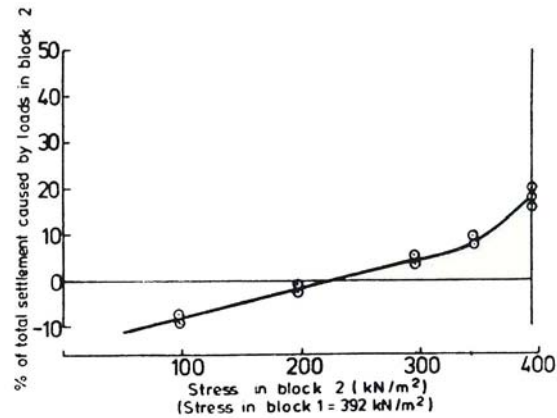


Figure 2.14. Contribution of second block of loading to total deformation (Shenton, 1974).

It is universally accepted that settlement is related to the logarithm of the number of repeated load applications, as shown in Figure 2.15 (Shenton, 1974). For this particular test, the relationship is seen to be linear after 10^3 cycles. Thus, the rate of accumulation of permanent strain with number of repeated load applications has generally been found to decrease with increasing number of applications. However, Lekarp et al. (2000b) reviewed the work of many researchers and found that this is not necessarily the only response. For low stress ratios, it is possible to define a limiting permanent strain and, for high stress ratios, there will be a continuous increase in the rate of accumulation of permanent strain with number of repeated load applications.

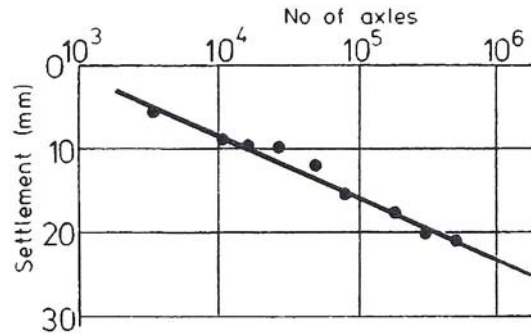


Figure 2.15. Effect of number of repeated load applications on settlement (Shenton, 1974).

Initial density has a significant effect on the accumulation of permanent strain. Lekarp et al. (2000b) noted that many researchers had found that a small decrease in initial density will increase significantly the permanent strain accumulated, and the effect is more significant for angular aggregates than rounded aggregates.

Principal stress rotation occurs in granular materials that are subjected to vehicular load. The effect of principal stress rotation has been found to increase the accumulation of permanent strain (Lekarp et al., 2000b). It should be noted that there is no principal stress rotation for ballast near the sleeper. The wheel loads are transferred through the sleeper to the ballast and the ballast near the sleepers is loaded by a concentrated load. Thus, the major principal stress directly beneath the sleeper will increase rapidly as the wheel load approaches and reduce rapidly as the wheel moves away from the sleeper. It is often assumed that 50% of a given wheel load is transferred to the sleeper below and 25% is transferred to each of the 2 adjacent sleepers. However, deeper ballast or soil will still experience principal stress rotation. The amount of ballast or soil which experiences principal stress rotation depends on the load spreading ability or stiffness of the ballast and the stiffness of the lower layers. For example, if the ballast has good load spreading ability, ballast closer to the sleeper-ballast level may experience principal stress rotation. If the ballast has low stiffness, then only the subgrade may be subjected to principal stress rotation effects.

Shenton (1974) investigated the influence of loading frequency on the accumulation of permanent strain in ballast. He found that the loading frequency does not affect the accumulation of permanent strain. Figure 2.16 shows a plot of normalised axial strain at 10^4 repeated load applications against frequency for the same value of deviator and confining stress. Clearly, there is no evidence to suggest that frequency affects the accumulation of permanent strain.

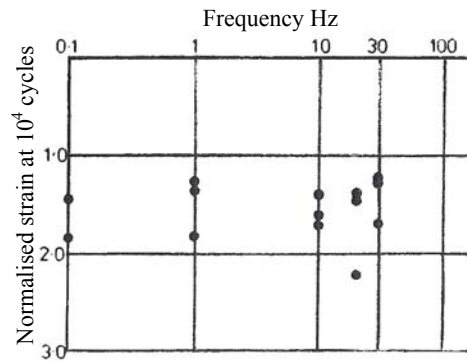


Figure 2.16. Effect of frequency on permanent strain (Shenton, 1974).

2.2.6 Sources of fouling material in ballast

Selig & Waters (1994) summarized a study by the University of Massachusetts on a wide variety of mainline track conditions across North America to identify the sources of fouling materials. The result of this study is shown in Figure 2.17. This study identified ballast breakdown to be the main source of fouling material. The other sources of fouling materials were found to be infiltration from sub-ballast or underlying granular material, or subgrade, surface materials and sleeper wear.

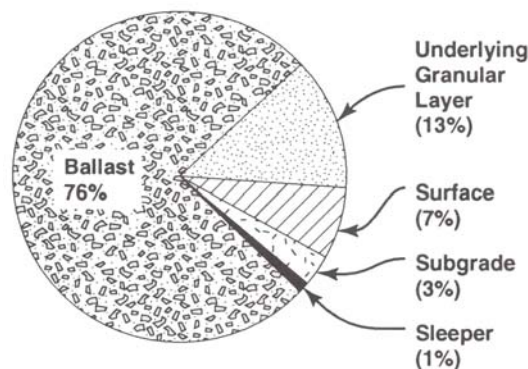


Figure 2.17. Sources of ballast fouling (Selig & Waters, 1994).

Newly placed ballast would already have some breakage due to transporting, dumping and compaction. During the ballast service life, ballast breakage occurs because of traffic loading, freeze-thaw action, weathering and maintenance tamping. Many researchers have identified maintenance tamping to be the main source of ballast breakdown. Wright (1983) investigated the effect of tamping in the track laboratory at British Railways. He found that approximately 2 to 4 kg of fines less than 14mm was generated per tamp for a single sleeper. Tamping has not only an immediate effect on ballast breakage, but also a long-term effect. Tamping loosens ballast and produces new particle contact points. These new contact points may fracture under contact stresses. Selig & Waters (1994) conducted box tests to investigate the effect of particle rearrangement on particle breakage. The results are shown in Figure 2.18. The results designated “maintained” refer to the box tests where the ballast was rearranged every 100,000 cycles to simulate the loosening effect of tamping. It can be seen that more breakage occurs in the tests where the ballast was rearranged.

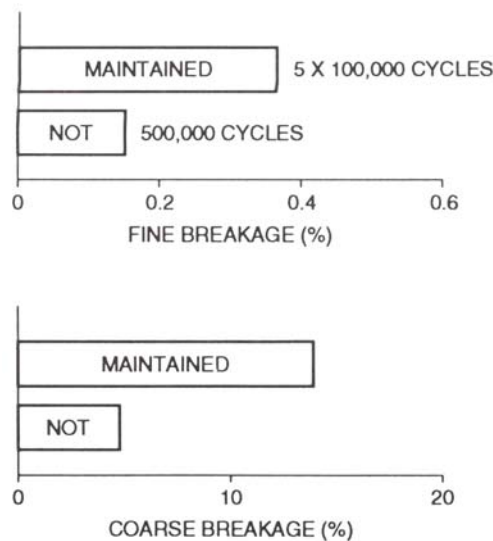


Figure 2.18. Effect of particle rearrangement on particle breakage (Selig & Waters, 1994).

Infiltration from sub-ballast is expected because of its direct contact with ballast. The infiltration will increase in the presence of water because of the pumping action of traffic, which occurs due to the reduced permeability of the ballast. The presence of water also causes clay slurry to form at the subgrade, which will “pump” up into

the ballast under traffic load. The main source of surface infiltration is wagon spillage and sleeper wear, which occurs for both wood and concrete sleepers.

2.2.7 Effect of fouling material on ballast behaviour

Fouling materials can have a beneficial or adverse effect on fouled ballast. The effect depends on the types of fouling material present, the degree of fouling and the water content. Han & Selig (1997) conducted box tests to investigate the effect of fouling materials on ballast settlement. Figure 2.19 shows the effect of different degrees of fouling and fouling materials on ballast settlement. It can be seen that ballast settlement increases with increasing degree of fouling for all fouling materials. Han & Selig (1997) noted that if the fouling material was moist silt, the ballast settled less than if moist clay was the fouling material, provided the degree of fouling was less than 20%. However, the reverse behaviour was observed if the degree of fouling was more than 20%. They proposed that this observed behaviour was due to cohesion developing as the degree of fouling increased. Figure 2.20 shows further tests conducted by Han & Selig (1997) to investigate the effect of water content on ballast settlement for different degrees of fouling and fouling materials. The dry clay chunks, as described by Han & Selig (1997), gave the least settlement for all degrees of fouling, because of their high strength and stiffness. As water was added to the clay, the settlement increased dramatically with increasing degree of fouling. This effect was thought to be due to ballast particles being lubricated by “extra” wet clay between them. A similar explanation applies to the dramatic increase in ballast settlement for wet silt with a degree of fouling higher than 30%. Han & Selig (1997) also noted that there is little difference in ballast settlement for different fouling materials and water content if the degree of fouling is less than 20%. They proposed that if the degree of fouling is less than 20%, ballast particles still form the structural skeleton of the ballast, where almost all the load is carried by the ballast particles and ballasts fouled by different materials will almost behave and settle in the same manner.

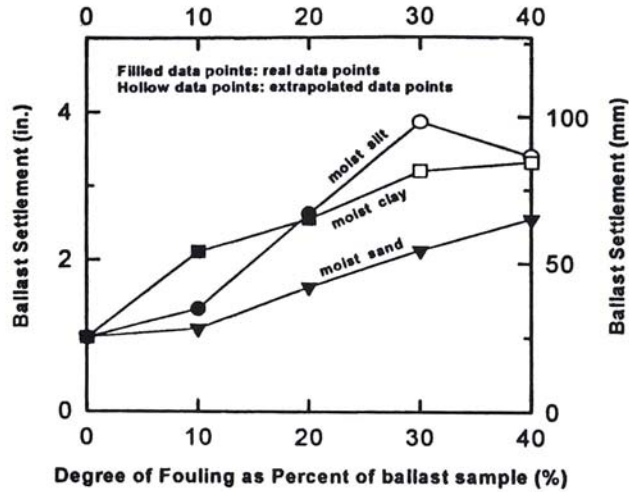


Figure 2.19. Effect of degree of fouling and type of fouling material on ballast settlement (Han & Selig, 1997).

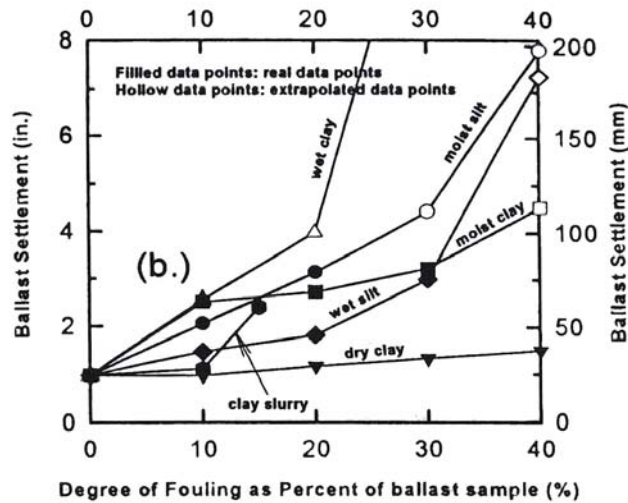


Figure 2.20. Effect of water content on ballast settlement for different degrees of fouling and fouling materials (Han & Selig, 1997).

2.2.8 Effect of fouling on drainage

One of the main functions of ballast is to provide large voids for drainage and storage of fouling materials. As the degree of fouling increases, the large voids will be slowly filled by fouling materials and the permeability of the ballast will slowly decrease. This will lead to an adverse effect on the ballast such as build up of pore

water pressure and mixing of the fouling materials with water, which then lubricate the contacts of the ballast particles.

Selig et al. (1993) documented the effect of the degree of fouling on permeability. Table 2.3 shows the measured hydraulic conductivity of ballast specimens ranging from clean to highly fouled. The degrees of fouling were measured using the fouling index, F_1 , which is given by:

$$F_1 = P_4 + P_{200} \quad (2.2)$$

where P_4 and P_{200} are the percentages by mass passing 4.75mm and 0.075mm sieves respectively. Clearly, the hydraulic conductivity of the ballast reduces considerably with increasing degree of fouling. For example, the hydraulic conductivity of clean ballast reduces by a factor of 10^4 when it becomes highly fouled. Selig et al. (1993) noticed that as the degree of fouling increases, there is a tendency for the hydraulic conductivity of the specimens to be highly dependent on how the voids are filled. Thus, he concluded that the source of fouling material and the extent to which the fouling materials are compacted determines the permeability of ballast.

| Fouling Category | Fouling Index | Hydraulic Conductivity, k_h | |
|-------------------|---------------|-------------------------------|-----------|
| | | (in./sec) | (mm/sec) |
| Clean | <1 | 1-2 | 25-50 |
| Moderately clean | 1-9 | 0.1-1 | 2.5-25 |
| Moderately fouled | 10-19 | 0.06-0.1 | 1.5-2.5 |
| Fouled | 20-39 | 0.0002-0.06 | 0.005-1.5 |
| Highly fouled | >39 | <0.0002 | <0.005 |

Table 2.3. Hydraulic conductivity values for ballast (Selig et al., 1993).

2.3 *Micromechanics of crushable aggregates*

The survival probability of a particle in an aggregate subjected to one-dimensional compression is determined by the applied macroscopic stress, the size of the particle and the coordination number, which is the number of contacts with neighbouring particles (McDowell et al., 1996). An increase in applied macroscopic stress would increase the average induced tensile stress in a particle. Thus, the probability of fracture of a particle must increase with any increase in applied macroscopic stress. There is a variation in soil particle strength because of the dispersion in internal flaw sizes. Large particles will exhibit a lower average tensile strength because they will tend to contain more and larger internal flaws compared to smaller particles. Thus, the fracture probability of a particle reduces with a decrease in particle size. The fracture probability of a particle would also reduce with an increase in the coordination number because the induced tensile stress in a particle is reduced by the compressive stress caused by the many contacts. The tensile strength of a soil particle can be obtained by compressing the particle between two flat platens. It has been found (McDowell & Amon, 2000) that the average strength and variation in strengths of soil particles is consistent with Weibull statistics (Weibull, 1951). McDowell & Bolton (1998) proposed that yielding of an aggregate subjected to one-dimensional compression was due to the onset of particle fracture and proposed that the yield stress of an aggregate ought to be proportional to the average tensile strength of the constituent grains. This section examines the use of Weibull statistics to quantify particle strength, and the role of particle strength in determining the yield stress of a granular aggregate.

2.3.1 Fracture mechanics

Ceramics are brittle materials having low fracture toughness. This means that when a stress is intensified at the crack-tip, the material will have little plasticity to resist the propagation of the crack and the material fails by fast fracture. In addition, ceramics always contain cracks and flaws and the severity depends on how the ceramic was formed, transported etc. Hence, the strength of a ceramic is determined

by its low fracture toughness and by the distribution of the sizes of the micro cracks it contains. The onset of mode I (i.e. tensile) fast fracture, is given by the equation:

$$K_{Ic} = \sigma \sqrt{\pi a} = \sqrt{EG_c} \quad (2.3)$$

where K_{Ic} is the critical stress intensity factor or fracture toughness, σ is the critical tensile stress, a is the crack size, E is the Young's modulus and G_c is the energy required to generate unit area of crack or the critical strain energy release rate. It can be seen from the equation that the critical combination of stress and crack length at which fast fracture commences is a material constant.

It is inherent in the strength of ceramics that there will be a statistical variation in strength because of the dispersion in flaw sizes. There is no single 'tensile strength' for a ceramic but there is a certain, definable, probability that a given sample will have a given strength. Since the critical stress at failure is inversely proportional to the critical flaw size (Griffith, 1920), a large particle is more likely to fail at a lower stress than a small particle, because it is more likely that the larger particle will contain more and larger flaws. Thus, as particles fracture, the resulting fragments become statistically stronger. Similarly, for a specimen loaded in such a way that there is a higher proportion of the volume under tensile stress, there is a higher probability of fracture for a given peak value of internal stress, because the volume under tension is more likely to contain a critical flaw.

Davidge (1979) found that Weibull (1951) statistics is applicable in many cases for analysing the variation in strength of ceramics. The simplest form of Weibull (1951) statistics is based on a "weakest link" model. This model basically means that if one element in a larger sample of interconnected identical elements fails, then the whole sample will fail. The survival probability $P_s(V_o)$ for an element of volume V_o to survive under a tensile stress σ is given by:

$$P_s(V_o) = \exp \left[- \left(\frac{\sigma}{\sigma_o} \right)^m \right] \quad (2.4)$$

The stress σ_o is the value of stress for specimens of volume V_o such that 37% of tested specimens survive, and m is the Weibull modulus, which decreases with increasing variability in strength, as shown in Figure 2.21. When $\sigma = 0$, all the samples survive and $P_s(V_o) = 1$. As σ increases, more and more samples fail and $P_s(V_o)$ decreases. For large stresses $\sigma \rightarrow \infty$, all the samples fail and $P_s(V_o) \rightarrow 0$. For a larger sample of volume $V = nV_o$, the survival probability of that sample would be $\{P_s(V_o)\}^n$. Thus the survival probability of a volume V is given by:

$$\begin{aligned}
 P_s(V) &= \left[\exp \left[- \left(\frac{\sigma}{\sigma_o} \right)^m \right] \right]^{V/V_o} \\
 &= \exp \left[- \frac{V}{V_o} \left(\frac{\sigma}{\sigma_o} \right)^m \right] \\
 &= \exp \left[- \left(\frac{\sigma}{\sigma_{ov}} \right)^m \right]
 \end{aligned} \tag{2.5}$$

where σ_{ov} is the stress for specimens of volume V such that 37% of tested specimens survive. It can be seen that σ_{ov} is a strong function of volume V , and is given by the equation:

$$\sigma_{ov} \propto V^{-1/m} \tag{2.6}$$

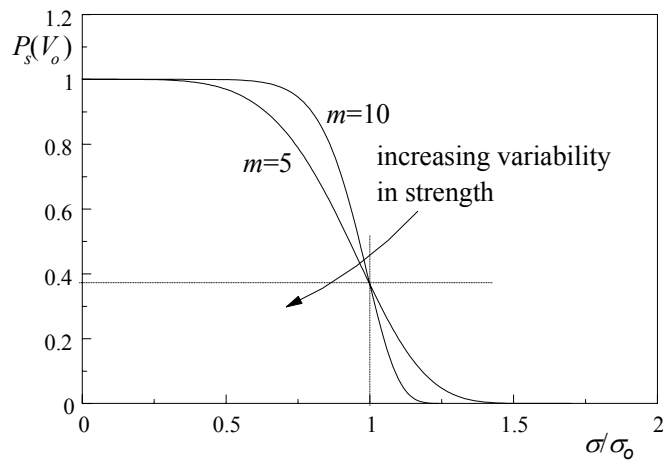


Figure 2.21. Weibull distribution of strengths.

2.3.2 Compression of a single particle

Lee (1992) compressed diametrically individual particles of Leighton Buzzard sand, oolitic limestone and carboniferous limestone, for a range of particle sizes, in a manner shown in Figure 2.22. Lee (1992) then used a similar approach to that for the Brazilian test for tensile strength of concrete and computed the tensile strength of the particles by the equation:

$$\sigma_f = \frac{F_f}{d^2} \quad (2.7)$$

where σ_f is the tensile stress at failure, F_f is the diametral fracture force applied and d is the average particle size calculated by averaging the smallest and largest dimensions of each particle. McDowell & Bolton (1998) defined a general characteristic stress σ as:

$$\sigma = \frac{F}{d^2} \quad (2.8)$$

where F is the force applied and d is the particle size, so that σ_f is the characteristic tensile stress induced within the particle at failure. A typical result of this kind of crushing test is shown in Figure 2.23, which is a plot of force against deformation (Lee, 1992). It can be seen in this plot that there are some initial peaks, which correspond to the bearing failures at contact points, before the maximum peak load is reached. The bearing failures correspond to the fracturing of asperities and rounding of the particle as small corners break off. The maximum peak load corresponds to a major fracture along the loading direction when the particle splits into 2 or more pieces. Hence, the tensile strength of the particle is calculated using the maximum peak load. Figure 2.24 shows the mean tensile strength σ_f as a function of the average particle size d . This figure also includes the 95% confidence levels of the data. Lee (1992) formed an empirical equation from the regression in Figure 2.22 as:

$$\frac{F_f}{d^2} = Kd^b \quad (2.9)$$

where K is a material constant and b is the size index that represents the slope of the plot, which is negative. From this, Lee (1992) proposed the equation:

$$\sigma_f \propto d^b \quad (2.10)$$

to describe the results, with values of b given by -0.357, -0.343 and -0.420 for Leighton Buzzard sand, oolitic limestone and carboniferous limestone, respectively. Equation 2.10 can be used to describe a material containing Griffith flaws (Griffith, 1920), and for which the maximum flaw size in a particle is proportional to the size of the particle, where it is expected that b will be equal to -0.5 (McDowell & Bolton, 1998).

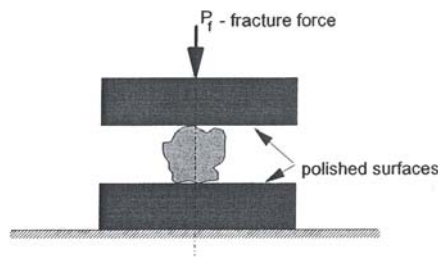


Figure 2.22. Single particle crushing test (Lee, 1992).

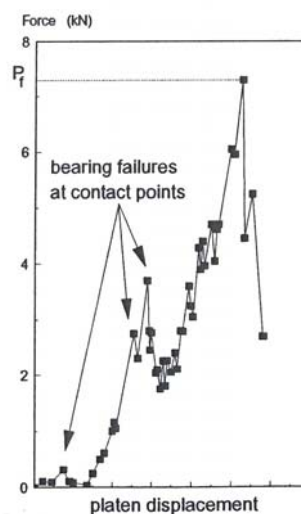


Figure 2.23. Typical plot of force against deformation for a typical particle (Lee, 1992).

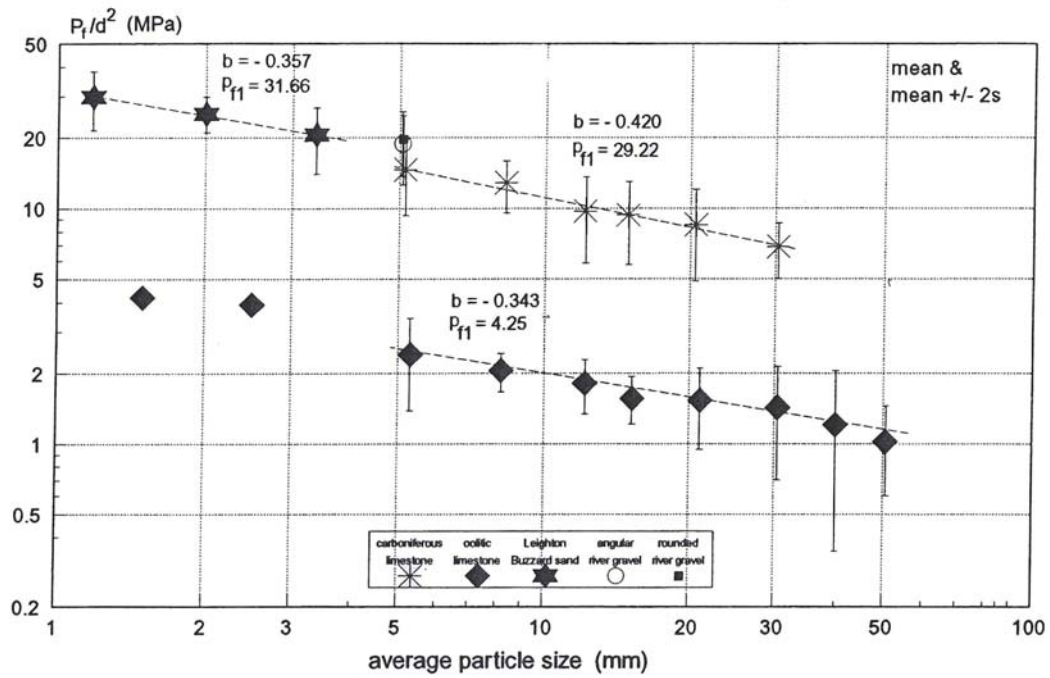


Figure 2.24. Results of single particle crushing tests (Lee, 1992).

2.3.3 Weibull statistics applied to soil particle strength

McDowell & Amon (2000) noticed that the application of Weibull statistics to analyse fracture data from irregular soil particles is difficult because there is no analytical solution for the stress distribution within a spherical particle and irregular particles undergo multiple fracture. However, in order to apply Weibull statistics, McDowell & Amon (2000) made an assumption that all particle loading geometries are similar. It should also be noted that the application of Weibull for a block of volume to survive assumes that failure occurs within the bulk of the material, and involves the integration of some function of stress over the volume of the particle under tension (McDowell & Amon, 2000). The resulting survival probability for a particle of size d is:

$$P_s(d) = \left[-\frac{d^3}{d_o^3} \left(\frac{\sigma}{\sigma_o} \right)^m \right] \quad (2.11)$$

where σ is the characteristic stress defined by equation 2.7 and σ_o is the characteristic stress for particle of size d_o such that 37% of particles survive.

McDowell & Amon (2000) compressed a wide range of particle sizes of Quiou sand in the same manner as Lee (1992) (Figure 2.22). The results are summarised in Table 2.4. It can be seen that the variation of Weibull modulus across the range of particle sizes is great but the average Weibull modulus is approximately equal to 1.5. McDowell & Amon (2000) deduced that for a Weibull distribution of strengths, the 37% tensile strength is proportional to the mean tensile strength. McDowell & Amon (2000) also showed that the average or 37% tensile strength is a strong function of particle size according to the equation:

$$\sigma_{o,d} \propto \sigma_{av} \propto d^{-3/m} \quad (2.12)$$

where $\sigma_{o,d}$ is the stress for particles of size d such that 37% of tested particles survive, σ_{av} is the average stress at failure, d is the particle size at failure and m is the Weibull modulus. It can therefore be noted that b in equation 2.10 is equivalent to $-3/m$. Figure 2.25 shows a log-log scale plot of the 37% strength as a function of average particle size at failure. It appears that there is a strong correlation between the 37% tensile strength and the average size of the particle. The data is described by the equation:

$$\sigma_{o,d} \propto d^{-1.96} \quad (2.13)$$

and this equation corresponds to $m=1.5$. Hence, McDowell & Amon (2000) concluded that Weibull statistics can usefully be applied to the tensile strength of Quiou sand, gravel and cobble-sized particles compressed between flat platens, based on the assumption that all particle loading geometries are similar. The low Weibull modulus implies extreme variability of the material tested. McDowell & Amon (2000) demonstrated that the relationship between the critical flaw size and the size of a test specimen influences the Weibull modulus. Suppose that for grains of soil of size d , the size of the critical flaw a is given by $a \propto d^x$. Hence, Griffith's law (Griffith, 1920) for a disordered material is represented by $x=1$ such that $\sigma_{av} \propto$

$d^{1/2}$ (see equation 2.3), which corresponds to a Weibull modulus of 6. For $x < 1$, as grain size decreases, the size of the critical flaw becomes a higher proportion of the size of the particle, representing a narrower distribution of flaws, less variability and $m > 6$. Engineering ceramics have $m \approx 10$. A value of $x > 1$ implies that as the particle size increases, the flaw size increases at a faster rate, implying an upper limit to the possible size of particle. This corresponds with $m < 6$. For a Weibull modulus of 1.5, the average force at failure should not vary greatly with particle size because the average force at failure is equal to the average stress at failure (which is approximately proportional to d^{-2}), multiplied by the square of the particle size at failure d_f^2 (McDowell & Amon, 2000). Figure 2.26 shows a log-log plot of average force at failure as a function of average particle size at failure for the data produced by McDowell & Amon (2000). Clearly, the average force at failure does not increase much with an increase in average particle size.

| Nominal size/ mm | Average size at failure/mm | Weibull modulus m | 37% tensile strength σ_{co} /MPa |
|---------------------|-------------------------------|------------------------|--|
| 1 | 0.83 | 1.32 | 109.3 |
| 2 | 1.72 | 1.51 | 41.4 |
| 4 | 3.87 | 1.16 | 4.2 |
| 8 | 7.86 | 1.65 | 0.73 |
| 16 | 15.51 | 1.93 | 0.61 |

Table 2.4. Weibull modulus and 37% strength for a wide range of particle sizes of Calcareous Quiou sand (McDowell & Amon, 2000).

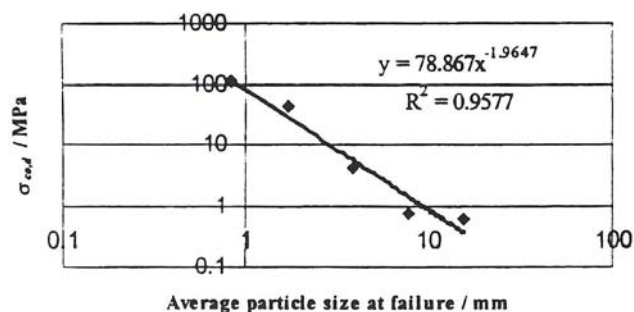


Figure 2.25. 37% strength as a function of average particle size at failure (McDowell & Amon, 2000).

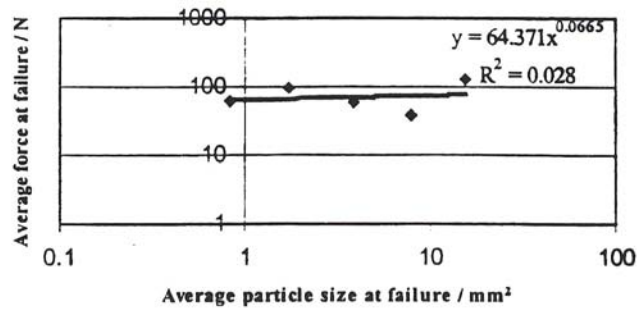


Figure 2.26. Average force at failure as a function of average size at failure (McDowell & Amon, 2000).

McDowell (2001) noted that different values of Weibull Modulus m might be obtained for a given material but different particle sizes, if the number of tests for each size is not sufficient. For example, for a sample size of 30, the population standard deviation can only be estimated to within approximately 25% of the true population value with 95% confidence. The Weibull modulus is related to the ratio of population standard deviation to population mean. In addition, the population mean can only be estimated with a certain accuracy depending on the population standard deviation. For example, with a population Weibull modulus of $m=1.5$, the mean can only be estimated to within 24% of the true population mean, and for $m=3$, the mean can only be estimated to within 13%. Thus, some variations in measured values of sample Weibull modulus are expected, as noticed in Table 2.4, and testing a wide range of particle sizes and plotting mean strength as a function of particle size according to equation 2.12 to deduce the Weibull modulus, gives a useful check on the value of m .

2.3.4 Particle survival in aggregates

McDowell et al. (1996) proposed that the probability of fracture of a particle is determined by the applied macroscopic stress, the size of the particle and the coordination number. The fracture probability of a particle of size d must increase with any increase in macroscopic stress σ , but reduce with a decrease in particle size, or an increase in coordination number. The fracture probability must decrease with a decrease in particle size according to Weibull statistics, since smaller particles

contain fewer and smaller flaws. A higher coordination number will reduce the induced tensile stress in a particle and the extent to which this occurs depends on the shape of the particles. For example, a higher coordination number will be more helpful in reducing the induced tensile stress for a rounded particle than for an angular particle, as illustrated in Figure 2.27 (McDowell et al., 1996).

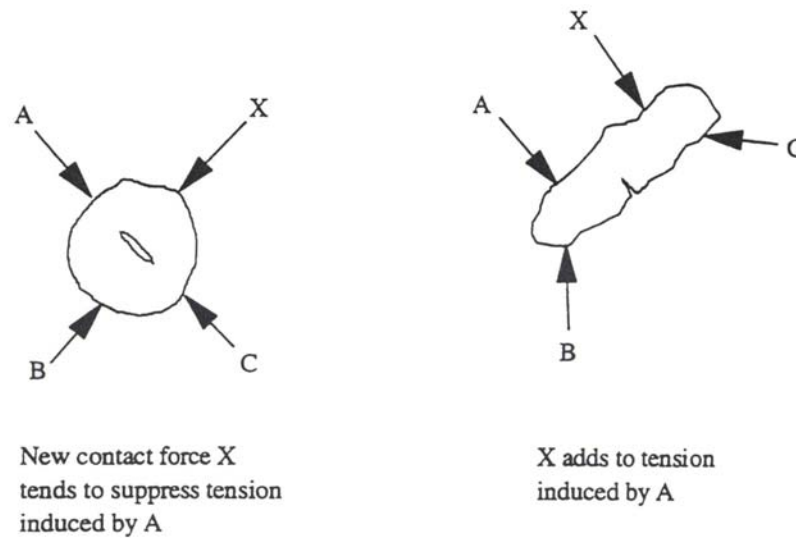


Figure 2.27. Large co-ordination numbers are less helpful for more angular particles (McDowell et al., 1996).

Thus, there are two opposing effects on particle survival: size and coordination number (McDowell & Bolton, 1998). However, smaller particles also have fewer contacts. For example, in a well-graded aggregate, the largest grains will tend to have the highest number of contacts because they are surrounded by many smaller particles. These smaller particles distribute the load over the large particles and reduce the internal tensile stresses. The smallest particles must have the fewest number of contacts on average, and therefore the highest induced tensile stresses. In addition, Sammis (1996) proposed that a particle is most vulnerable when loaded by neighbours of the same size: only then it is possible for the particle to be loaded at opposite poles, and this maximizes the induced tensile stress in a particle. Hence, if particle size dominates over coordination number in the compression of an initially uniform aggregate, then the largest particles are always the most likely to fracture (McDowell et al., 1996). This will lead to a uniform matrix of fine particles at the end of the test: behaviour which is not evident in the geotechnical literature.

However, if the coordination number dominates over particle size, then the smallest particles will always have the highest probability of fracture. This will lead to a disparity of particle sizes, in which a proportion of the original grains is retained under the protection of a uniform compressive boundary stress created by its many neighbours (McDowell & Bolton, 1998). This type of behaviour is evident in geotechnical literature, for example in Figure 2.28, which shows the evolving particle size distribution curves with increasing stress for one-dimensionally compressed Ottawa sand (Fukumoto, 1992).

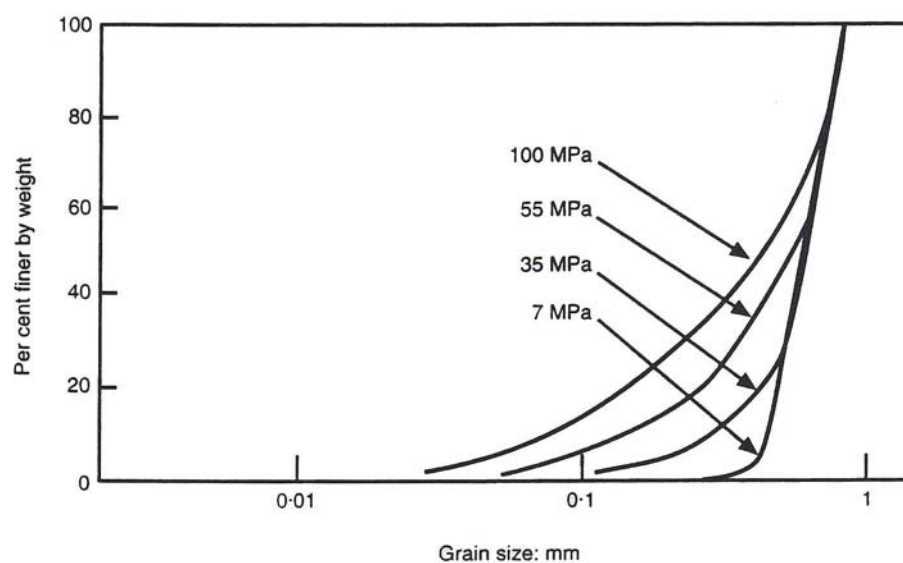


Figure 2.28. Evolving particle size distribution curves for one-dimensionally compressed Ottawa sand (Fukumoto, 1992).

Oda (1977) analysed the co-ordination number in assemblies of glass balls. He found that the mean value of co-ordination number is closely related to the mean value of voids ratio, independent of grain size distribution. Figure 2.29 shows that as the voids ratio decreases, the average co-ordination number increases for all grain size distributions. This will reduce the average tensile stresses induced in the particles, and thus increase the yield stress of the aggregate. Yielding of aggregates is discussed in the next section.

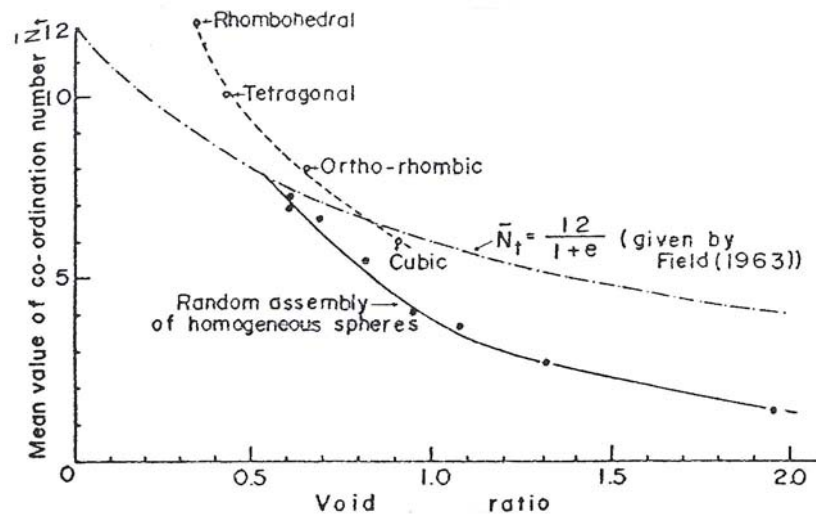


Figure 2.29. Relation between mean coordination number and voids ratio (Oda, 1977).

2.3.5 Yielding of granular materials

McDowell & Bolton (1998) examined the micro mechanics of soils subjected to one-dimensional compression. They noted that at low stresses, the behaviour of soils subjected to one-dimensional compression is quasi-elastic and small irrecoverable deformations may occur due to particle rearrangement. At high stresses, however, further compaction cannot be due to particle rearrangement alone. Thus, they proposed that particle breakage is a prerequisite for further compaction beyond yielding, which is known to be a point where major plastic deformation begins. For an aggregate subjected to one-dimensional compression, if all particles were subjected to the same loading geometry, it would be expected that there would be a macroscopic stress at which the survival probabilities of the particles was 37%. It would be expected that this stress should be proportional to σ_o , the 37% strength for single particles loaded in this way, which also corresponds approximately with the maximum rate of particle fracture with increasing stress (McDowell & Bolton, 1998). McDowell & Bolton (1998) also noted that not all particles are loaded in the same way. However, it may be assumed that all particles will eventually be in the path of the columns of strong force that transmit the macroscopic stress. Cundall & Strack (1979) showed in their numerical simulations using the discrete element method, that the applied major principal stress was transmitted through columns of

strong force as shown in Figure 2.30. The path of these columns of strong force changes as the array of the particles changes due to particle fracture and/or rearrangement. For those particles which are in the path of the columns of strong force, the loading geometry might be assumed to be similar to that loaded by two flat platens. Hence, McDowell & Bolton (1998) proposed that the yield stress must be proportional to the average tensile strength of grains, as measured by crushing between flat platens, and defined yield stress as a value of macroscopic stress which causes maximum rate of grain fracture under increasing stress.

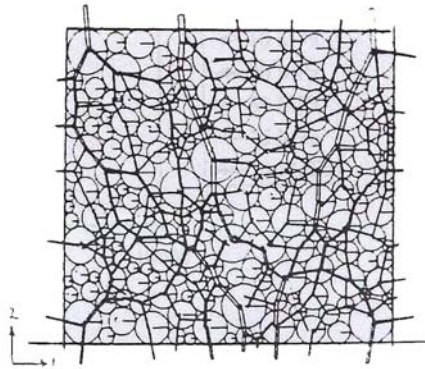


Figure 2.30. Discrete element simulation of array of photoelastic discs $F_H / F_V = 0.43$ (Cundall & Strack, 1979).

One-dimensional compression tests on densely compacted dry silica Leighton Buzzard sand of various initial uniform gradings have been described by McDowell (2002). The initial voids ratio was approximately the same for each aggregate, as all particles were of similar angularity and compacted in the same way to maximum density. Figure 2.31 shows the test results. It is obvious that the stress level in the yielding region depends on the initial grain size and increases with reducing particle size. McDowell (2002) examined Figure 2.30, and noted that the major principal stress applied was only transmitted through two or three columns of strong force for an array approximately 12 particles wide. McDowell (2002) then used a simple estimation that the characteristic stress induced in the particles forming the columns of strong force should be four times the applied macroscopic stress, in order to predict the yield stress of the aggregate as $\frac{1}{4}$ of the 37% tensile strength of the constituent grains in the aggregate. The results are shown in Figure 2.32, which predicts the yield stress fairly well and this further strengthens the proposition made

by McDowell & Bolton (1998) that yield stress should be proportional to the tensile strength of the individual grains.

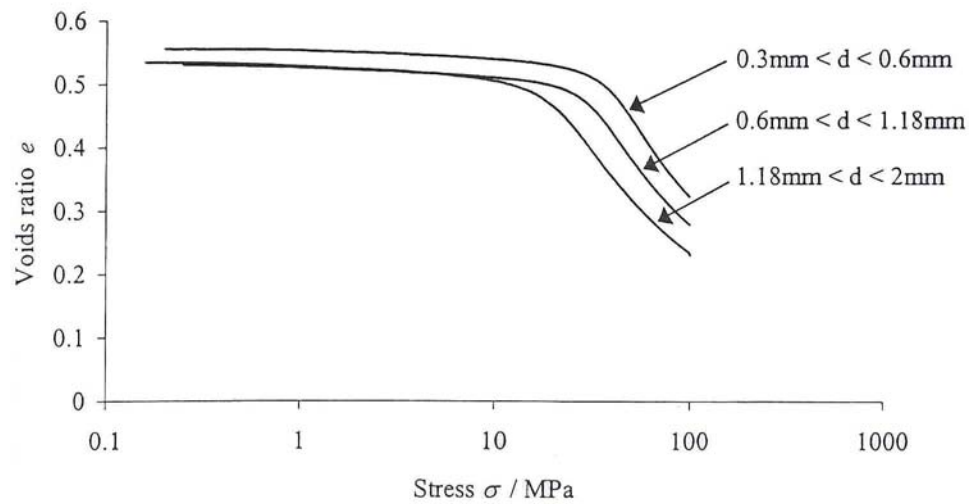


Figure 2.31. Compression plots for different uniform gradings of sand (McDowell, 2002).

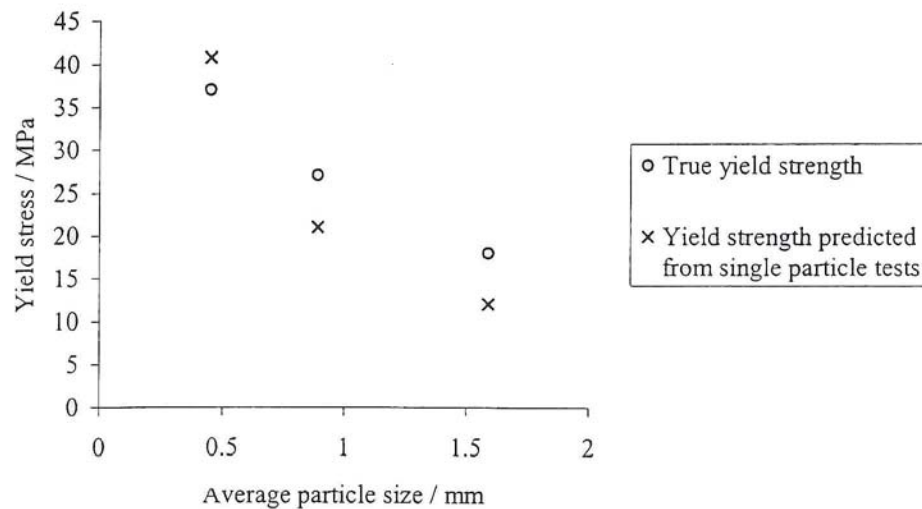


Figure 2.32. Yield stress predicted from single particle crushing tests, assuming yield stress=(37% tensile strength)/4 (McDowell, 2002).

Nakata et al. (1999) used a simple approach to calculate the average force acting on a single particle embedded in a soil matrix. They derived a characteristic tensile stress σ_{sp} of the single particle in a soil matrix as:

$$\sigma_{sp} = \sigma \left(\sqrt[3]{\frac{(1+e)\pi}{6}} \right)^2 \quad (2.4)$$

where σ is the applied macroscopic stress and e is the voids ratio. This equation indicates that the characteristic tensile stress σ_{sp} of a single particle in a soil matrix is not only a function of the applied stress, but also the voids ratio e . Figure 2.33 showed one-dimensional compression test results on Toyoura sand with different initial voids ratios (Nakata et al., 2001). It is obvious in this figure that the yield stress decreased with increasing initial voids ratio. This observation is also consistent with the discussion presented in the last section (2.3.4) i.e. the increase in voids ratio corresponds to a decrease in co-ordination number, which would increase the induced tensile stress in the particles and lead to a decrease in yield stress of the aggregate.

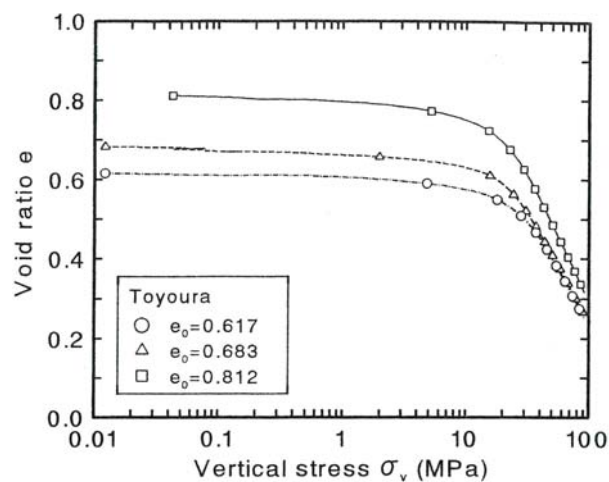


Figure 2.33. Effect of initial voids ratio on one-dimensional compression curve (Nakata et al., 2001).

However, Nakata et al. (2001) note that the characteristic tensile stress does not take into account the non-uniform distribution of inter-particle stresses, and that the ratio of the average single particle strength to the characteristic tensile stress gives an indication of the ratio of active to non-active particles, which increases with increasing angularity. This means that for a given average particle strength, a uniform rounded material should yield at a lower yield stress than an angular one.

2.4 Discrete element modelling using PFC^{3D}

PFC^{3D} has the ability to model entire boundary problems directly with a large number of particles, so that the behaviour of granular materials can be simulated. However, there is a need to reduce computational time so that results can be obtained within an acceptable time and the effect of different loading conditions can be investigated. The recent application of PFC^{3D} to model soil particle fracture has demonstrated that PFC^{3D} has the ability to re-produce the average strength and variation in strength of real soil particles, consistent with Weibull statistics (McDowell & Harireche, 2002a). In addition, it was found that the lowest computational time could be obtained by using the highest speed of loading, which does not affect the results (McDowell & Harireche, 2002a). A preliminary study of triaxial test simulations on an assembly of agglomerates found that it was possible to produce yield surfaces similar to those predicted by plasticity models such as Cam Clay (Robertson, 2000).

2.4.1 Discrete element method and PFC^{3D}

The Discrete Element Method (DEM) is defined as applying to programs that allow finite displacement and rotations of discrete bodies, including complete detachment, and recognise new contacts automatically as the calculation progresses (Cundall & Hart, 1992). In DEM, the interaction of the particles is treated as a dynamic process with states of equilibrium developing whenever the internal forces balance. The equilibrium contact forces and displacement of a stressed assembly are found through a series of calculations tracing the movements of the individual particles. These movements are the result of the propagation through the particle system of disturbances caused by specified wall and particle motion and/or body forces. This is a dynamic process in which the speed of propagation depends on the physical properties of the discrete system.

The calculations performed in DEM alternate between the application of Newton's second law to the particles and a force-displacement (i.e. constitutive) law at the

contacts. Newton's second law is used to determine the motion of each particle arising from the contact and body forces acting upon it, while the force-displacement law is used to update the contact forces arising from the relative motion at each contact.

The dynamic behaviour in DEM is represented by a timestepping algorithm in which the velocities and accelerations are assumed to be constant within each timestep. The DEM is based upon the idea that the timestep chosen may be so small that, during a single timestep, disturbance cannot propagate from any particle further than its immediate neighbours. Then, at all times, the forces acting on any particle are determined exclusively by its interaction with the particles with which it is in contact. This numerical scheme is identical to that used by the explicit finite-difference method for continuum analysis, thus making it possible to simulate the non-linear interaction of a large number of particles without excessive memory requirements or the need for an iterative procedure.

PFC^{3D} models the movement and interaction of stressed assemblies of rigid spherical particles using DEM. The distinct particles displace independently from one another and interact only at contacts or interfaces between the particles. The particles are assumed to be rigid and have negligible contact areas (contact occurs at a point). The behavior at the contacts uses the soft contact approach whereby the rigid particles are allowed to overlap one another at contact points. The critical timestep calculated for the timestepping algorithm in PFC^{3D} is not equal to the minimum eigenperiod of the total system because of impractical computational time. PFC^{3D} uses a simplified procedure such that a critical timestep is calculated for each particle and for each degree of freedom assuming that all degrees of freedom are uncoupled. The final critical timestep is the minimum of all the calculated critical timesteps. The actual timestep used in any calculation cycle is then taken as a fraction of this estimated critical value. PFC^{3D} enables the investigation of features that are not easily measured in laboratory tests, such as co-ordination numbers, inter-particle contact forces and the distribution of normal contact vectors. Furthermore, it is possible to compose bonded particles into agglomerates and simulate fracture when the bonds break.

2.4.2 Calculation cycle

The calculation cycle in PFC^{3D} is a timestepping algorithm that requires the repeated application of the law of motion to each particle, a force-displacement law to each contact, and a constant updating of wall positions. The external loads are applied to the system by moving the walls with fixed velocities- i.e. by strain control (stress control can be achieved by use of a servomechanism which will be discussed in section 2.4.4). The calculation cycle is illustrated in Figure 2.34.

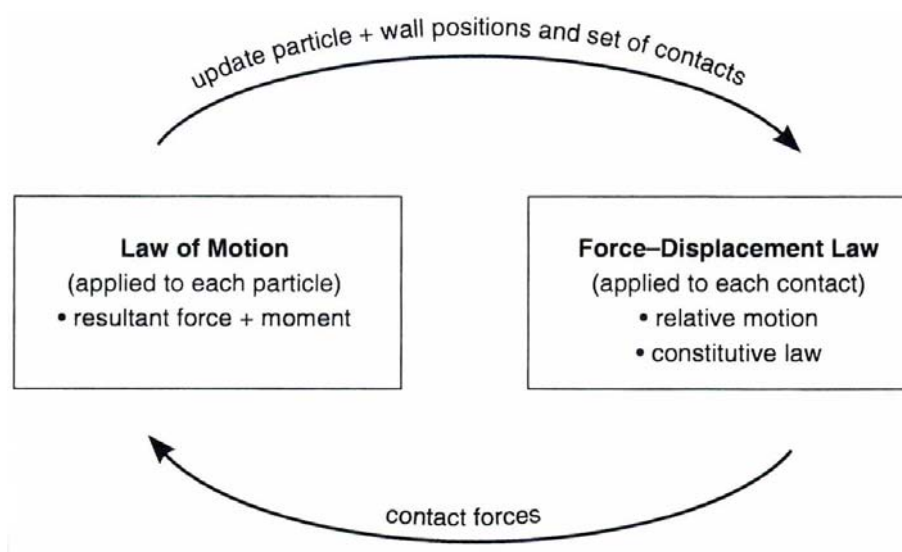


Figure 2.34. Calculation cycle use in PFC^{3D} (Itasca Consulting Group, Inc., 1999).

At the start of each timestep, the set of contacts is updated from the known particle and wall positions. The force-displacement law is then applied to each contact to update the contact forces based on the relative motion between the two entities at the contact and the contact constitutive model. Next, the law of motion is applied to each particle to update its acceleration, velocity and position based on the resultant force and moment arising from the contact forces and any body forces acting on the particle such as gravity. Lastly, the wall positions are updated based on the specified wall velocities.

The force-displacement law at a contact is applied at the start of each cycle to each contact to obtain new contact forces. The contact force vector F_i , which represents

the action of one entity on the other can be determined by adding the normal and shear force vectors at the contact as:

$$F_i = F_i^n + F_i^s \quad (2.15)$$

where F_i^n and F_i^s are the normal and shear contact force vectors, respectively. The normal contact force vector is simply determined by the overlap between two contacting entities as:

$$F_i^n = K^n U^n n_i \quad (2.16)$$

where K^n is the normal stiffness at the contact, U^n is the overlap of the two contacting entities and n_i is the unit normal vector directed along the line between ball centres, for the ball to ball contact, or directed along the line defining the shortest distance between the ball centre and the wall, for ball to wall contact. The shear contact force, however, is calculated in a more complicated manner because it is computed in an incremental fashion. When a contact is formed, the total shear force at that contact is set to zero. Relative shear displacement at the contact point of the two contacting entities will cause an increment in shear force to develop at the contact. This increment in shear force is calculated by considering the relative velocity, which is defined as the contact velocity V_i , between the two entities at the contact point. This contact velocity is a function of translational velocity and the rotational velocity of the two contacting entities. The shear component of this contact velocity is used to determine the incremental shear displacement as:

$$\Delta U_i^s = V_i^s \Delta t \quad (2.17)$$

where ΔU_i^s is the increment in shear displacement, V_i^s is the shear component of the contact velocity and Δt is the critical timestep. The increment in shear force due to the increment in shear displacement is given by:

$$\Delta F_i^s = -K^s \Delta U_i^s \quad (2.18)$$

where ΔF_i^s is the increment in shear force and K^s is the shear stiffness at the contact. Finally, the new shear force at the contact is found by summing the current elastic shear force at the contact with the increment in shear force as:

$$F_i^s = \{F_i^s\}^{\text{current}} + \Delta F_i^s \quad (2.19)$$

where $\{F_i^s\}^{\text{current}}$ is the current elastic shear force. The current elastic shear force is updated every timestep to take account of the motion of the contact. The new total resultant forces and moments on the two contacting entities will be used in the next timestep, to calculate the accelerations via Newton's second law, which are integrated via the time-stepping scheme to give velocities and displacement.

The motion of a single rigid particle is determined by the resultant force and moment vectors acting upon it and can be described in terms of the translational and rotational motion of the particle. The equations of motion can be expressed as two vector equations, one of which relates the resultant force to the translational motion and the other of which relates the resultant moment to the rotational motion. The equation for translational motion can be written in the vector form:

$$F_i = m(\ddot{x}_i - g_i) \quad (2.20)$$

where F_i is the sum of all externally applied forces acting on the particle, m is the mass of the particle, \ddot{x}_i is the acceleration of the particle at the centre of mass, and g_i is the body acceleration vector (e.g., acceleration due to gravity). The equation for rotational motion can be written in the vector form:

$$M_i = I\dot{\omega}_i \quad (2.21)$$

where M_i is the resultant moment acting on the particle, I is the moment of inertia of the particle about its centred gravity ($I = \frac{2}{5} mR^2$ for a spherical particle, where R is the radius), and $\dot{\omega}_i$ is the angular acceleration of the particle.

At each timestep, the equations of motion given by equations 2.20 and 2.21 are integrated twice, using a centred finite-difference procedure, for each particle to provide updated velocities and new positions. The translational velocity \dot{x}_i and angular velocity ω_i are computed at the mid-intervals of $t \pm n\Delta t/2$, where n is a positive integer, and the position x_i , translational acceleration \ddot{x}_i , angular acceleration $\dot{\omega}_i$, resultant force F_i and resultant moment M_i are computed at the primary intervals of $t \pm n\Delta t$. The translational and rotational accelerations at time t are calculated as:

$$\begin{aligned}\ddot{x}_i^{(t)} &= \frac{1}{\Delta t} \left(\dot{x}_i^{(t+\Delta t/2)} - \dot{x}_i^{(t-\Delta t/2)} \right) \\ \dot{\omega}_i^{(t)} &= \frac{1}{\Delta t} \left(\omega_i^{(t+\Delta t/2)} - \omega_i^{(t-\Delta t/2)} \right)\end{aligned}\tag{2.22}$$

The translational and rotational velocities at time $(t + \Delta t/2)$ are computed by inserting equation 2.22 into equations 2.20 and 2.21 as:

$$\begin{aligned}\dot{x}_i^{(t+\Delta t/2)} &= \dot{x}_i^{(t-\Delta t/2)} + \left(\frac{F_i^{(t)}}{m} + g_i \right) \Delta t \\ \omega_i^{(t+\Delta t/2)} &= \omega_i^{(t-\Delta t/2)} + \left(\frac{M_i^{(t)}}{I} \right) \Delta t\end{aligned}\tag{2.23}$$

Finally, the velocities in equation 2.23 are used to update the position of the particle centre as:

$$x_i^{(t+\Delta t)} = x_i^{(t)} + \dot{x}_i^{(t+\Delta t/2)} \Delta t\tag{2.24}$$

The calculation cycle for the law of motion can be summarized as follows: The values of resultant force and moment on a ball, $F_i^{(t)}$ and $M_i^{(t)}$ respectively, are determined using the force-displacement law. Using the translational and angular velocities of the last calculation cycle, $\dot{x}_i^{(t-\Delta t/2)}$ and $\omega_i^{(t-\Delta t/2)}$ respectively, equation

2.23 is then used to obtain $\dot{x}_i^{(t+\Delta t/2)}$ and $\omega_i^{(t+\Delta t/2)}$, which are the translational and angular velocity for the next calculation cycle. The new particle position, $x_i^{(t+\Delta t)}$, is obtained using equation 2.24. The values of $F_i^{(t+\Delta t)}$ and $M_i^{(t+\Delta t)}$, to be used in the next cycle, are obtained by application of the force-displacement law again.

2.4.3 Contact constitutive models

The overall constitutive behaviour of a material is simulated in PFC^{3D} by associating a simple constitutive model with each contact. The constitutive model acting at a particular contact consists of three parts: a stiffness model (consisting of a linear or a simplified Hertz-Mindlin Law contact model), a slip model, and a bonding model (consisting of a contact bond and/or a parallel bond model).

The stiffness model relates the contact forces and relative displacements in the normal and shear directions via the force-displacement law. PFC^{3D} provides 2 types of contact stiffness model: a linear model and a simplified Hertz-Mindlin model. The linear contact model is defined by the normal and shear stiffnesses k_n and k_s (force/displacement) of the two contacting entities, which can be two balls or a ball and a wall. The normal stiffness is a secant stiffness, which relates the total normal force to the total normal displacement, while the shear stiffness is a tangent stiffness, which relates the increment of shear force to the increment of the shear displacement. The contact normal and shear stiffnesses K^n and K^s , which are denoted by the upper case K , are computed by assuming that the stiffnesses k_n and k_s of the two contacting entities act in series, and are given by:

$$K^n = \frac{k_n^{[A]}k_n^{[B]}}{k_n^{[A]} + k_n^{[B]}} \quad (2.25)$$

$$K^s = \frac{k_s^{[A]}k_s^{[B]}}{k_s^{[A]} + k_s^{[B]}}$$

where superscripts [A] and [B] denote the two entities in contact. The simplified Hertz-Mindlin model is defined by the elastic properties of the two contacting balls:

i.e. shear modulus G and Poisson's ratio ν . When the Hertz-Mindlin model is activated in PFC^{3D}, the normal and shear stiffnesses are ignored and walls are assumed to be rigid. Hence, for ball to wall contacts, only the elastic properties of the ball are used and for the ball to ball contacts, the mean values of the elastic properties of the two contacting balls will be used. Tensile force is not defined in Hertz-Mindlin model. Thus, the model is not compatible with any type of bonding model. It should also be noted that PFC^{3D} does not allow contact between a ball with the linear model and a ball with the Hertz model.

The slip model limits the shear force between two contacting entities. A ball and a wall can each be given a friction coefficient, and the friction coefficient at the contact, μ , is taken to be the smaller of the values of the two contacting entities. The slip model will be deactivated in the presence of a contact bond and will be automatically activated when the bond breaks. The maximum elastic shear force, F_{\max}^s , that the contact can sustain before sliding occurs is given by:

$$F_{\max}^s = \mu |F_i^n| \quad (2.26)$$

where F_i^n is the normal force at the contact. If the shear force at the contact calculated by equation 2.19 exceeds this maximum elastic shear force, the magnitude of the shear force at the contact will be set equal to the maximum elastic shear force, F_{\max}^s . It should be noted that setting $\mu = 0$ means that the two contacting entities will slip at all times because elastic shear force cannot be sustained.

The bonding model in PFC^{3D} allows balls to be bonded together to form arbitrary shapes. There are two types of bonding model in PFC^{3D}: a contact-bond model and a parallel-bond model. The contact-bond model is a simple contact bond which can only transmit force and is defined by two parameters: the normal contact bond strength F_c^n (in Newtons) and shear contact bond strength F_c^s (in Newtons). A contact bond can be envisaged as a point of glue with constant normal and shear stiffness at the contact point. The contact bond will break if either the magnitude of the tensile normal contact force or the shear contact force exceeds the bond strength specified. Thus, the shear contact force is limited by the shear contact bond strength

instead of the maximum elastic shear force given by equation 2.26. As a result, either the contact-bond model or the slip model is active at any given time at a contact.

2.4.4 Wall control

Load is applied in PFC^{3D} by specifying wall velocity: i.e. tests are usually strain-controlled. To achieve stress-control, a numerical servomechanism is implemented. This is described in PFC^{3D} manuals (Itasca Consulting Group, Inc., 1999). The wall velocity is adjusted in a diminishing manner as the stress on the wall approaches the target stress. The wall velocity, $\dot{u}^{(w)}$, for each timestep is a function of the difference between measured and required stress on the wall, $\sigma^{measured}$ and $\sigma^{required}$ respectively, and a ‘gain’ parameter, G , as follows:

$$\dot{u}^{(w)} = G(\sigma^{measured} - \sigma^{required}) \quad (2.27)$$

The maximum increment in wall force $\Delta F^{(w)}$ arising from the wall moving with a velocity $\dot{u}^{(w)}$ in one timestep, Δt , is given by:

$$\Delta F^{(w)} = k_n^{(w)} N_c \dot{u}^{(w)} \Delta t \quad (2.28)$$

where N_c is the number of contacts on the wall and $k_n^{(w)}$ is the average normal stiffness of these contacts. Thus, the change in mean wall stress $\Delta \sigma^{(w)}$ due to this maximum increment in wall force is calculated as follows:

$$\Delta \sigma^{(w)} = \frac{k_n^{(w)} N_c \dot{u}^{(w)} \Delta t}{A} \quad (2.29)$$

where A is the wall area. It should be noted that $\Delta F^{(w)}$ given by equation 2.28 is the maximum increment in wall force, for same number of contacts, because it does not consider movement of the balls at the contacts: i.e. it assumes that the balls in contact with the wall are stationary. Hence, when loading an assembly of balls, this

maximum increment in wall force is unlikely to be achieved because the balls are moving, unless the assembly is extremely stiff. However, there is always a possibility that new contacts occur within a timestep or before updating the gain parameter, which is performed every specified number of cycles by updating the number of contacts on the wall. This might cause the increment in wall force to exceed the maximum increment in wall force calculated by equation 2.28. If this happens and the target stress is exceeded, this may lead to an unbounded oscillation about the target stress, which will lead to instability of the system. Hence, a relaxation factor, α , is introduced to make sure that the absolute value of the change in wall stress is less than the absolute value of the difference between the measured and the target stresses as:

$$|\Delta\sigma^{(w)}| < \alpha|\Delta\sigma| \quad (2.30)$$

where $\Delta\sigma$ is the difference between the measured and target stresses and $\alpha < 1$. Substituting equations 2.27 and 2.29 into equation 2.30 gives:

$$\frac{k_n^{(w)} N_c G |\Delta\sigma| \Delta t}{A} < \alpha |\Delta\sigma| \quad (2.31)$$

and the gain parameter is determined as:

$$G = \frac{\alpha A}{k_n^{(w)} N_c \Delta t} \quad (2.32)$$

It should be noted that the servomechanism can also be used to keep the stress on the wall constant, e.g. constant confining stress in a triaxial test.

2.4.5 Modelling soil particle fracture

Robertson (2000) used contact bonds to bond regularly packed balls of identical size in order to form approximately spherical agglomerates. These agglomerates were

intended to represent soil grains and allowed soil particle fracture to be simulated. Robertson (2000) initially examined three types of regular packing: face centred cubic (FCC), body centred cubic (BCC) and hexagonal close packed (HCP). He found that the results for HCP were the most consistent and adopted this packing for his simulations.

Figure 2.35 shows an individual HCP agglomerate of 527 balls compressed diametrically between two platens (Robertson, 2000). The agglomerate was randomly rotated before the load was applied. A typical result of this test is presented in Figure 2.36, which shows a force-strain curve, and the fractured agglomerate. The agglomerate seems to have a well-defined peak strength represented by the sudden failure of the agglomerate. However, it appears that there is an initial gap before the force begins to rise steadily. Robertson (2000) explained this delay as due to unstable rotation of the particle. McDowell & Harireche (2002a) showed that by allowing the agglomerate to stabilize under the application of gravity, the force will increase from the beginning of the test because the agglomerate is in a stable position when load is applied. The use of frictionless walls in the tests by Robertson (2000) means that slip was allowed to occur at the ball to wall contact at all times. If the walls had been assigned a coefficient of friction, the force should increase slowly or erratically at the early stage of the test and rise rapidly prior to failure. Of course, the failure mechanism would then be different and the peak strength obtained would be different too. Nevertheless, stabilizing the agglomerate under gravity is considered to be a more realistic approach.

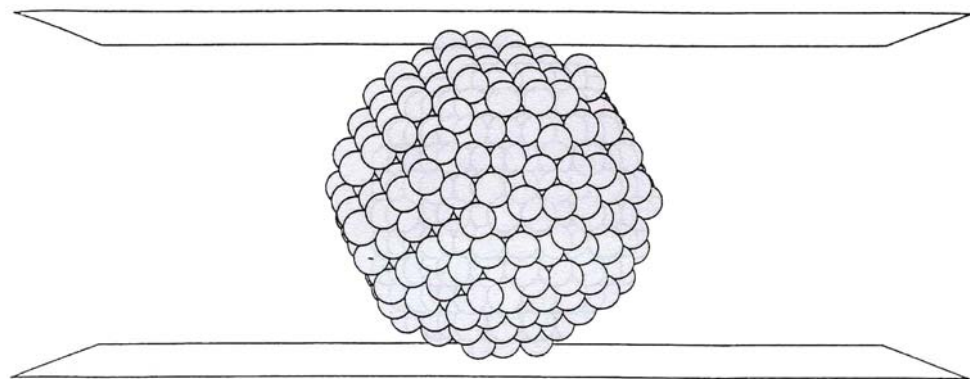


Figure 2.35. Crushing test on agglomerate (Robertson, 2000).

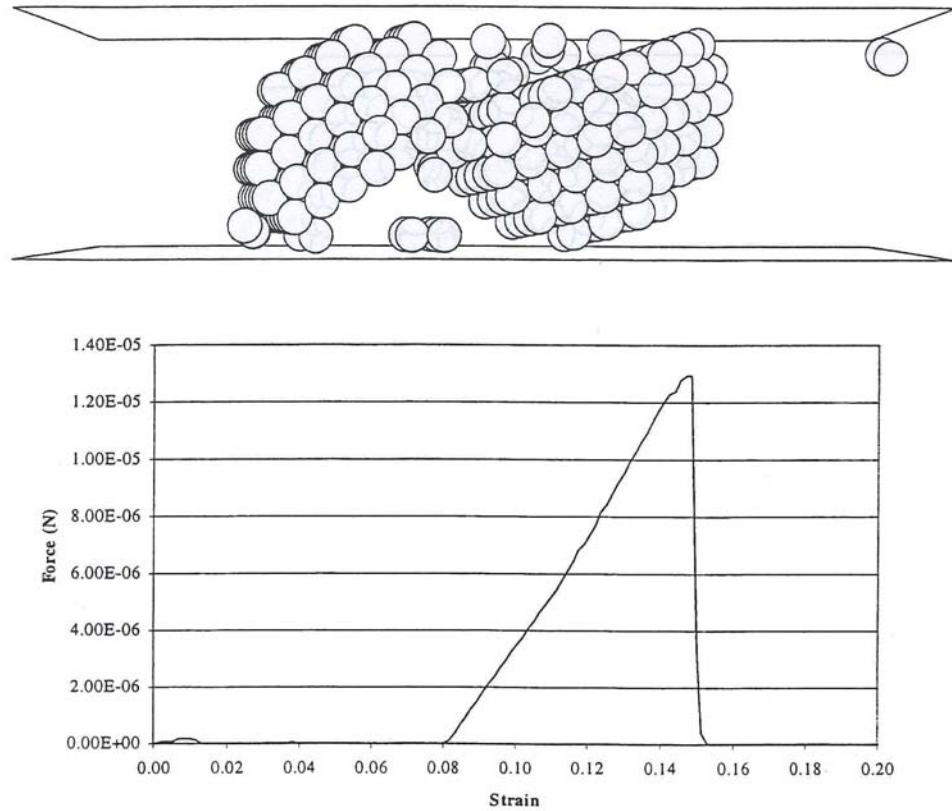


Figure 2.36. Typical result of a crushing test on an agglomerate (Robertson, 2000).

Robertson (2000) showed that it is possible to produce a Weibull (1951) distribution of soil particle strengths by randomly removing some of the regularity in the agglomerate. He introduced three types of flaws to the agglomerate: removing bonds, reducing some bond strengths and removing balls. It should be noted that changing the particle orientation is also one way of introducing irregularity to the agglomerate. After an extensive range of simulations examining the effect of altering the percentage and distribution of flaws in the agglomerate, Robertson (2000) concluded that a Weibull distribution of strengths was best reproduced by randomly removing balls in the agglomerate and the Weibull modulus depended on the range of the number of balls removed. For example, Robertson (2000), McDowell & Harireche (2002a) found that randomly removing 0-25% of the balls in the agglomerate gave a Weibull modulus of $m \approx 3$ with 30 tests or more. Increasing the range of balls removed increases the variability and reduces m . Following this, McDowell & Harireche (2002a) examined the size effect on strength of agglomerates with randomly removed balls. They compared the stress at failure of a 0.5 mm diameter agglomerate comprising initially 135 balls, with 0-25% balls

subsequently removed, and a 1 mm diameter agglomerate comprising initially 1477 balls, with 0-25% balls subsequently removed. They found that the stress at failure of the 1 mm diameter agglomerate was higher than that of the 0.5 mm diameter agglomerate: this disagrees with the actual size effect on soil particle strength as discussed in section 2.3.3. This effect is explained by McDowell & Harireche (2002a) as due to differences in geometry between agglomerate sizes caused by HCP and random rotation. McDowell & Harireche (2002a) introduced further randomness to the agglomerate in order to attempt to produce the correct size effect on average strength. They found that the size effect on strength could be reproduced by initially removing a certain percentage of balls in the agglomerate in order to partly replicate a dense random packing before introducing flaws. Figure 2.37 shows the Weibull distribution of strength tests for crushing on 0.5mm and 1mm diameter agglomerates. In these tests, 30% of the balls were initially removed at random before a further random 0-25%.

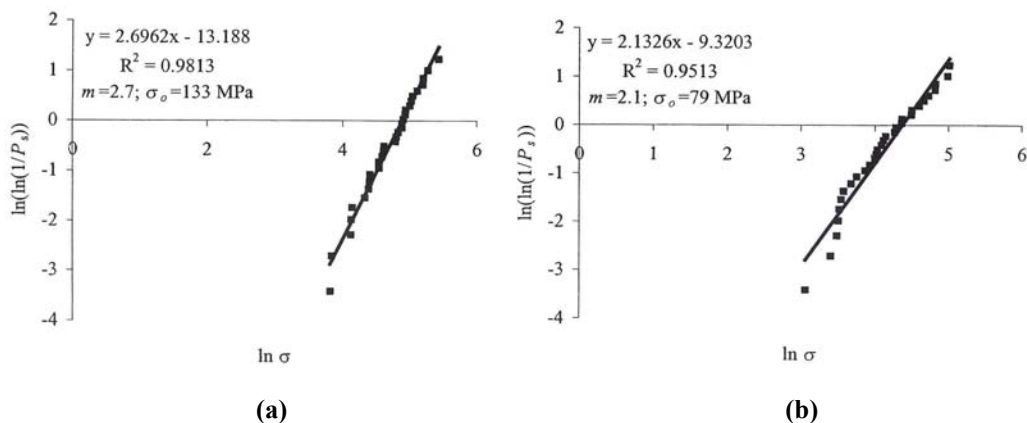


Figure 2.37. Weibull probability plot for (a) 0.5mm and (b) 1mm diameter agglomerates (McDowell & Harireche, 2002a).

Robertson (2000) noticed that the timestep determined by PFC^{3D} is extremely small when realistic ball stiffnesses are used ($t_{crit} = \sqrt{m/k}$). Thus, Robertson (2000) used differential density scaling as a solution. Differential density scaling modifies the inertial mass of each particle at the start of each cycle so that the critical timestep for the system is unity. When differential density scaling is active, only the final steady-state solution is valid because the time scale involved is meaningless. The mass of each particle calculated is also fictitious. However, the solution will converge faster

because all the balls will have equal time response. Thus, differential density scaling is only useful if there are large differences in ball mass and/or stiffness. It was in fact not necessary for Robertson (2000) to use differential density scaling because the balls in his agglomerates were of the same size and had the same stiffness. Instead of using differential density scaling, he should have loaded the agglomerate with a high wall velocity, but not so high as to affect the results. This would reduce the computational time, whilst keeping the default critical timestep. The reason for this is that a certain number of time increments are required for a load pulse to propagate through a system and for the system to come to equilibrium, for a given number of entities in the system. Consider a 50-ball chain. A load pulse applied to one end of the ball will take 50 timesteps to reach the other end. Using Differential Density Scaling cannot change this fact. For equilibrium to occur in this system, a number of such wave transits must occur. Thus, the response or behaviour of any system depends on the time interval of an applied load pulse and whether equilibrium will occur before the application of the next load pulse. It should also be noted that the number of time increments needed increases with increasing number of entities in the system. Therefore, the best approach is to use the highest possible wall velocity so long as the results are not affected. Figure 2.38 gives an example of how this highest possible wall velocity can be determined (McDowell & Harireche, 2002a). The figure shows three different wall velocities applied to the same agglomerate. A wall velocity of 0.64ms^{-1} appears to be the highest that can be applied to the agglomerate tested without affecting the post-peak strength behaviour.

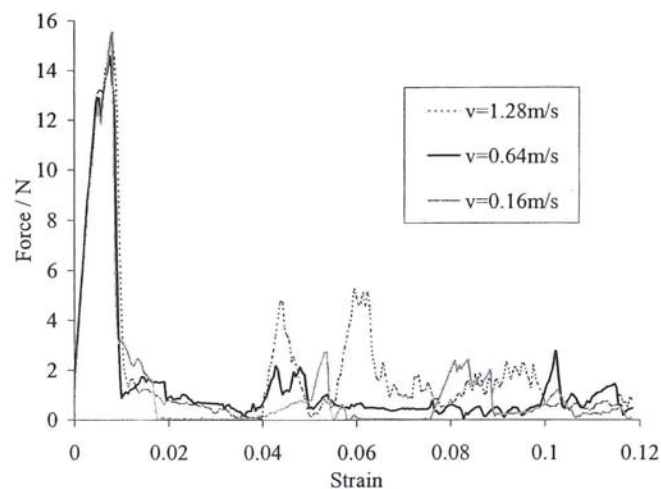


Figure 2.38. Force-strain plots for different platen velocities (McDowell & Harireche, 2002a).

2.4.6 Compression tests on an assembly of agglomerates

Compression tests can be performed in PFC^{3D} on an assembly of agglomerates within a cube defined by six walls. Load may be applied by moving the walls one at a time or simultaneously. The assembly of agglomerates is created by first creating a random assembly of balls, each of the required agglomerate size, at a specified porosity. The minimum porosity of an assembly of agglomerates is determined by trial and error. The initial assembly of balls is generated with a specified porosity and slight overlap of balls is permitted. These balls are cycled to equilibrium and then replaced by agglomerates. When balls are replaced by agglomerates, the overlap will be reduced. The agglomerates will be cycled to equilibrium again before the load is applied. The coefficient of friction is initially set to zero so that the assembly will rearrange easily and to its final state prior to loading. The maximum contact force is checked after cycling to equilibrium to obtain an acceptably low value. It should be noted that the overlap depends solely on the geometry of the agglomerate for a given porosity, but the contact force depends on both overlap and normal stiffness. Thus, the minimum achievable porosity of an assembly of agglomerates depends on the geometry of the agglomerates and the normal stiffness. The method of replacing balls with agglomerates is described by Robertson (2000).

Using the servomechanism described in section 2.4.4, it is possible to load a triaxial sample according to the required stress path. Robertson (2000) carried out triaxial stress path tests on an assembly of agglomerates to observe bond breakage using PFC^{3D}. He found that contours of equal percentages of bonds breaking in deviatoric stress – mean stress q - p space were similar to the shapes of typical yield surfaces predicted by plasticity models, as shown in Figure 2.39. This sample was loaded isotropically to $p=20\text{MPa}$ and unloaded to $p=10\text{MPa}$ before following the required stress path.

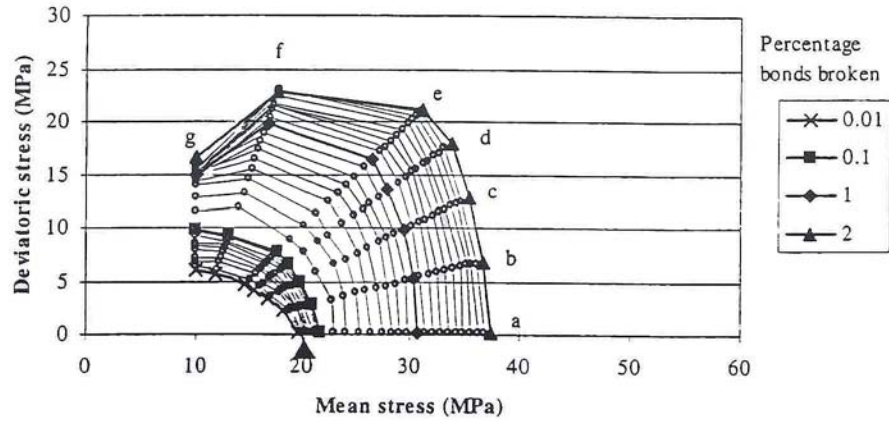


Figure 2.39. Typical contours of equal percentages of bonds breaking in deviatoric stress-mean stress space (Robertson, 2000).

McDowell & Harireche (2002b) simulated a one-dimensional compression test using agglomerates with the strength and distribution of strength of silica sand using PFC^{3D}. They showed that yielding coincides with the onset of bond fracture, as shown in Figures 2.40 and 2.41, which supports the hypotheses by McDowell & Bolton (1998) that yielding is due to the onset of particle breakage: the point of maximum curvature on the V/V_0 - $\log \sigma$ plot occurs at a strain of about 30%, which is when bond breakage begins (Figure 2.41). McDowell & Harireche (2002b) also showed that yield stress is proportional to the 37% agglomerate tensile strength, as shown in Figures 2.42 (a) and (b). Figure 2.42 (a) shows the result of one-dimensional compression test with the bond strength of the agglomerates increased by a factor of 2. Figure 2.42 (b) shows the same results with the macroscopic stress normalised by the 37% tensile strength σ_0 of the agglomerates.

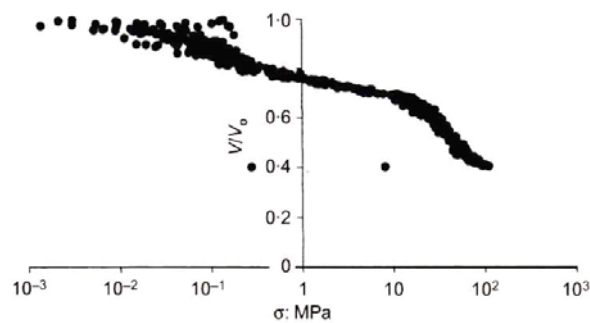


Figure 2.40. Compression curve (McDowell & Harireche, 2002b).

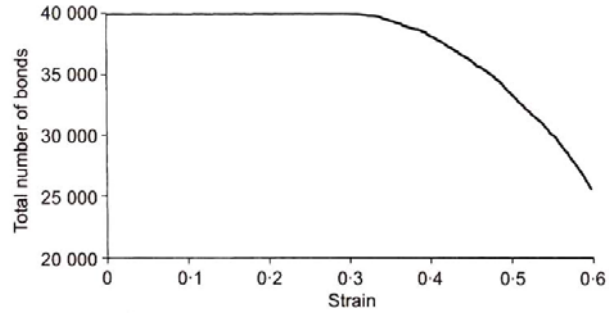
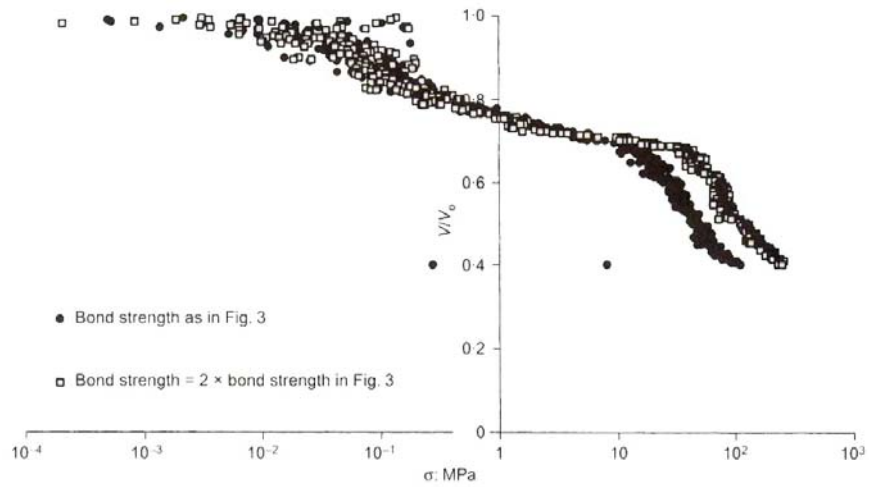
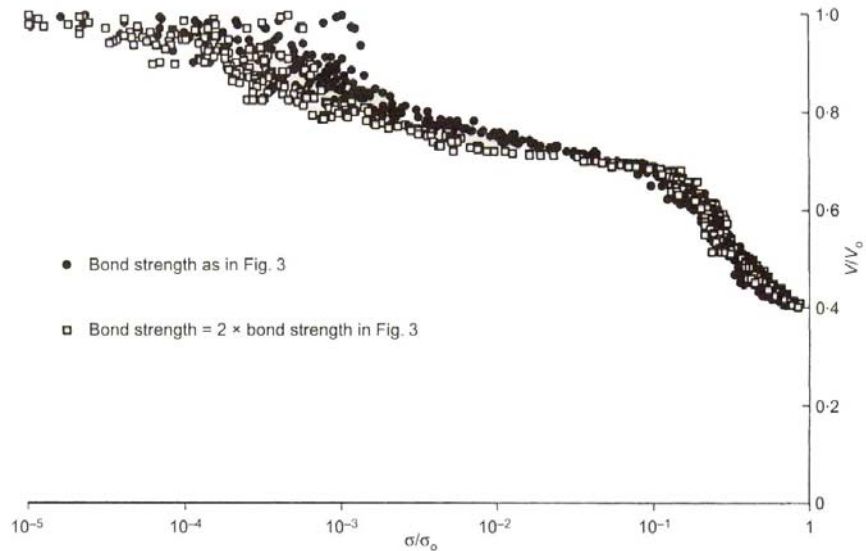


Figure 2.41. Number of intact bonds as a function of strain (McDowell & Harireche, 2002b).



(a)



(b)

Figure 2.42. (a) Effect of scaling bond strength on the compression curve; and (b) compression curve with stress normalised by 37% agglomerate tensile strength σ_0 (McDowell & Harireche, 2002b).

2.5 Summary

One of the most important functions of ballast is to facilitate the maintenance of track geometry by rearrangement of particles. However, ballast is also one of the main sources of track geometry deterioration and ballast breakdown has been identified as the main source of fouling in ballast. The interaction between the track superstructure components under a moving wheel load causes a large impact load, which increases with increasing train speed and track irregularity (i.e. the impact load increases with an increase in the size of the gap underneath the sleeper). This impact load increases the stresses in the ballast which, as a result, increases ballast settlement and leads to a larger gap underneath the sleeper. Thus, track geometry tends to degrade in an accelerating manner. Track which has lost its geometry has to be maintained. The most effective method of restoring track geometry, especially for those involving long wavelength faults, is by maintenance tamping. However, maintenance tamping has also been found to be the main source of ballast breakdown. The fouling materials can cause severe track deterioration if the degree of fouling is high and in the presence of water. The source of fouling material is important because the effect of fouling material on ballast is highly dependent on the type of fouling material and how the voids in the ballast were filled.

There is a wide range of ballast materials because of the lack of universal agreement on the specifications for ballast. The strength of ballast has been conventionally measured by abrasion tests, or the ACV test, both of which are considered as inappropriate. Abrasion tests involve revolving particles in rotating cylinder or drum: a geometry which does not appear to be relevant to loading beneath the track under traffic. The ACV test involves only small particles, and will not reflect properly the strengths of the large particles used in the track. Thus, there is a need for new ballast testing methods which assess the quality of different ballast materials scientifically and provide results reflecting the field performance of different ballast materials. In order to determine such tests, research on the micro mechanics of crushable soils has been examined and applied to ballast. In particular, it has been found that for crushable soils, the single particle crushing test has been found to provide useful data. For a single particle compressed diametrically between flat

platens, the tensile strengths of soil particles of a given size follow a Weibull distribution, which gives a size effect on strength such that larger particles have a lower average tensile strength than smaller particles. Experimental results have also shown that for oedometer tests on sands, the yield stress is approximately proportional to the average tensile strength of the constituent grains. The reason for this is that the macroscopic stress applied to an array of particles is transmitted through columns of strong force and those particles which are located in the columns of strong force can be assumed to have a loading geometry similar to that when loaded by two flat platens.

The micro mechanics of ballast can also be investigated using the discrete element program PFC^{3D}. The main advantage of this program is that a prepared sample can be re-used again for different loading conditions, whilst keeping the same loading geometry. Thus, the effect of different loading conditions can be investigated in a controlled manner. Recent research has shown that it is possible to simulate the behaviour of granular materials using bonded spherical particles i.e. single particle crushing, oedometer and triaxial tests.

The remainder of this thesis examines the use of single particle crushing tests, oedometer tests, index tests, box tests and petrographic analysis to quantify the performance of ballast, and the use of discrete element modelling to gain insight into the micromechanics of ballast behaviour.

Chapter 3

Single Particle Crushing Tests

3.1 Introduction

The single particle crushing test is an indirect tensile test to measure the tensile strength of ballast particles by compressing individual particles between two flat platens to induce tensile stresses within the ballast particles. A ballast particle compressed in this manner will fail by fast fracture and break into two or more pieces if the tensile stress induced at some location within the particle reaches a critical value for the ballast particle, depending on the distribution of flaws in the material. Section 2.3 in the literature review has shown that the behaviour of a crushable soil is governed by the tensile strengths of its constituent particles. Thus, this chapter will present the results of single particle crushing tests on six types of ballast: A, B, C, D, E and F. The mineralogy of these ballasts can be found in the appendix.

The main assumption in this test is that failure of ballast particles is caused by the generation of a continuous stress field within a homogeneous and isotropic particle. It is also necessary to assume that all particles are geometrically similar, and assume that the ballast particle contact area is small (ideally, spherical particles should be used). Shipway and Hutchings (1993) found that for reducing contact areas, the proportion of the sphere radius under tension increases, and bulk fracture is more likely to occur than surface fracture. However, in practice, it is difficult to minimise the ballast particle contact area because ballast particles are irregular in shape. Thus,

quasi-spherical ballast particles have been chosen for these tests in order to minimise the contact area and keep similar particle geometries. It is also noted that large contact area would occur if the particle was compressed between ‘soft’ platens that deform plastically. Thus, the platens were made of case-hardened mild steel to minimise the contact area.

3.2 Test procedures

Ballast particles were dried and sieved to obtain three sieve size fractions: 10-14mm, 20-28mm (19-25mm for ballast E, due to availability) and 37.5-50mm. Thirty quasi-spherical ballast particles were chosen for each size fraction, to be compressed between two flat platens. Individual ballast particles were checked for irregular shape by first confirming that the contact areas were approximately at the centres of the particles and that these contact areas were small. It is difficult to minimise the contact area at the bottom platen as the particle needs to be in stable equilibrium when compressed between platens. So, only the top contact area can be minimised. Besides, particles that are likely to fail in bending should be identified and omitted. For example, if the particle has two or more obvious contact points on the bottom platen (i.e. the particle geometry contains an arch at the bottom), then fracture is likely to occur by bending.

The chosen ballast particles were compressed individually in a configuration shown in Figure 3.1. The figure shows two flat platens made from case-hardened mild steel, and which are attached to a Zwick testing machine. Both platens have a diameter of 140mm. A hollow Perspex cylinder, which is slightly larger than the two platens, is used to confine broken pieces. The Zwick testing machine applies a constant rate of loading of 1mm/min to compress the ballast particle until the ballast particle fails by breaking into two or more pieces. The Zwick testing machine measures the applied force and has a gauge attached to the machine which allows displacement to be read visually. The force was measured to an accuracy of 50N and the displacement was read with an accuracy of 0.5mm.



Figure 3.1. Single particle crushing test set-up.

The rate of loading was chosen to be 1mm/min because it was found that at high loading velocities, broken fragments could not fall away from the bulk particle and were continuously loaded, thus, giving an artificially high tensile strength because two or more particles were being compressed instead of one. Nevertheless, it was noted that the rate of loading of 1mm/min does not guarantee that broken fragments will fall away from the bulk particle. Therefore, the particle tested had to be checked for breakages every time there was a drop in the applied load. In the case of uncertainty, the test was stopped so that the particle tested could be examined closely and the test resumed if there were no intact broken fragments. Besides checking whether broken fragments had fallen away from the bulk particle or not, a decision also had to be made as to whether a drop in load corresponded to particle failure. The simplest approach was to declare a particle failure when the bulk of the ballast particle had broken into two or more pieces. However, in some cases, only a portion of the original particle was broken. In this case, if the total broken fragments accounted for more than 1/3 of the original particle volume, the particle was declared as failed, and the corresponding peak force was used to compute the tensile strength.

3.3 Results

3.3.1 Computation of results

A measure of tensile stress at failure for each ballast particle was determined by dividing the failure force (peak force) by the square of the particle size at failure ($\sigma_f = F_f / d_f^2$). The tensile stresses at failure data for each set of tests were ranked in ascending order to compute the survival probability for each tensile stress at failure. The survival probability was computed using the mean rank position: $P_s = 1 - i / (N + 1)$ where i is the i th ranked sample from a total of N (Davidge, 1979). So, for 30 particles, the lowest value of F_f / d_f^2 gives a particle survival probability of 30/31, and the strongest particle gives a particle survival probability of 1/31.

The ballast tensile strength and variation in strength in each set of tests was quantified using Weibull (1951) statistics, such that the survival probability of a particle of size d under a tensile stress σ is given by:

$$P_s(d) = \exp\left[-\left(\frac{\sigma}{\sigma_o}\right)^m\right] \quad (3.1)$$

where m is the Weibull modulus and σ_o is the tensile stress such that 37% of the particles survive, or the “37% tensile strength” of the sample. The Weibull modulus relates to the coefficient of variation and reduces with increasing variability in strength (section 2.3.1). By re-writing equation 3.1 as:

$$\ln\left[\ln\left(\frac{1}{P_s(d)}\right)\right] = m \ln\left(\frac{\sigma}{\sigma_o}\right) \quad (3.2)$$

the Weibull modulus m and the 37% tensile strength for each set of tests can be simply calculated from a Weibull survival probability plot, which is a plot of $\ln(\ln(1/P_s))$ against $\ln\sigma$. The Weibull modulus m is the slope of the line of best fit, and the value of σ_o is the value of σ when $\ln(\ln(1/P_s)) = 0$. The Weibull probability plots for all the ballasts are given in Figure 3.2.

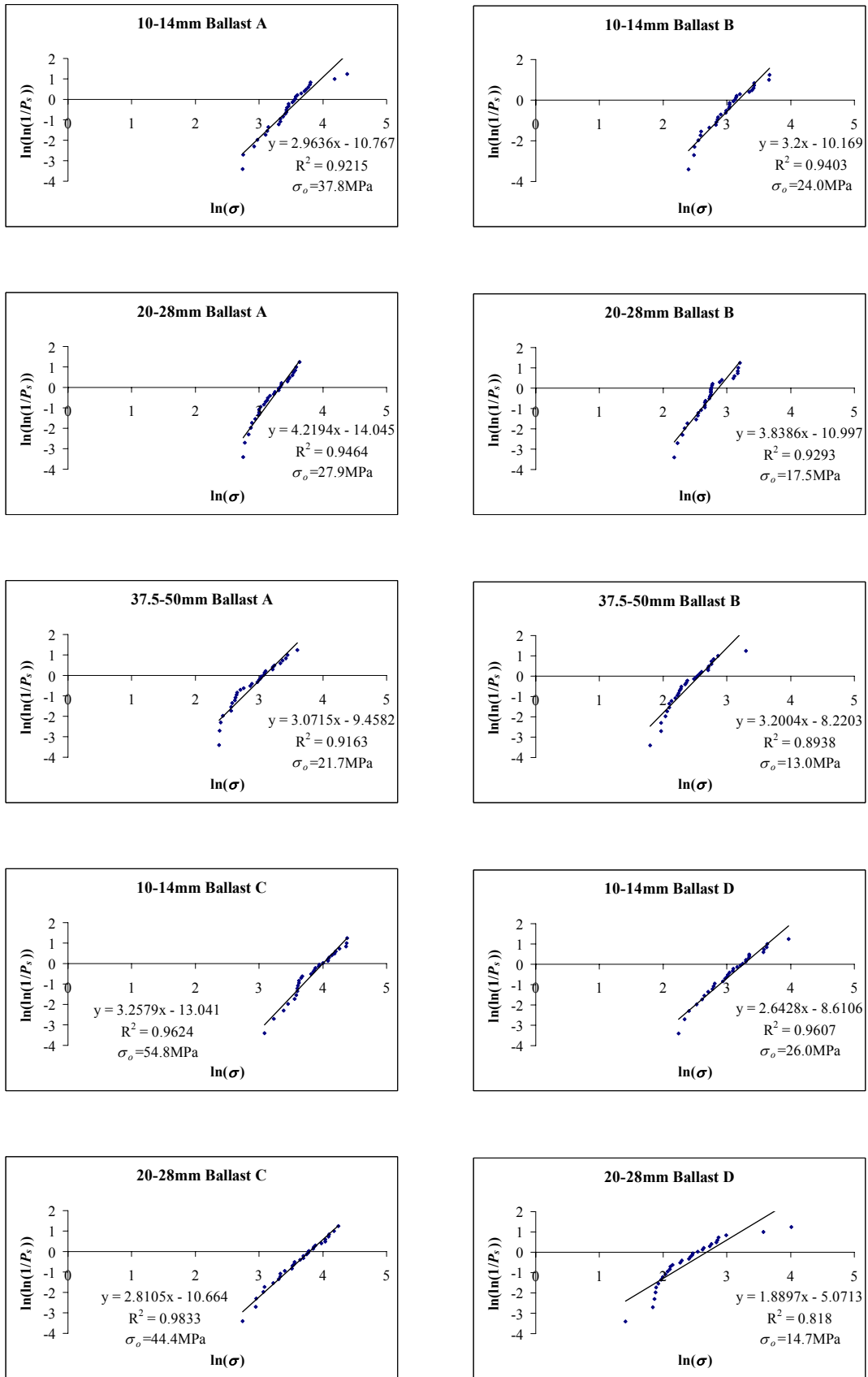


Figure 3.2. Weibull survival probability plots (continues over page).

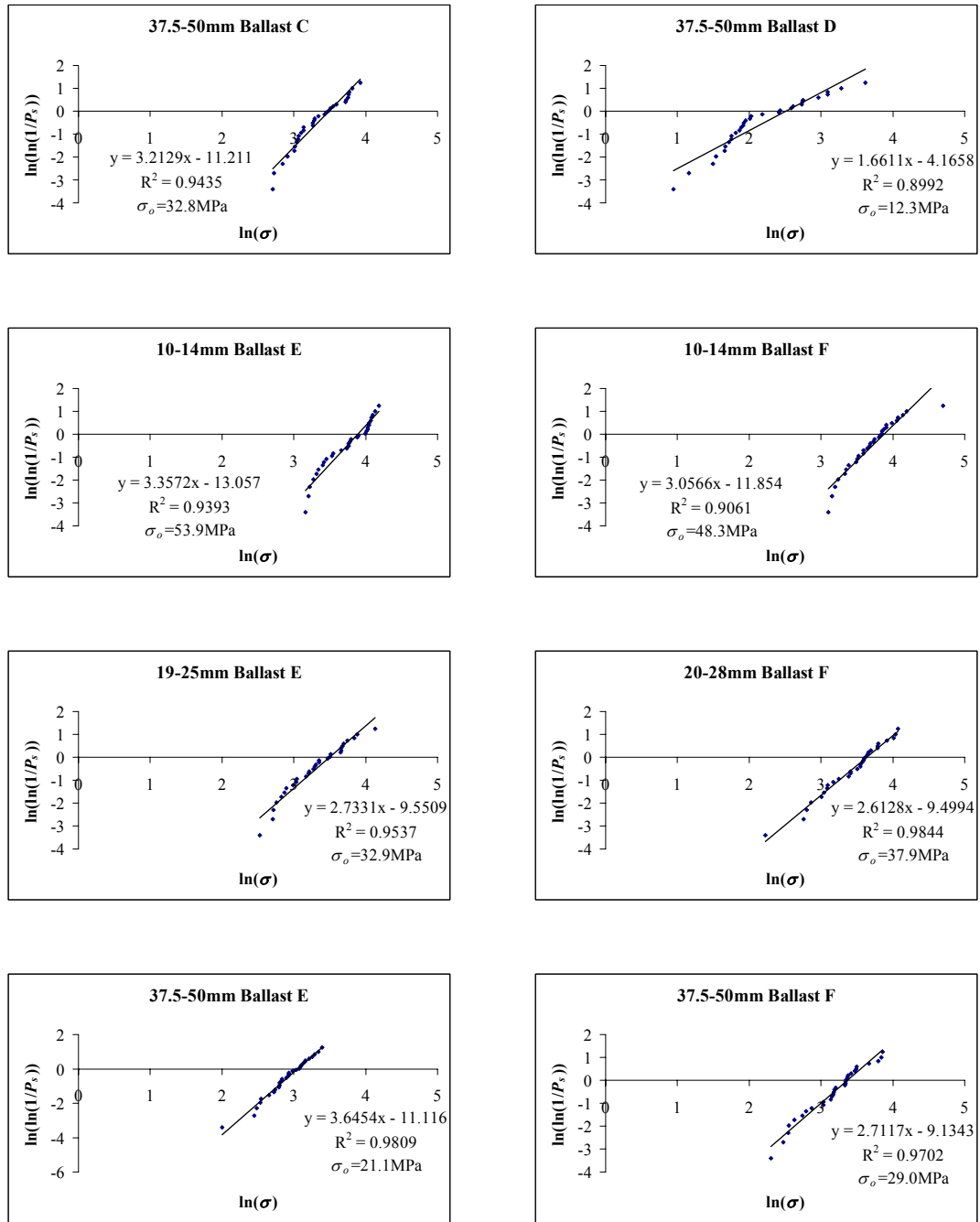


Figure 3.2. Weibull survival probability plots.

3.3.2 Summary of results

The results computed from the Weibull survival probability plots for all six types of ballast tested are summarised according to the sieve size range in Table 3.1. Besides listing the 37% tensile strength (σ_0), Weibull modulus (m), coefficient of correlation (R^2), the average initial particle size (d_i), the average particle size at failure (d_f) and

the relative ranking according to tensile strength are also listed. It can be seen that smaller ballast particles are statistically stronger than larger particles, thus revealing the size effect on the strength of ballast. It is also noted that ballast C is the strongest with the highest tensile strength for all size categories. However, the order of ranking for other ballasts changes from one size category to another. This indicates the different size effect for different ballast materials. The size effect on the strength of ballast can be described by the equation:

$$\sigma_o \propto d^b \quad (3.3)$$

where b is the slope of the line of best fit on a $\text{Log}(\sigma_o)$ against $\text{Log}(d_f)$ plot as shown in Figure 3.3. It is very obvious in this figure that there is a size effect on strength for ballast and that the size effect is material dependent, as shown by the different slopes. Ballast E has the strongest size effect while A, B, C and F ballasts have approximately the same size effect.

| 10-14mm Ballast | σ_o (MPa) | m | R^2 | d_i (mm) | d_f (mm) | Ranking |
|--------------------|---------------------|------|--------|---------------|---------------|---------|
| A | 37.8 | 2.96 | 0.9215 | 8.6 | 7.8 | 4 |
| B | 24.0 | 3.20 | 0.9403 | 9.0 | 8.5 | 6 |
| C | 54.8 | 3.26 | 0.9624 | 8.9 | 8.4 | 1 |
| D | 26.0 | 2.64 | 0.9607 | 9.6 | 8.9 | 5 |
| E | 48.9 | 3.36 | 0.9393 | 9.7 | 9.2 | 2 |
| F | 48.3 | 3.07 | 0.9061 | 9.5 | 8.6 | 3 |

| 20-28mm Ballast | σ_o (MPa) | m | R^2 | d_i (mm) | d_f (mm) | Ranking |
|--------------------|---------------------|------|--------|---------------|---------------|---------|
| A | 27.9 | 4.22 | 0.9464 | 19.4 | 18.2 | 4 |
| B | 17.5 | 3.84 | 0.9293 | 17.4 | 16.8 | 5 |
| C | 44.4 | 2.81 | 0.9833 | 17.3 | 16.5 | 1 |
| D | 14.7 | 1.89 | 0.8180 | 19.7 | 18.8 | 6 |
| E (19-25mm) | 32.9 | 2.73 | 0.9537 | 18.5 | 17.3 | 3 |
| F | 37.9 | 2.61 | 0.9844 | 18.0 | 16.7 | 2 |

| 37.5-50mm Ballast | σ_o (MPa) | m | R^2 | d_i (mm) | d_f (mm) | Ranking |
|----------------------|---------------------|------|--------|---------------|---------------|---------|
| A | 21.7 | 3.07 | 0.9163 | 31.1 | 29.6 | 3 |
| B | 13.0 | 3.20 | 0.8938 | 37.0 | 35.9 | 5 |
| C | 32.8 | 3.21 | 0.9435 | 31.7 | 29.8 | 1 |
| D | 12.3 | 1.66 | 0.8992 | 36.3 | 34.3 | 6 |
| E | 21.1 | 3.65 | 0.9809 | 33.1 | 31.3 | 4 |
| F | 29.0 | 2.71 | 0.9702 | 33.7 | 30.8 | 2 |

Table 3.1. Summary of single particle crushing test results.

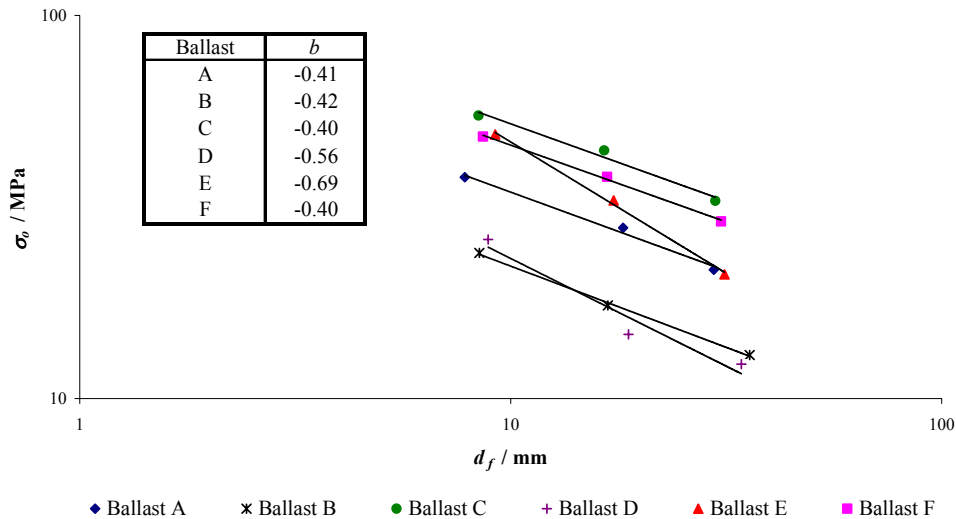


Figure 3.3. 37% tensile strength against average particle size at failure plot.

3.4 Discussion

The size effect of all the ballasts tested was smaller than suggested by the theoretical prediction (e.g. $\sigma_o \propto d^{3/m}$) because of the process by which the ballast particles tested have been produced. At the quarry, the large particles which have survived the grinding process are statistically strong because weaker particles would not have survived the process. In other words, the grinding process offers a proof test, whereby the largest particles which survive are statistically strong. This effect can be seen in each of the Weibull survival probability plots (Figure 3.2). Most of the plots have a downward curvature (i.e. lack of fit at low survival probabilities), which suggests that the ballast particles have a minimum strength.

It was noted that the size effect of ballast E is the only one that satisfies Weibull (1951) statistics in the sense that the slope of the line of best fit on a $\text{Log}(\sigma_o)$ against $\text{Log}(d_f)$ plot is approximately $-3/m$, as derived by McDowell & Amon (2000). McDowell & Amon (2000) derived this theoretical size effect based on the assumption that the material is homogeneous and isotropic whereby the maximum stress can be integrated over the volume of the particle. It was found in the petrographic analysis (Large, 2003) that ballast C and ballast E are the only 2

ballasts that are homogeneous and isotropic. However, the exact reason that ballast C does not satisfy Weibull (1951) statistics for a block of volume to survive is not known. For the materials tested by McDowell & Amon (2000) and McDowell (2002), which satisfied Weibull (1951) statistics, each material consisted predominantly of one mineral. It may be that for other isotropic and homogeneous ballast, the relative proportions of each mineral may be a function of particle size. It is noted that in the petrographic analysis, ballast E is the only ballast that consists predominantly of one mineral, namely feldspar.

It should also be noted that the Weibull analysis applied to soil particles (McDowell & Amon, 2000) assumes that all loading geometries are similar. This will not necessarily be the case as different ballasts have different shape characteristics. The basic assumption in this case would then be that the tensile stress field near the centre of the particle is approximately the same in each case. In addition, for the tests performed here, particles were chosen for the single particle crushing tests which were quasi-spherical (as near as possible) to eliminate the effect of particle shape on the results.

Another explanation for the reason why the ballasts, in general, do not exhibit the Weibull size effect could be that the fracture of ballast particles in single particle crushing tests is not initiated from the bulk of the material. Shipway & Hutchings (1993) computed the elastic stress distributions in a sphere under diametral compression and then compared the normalised maximum values of surface tensile stress with the peak tensile stress on the axis for all values of a_c/R (ratio of the contact radius to radius of the sphere), as shown in Figure 3.4. It can be seen that the maximum internal tensile stress on the axis is always greater than the maximum surface stress for a small contact area ($a_c/R < 0.6$), but the difference between the two stresses is no more than a factor of 2 for $0.15 < a_c/R < 0.6$. Shipway & Hutchings (1993) noted that the surface stress that is needed to cause fracture in many rocks and other brittle materials is substantially lower than the bulk fracture stress, due to the presence of surface flaws. Thus, spheres of such materials may fail at critical values of the maximum surface stress provided that a_c/R is large enough. In this case, the application of Weibull (1951) statistics involves the integration of some function of stress over the area of the particle under tension, instead of over the

volume of the particle as done by McDowell & Amon (2000). Following the procedures and assumptions introduced by McDowell & Amon (2000), the application of Weibull (1951) statistics involving the integration of some function of stress over the area of the particle under tension would yield a 37% tensile strength σ_o proportional to $d^{2/m}$. This solution for the size effect of particle strength is closer to that observed in Figure 3.3 (see also Table 3.2).

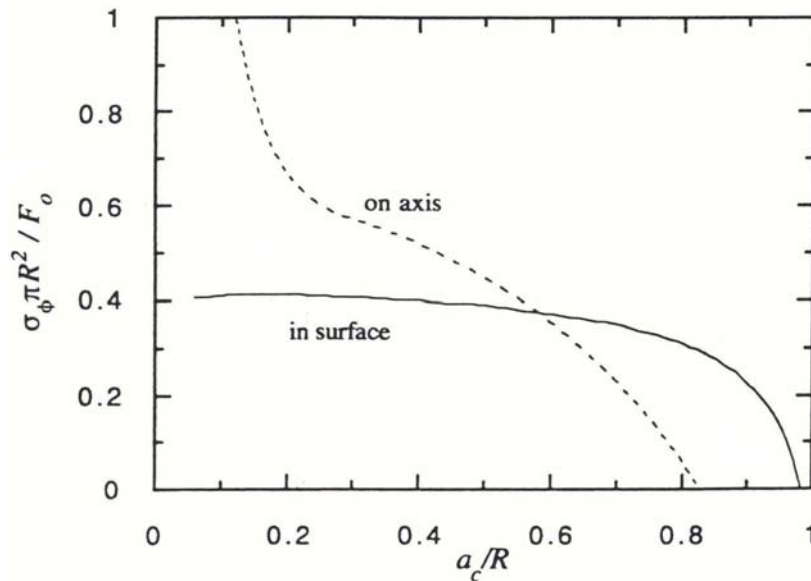


Figure 3.4. Variation of the normalised maximum tensile stress on the axis and on the surface with a_c/R (Shipway & Hutchings, 1993).

| Ballast | Average m | $-3/m$ | $-2/m$ | b |
|---------|-------------|--------|--------|-------|
| A | 3.42 | -0.88 | -0.58 | -0.41 |
| B | 3.41 | -0.88 | -0.59 | -0.42 |
| C | 3.09 | -0.97 | -0.65 | -0.40 |
| D | 2.06 | -1.46 | -0.97 | -0.56 |
| E | 3.25 | -0.92 | -0.62 | -0.69 |
| F | 2.80 | -1.07 | -0.71 | -0.40 |

Table 3.2. Comparison of theoretical prediction of size effect with the actual size effect for different ballast materials.

3.5 Conclusions

The tensile strength of a ballast particle can be obtained by compressing the particle between two flat platens. In order to ensure that ballast particles fail by bulk fracture, quasi-spherical ballast particles with small contact areas have to be chosen. Besides choosing quasi-spherical ballast particles, particles that are likely to fail in bending were also identified and omitted. Thus, ballast particles used in this test were geometrically similar. Precautions were made during the test to avoid compressing two or more pieces of broken fragments that would yield an artificially high failure force. Ballast particles in this test were declared as failed when the bulk of the particle or a significant portion (more than 1/3) of the original particle had broken. The failure load or peak load (for the latter) was then used to compute the tensile strength of the ballast particle.

The single particle crushing test results fit the Weibull survival probability plot well. The results showed that there is a size effect on the strength of ballast, such that smaller ballast particles are statistically stronger. The results also showed that the size effect on the strength of ballast is material dependent. Thus, the usefulness of the ACV test, which tests 10-14mm ballast particles, to predict the relative performance of railway ballasts that consist predominantly of 28-50mm ballast particles, is in doubt.

The actual size effect of ballast might not be expected to follow the theoretical size effect because ballasts are processed, whereby ballast at each size range has a minimum strength instead of a wide distribution of strength that extends to zero strength. The theoretical size effect as defined by McDowell & Amon (2000) can only be applied to materials that are homogeneous and isotropic. It is also best if materials consist predominantly of one mineral, for Weibull to apply; otherwise the relative proportions of each mineral may be a function of particle size, giving a size-dependent Weibull modulus. The application of Weibull (1951) statistics that involves the integration of some function of stress over the surface area may be more appropriate to analyse the size effect of ballast because the contact area may be large

during the test and because of the presence of surface flaws in ballast particles; however, this is purely conjecture.

Chapter 4

Large Oedometer Tests

4.1 Introduction

The large oedometer test is the same in principle as the ACV test (section 2.2.3), where a ballast sample is compressed one-dimensionally to a certain macroscopic stress in an oedometer or a cylindrical steel mould. McDowell (2002) and McDowell & Harireche (2002b) have shown that for a sample of uniformly graded granular material subjected to one-dimensional compression, the yield stress (defined as the point on a plot of voids ratio against the logarithm of applied macroscopic stress, such that major plastic deformation occurs beyond this point) is proportional to the average tensile strength of the constituent particles. Thus, the ACV test, which tests 10-14mm ballast particles, cannot be expected to give a good indication of the performance of railway ballast in the track, because of the different size effect on strength for different ballast materials. Thus, a large oedometer test was designed to test track ballast. Six types of ballast were tested: A, B, C, D, E and F.

The only assumption in this oedometer test is that the ballast samples have been tested under uniform stresses. It was noted by McDowell et al. (2003) that large wall friction, resulting from a high sample aspect ratio (height/diameter of the sample), can cause the stress at the top of the sample to be significantly different from the stress at the bottom. Thus, considering the effect of wall friction and the limitation of the test apparatus, an aspect ratio of 0.5 was chosen in an attempt to minimise wall friction, whilst maintaining a sample thickness of a sufficient number of particles.

The maximum ratio of the stress at the top of the sample to the stress at the bottom can be calculated by (assuming an angle of internal friction of 30° for the ballast and a ballast-wall coefficient of friction of 0.5):

$$\frac{\sigma_1}{\sigma_2} = \exp\left(\frac{H}{D}\right) \quad (4.1)$$

where σ_1 and σ_2 are the stress at the top and bottom of the sample respectively, H is the height of the sample, and D is the diameter of the sample (McDowell et al., 2003). From this equation, the maximum ratio of the stress at the top of the sample to the stress at the bottom for an aspect ratio of 0.5 is 1.6.

4.2 Test procedures

Ballast samples were dried and sieved to obtain three sieve size fractions: 10-14mm, 37.5-50mm and specification ballast. The specification ballast consists of 60% by mass of 25-37.5mm and 40% by mass of 37.5-50mm, and conforms to the original (2000) specification (RT/CE/S/006 Issue 3, 2000). Each prepared ballast sample was first poured into a 300mm diameter oedometer and levelled by hand. The ballast sample was then compacted to maximum achievable density using a vibrating table with the top platen of the oedometer used as a surcharge (3.5kPa). The depth of the ballast sample was constantly checked during compaction, and the compaction process was stopped when the depth of the sample was found to be constant with time. This procedure was adopted to obtain maximum density for each ballast sample. Each compacted ballast sample was approximately 150mm thick, giving an aspect ratio of approximately 0.5.

The compacted ballast sample was transferred to an Instron testing machine, with a 2000kN capacity, and potentiometers were installed to measure the vertical displacement of the top platen of the oedometer as shown in Figure 4.1. The ballast sample was compressed to 1500kN, which is equivalent to 21MPa. This applied stress is the same as the stress applied to a sample in an ACV test. The rate of

loading was chosen to be 1mm/min to avoid the top platen catching the side wall of the oedometer and jamming during loading. The loading time to achieve 1500kN with this rate of loading is approximately 40 minutes. Even though the loading time of the large oedometer test is 4 times higher than the loading time of the ACV test, it should not affect the results and the large oedometer test can be compared with the ACV test because granular materials are not affected significantly by the rate of loading (Shenton, 1974) unless the rates are orders of magnitude apart. McDowell et al. (2003) justified the use of this rate of loading by showing that the ACVs (percentages passing 2.36mm) for the 10-14mm ballast were approximately equal for the large oedometer test and the ACV test. The tested sample was sieved to obtain the particle size distribution, which was then used to compute the ACV and Hardin's total breakage factor (Hardin, 1985), B_t .

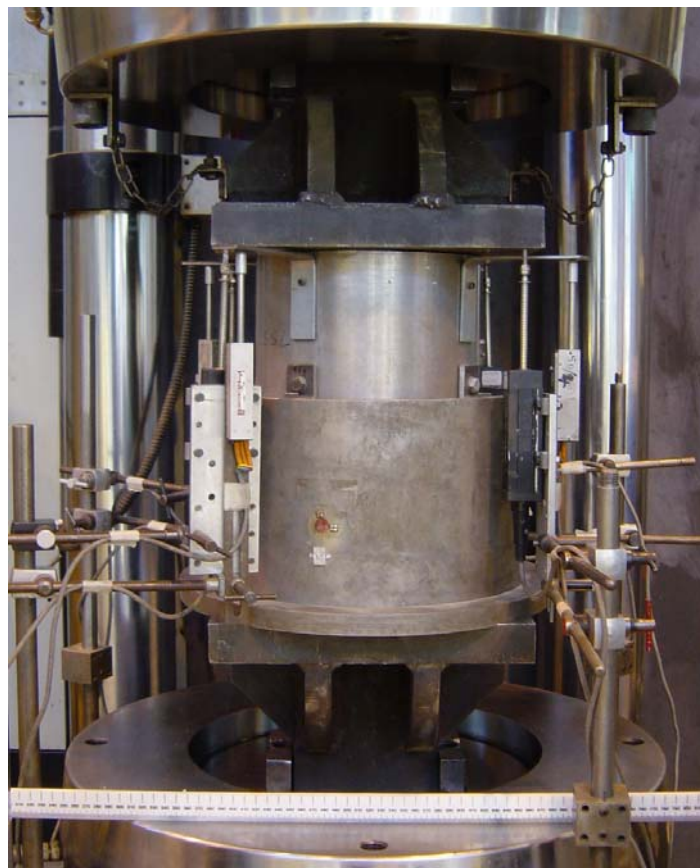


Figure 4.1. Oedometer test set-up.

4.3 Results

4.3.1 Computation of results

Two methods can be used to determine the relative resistance to crushing of a tested ballast sample: one is by the ACV which is the amount of fines passing the 2.36mm sieve produced after the test, and another is by examining the change in the whole mass grading curve (note that the percentage by mass passing the 2.36mm sieve is here still called the ACV, even though the oedometer test is on 37.5-50mm and specification ballast particles as opposed to 10-14mm particles in the standard ACV test). For this purpose, Hardin's (1985) total breakage factor can be used; this measures the area swept out by the particle size distribution plot.

The determination of the ACV is simple: it is the percentage of particles by mass passing the 2.36mm sieve. Hardin's (1985) total breakage factor, however, requires more complex analysis. The first step to obtain the total breakage factor is to obtain the breakage potential. The breakage potential is defined by:

$$B_p = \int_0^1 b_p df \quad (4.2)$$

where b_p is the potential for breakage of a particle of a given size and df is a differential of percentage passing by mass divided by 100. The potential of breakage of a particle of a given size, D (in mm), can be represented by:

$$b_p = \log_{10} \left[\frac{D}{0.063} \right] \quad \text{for } D \geq 0.063 \quad (4.3)$$
$$b_p = 0 \quad \text{for } D < 0.063$$

where 0.063 is the largest silt size in mm. The largest silt size was chosen by Hardin (1985) because he assumed that particles that are smaller than this will have insignificant effect on the aggregate behaviour. However, if the percentage is

significant, then permeability will clearly be affected. The breakage potential for a given particle size distribution is the shaded area shown in Figure 4.2.

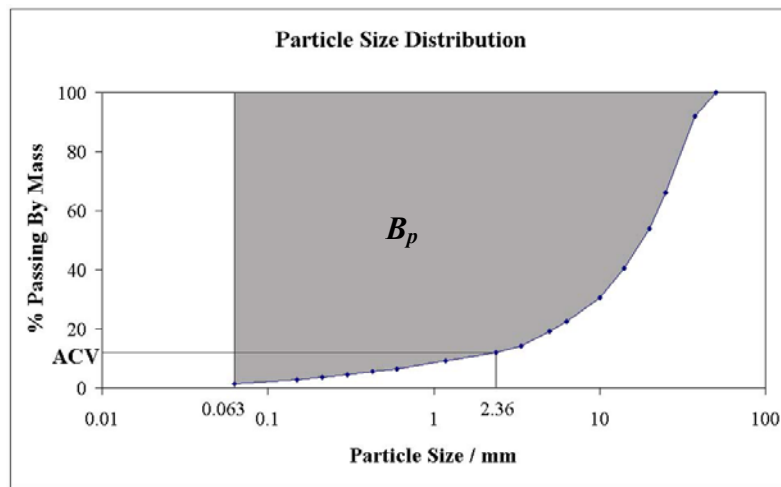


Figure 4.2. Breakage potential, B_p .

The total breakage is defined as:

$$B_t = \int_0^1 (b_{po} - b_{pl}) df \quad (4.3)$$

where b_{po} is the original value of b_p , and b_{pl} is the value of b_p after loading. Thus, the total breakage B_t is the area swept out by the particle size distribution, as shown in Figure 4.3.

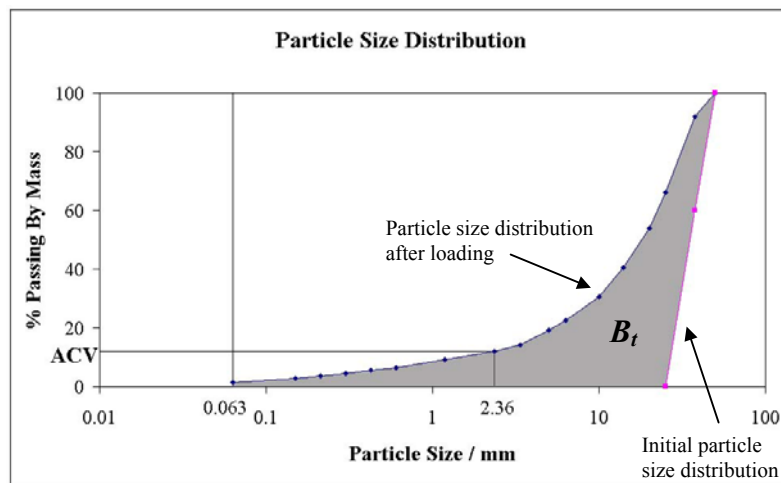


Figure 4.3. Total breakage, B_t .

4.3.2 Large oedometer test on 10-14mm ballast

The one-dimensional compression plot for the large oedometer tests on 10-14mm ballast, for each of the ballasts tested (except for ballast D because of data logging error during the test), is shown in Figure 4.4. The initial and final voids ratios (ie. at the end of one-dimensional compression), and the coefficient of compressibility C_c , are summarized in Table 4.1. The particle size distribution curves for the large oedometer tests on 10-14mm ballast, for each of the six ballasts tested, are shown in Figure 4.5.

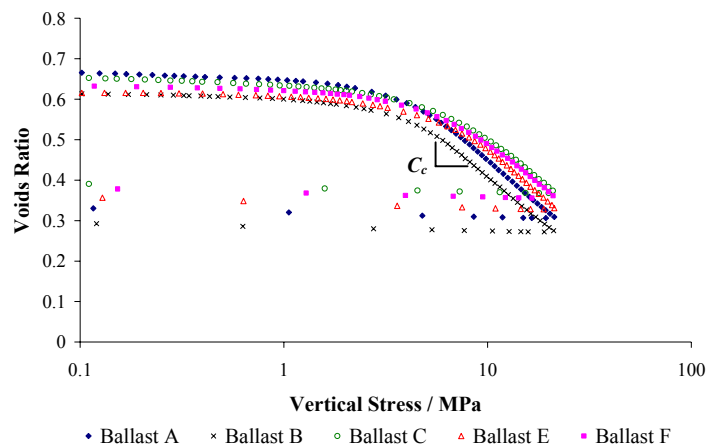


Figure 4.4. One-dimensional compression plot for large oedometer tests on 10-14mm ballast.

| Ballast | Voids Ratio (10-14mm) | | C_c |
|---------|-----------------------|-------|-------|
| | Initial | Final | |
| A | 0.67 | 0.31 | 0.44 |
| B | 0.62 | 0.27 | 0.42 |
| C | 0.65 | 0.37 | 0.41 |
| D* | 0.67 | NA | NA |
| E | 0.61 | 0.33 | 0.44 |
| F | 0.63 | 0.36 | 0.40 |

Table 4.1. Summary of voids ratios and coefficient of compressibility for large oedometer tests on 10-14mm ballast.

* Note: The result for ballast D is unavailable due to a data logging error during the test.

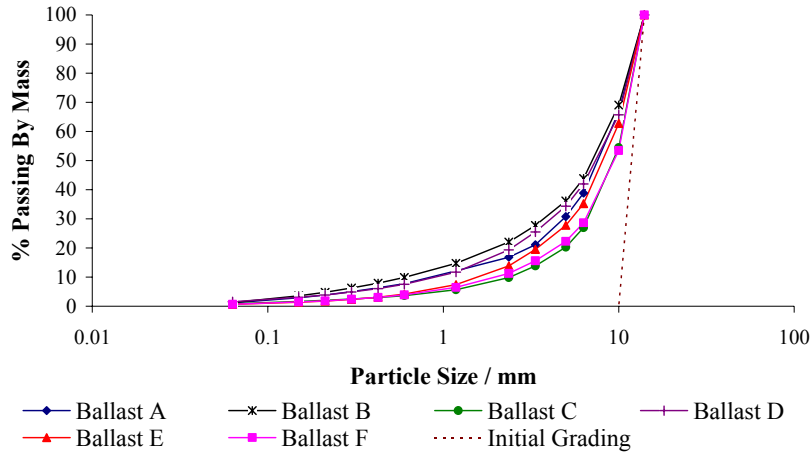


Figure 4.5. Particle size distributions for large oedometer tests on 10-14mm ballast.

The ACV and B_t values for each ballast are listed in Table 4.2 together with the 37% tensile strength σ_o , of 10-14mm ballast particles in each case. The relative ranking of each ballast based on each parameter is shown by the subscript next to each value. Figure 4.6 shows the plot of B_t against ACV for oedometer tests on 10-14mm ballast. As anticipated, there is a good correlation between these 2 values. Figures 4.7 and 4.8 show the plots of ACV and B_t respectively for oedometer tests on 10-14mm ballast, against σ_o (37% tensile strength) for 10-14mm ballast particles. It can be seen that there is a strong correlation between each of the oedometer test parameters ACV and B_t , for tests on 10-14mm ballast, and the tensile strength σ_o , of 10-14mm ballast particles.

| Ballast | ACV (%) | B_t | σ_o (MPa) |
|---------|---------------------|---------------------|---------------------|
| A | 16.8 ₍₄₎ | 0.37 ₍₄₎ | 37.8 ₍₄₎ |
| B | 22.0 ₍₆₎ | 0.44 ₍₆₎ | 24.0 ₍₆₎ |
| C | 9.8 ₍₁₎ | 0.25 ₍₁₎ | 54.8 ₍₁₎ |
| D | 19.3 ₍₅₎ | 0.39 ₍₅₎ | 26.0 ₍₅₎ |
| E | 13.8 ₍₃₎ | 0.31 ₍₃₎ | 48.9 ₍₂₎ |
| F | 11.2 ₍₂₎ | 0.26 ₍₂₎ | 48.3 ₍₃₎ |

Table 4.2. ACV and B_t values for large oedometer tests on 10-14mm ballast and σ_o of 10-14mm ballast particles.

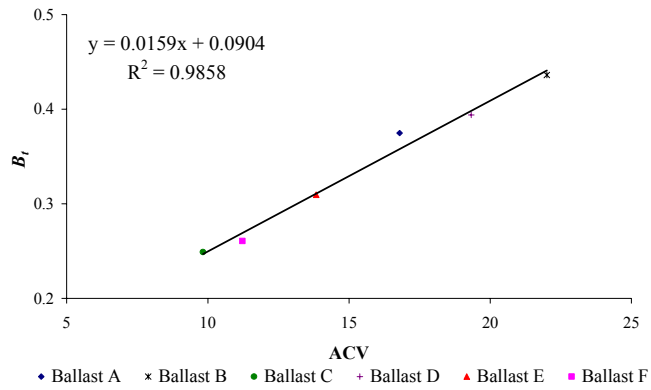


Figure 4.6. B_t against ACV for oedometer test on 10-14mm ballast.

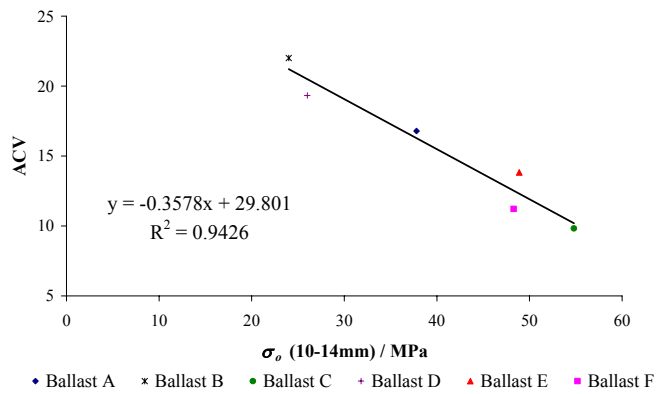


Figure 4.7. ACV for oedometer test on 10-14mm ballast against σ_o (10-14mm).

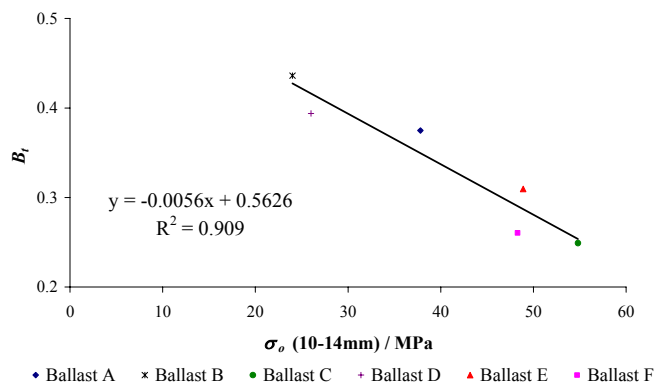


Figure 4.8. B_t for oedometer test on 10-14mm ballast against σ_o (10-14mm).

4.3.3 Large oedometer test on 37.5-50mm ballast

The one-dimensional compression plot for the large oedometer tests on 37.5-50mm ballast, for each of the six ballasts tested, is shown in Figure 4.9. The initial and final voids ratios, and the coefficient of compressibility C_c , are summarized in Table 4.3. The particle size distribution curves for the large oedometer tests on 37.5-50mm ballast, for the six ballasts tested, are shown in Figure 4.10.

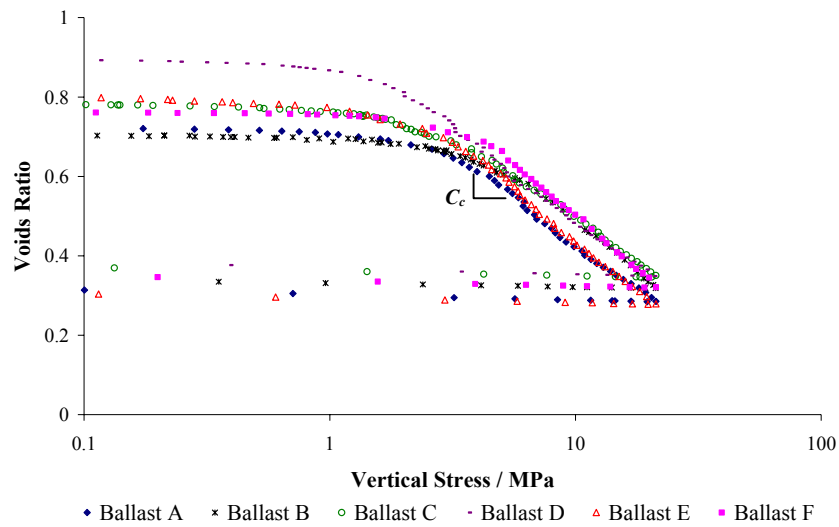


Figure 4.9. One-dimensional compression plot for large oedometer tests on 37.5-50mm ballast.

| Ballast | Voids Ratio (37.5-50mm) | | C_c |
|---------|-------------------------|-------|-------|
| | Initial | Final | |
| A | 0.73 | 0.29 | 0.43 |
| B | 0.71 | 0.32 | 0.53 |
| C | 0.78 | 0.35 | 0.45 |
| D | 0.90 | 0.36 | 0.45 |
| E | 0.80 | 0.28 | 0.48 |
| F | 0.76 | 0.32 | 0.53 |

Table 4.3. Summary of voids ratios and coefficient of compressibility for large oedometer tests on 37.5-50mm ballast.

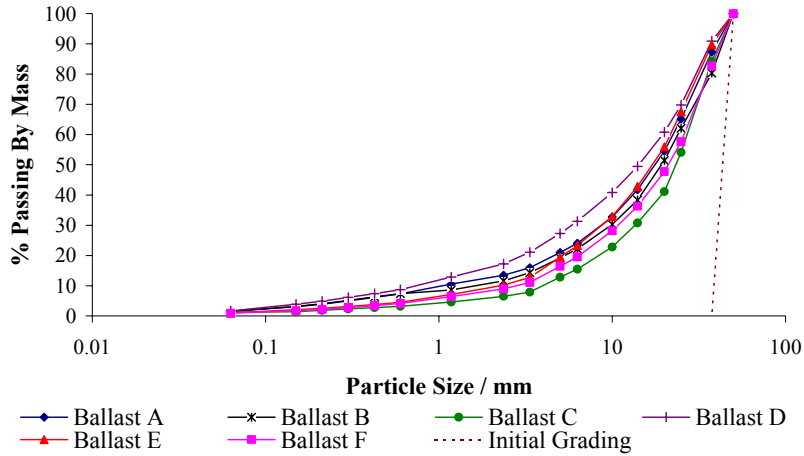


Figure 4.10. Particle size distributions for large oedometer tests on 37.5-50mm ballast.

The ACV and B_t values for each ballast are listed in Table 4.4, together with the 37% tensile strength σ_o , of 37.5-50mm ballast particles in each case. The relative ranking of each ballast based on each parameter is shown by the subscript next to each value. Figure 4.11 shows the plot of B_t against ACV for oedometer tests on 37.5-50mm ballast. As anticipated, there is a good correlation between these 2 values. Figures 4.12 and 4.13 show the plots of ACV and B_t for oedometer tests on 37.5-50mm ballast, respectively, against σ_o of 37.5-50mm ballast particles. It can be seen that there is some correlation between each of the oedometer test parameters ACV and B_t , for tests on 37.5-50mm ballast, and the tensile strength σ_o , of 37.5-50mm ballast particles.

| Ballast | ACV (%) | B_t | σ_o (MPa) |
|---------|---------------------|---------------------|---------------------|
| A | 13.5 ₍₅₎ | 0.61 ₍₅₎ | 21.7 ₍₃₎ |
| B | 11.6 ₍₄₎ | 0.57 ₍₃₎ | 13.0 ₍₅₎ |
| C | 6.5 ₍₁₎ | 0.44 ₍₁₎ | 32.8 ₍₁₎ |
| D | 17.2 ₍₆₎ | 0.71 ₍₆₎ | 12.3 ₍₆₎ |
| E | 10.2 ₍₃₎ | 0.58 ₍₄₎ | 21.1 ₍₄₎ |
| F | 9.0 ₍₂₎ | 0.50 ₍₂₎ | 29.0 ₍₂₎ |

Table 4.4. ACV and B_t values for large oedometer tests on 37.5-50mm ballast and σ_o of 37.5-50mm ballast particles.

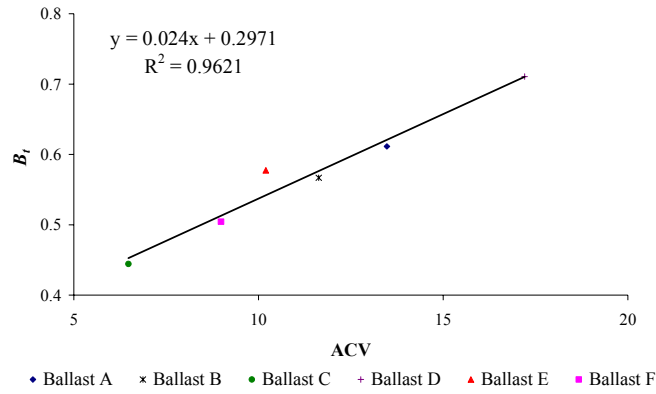


Figure 4.11. B_t against ACV for oedometer test on 37.5-50mm ballast.

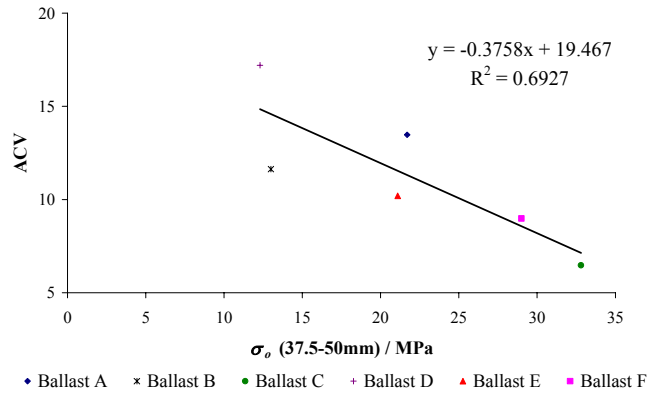


Figure 4.12. ACV for oedometer test on 37.5-50mm ballast against σ_o (37.5-50mm).

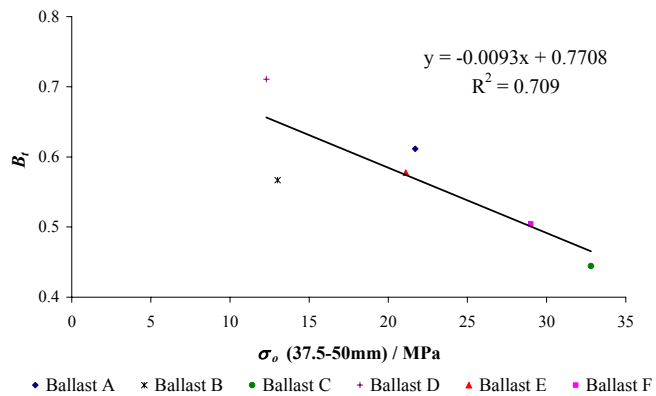


Figure 4.13. B_t for oedometer test on 37.5-50mm ballast against σ_o (37.5-50mm).

The results from Table 4.4 were re-examined and it was noted that ACV, B_t and σ_o correlate very well for ballasts C, D and F. However, the results for ballasts A, B

and E do not correlate so well. The most obvious disagreement is that σ_o for ballast B is significantly lower than that for ballasts A and E, but the ACV and B_t values are close to ballasts A and E. This could be attributed to the fact that ballast B is significantly less ‘flaky’ than ballasts A and E, as shown by the flakiness index in Table 4.5 (flakiness test was conducted by Lafarge Aggregates Limited). Past research (Gur et al., 1967; Selig & Roner, 1987) has shown that higher flakiness increases ballast breakage. Thus, flakiness will affect ballast degradation in the oedometer test, but will not affect the tensile strength much because the single particle crushing tests were conducted on quasi-spherical, geometrically similar ballast particles. Ballast B is then expected to exhibit less breakage in the oedometer test, but the fact that the amount of degradation is approximately the same as for ballasts A and E, must be because the value of σ_o for ballast B is significantly lower than for these two ballasts.

| Ballast | Flakiness index |
|---------|-----------------|
| A | 14 |
| B | 5 |
| C | 31 |
| D | 19 |
| E | 31 |
| F | 21 |

Table 4.5. Flakiness indices (according to BS812 Section 105.1, 1989).

Another discrepancy in the results of Table 4.4 is that B_t and σ_o are nearly the same for ballasts A and E but the ACV for ballast A is higher than for ballast E. This observation is shown clearly in Figure 4.14 where only the particle size distributions for ballast A and E have been plotted. The plot shows that ballasts A and E have the same amount of coarse breakages but ballast A has more fines produced by the oedometer test than ballast E. Thus, the ACV, which is a measure of the amount of fines, gives a higher value for ballast A. The reason for this could be attributed to the fact that ballast E has a stronger size effect on strength than ballast A as shown in the Figure 3.3, Table 4.2, and Table 4.4. Thus, as the particle size decreases, the

strength of ballast E increases more rapidly than that of ballast A, because small particles of ballast E are statistically stronger than small particles of ballast A.

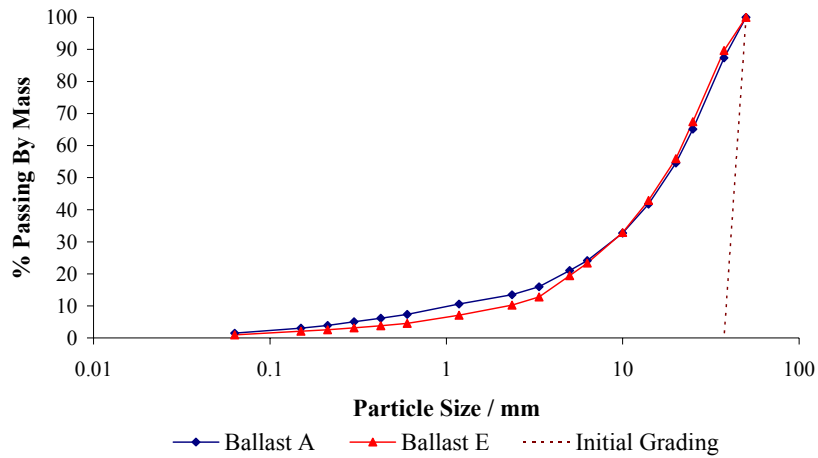


Figure 4.14. Particle size distributions for large oedometer tests on 37.5-50mm ballasts A and E.

4.3.4 Large oedometer test on specification ballast

The one-dimensional compression plot for the large oedometer tests on specification ballast, for each of the six ballasts tested, is shown in Figure 4.15. The initial and final voids ratios, and the coefficient of compressibility C_c , are summarized in Table 4.6. The particle size distribution curves for the oedometer tests on specification ballast for the six ballasts tested are shown in Figure 4.16. The ACV and B_t values for each ballast are listed in Table 4.7 together with the weighted average value σ_{ow} , of specification ballast particles in each case. The weighted average value σ_{ow} was computed by combining the values of σ_o for the 37.5-50mm ballast particles and 25-37.5mm ballast particles using 40% and 60% weightings respectively (according to the percentage of each ballast size in the specification ballast). The value of σ_o relating to the average size in the 25-37.5mm ballast particles was extrapolated from a plot of σ_o against mean nominal size because this particle size was not tested in the single particle crushing test. The relative ranking of each ballast based on each parameter is again shown by the subscript next to each value in the table.

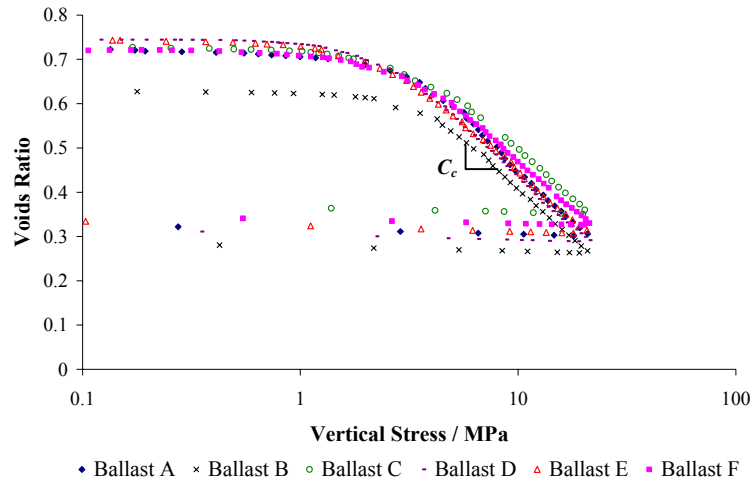


Figure 4.15. One-dimensional compression plot for large oedometer tests on specification ballast.

| Ballast | Voids Ratio (Specification) | | C_c |
|---------|-----------------------------|-------|-------|
| | Initial | Final | |
| A | 0.73 | 0.30 | 0.47 |
| B | 0.63 | 0.26 | 0.44 |
| C | 0.73 | 0.35 | 0.45 |
| D | 0.75 | 0.29 | 0.46 |
| E | 0.75 | 0.31 | 0.46 |
| F | 0.72 | 0.33 | 0.43 |

Table 4.6. Summary of voids ratios and coefficient of compressibility for large oedometer tests on specification ballast.

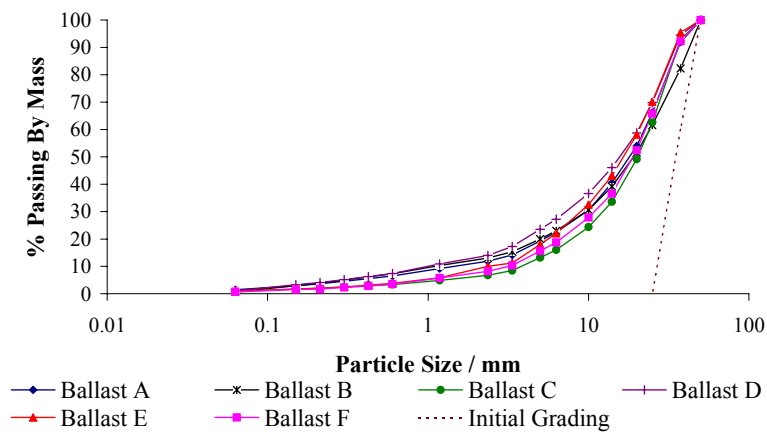


Figure 4.16. Particle size distributions for large oedometer tests on specification ballast.

| Ballast | ACV (%) | B_t | σ_{ow} (MPa) |
|---------|---------------------|---------------------|---------------------|
| A | 11.9 ₍₄₎ | 0.50 ₍₅₎ | 23.6 ₍₄₎ |
| B | 13.1 ₍₅₎ | 0.49 ₍₃₎ | 14.2 ₍₅₎ |
| C | 6.8 ₍₁₎ | 0.40 ₍₁₎ | 35.6 ₍₁₎ |
| D | 14.0 ₍₆₎ | 0.57 ₍₆₎ | 13.8 ₍₆₎ |
| E | 10.0 ₍₃₎ | 0.49 ₍₃₎ | 24.4 ₍₃₎ |
| F | 8.2 ₍₂₎ | 0.43 ₍₂₎ | 31.5 ₍₂₎ |

Table 4.7. ACV and B_t values for large oedometer tests on specification ballast and σ_{ow} of specification ballast particles.

Figure 4.17 shows the plot of B_t against ACV for oedometer tests on specification ballast. As anticipated, there is a good correlation between these 2 values. Figures 4.18 and 4.19 show the plots of ACV and B_t respectively for oedometer tests on specification ballast, against σ_{ow} of specification ballast particles. It can be seen that there is also a good correlation between each of the oedometer test parameters ACV and B_t , for tests on specification ballast, and σ_{ow} . Similar to the 37.5-50mm oedometer test results, Table 4.7 shows that ACV, B_t and σ_o correlate very well for ballasts C, D and F, but not so well for ballasts A, B and E. However, as discussed in the previous section, ballast B has a lower particle strength (measured for quasi-spherical particles on all ballasts), but is less ‘flaky’ than ballasts A and E; and ballast E has a greater size effect than ballast A. Another particle size distribution plot for the large oedometer tests on specification ballasts A and E is shown in Figure 4.20 to reinforce the latter point.

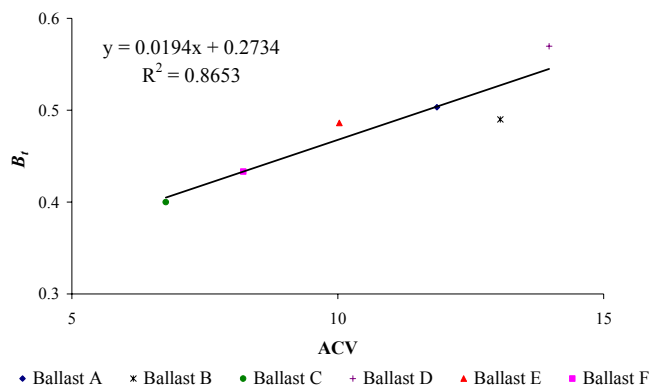


Figure 4.17. B_t against ACV for oedometer test on specification ballast.

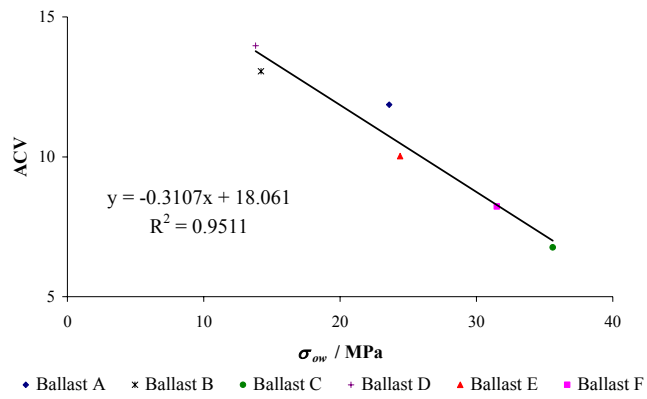


Figure 4.18. ACV for oedometer test on specification ballast against σ_{ow} .

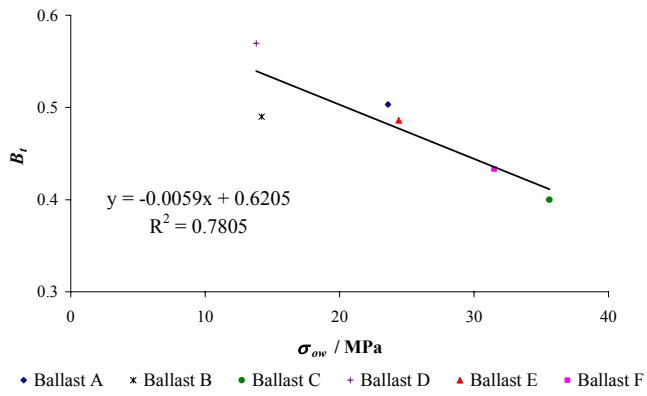


Figure 4.19. B_t for oedometer test on specification ballast against σ_{ow} .

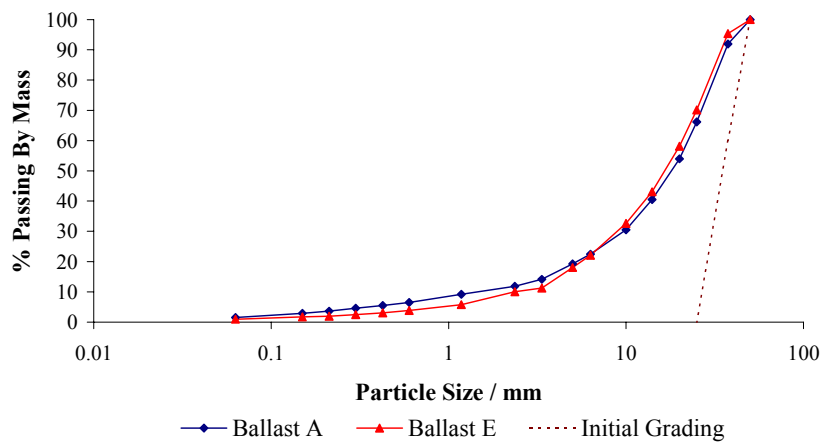


Figure 4.20. Particle size distributions for large oedometer tests on specification ballasts A and E.

4.3.5 Summary of results

The ACV and B_t values for all the large oedometer tests are summarised in Table 4.8 and Table 4.9 respectively. It is noticed that the oedometer tests on 37.5-50mm and specification ballast have similar ACV and B_t rankings. This is anticipated because the specification ballast consists of mainly large ballast particles. The problem of using the oedometer test on 10-14mm ballast to predict the performance of track ballast is verified here, where the ACV for ballast B is the worst for the large oedometer tests on 10-14mm ballast whilst it is comparable with ballasts A and E in the large oedometer tests on specification ballast.

| Ballast | ACV (%) | | |
|---------|---------------------|---------------------|---------------------|
| | 10-14mm | 37.5-50mm | Specification |
| A | 16.8 ₍₄₎ | 13.5 ₍₅₎ | 11.9 ₍₄₎ |
| B | 22.0 ₍₆₎ | 11.6 ₍₄₎ | 13.1 ₍₅₎ |
| C | 9.8 ₍₁₎ | 6.5 ₍₁₎ | 6.8 ₍₁₎ |
| D | 19.3 ₍₅₎ | 17.2 ₍₆₎ | 14.0 ₍₆₎ |
| E | 13.8 ₍₃₎ | 10.2 ₍₃₎ | 10.0 ₍₃₎ |
| F | 11.2 ₍₂₎ | 9.0 ₍₂₎ | 8.2 ₍₂₎ |

Table 4.8. Summary of ACV values for large oedometer tests.

| Ballast | B_t | | |
|---------|---------------------|---------------------|---------------------|
| | 10-14mm | 37.5-50mm | Specification |
| A | 0.37 ₍₄₎ | 0.61 ₍₅₎ | 0.50 ₍₅₎ |
| B | 0.44 ₍₆₎ | 0.57 ₍₃₎ | 0.49 ₍₃₎ |
| C | 0.25 ₍₁₎ | 0.44 ₍₁₎ | 0.40 ₍₁₎ |
| D | 0.39 ₍₅₎ | 0.71 ₍₆₎ | 0.57 ₍₆₎ |
| E | 0.31 ₍₃₎ | 0.58 ₍₄₎ | 0.49 ₍₃₎ |
| F | 0.26 ₍₂₎ | 0.50 ₍₂₎ | 0.43 ₍₂₎ |

Table 4.9. Summary of B_t values for large oedometer tests.

4.3.6 Additional tests

It is interesting to note that ballast D is not always the weakest ballast (Tables 4.2, 4.4 and 4.7) based on single particle crushing tests and large oedometer tests, and for the cases where it is the weakest, it is not much weaker than the next strongest material. However, WAV, LAA and MDA tests showed that ballast D is considerably weaker than all the other ballasts, as shown in Table 4.10 (WAV test was conducted by Test Houses Limited, and LAA and MDA tests were conducted by Lafarge Aggregates Limited). It was noticed that the WAV and MDA tests both test ballast under wet conditions. The water absorption of ballast D is at least 3 times higher than any other ballast, as shown in Table 4.11 (the water absorption tests were conducted by Lafarge Aggregates Limited):

| Ballast | WAV | LAA | MDA |
|---------|-----|-----|-----|
| A | 2.8 | 13 | 4 |
| B | 3.2 | 9 | 6 |
| C | 1.9 | 8 | 4 |
| D | 7.4 | 30 | 12 |
| E | 1.6 | 13 | 3 |
| F | 2.6 | 10 | 6 |

Table 4.10. WAV, LAA, and MDA values.

| Ballast | Water Absorption % |
|---------|--------------------|
| A | 0.3 |
| B | 0.5 |
| C | 0.4 |
| D | 1.5 |
| E | 0.5 |
| F | 0.5 |

Table 4.11. Water absorption values.

It was considered interesting to know the effect of water on ballast D in the large oedometer test, so two wet tests were conducted for this purpose. The wet large oedometer test was a drained (not saturated) oedometer test with the ballast just soaked in water over the weekend before the test. The other ballast chosen for the wet large oedometer test was ballast B because the 37% tensile strengths for 10-14mm and 37.5-50mm ballast particles are close to the 37% tensile strengths for ballast D. The grading of the wet large oedometer test was the same as for the specification ballast tested dry.

The one-dimensional compression plot for the large oedometer tests on dry and wet specification ballasts B and D, is shown in Figure 4.21. The initial and final voids ratios, and the coefficient of compressibility C_c , are summarized in Table 4.12.

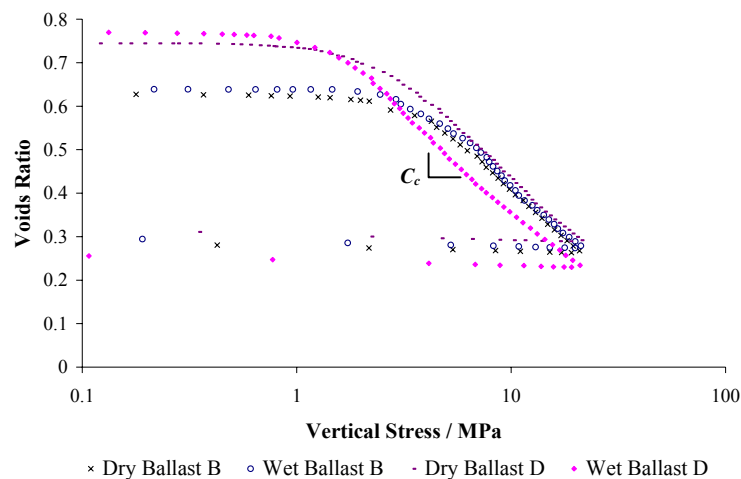


Figure 4.21. One-dimensional compression plot for large oedometer tests on dry and wet specification ballasts B and D.

| Ballast | Voids Ratio (Specification) | | C_c |
|---------|-----------------------------|-------|-------|
| | Initial | Final | |
| Dry B | 0.63 | 0.26 | 0.44 |
| Wet B | 0.64 | 0.27 | 0.47 |
| Dry D | 0.75 | 0.29 | 0.46 |
| Wet D | 0.77 | 0.22 | 0.42 |

Table 4.12. Summary of voids ratios and coefficient of compressibility for large oedometer tests on dry and wet specification ballasts B and D.

The particle size distribution curves for the large oedometer tests on dry and wet specification ballasts B and D, are shown in Figure 4.22. Clearly, there is an increase in breakage for the wet oedometer tests and the increase in breakage is more significant in ballast D than in ballast B. The ACV and B_t values are listed in Table 4.13. It can be seen that the ACV and B_t values increase significantly in ballast D.

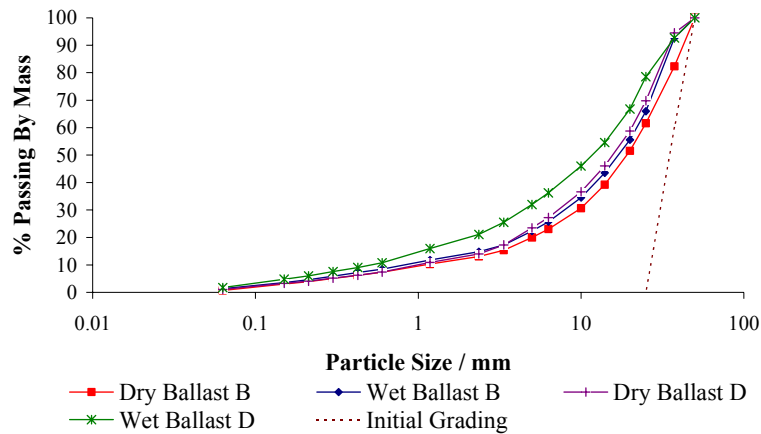


Figure 4.22. Particle size distributions for large oedometer tests on dry and wet specification ballasts B and D.

| Ballast | ACV (%) | B_t |
|---------|---------|-------|
| Dry B | 13.1 | 0.49 |
| Wet B | 14.8 | 0.56 |
| Dry D | 14.0 | 0.57 |
| Wet D | 21.1 | 0.71 |

Table 4.13. ACV and B_t values for large oedometer tests on dry and wet specification ballasts B and D.

4.4 Discussion

It is interesting to know whether the ACV and B_t values of the large oedometer tests are strong functions of the 37% tensile strength σ_o of the ballast particles or not. It was noted that it is not possible to compare the ACV (% passing 2.36mm) of all the large oedometer tests directly because of different initial gradings. Thus, the sieve

size used to define ACV could be scaled (e.g. linearly) with the average size of the initial grading. An ACV that has been scaled to take account of the average size of the initial grading is denoted as ACV_d . The sieve size used to define ACV_d for different gradings can therefore be calculated by:

$$\text{Sieve size} = \frac{2.36 \times (\text{average sieve size in mm})}{12} \text{ mm} \quad (4.4)$$

From equation 4.4, the sieve sizes used to define ACV_d for the large oedometer tests on 37.5-50mm and specification ballast are 8.65mm and 7.08mm respectively. The ACV_d values for all the large oedometer tests were obtained from the particle size distribution plots and summarized in Table 4.14. The relative ranking of each ballast based on each parameter is again shown by the subscript next to each value in the table.

| Ballast | ACV_d (%) | | |
|---------|----------------------------------|------------------------------------|--|
| | 10-14mm (% passing 2.36mm) | 37.5-50mm (% passing 8.65mm) | Specification (% passing 7.08mm) |
| A | 16.8 ₍₄₎ | 30 ₍₄₎ | 25 ₍₃₎ |
| B | 22.0 ₍₆₎ | 28 ₍₃₎ | 25 ₍₃₎ |
| C | 9.8 ₍₁₎ | 21 ₍₁₎ | 18 ₍₁₎ |
| D | 19.3 ₍₅₎ | 38 ₍₆₎ | 29 ₍₆₎ |
| E | 13.8 ₍₃₎ | 30 ₍₄₎ | 25 ₍₃₎ |
| F | 11.2 ₍₂₎ | 25 ₍₂₎ | 21 ₍₂₎ |

Table 4.14. Summary of ACV_d values for large oedometer tests.

Figures 4.23 and 4.24 show the plots of ACV_d and B_t respectively for all the large oedometer tests against the 37% tensile strength σ_o of ballast particles (σ_{ow} for the specification ballast particles). It can be seen that there is a good correlation between each of the large oedometer test parameters ACV_d and B_t , and the 37% tensile strength σ_o of ballast particles. A closer examination of the data found that the correlation can be improved. Table 4.15 presents ACV_d , B_t , σ_o , and initial voids

ratio e_i for 10-14mm ballast B and 37.5-50mm ballast C. It can be seen that ACV_d and B_t values for the 2 ballasts are approximately equal, but σ_o and e_i are very different. There seems to be a compensating effect between σ_o and e_i . For example, the aggregate in the large oedometer test on 10-14mm ballast B, which compressed ballast particles with low tensile strength, was strengthened by a denser assembly, as shown by the low initial voids ratio. This observation is consistent to that discussed in section 2.3.4: i.e. the decrease in voids ratio increases the co-ordination number of the assembly, thus reducing the average tensile stress induced in the particles. Therefore, a better correlation should be obtained if ACV_d and B_t values were correlated with a parameter which considers both σ_o and e_i . It should be noted that each large oedometer test was compacted in the same manner to maximum density (i.e. relative density of 1), so that the initial voids ratio e_i has to be a function of the particle shape for each ballast.

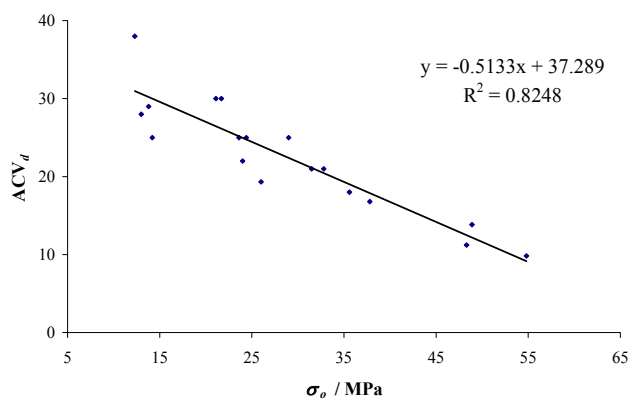


Figure 4.23. ACV_d against σ_o .

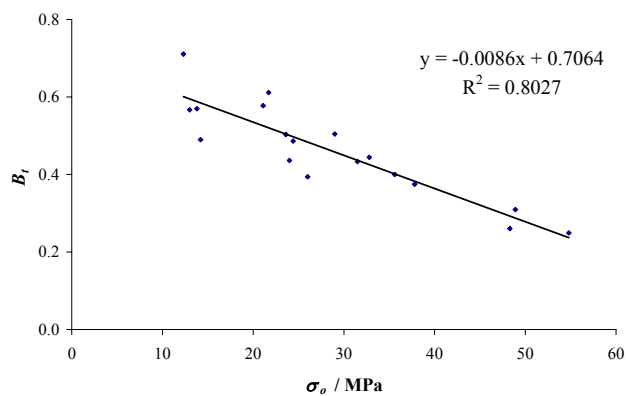


Figure 4.24. B_t against σ_o .

| Ballast | ACV _d (%) | B _t | σ _o (MPa) | e _i |
|---------------|----------------------|----------------|----------------------|----------------|
| B (10-14mm) | 22.0 | 0.44 | 24.0 | 0.62 |
| C (37.5-50mm) | 21.0 | 0.44 | 32.8 | 0.78 |

Table 4.15. ACV_d, B_t, σ_o and e_i for 10-14mm ballast B and 37.5-50mm ballast C.

A new parameter called relative strength index R_s that considers the compensating effect of σ_o and e_i was proposed. This parameter is defined by:

$$R_s = \frac{R_e + R_\sigma}{2} \quad (4.5)$$

where R_e and R_σ are the relative voids ratio and the relative tensile strength respectively. R_e and R_σ are defined by:

$$R_e = \frac{e_{i,\max} - e_i}{e_{i,\max} - e_{i,\min}} \quad (4.6)$$

$$R_\sigma = \frac{\sigma_o - \sigma_{o,\min}}{\sigma_{o,\max} - \sigma_{o,\min}} \quad (4.7)$$

where $e_{i,\max}$ and $e_{i,\min}$ are the maximum and minimum initial voids ratio e_i of all the large oedometer tests respectively, and $\sigma_{o,\max}$ and $\sigma_{o,\min}$ are the maximum and minimum 37% tensile strength σ_o of all the large oedometer tests respectively. For example, a large oedometer test that has the lowest initial voids ratio e_i , and that has ballast particles with the highest 37% tensile strength σ_o , would have an R_s of 1. Figures 4.25 and 4.26 show the plots of ACV_d and B_t respectively for all the large oedometer tests against the relative strength index R_s . It can be seen that the large oedometer test parameters, ACV_d and B_t, are better correlated with R_s than with σ_o (Figures 4.23 and 4.24).

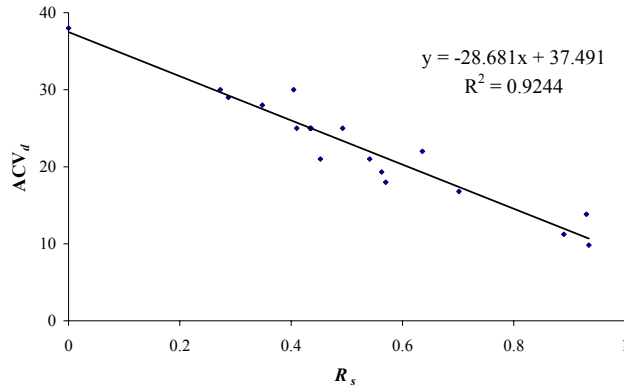


Figure 4.25. ACV_d against R_s .

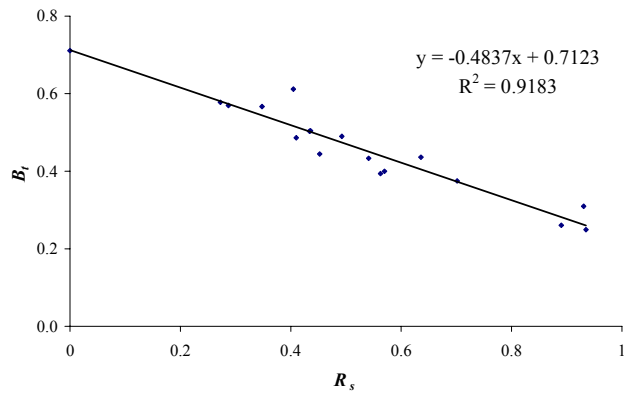


Figure 4.26. B_t against R_s .

4.5 Conclusions

A large oedometer was designed and manufactured to test ballast particles of the size used in the trackbed. The aspect ratio of the large oedometer was chosen to be 0.5 because of the effect of wall friction and the limitation of the test apparatus. The ballast samples were prepared in the oedometer by compacting them to maximum achievable density (i.e. relative density of 1), so that tests can be compared consistently. Even though the loading time of the large oedometer test is 4 times higher than the loading time of the ACV test, the results should not be affected by this and the large oedometer test on 10-14mm ballast can be considered as an ACV test.

The relative performance of small ballast particles cannot be used to predict the relative performance of large ballast particles because of the size effect on the strength of ballast particles. Ballasts that are less “flaky” seem to undergo less breakage, wet ballast appears to be weaker than dry ballast and the degree of strength reduction should be a function of the water absorption of the ballast. More information on aggregate degradation is obtained if ACV and B_t values are available. For example, for large ballast particles tested in an oedometer, ACV alone gives information on the mass of fines generated but nothing about the total amount of breakage. As opposed to ACV, B_t only gives information on the total amount of breakage but nothing on the mass of fines present, which is important when evaluating the permeability of the ballast. Thus, better evaluation of ballast performance will be achieved if both ACV and B_t values are available.

There is a good correlation between each of the large oedometer test parameters ACV_d (scaled ACV value with respect to the initial grading) and B_t , and the 37% tensile strength σ_o of ballast particles. Some discrepancies in the data were noted to be due to the fact that the initial voids ratio e_i of the sample was not considered. Thus, a better correlation was found when ACV_d and B_t were correlated with a new parameter, namely relative strength index R_s , which considers both the 37% tensile strength σ_o of ballast particles and the initial voids ratio e_i of the sample.

Chapter 5

Box Tests

5.1 Introduction

It is clearly important that ballast tests used for specification of materials correlate with ballast field performance. Due to varying field conditions, it is not practical to make comparisons of different ballasts in-situ. Thus, a controlled ballast test was performed in the laboratory in order to compare ballast performance consistently. A box was designed to simulate a sample of ballast undergoing a cycle of construction, loading and maintenance by tamping in a simplified and controlled manner.

The box has a length of 700mm, width of 300mm and height of 450mm, and can be envisaged as representing a section of ballast underneath the rail seat as shown in Figure 5.1. The box is made mainly of case-hardened steel with one side of the box (a longer side) made of reinforced Perspex, so as to be able to observe degradation during the test. The base of the box is made of wood and a 10mm thick rubber sheet was placed between the ballast and the wood in order to replicate a typical stiffness for the trackbed. The box tests were conducted on four types of ballast: A, B, C and D.

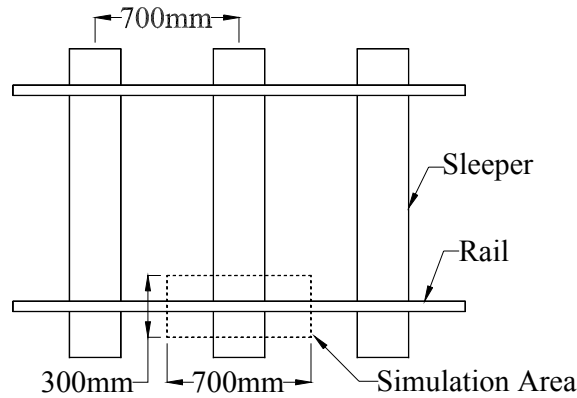


Figure 5.1. Plan of rail and sleepers showing section represented by the box test.

5.2 Test procedures

In order to compare performance consistently in the box tests, all ballast samples had the same grading. The chosen grading conformed to the original (2000) specification (RT/CE/S/006 Issue 3, 2000) track ballast grading and was the same as the specification ballast (which consists of 60% by mass of 25-37.5mm and 40% by mass of 37.5-50mm) in the large oedometer test. The box tests were conducted with wet ballast because track ballast in the United Kingdom is often in the wet condition, and ballast in the wet condition is considered to be more critical (Selig & Waters, 1994). Thus, as for the wet large oedometer test (section 4.3.6), each ballast sample was soaked in water over a weekend to ensure that all ballast particles were wet before the test, and that water had been given enough time to be absorbed. Wet ballast prepared in this method was clearly shown in section 4.3.6 to perform differently from dry ballast.

Each prepared ballast sample was poured into the box until the ballast thickness reached 300mm, and the top of the ballast was then levelled by hand. A rectangular hollow steel section with dimensions 250×300×150mm representing a section of sleeper, was then placed on the ballast and additional ballast was poured on both sides of the sleeper to the top of the box to represent crib ballast. In order to restrain the sleeper from moving horizontally or tilting to one side, a steel piston was

attached to the sleeper and a guide plate for the loading piston was attached to the box frame to guide the sleeper during cyclic loading. This sleeper guiding mechanism is shown in Figure 5.2. Ballast settlement was measured by an LVDT mounted against a bracket attached to the steel piston. It was thought that measuring the deflection at the piston would give the average deflection of the sleeper (since the sleeper could be tilting slightly). However, it was noted that the deflection measured at the piston was slightly higher than the average deflection measured at the edges of the sleeper because the sleeper was bending when loaded through the piston. This effect means that the measured ballast stiffness is an underestimate of the true ballast stiffness. However, the measurement of ballast settlement will not be affected because permanent settlements were recorded at minimum load. The percentage error in the measurement of ballast stiffness depends on the ballast stiffness: the error has been estimated to be approximately 10% at a measured stiffness of 300kPa/mm (so the true ballast stiffness would be approximately 330kPa/mm), approximately 15% for a measured stiffness of 450kPa/mm, and approximately 21% for a measured stiffness of 600kPa/mm. The ballast was loaded cyclically with a sinusoidal load pulse, which is the cyclic load experienced by pavement elements beneath a moving wheel load (Brown, 1996), with minimum load of approximately 3kN and maximum load of approximately 40kN (roughly equivalent to an axle load of 20-25 tonnes) for 1,000,000 cycles, at a frequency of 3Hz. The set up of the ballast box test prior to loading is shown in Figure 5.2 and Figure 5.3.

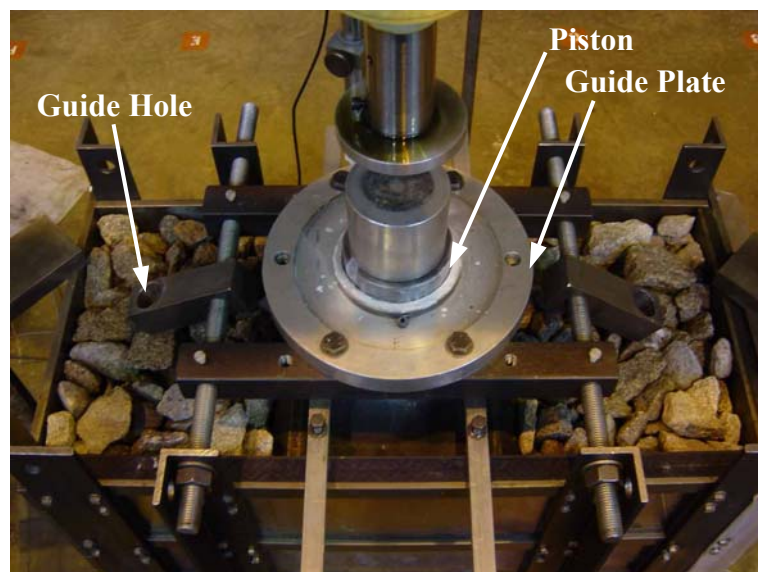


Figure 5.2. Box test set-up (from the top of the box).

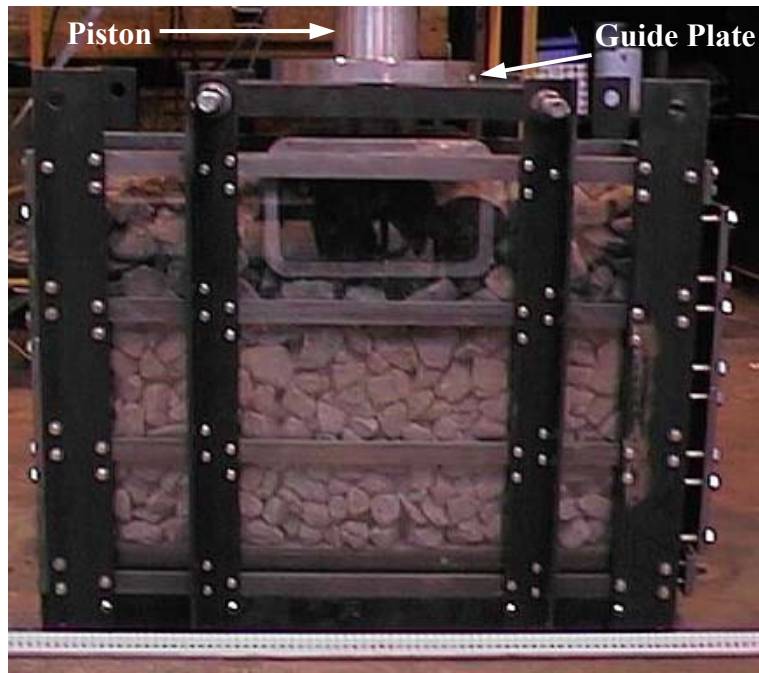


Figure 5.3. Box test set-up (front view).

The ballast tamping process was simulated in the box test by inserting a one inch wide chisel using a Kango hammer into the ballast (Figure 5.4). Before the chisel was inserted into the ballast, the sleeper was lifted until the top of the sleeper was level with the top of the box. At this level, the bottom of the sleeper is 300mm from the bottom of the ballast layer. Thus, the ballast can be tamped to regain (approximately) its original thickness. The chisel was then inserted towards the ballast underneath the sleeper through a guide hole, 160mm from the sleeper edge, at an angle of approximately 10° to the vertical. Figure 5.2 shows the guide holes: one at each side of the sleeper. Three ‘tamps’ were applied at each side of the sleeper and each ‘tamp’ was applied at different locations. For example, the chisel was inserted at a location 95mm from the Perspex wall, followed by inserting it at 205mm from the Perspex wall, and finally at 150mm from the Perspex wall. Each insertion took approximately 2 seconds and tamping was conducted at 100; 500; 1,000; 5,000; 10,000; 50,000; 100,000 and 500,000 cycles. Two litres of water was poured evenly on each side of the sleeper before tamping to ensure that the ballast remained wet during the test. Ballast was also wetted at 300,000 and 750,000 cycles (i.e. midway between 100,000-500,000 and 500,000-1,000,000 cycles respectively). Water and fines which drained out of the box were retained on an aluminium tray underneath the box (the box is free-draining via narrow gaps at the base between

panels in the sides and back of the box). In order to ensure that the same amount of ballast was available to be ‘pushed’ underneath the sleeper, and to maintain the correct amount of crib ballast, additional ballast was added to the top of the box after tamping.

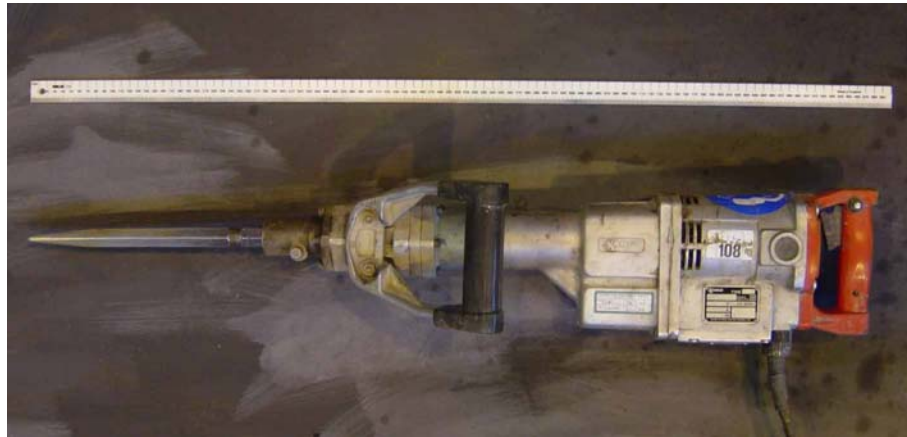


Figure 5.4. Kango hammer with one inch wide chisel.

After testing (1 million cycles) the ballast was taken out of the box in a systematic way, in order to identify the changes in grading for each section. For example, ballast in the box was separated into 7 sections as shown in Figure 5.5 and each section was dried and sieved separately to obtain the grading of each section. The fines retained on the aluminium tray were sieved, together with Section 7 since most of the fines were in this section. The degradation process was assumed to be symmetrical within the box, as shown by the numbering in Figure 5.5 - so the sections numbered ‘2’ were sieved together.

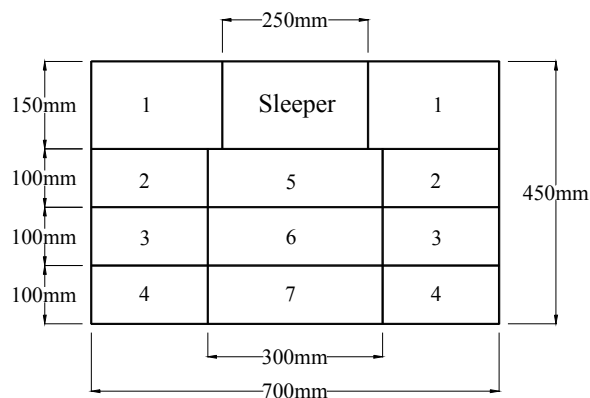


Figure 5.5. Elevation showing different sections for removal of ballast from the box.

5.3 Results

5.3.1 Box test on ballast A

Initially two box tests on ballast A were conducted to investigate the repeatability of the test. The changes in sleeper level against number of cycles for these two box tests (namely, Ballast A(1) and Ballast A(2)), are shown in Figures 5.6 and 5.7 respectively. The sleeper level is taken as the sleeper deflection at the minimum load (3kN) applied by the sinusoidal load pulse. Each ‘spike’ on the plots represents a tamping process as the sleeper was lifted to the top of the box.

It can be seen that the simulated tamping process managed to squeeze ballast to fill the gap underneath the sleeper, and sometimes the sleeper was pushed upwards by tamping, so that some ‘spikes’ are above the top of the box. This was also obvious from viewing through the Perspex wall: ballast was clearly seen to fill the gap underneath the sleeper during tamping. It can be seen that tamping improves the performance of ballast, shown by the reduced rate of settlement at 1 million cycles compared to 100 cycles on the plots (note that the x -axis is logarithmic). Tamping seems to gradually improve the performance of the ballast after each tamp and the degree of improvement decreases in the later stages of the tests.

It is difficult to compare the two ballast A box tests using the plots of sleeper level against number of cycles, because the initial sleeper levels were different. Thus, settlement, which is represented by the change in sleeper level, against number of cycles, is plotted for both ballast A tests in Figure 5.8. The figure shows that the settlement profile for ballast A can be reproduced and that the settlement at the end of each tamping interval reduces with increasing number of tamps. The observed behaviour in the box tests appeared to represent that expected from a real trackbed and therefore the procedures adopted were considered to be appropriate for further tests.

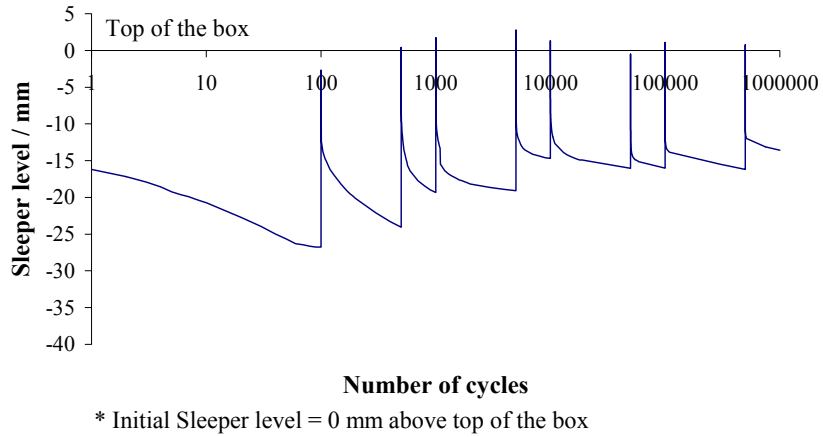


Figure 5.6. Sleeper level against number of cycles for ballast A(1).

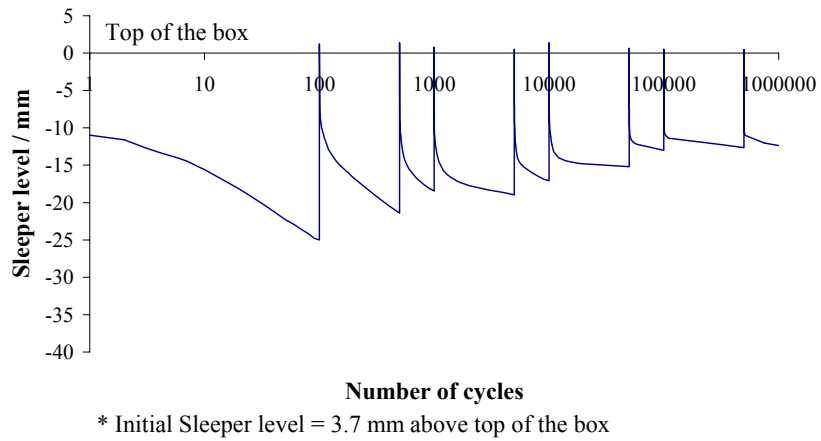


Figure 5.7. Sleeper level against number of cycles for ballast A(2).

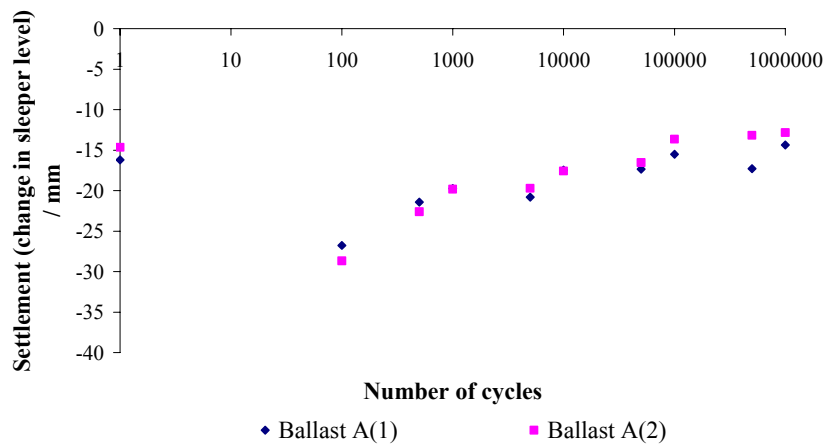


Figure 5.8. Settlement against number of cycles for ballast A.

The plots of stiffness against number of cycles for both tests on ballast A are shown in Figure 5.9. The stiffness, K , at any one cycle is calculated as:

$$K = \frac{\sigma_{\max} - \sigma_{\min}}{\delta_r} \quad (5.1)$$

where σ_{\max} and σ_{\min} are the maximum and minimum applied stresses respectively, and δ_r is the sleeper resilient displacement. The “modified FWD stiffness range” on the plot is the range of stiffnesses measured on railway tracks in the United Kingdom using the Falling Weight Deflectometer (FWD), modified to take account of the higher applied stress level in the box. The FWD stiffness range for railway tracks in the United Kingdom has been found to be 30→100kN/mm/sleeper end (draft Network Rail Code of Practice, 2003). The FWD applies a 125kN load on each sleeper through a beam, which is shaped to distribute the load to both ends of the sleeper (Sharpe et al., 1998). Thus, the sleeper displacement range for railway tracks in the United Kingdom subjected to a 125kN load is:

$$\begin{aligned} \delta &= \frac{125}{2 \times (30 \rightarrow 100)} \\ &= 0.625 \rightarrow 2.083 \text{mm} \end{aligned}$$

The maximum stress underneath a sleeper, according to Shenton (1974) is 250kPa for a 100kN applied load. Thus, by linear extrapolation, the maximum stress underneath the sleeper for a 125kN load would be:

$$\begin{aligned} \sigma_{\max} &= \frac{125 \times 250}{100} \\ &= 312.5 \text{kPa} \end{aligned}$$

and the FWD stiffness range in term of stress is:

$$\begin{aligned} K &= \frac{\sigma_{\max}}{0.625 \rightarrow 2.083} \\ &= 150 \rightarrow 500 \text{kPa/mm} \end{aligned}$$

Stiffness of ballast increases with applied stress (as discussed in section 2.2.4). Thus, ballast stiffness in the box is expected to be higher because the stress level applied in the box is approximately 533kPa. According to the result of a repeated load triaxial test on crushed granite ballast by Alva-Hurtado (1980) (Figure 2.10), the stiffness K can be approximately related to the bulk stress θ by:

$$K \propto \theta^{0.6} \quad (5.2)$$

Therefore, the modified FWD stiffness range, taking into account the applied stress level in the box, is given by this approximate analysis that assumes K_o in the box is independent of the applied stress level:

$$\begin{aligned} K &= (150 \rightarrow 500) \times \left(\frac{533}{312.5} \right)^{0.6} \\ &= 207 \rightarrow 689 \text{ kPa/mm} \end{aligned}$$

It can be seen in Figure 5.9 that the measured stiffnesses for the ballast A are repeatable (although the LVDT was stuck at one point during ballast A(1) test, which resulted in an artificially high stiffness) and within the modified FWD stiffness range. Thus, it can be deduced that the box test replicates field stiffness conditions. It is noted that the ballast stiffness increases with increasing number of tamps. This is consistent with the fact that tamping improves ballast performance as discussed previously.

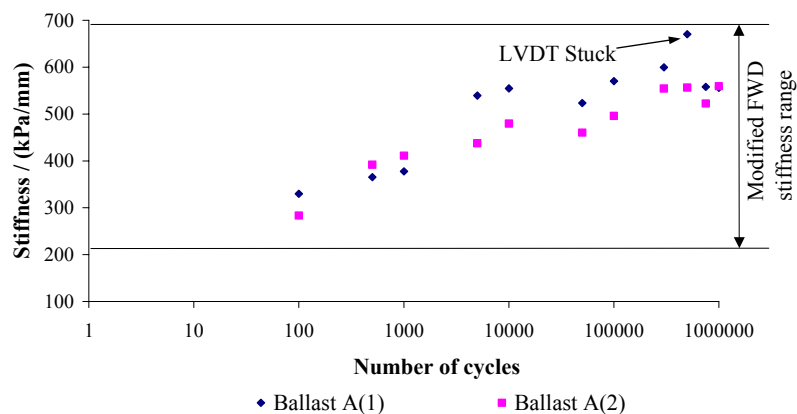


Figure 5.9. Stiffness against number of cycles for ballast A.

The particle size distributions for both the ballast A samples are shown in Figure 5.10. It can be seen that there is only a slight change in the particle size distributions if all the ballast in the box is sieved. Nevertheless, it is noted that particle size distribution is repeatable as the two grading curves are coincident. This repeatability is also confirmed by the total breakage factor (B_t) as shown in Table 5.1.

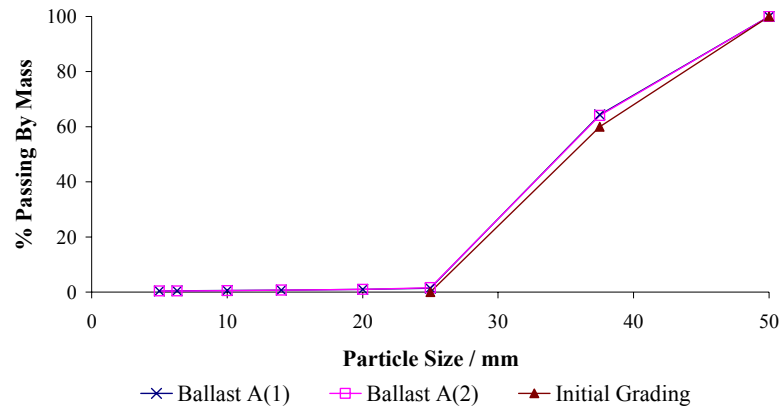


Figure 5.10. Particle size distributions for box tests on ballast A.

| Ballast | B_t |
|---------|-------|
| A(1) | 0.022 |
| A(2) | 0.021 |

Table 5.1. B_t values for box tests on ballast A.

In order to investigate ballast breakage at different locations in the box, the ballast was divided into 7 sections as in Figure 5.5. Due to the small amounts of breakage in the box, only the increase in percentage passing the 37.5mm sieve is used to represent breakage in each section (Figures 5.11 and 5.12). It can be seen that the breakage in different sections is not repeatable and this could be caused by the method used to obtain samples for grading from each section: i.e. ballast in each section was separated by hand. Thus, it is possible that ballast particles (especially small ones) dropped to lower sections during this process and this is evident as some sections have a negative increase in percentage passing 37.5mm. However, it is obvious in these two tables that most of the breakage occurs underneath the sleeper. If repeatability is affected by ballast particles migrating to lower sections during

sample retrieval, sieving ballast in ‘columns’ should be repeatable. The particle size distributions for ballast underneath the sleeper for both ballast A samples are shown in Figure 5.13. This figure shows that the particle size distributions for ballast underneath the sleeper can be reproduced and this is confirmed by the total breakage factor in Table 5.2. It is also clear by comparing Table 5.1 and Table 5.2 that the value of B_i is 50% higher underneath the sleeper compared with the value obtained for the box as a whole.

| | | |
|------|---------|------|
| 0.1 | Sleeper | 0.1 |
| 9.4 | 12.6 | 9.4 |
| -5.9 | 5.6 | -5.9 |
| 7.1 | 7.9 | 7.1 |

Figure 5.11. Increase in percentage passing the 37.5mm sieve at different locations (see Figure 5.5) within the box for ballast A(1).

| | | |
|------|---------|------|
| -4.2 | Sleeper | -4.2 |
| 3.5 | 8.2 | 3.5 |
| 10.8 | 9.4 | 10.8 |
| 2.5 | 7.0 | 2.5 |

Figure 5.12. Increase in percentage passing the 37.5mm sieve at different locations within the box for ballast A(2).

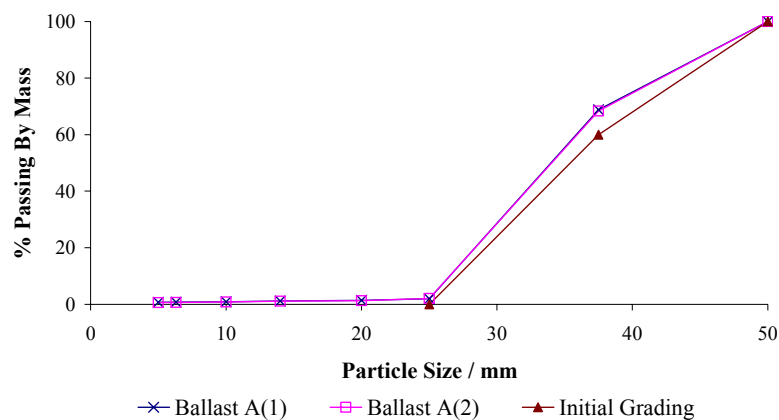


Figure 5.13. Particle size distributions for ballast underneath the sleeper for box tests on ballast A.

| Ballast | B_t under sleeper |
|---------|---------------------|
| A(1) | 0.036 |
| A(2) | 0.033 |

Table 5.2. B_t for ballast underneath the sleeper for box tests on ballast A.

5.3.2 Controlled box tests on ballast A

Three box tests on ballast A were conducted to quantify the source of breakage: a dry box test with tamping and traffic loading to quantify the effect of water, denoted as ballast A(3); two wet box tests with only traffic loading to quantify the effect of traffic, denoted as ballast A(4) and A(5) (two tests because of a mistake in handling the first tested sample; re-test to obtain the grading of the tested sample); and a wet box test with only tamping to quantify the effect of tamping, denoted as ballast A(6).

The plot of settlement against number of cycles for the dry box test (ballast A(3)) is shown in Figure 5.14, together with the standard wet box test result (ballast A(2)). The settlement profile of the dry box test is similar to that of the wet box test where the settlement at the end of each tamping interval reduces with the number of tamps. The stiffnesses for the dry and wet box tests are shown in Figure 5.15. It can be seen that the stiffness of the dry box test is slightly lower than that of the wet box test. This is probably due to a bolt ‘failure’, where a bolt which was attached to the wood base to keep part of the bottom Perspex wall in place, became detached and may have caused an apparent softening effect. The particle size distribution for the dry and wet box tests are shown in Figure 5.16. It can be seen that there is slightly more breakage in the dry box test. Raymond & Bathurst (1987) concluded in their single tie-ballast system tests that the generation of fines at a given load level and cumulative tonnage increases with increasing ballast support compressibility. They explained this as the increase in repetitive aggregate movements with decreasing elastic stiffness. Thus, it may be expected that the lower stiffness of the dry box test which results in a higher strain in the ballast, would lead to more inter-particle abrasion and that it would undergo more degradation.

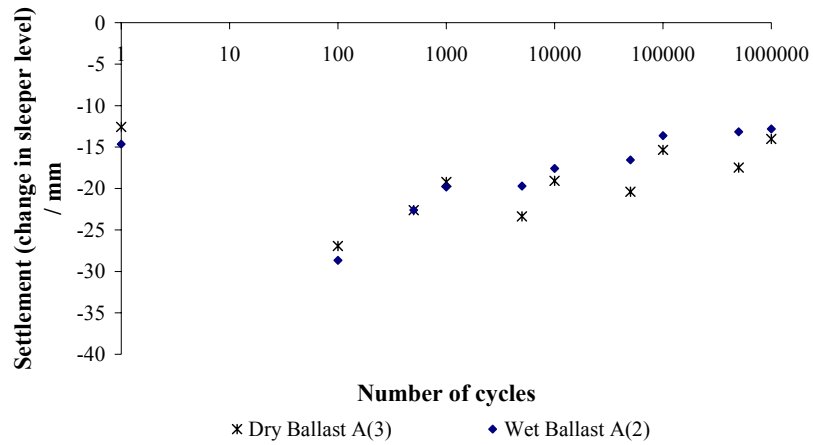


Figure 5.14. Settlement against number of cycles for box tests on dry and wet ballast A.

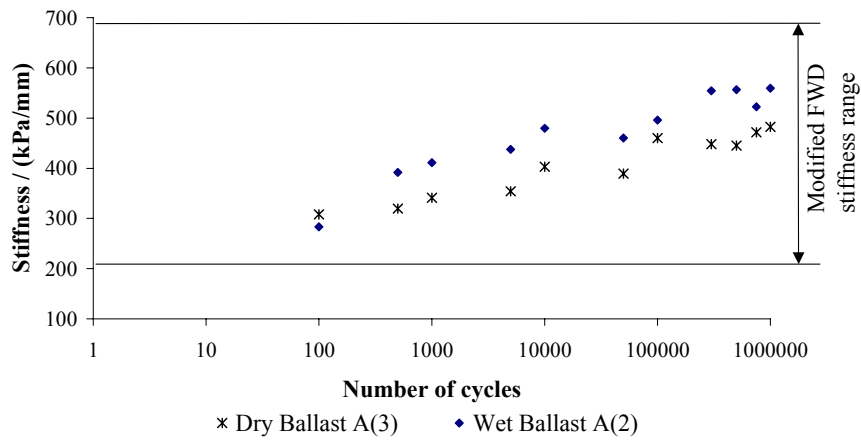


Figure 5.15. Stiffness against number of cycles for box tests on dry and wet ballast A.

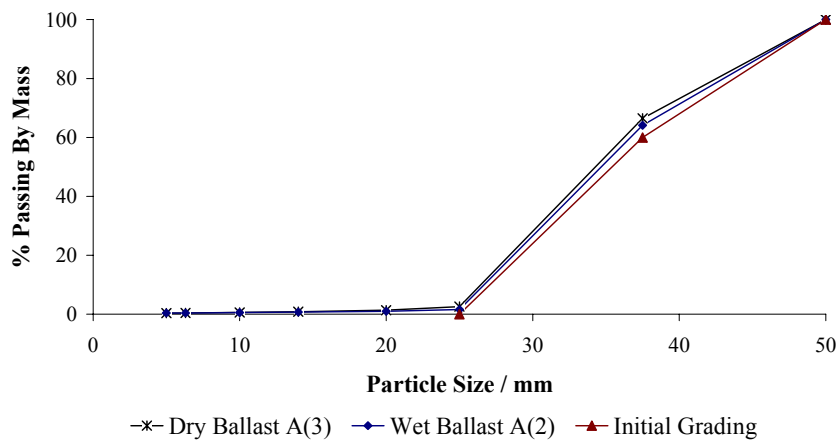


Figure 5.16. Particle size distributions for box tests on dry and wet ballast A.

The plot of settlement against number of cycles for the two wet box tests on ballast A with only traffic loading is shown with the standard wet ballast A(2) test result in Figure 5.17 (presented as the change in sleeper level and cumulative settlement). The settlement in the traffic-only test was higher than the standard test if it is compared with the change in sleeper level because there was no tamping interval at which the settlement was reset to approximately zero. Thus, the settlement of the traffic-only tests continued to increase with number of cycles. However, if the settlement of the traffic-only test is compared with the cumulative settlement of the standard test, it is much lower. This is anticipated, as tamping loosens ballast near the bottom side of the sleeper to fill the gap created by lifting the sleeper, so the standard test had a higher cumulative settlement than the traffic-only test. It is noted that the traffic-only test was not repeatable as the difference in settlement of the two tests at 1 million cycles is approximately 10mm. This could mean that ballast that is not tamped has higher variation in settlement.

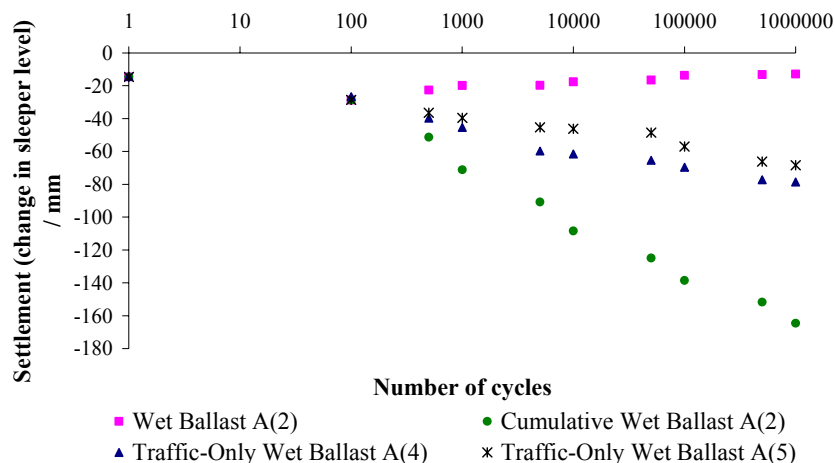


Figure 5.17. Settlement against number of cycles for traffic-only box tests and standard box test on wet ballast A.

The stiffnesses for the traffic-only wet box tests and the standard wet ballast A(2) test (Figure 5.18) show a similar trend and magnitude. Thus, it can be deduced that the final stiffnesses in both types of box test were achieved by either ‘squeezing’ additional ballast towards the bottom of the sleeper or compacting ballast underneath the sleeper with increasing settlement. Since tamping loosens ballast near the bottom of the sleeper (i.e. the upper layer of ballast underneath the sleeper), it can

also be said that the final stiffness of the standard wet ballast A(2) test was achieved by the compaction of the lower layer of the ballast and increasing overall density of the ballast in the box, due to the addition of crib ballast after each tamp.

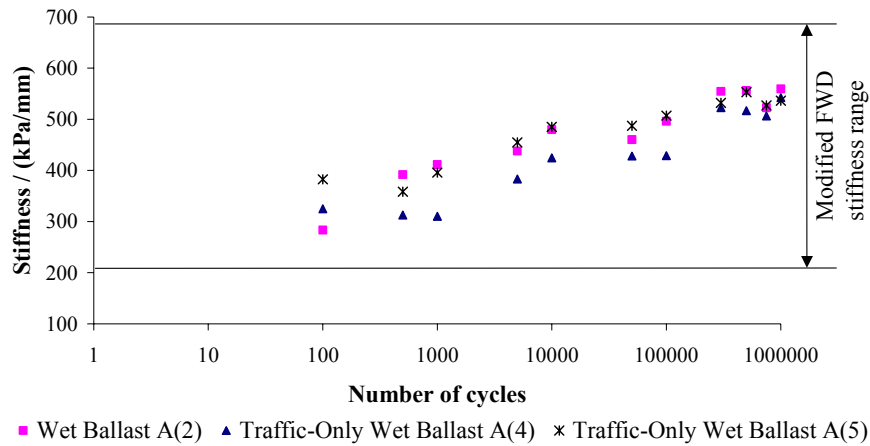


Figure 5.18. Stiffness against number of cycles for traffic-only box tests and standard box test on wet ballast A.

The changes in particle size distributions for the traffic-only and tamping-only box tests on wet ballast A are very small. Thus, only the total breakage factor will be presented. The total breakage factors for the whole box and for ballast underneath the sleeper for the various tests, with and without tamping, are shown in Table 5.3. It is evident that the breakage factors in the traffic-only and tamping-only box tests superpose to give approximately the value obtained in the standard wet box test that included both traffic loading and tamping.

| Ballast | B_t for whole box | B_t under sleeper |
|-------------------------------|---------------------|---------------------|
| Standard Wet ballast A(2) | 0.021 | 0.033 |
| Dry ballast A(3) | 0.025 | 0.041 |
| Traffic-only wet ballast A(5) | 0.013 | 0.028 |
| Tamping-only wet ballast A(6) | 0.010 | 0.007 |

Table 5.3. Total breakage B_t for controlled box tests on ballast A.

5.3.3 Box test on 10-14mm Ballast A

Since there is a size effect on the strength of ballast, it is interesting to know the performance of 10-14mm ballast in a box test compared to specification ballast. (This is also of interest since the ballast size used in stoneblowing is in the range of 14-20mm) Figure 5.19 shows the plot of sleeper level against number of cycles for the 10-14mm ballast A(7) box test. It was found that the gap created by lifting the sleeper was not completely filled with ballast after tamping. This was observed from the front Perspex wall and can also be seen in Figure 5.19, where none of the ‘spikes’ are above the top of the box. This could mean that small ballast particles cannot be tamped efficiently (e.g. difficult to tamp degraded ballast). Nevertheless, Figure 5.19 shows that the sleeper level profile for 10-14mm ballast A(7) is similar to the box test on track ballast sized ballast A(2) (Figure 5.7), where the settlement at the end of each tamping interval reduces with the number of tamps. This is more obvious in Figure 5.20 where the settlement against number of cycles for the 10-14mm and the track ballast sized ballast A(2) are plotted. Since the settlement profile for 10-14mm ballast A(7) is similar to the track ballast sized ballast A(2), it is expected that the stiffness profile would be the same as well. Figure 5.21 shows the plot of stiffness against number of cycles for the 10-14mm ballast A(7) and the track ballast sized ballast A(2). It can be seen from this figure that the stiffness at the end of each tamping interval increases with the number of tamps. The total breakage factors for ballast underneath the sleeper for the 10-14mm ballast A(7) and the track ballast sized ballast A(2) are shown in Table 5.4. It can be seen that the total breakage factor for the 10-14mm ballast A(7) is slightly less than the track ballast sized ballast A(2), which is expected as smaller ballast particles are statistically stronger (Table 3.1).

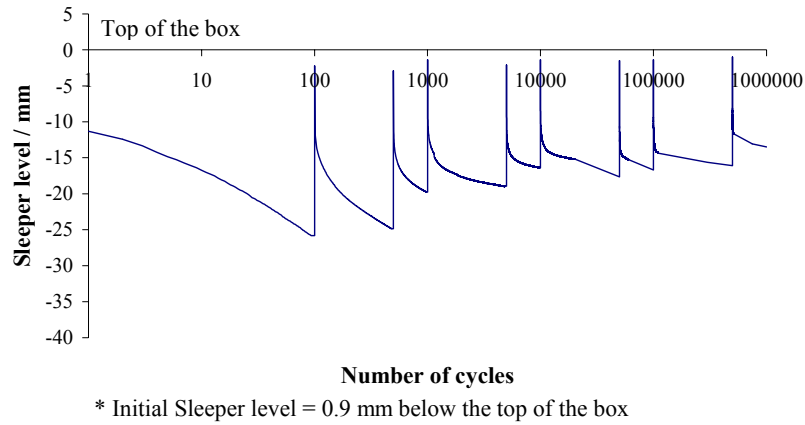


Figure 5.19. Sleeper level against number of cycles for box test on 10-14mm ballast A(7).

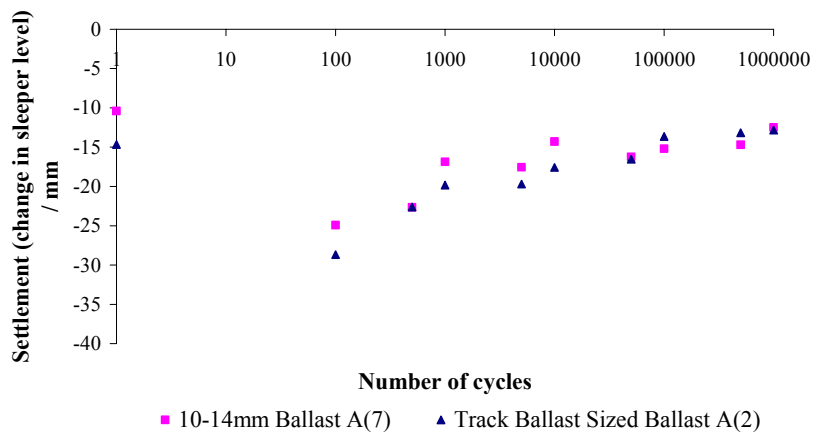


Figure 5.20. Settlement against number of cycles for box tests on 10-14mm and track ballast sized ballast A.

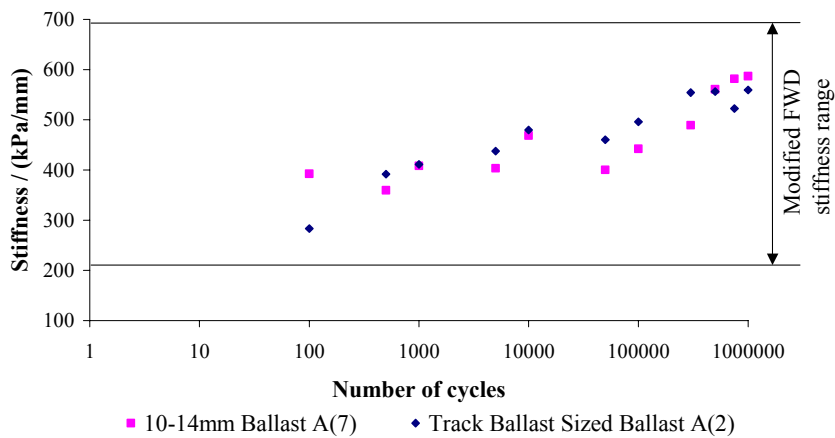


Figure 5.21. Stiffness against number of cycles for box tests on 10-14mm and track ballast sized ballast A.

| Ballast | B_t under sleeper |
|--------------------------|---------------------|
| 10-14mm ballast A(7) | 0.026 |
| Track Ballast Sized A(2) | 0.033 |

Table 5.4. B_t for ballast underneath the sleeper for box tests on 10-14mm and track ballast sized ballast A.

5.3.4 Box tests on ballasts B, C and D

Box tests were also conducted on ballasts B, C and D to compare with ballast A. The plots of sleeper level against number of cycles for ballasts B, C and D are shown in Figures 5.22, 5.23 and 5.24 respectively. The sleeper level profiles for ballasts B and C are similar to those of ballast A, and tamping seems to improve the performance of the ballast. Ballast D, however, appears to have a completely different sleeper level profile. It can be seen that the sleeper level at the end of each tamping interval did not change much. Thus, tamping only seemed to improve the performance of ballast D in the sense that the last tamping interval took 500,000 cycles to reach a sleeper level approximately equal to the sleeper level at the end of the first tamping interval after 100 cycles. Figure 5.24 also shows that the final sleeper level (before each tamp) for ballast D becomes lower after 100,000 cycles, whereas the level generally increases for the other ballasts. This would seem to indicate a deterioration in the performance of ballast D after about 100,000 cycles.

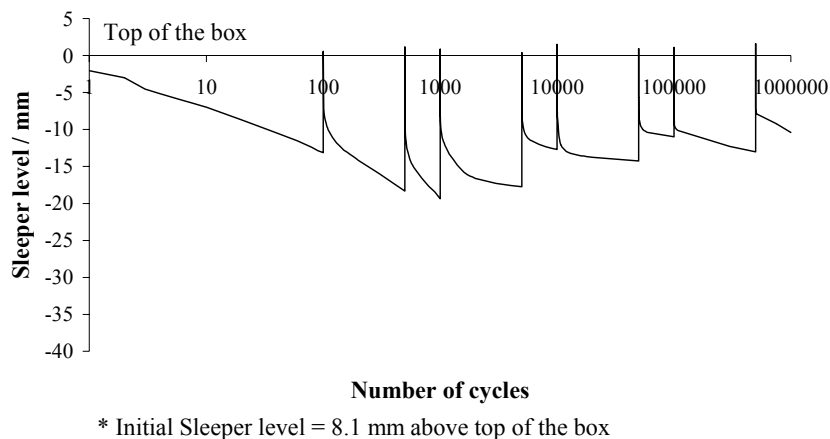


Figure 5.22. Sleeper level against number of cycles for box test on ballast B.

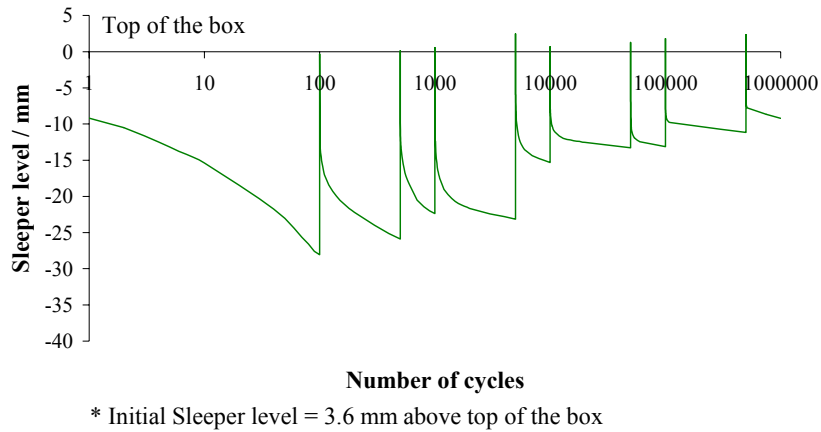


Figure 5.23. Sleeper level against number of cycles for box test on ballast C.

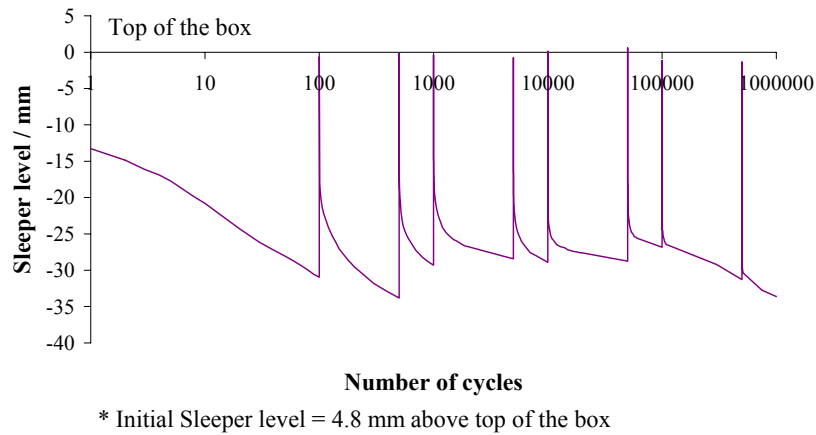


Figure 5.24. Sleeper level against number of cycles for box test on ballast D.

The plots of settlement against number of cycles for ballasts A(2), B, C and D are shown in Figure 5.25. The figure shows that the settlement profiles for ballasts A(2), B and C are similar in the sense that settlement reduces with number of cycles. It is also clear in this plot that the settlement profile for ballast D is significantly different from the other ballasts. The plots of stiffness against number of cycles for ballasts A(2), B, C and D are shown in Figure 5.26. As expected, the stiffnesses of ballasts A(2), B and C increase with number of tamps. However, the stiffness of ballast D remained approximately constant throughout the test.

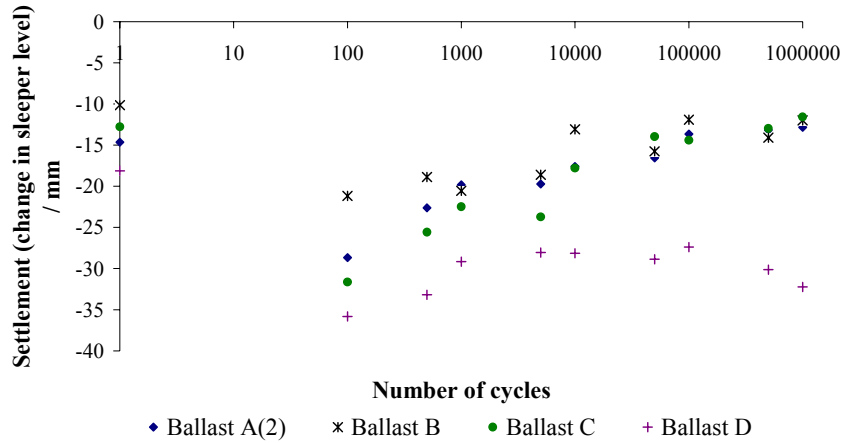


Figure 5.25. Settlement against number of cycles for box tests on different ballasts.

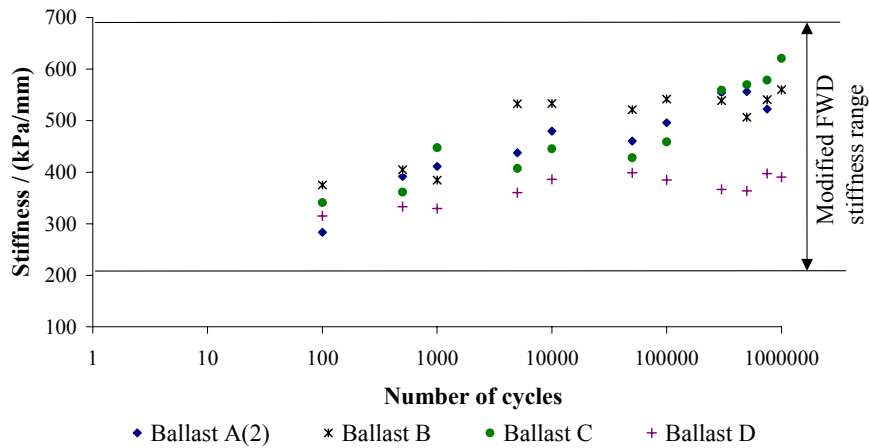


Figure 5.26. Stiffness against number of cycles for box tests on different ballasts.

Since most ballast breakage occurs underneath the sleeper, only the particle size distributions for ballast underneath the sleeper are presented for the four ballasts. The particle size distributions for ballast underneath the sleeper for ballasts A(2), B, C and D are shown in Figure 5.27. It is obvious in this plot that ballast D degrades much more than any other ballast tested. This is also shown in terms of the total breakage factor in Table 5.5, where the total breakage of ballast D is at least 6 times more than that of any other ballast. This result is consistent with the petrographic analysis (Large, 2003), where ballast D was shown to have the worst performance, as some of the feldspars in the samples were markedly soft, indicating that some of the samples may have been altered at low temperature to clay minerals. It can also be

seen that ballasts B and C have similar amounts of ballast fracture, and the amount of breakage is slightly less than ballast A(2).

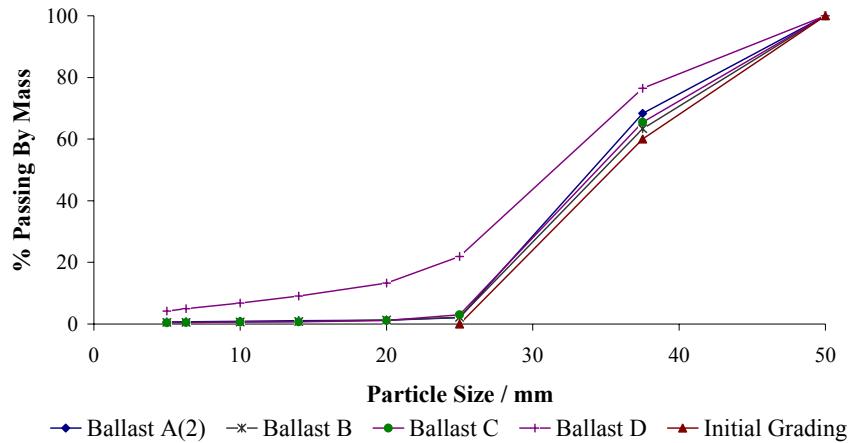


Figure 5.27. Particle size distributions for ballast underneath the sleeper for box tests on different ballasts.

| Ballast | B_t under sleeper |
|---------|---------------------|
| A(2) | 0.033 |
| B | 0.023 |
| C | 0.025 |
| D | 0.187 |

Table 5.5. B_t for ballast underneath the sleeper for box tests on different ballasts.

5.3.5 Summary and correlation of results with ballast index tests, single particle crushing tests, and large oedometer tests

Table 5.6 summarizes all the standard box test results of the 4 ballasts tested, the control tests on ballast A, and the 10-14mm ballast A(7). This table presents the stiffness, settlement since the last tamp (i.e. at 500,000 cycles), total breakage factor B_t for ballast underneath the sleeper, the initial voids ratio e_i , the final voids ratio e_f for ballast underneath the sleeper, and the final voids ratio e_f for the whole box. It is clear in this table that ballast C has the best performance and ballast D has the worst. It is also obvious in this table that the final voids ratios for ballast underneath the

sleeper (denoted as “ e_f under sleeper”) are lower than the final voids ratios for the whole box. This is anticipated as ballast underneath the sleeper was subjected to traffic loading and/or “squeezed” during tamping, thus was compacted to a higher density. The final voids ratio for the whole box for the dry test (ballast A(3)) is expected to be higher because the box bulged (due to a bolt becoming detached from the box), which means that since the final total nominal box volume was used to calculate e_f , this is an underestimate of the true volume, giving an underestimate of e_f .

| Ballast | Stiffness* / kPa/mm | Settlement since last tamp* / mm | B_t under sleeper | Voids Ratio: e | | |
|---------|------------------------|--|------------------------|--------------------|------------------------|--------------------|
| | | | | e_i whole box | e_f under sleeper | e_f whole box |
| A(2) | 559.4 | 12.8 | 0.033 | 0.91 | 0.61 | 0.76 |
| A(3) | 482.3 | 14.0 | 0.041 | 0.93 | 0.61 | 0.69 |
| A(5) | 536.4 | NA | 0.028 | 0.91 | 0.63 | 0.79 |
| A(6) | NA | NA | 0.007 | 0.92 | 0.65 | 0.76 |
| A(7) | 586.9 | 12.5 | 0.026 | 0.88 | 0.60 | 0.73 |
| B | 560.2 | 12.0 | 0.023 | 0.82 | 0.56 | 0.62 |
| C | 620.9 | 11.6 | 0.025 | 0.97 | 0.63 | 0.72 |
| D | 390.2 | 32.2 | 0.187 | 0.98 | 0.55 | 0.69 |

Table 5.6. Summary of all box test results.

* Note: After 1 million cycles and 8 tamps.

Figures 5.28-5.31 show the correlation of the total breakage factors (B_t) for ballast underneath the sleeper in the box tests with the original (2000) and new (2005) ballast index test results: namely WAV, ACV, LAA and MDA (the ACV test result was the ACV for the 10-14mm ballast in the large oedometer test). It can be seen that the values of B_t underneath the sleeper in the box test correlate well with WAV, MDA and LAA, but do not correlate well with ACV. Figures 5.32 and 5.33 show the correlation of the total breakage factors B_t for ballast underneath the sleeper in the box tests with the oedometer tests on specification ballast. It can be seen that the values of B_t underneath the sleeper in the box tests do not correlate well with the

oedometer tests on specification ballast. Figure 5.34 shows the correlation of the total breakage factors B_t for ballast underneath the sleeper in the box tests with the weighted tensile strength σ_{ow} of specification ballast. It can be seen that the correlation between the values of B_t underneath the sleeper in the box tests and the weighted tensile strength σ_{ow} of specification ballast is poor. The relative strength index R_s , as defined in section 4.4 equation 4.5, is again used here to consider the effect of voids ratio in addition to the tensile strength σ_{ow} . The relative voids ratio, as defined by equation 4.6, for each box test was calculated using the initial voids ratio e_i in each box test, and the maximum and minimum initial voids ratios, $e_{i,max}$ and $e_{i,min}$ respectively, for all the box tests. It should be noted that the relative density of all the box tests is again assumed to be equal i.e. the relative density of ballast in the box tests is assumed to be zero because ballast sample was poured into the box and can be envisaged as in the loosest state. Figure 5.35 shows the correlation of the total breakage factors (B_t) for ballast underneath the sleeper in the box tests with the relative strength index R_s . It can be seen that the values of B_t underneath the sleeper in the box tests correlate well with the relative strength R_s , which again emphasizes the importance of the voids ratio of the aggregate in addition to the tensile strength of ballast particles.

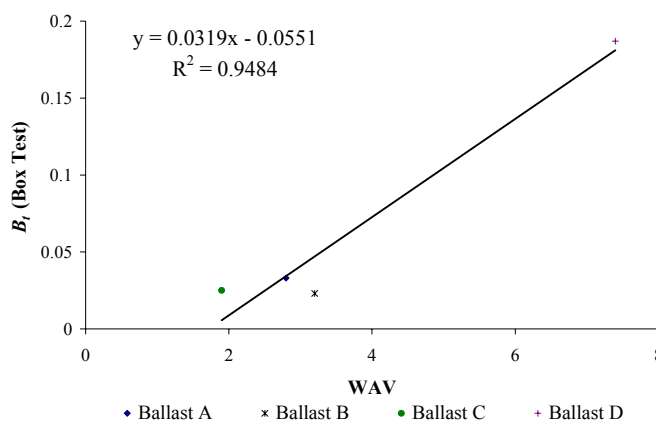


Figure 5.28. B_t (Box Test) for ballast underneath the sleeper against WAV.

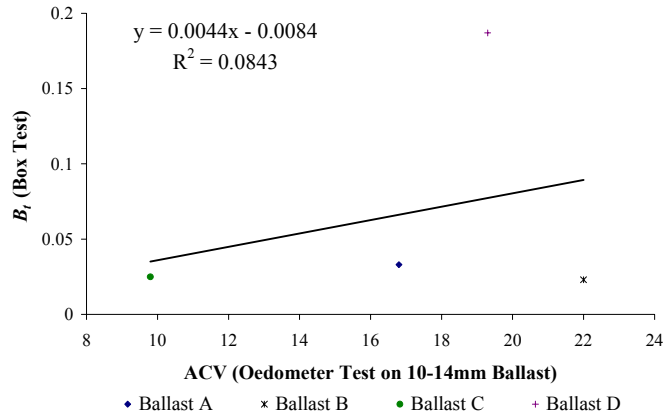


Figure 5.29. B_r (Box Test) for ballast underneath the sleeper against ACV for oedometer test (10-14mm).

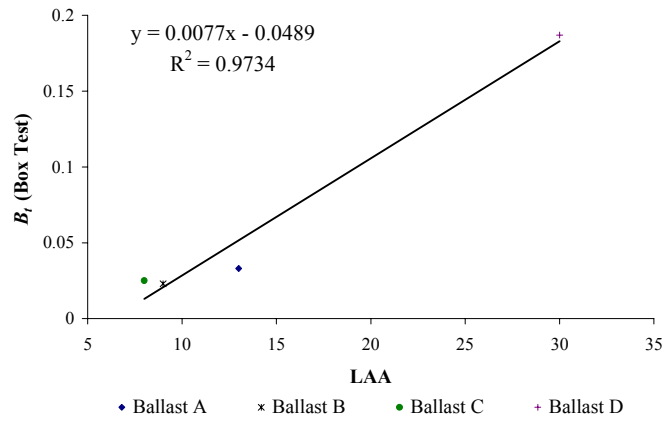


Figure 5.30. B_r (Box Test) for ballast underneath the sleeper against LAA.

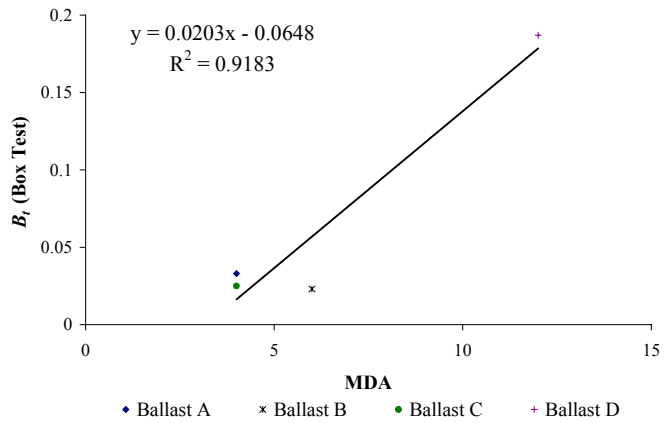


Figure 5.31. B_r (Box Test) for ballast underneath the sleeper against MDA.

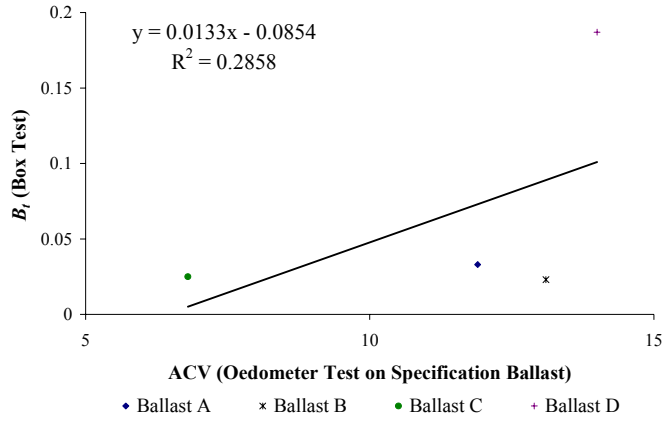


Figure 5.32. B_t (Box Test) for ballast underneath the sleeper against ACV for oedometer test (specification).

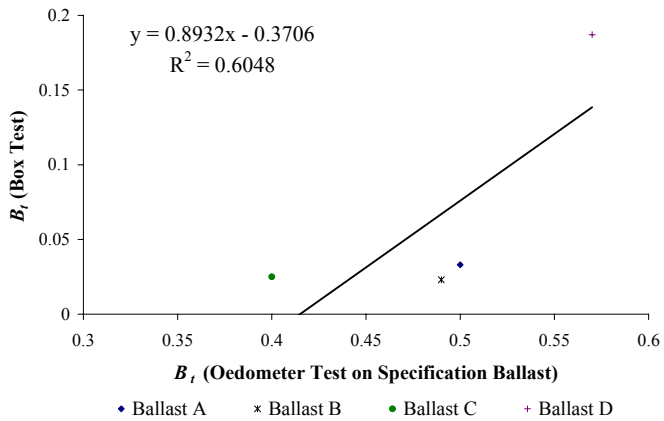


Figure 5.33. B_t (Box Test) for ballast underneath the sleeper against B_t for oedometer test (specification).

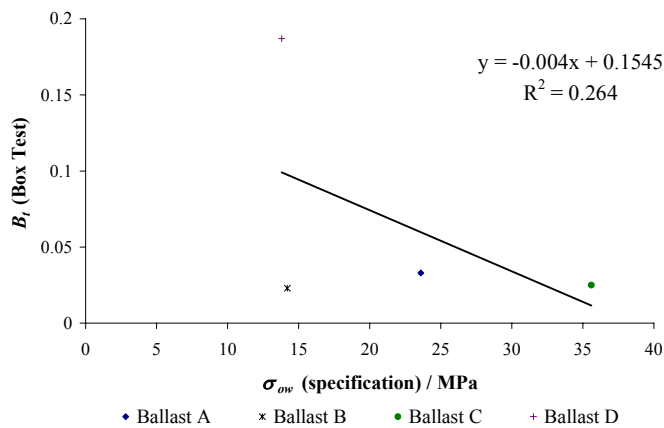


Figure 5.34. B_t (Box Test) for ballast underneath the sleeper against σ_{ow} (specification).

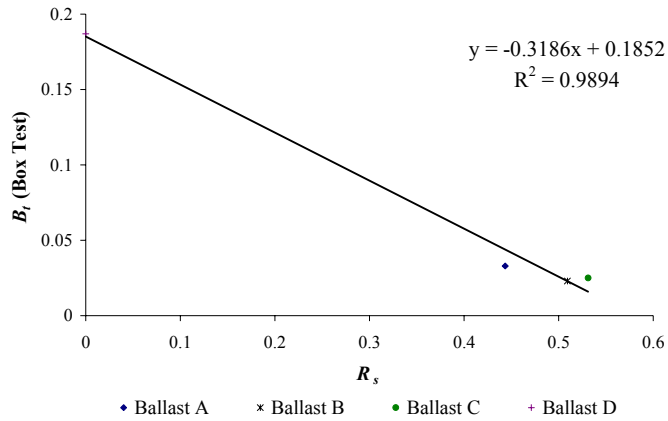


Figure 5.35. B_t (Box Test) for ballast underneath the sleeper against relative strength index R_s .

5.4 Discussion

The settlement and stiffness plots of the 2 ballast A samples were shown to be repeatable (see Figures 5.8 and 5.9). However, it is noted that the sleeper level plot of the 2 box tests on ballast A can be significantly different, as shown in Figure 5.36, which is a plot of sleeper level against number of cycles for the 2 ballast A samples. This difference must be due to the different initial sleeper levels and the different sleeper levels after tamping of the 2 ballast A samples because the settlement plot is repeatable- see Figure 5.8. This indicates that the effect of tamping was consistent between tests. This difference in sleeper level emphasizes the importance of minimising the differences in initial sleeper levels and sleeper levels after tamping in order to minimise differential settlement, which is important to maintain good track geometry.

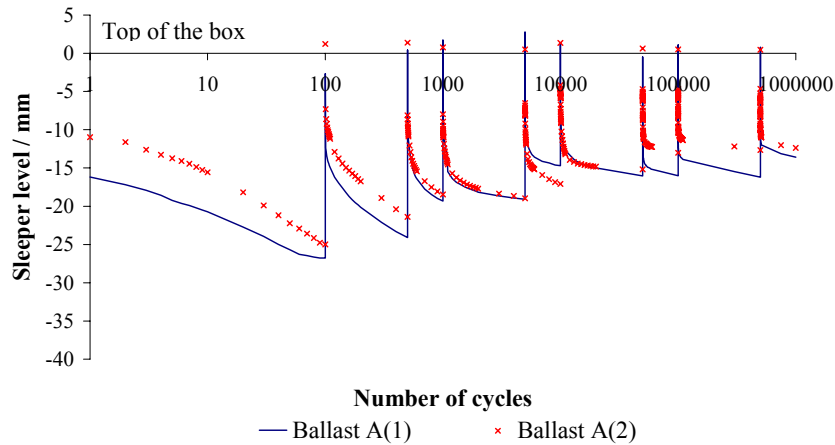


Figure 5.36. Sleeper level against number of cycles for the 2 ballast A samples.

It is noted that the simulated tamping improves the performance of ballast. This effect is likely to represent the early life of ballast in the field. At the later stages of ballast life, tamping is likely to reduce the performance of ballast as the amount of particle breakage increases: Figure 5.37 shows how the tamping cycle length usually decreases with increasing numbers of wheel passes (Selig & Waters, 1994), and that the rate of settlement at the end of each tamp is increasing. This behaviour is likely to be associated with significant ballast breakage, as the ballast is subjected to more traffic loading and tamping cycles, and fines in the ballast lead to water retention in the trackbed, reducing the permeability of the ballast. Under this condition, repeated loading from trains would cause an increase in the pore water pressure in the ballast and lead to rapid deterioration of the ballast. A deterioration in ballast behaviour was observed at the end of the box test on ballast D, for which breakage has been shown to be significant.

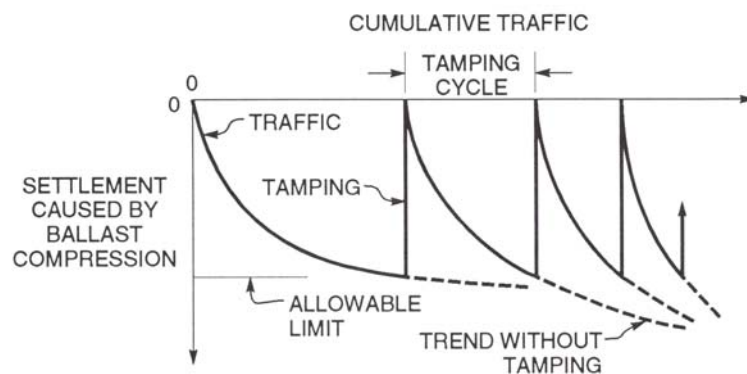


Figure 5.37. Tamping effect on ballast settlement (Selig & Waters, 1994).

It was also found that the effect of rearrangement of ballast caused by tamping does not seem to affect the total particle breakage in the box i.e. the total breakage factors for ballast, in the whole box and underneath the sleeper, in the traffic-only box test and the tamping-only box test were approximately superimposable to give the total breakage factor of ballast in the standard wet box test with both traffic loading and tamping. This result was surprising as it was anticipated that particle rearrangement would lead to more breakage under traffic loading as discussed in section 2.2.6 (i.e. the standard wet box test should have a higher total breakage factor than the sum of the total breakage factors in the traffic-only and tamping-only box tests). A possible explanation for this result is that after ballast is tamped, additional ballast is added at the cribs, which increases the overall density in the box compared to that at the end of the previous tamp. Thus, the additional breakage caused by particle rearrangement may have been counteracted by a denser ballast packing, which reduced ballast breakage.

The total ballast breakage for ballast underneath the sleeper for ballast B is similar to that for ballast C and is slightly lower than that for ballast A- see Table 5.5. This result is not consistent with the large oedometer tests on specification ballast where it was clear that ballast A was comparable with ballast B, and ballast C was the best performing ballast - see Table 4.8 and 4.9. The reason for this could be that the simulated tamping caused less rearrangement in the ballast B. Figure 5.38 shows sleeper settlement at 66 weeks after tamping as a function of tamping lift (Selig & Waters, 1994). It can be seen that for relatively low lifts, the settlement at 66 weeks after tamping is equal to the tamping lift, which means that there was no lasting improvement of ballast settlement by tamping. However, for relatively high lifts (greater than 20mm), there was a lasting improvement on ballast settlement caused by tamping. The explanation given by Selig & Waters (1994) for this observation is that for low tamping lifts, the ballast underneath the sleeper was only able to dilate to fill the gap underneath the sleeper during tamping because there was not enough room for extensive rearrangement of ballast particles. However, for high tamping lifts, the gap underneath the sleeper is large enough for ballast particles to extensively rearrange during tamping. Thus new ballast can flow underneath the sleeper, as opposed to only dilation of the existing ballast beneath the sleeper occurring.

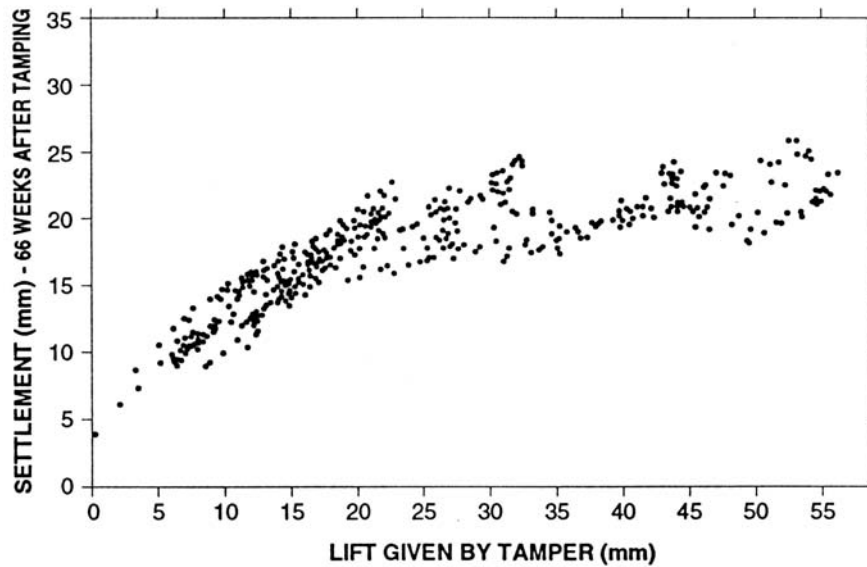


Figure 5.38. Sleeper settlement as a function of tamping lift (Selig & Waters, 1994).

From this perspective, the plots of sleeper level against number of cycles for ballasts A, B and C (Figure 5.7, Figure 5.22, and Figure 5.23) were re-examined. It can be seen that the sleeper levels after the first 100 cycles for ballasts A and C are more than 20mm below the top of the box, which means that the gap underneath the sleeper before tamping is more than 20mm. Therefore, the ballast can rearrange during tamping and there is an improvement of ballast settlement by tamping as shown by higher sleeper level (reduced settlement) at the end of the next tamping interval. The sleeper level in the first 100 cycles for ballast B, however, is less than 20mm. Thus, ballast cannot rearrange much during tamping and there is no improvement of ballast settlement by tamping as shown by the lower sleeper level (increased settlement) at the end of the next tamping interval. Therefore, it might be concluded that ballast B exhibits a lower amount of degradation than anticipated because the ballast underneath the sleeper did not rearrange as much as ballasts A and C. Thus ballast particles of ballast B have fewer new contacts, and the aggregate geometry is approximately constant.

The box test results seem to correlate very well with WAV, LAA, and MDA values. This is thought to be due to the rearrangement of particles in the box test caused by the simulated tamping, where new contacts created were subjected to wear during traffic loading. It was noted that the box test results do not correlate well with the

ACVs found in the large oedometer tests on 10-14mm ballast. This was anticipated because of the size effect on particle strength. However, the box test results also do not correlate well with the results from the oedometer tests on specification ballast. This could be due to the fact that ballast particles in the oedometer tests were not subjected to the extensive rearrangement caused by the simulated tamping. The poor correlation could also be because the oedometer tests were conducted in the dry condition, whereas the box tests were performed in the wet conditions, and it has been shown by conducting an oedometer test on wet ballast D, that the effect of water absorption can be significant (section 4.3.6).

5.5 Conclusions

A box was designed and manufactured to simulate ballast loading condition in the trackbed in a simplified and controlled manner. Wet ballast was used in the box test to reflect track ballast conditions in the United Kingdom and also because ballast in wet condition is more critical. Ballast in the box was cyclically loaded with a sinusoidal load pulse with minimum load of 3kN and maximum load of 40kN, at a frequency of 3Hz. This is thought to represent the traffic loading of ballast in the trackbed. The ballast tamping process was simulated by inserting a one inch wide chisel using a Kango hammer into the ballast through a guide hole, so that the simulated tamping process is repeatable. Tested ballast samples were taken out of the box in a systematic way in order to quantify degradation at various sections in the box (e.g. ballast underneath the sleeper).

Two box tests on ballast A showed that the box test is repeatable in the sense that settlements, stiffnesses and particle size distributions can be reproduced. It was shown that the settlement profiles of the two ballast A box tests have similar trends and magnitudes, even though the sleeper level profiles can be significantly different. It was also shown that the stiffnesses of the two ballast A box tests are similar and within the expected stiffness range for trackbeds in the United Kingdom. The simulated tamping process was found to be appropriate because it was able to improve ballast performance in the sense that there was a decrease in settlement and

an increase in stiffness after each tamp, which is likely to represent the early life of ballast in the field. The separation of ballast in the box by hand was not found to be useful when comparing the breakage in different ballast layers, because the particle size distributions of different ballast layers were not repeatable as fines fell to the bottom of the box. However, it was found to be useful to compare the breakage in different 'columns' of ballast, and this was repeatable. It was shown that the particle size distributions for ballast underneath the sleeper were repeatable and that most ballast breakage occurs underneath the sleeper.

It was noted that a problem occurred during the dry box test, where a bolt became detached from the wood base. This bolt failure could lead to an apparent softening effect of the ballast in the box. Thus, the dry box test cannot be compared accurately with the wet box test. Nevertheless, the difference between these two tests was expected to be minimal because the water absorption of ballast A is small. It was shown that the settlement of the traffic-only box test was not repeatable and this could mean that ballast that is not tamped exhibits a higher variability in settlement. It was also shown that ballast stiffness of the traffic-only box test is not affected by tamping. Thus, it can be concluded that an increase in ballast stiffness is achieved either by 'squeezing' additional ballast towards the bottom of the sleeper by tamping or compacting ballast underneath the sleeper as settlement increases. It is also thought that the increase in ballast stiffness in the standard box test (i.e. with tamping and traffic loading) is achieved by compaction of the lower layer of the ballast in the box, which is not disturbed by tamping, and a progressive increase in ballast density within the box. It was found that ballast breakage in the traffic-only box test and the tamping-only box test were approximately superimposable to give ballast breakage in the standard wet box test. This was not anticipated because the standard wet box test was subjected to the effect of rearrangement; this should give a higher degree of breakage than the sum of the amounts of breakage in the traffic-only and tamping-only box tests. It is thought that tamping tends to increase the degree of particle breakage in the box, by both the physical damage caused by the tamping and the subsequent breakage caused by the formation of new contacts, but this is counteracted by the addition of crib ballast, which increases density and the number of particle contacts.

The settlement and stiffness profiles for the 10-14mm ballast A are similar to those for ballast A track ballast sized particles, even though there was a difference observed during tamping, where the gap created by lifting the sleeper was not completely filled with ballast after tamping for the 10-14mm ballast A. This effect would appear to mean that small ballast particles cannot be tamped efficiently. It was found that the total breakage factor for ballast underneath the sleeper for the 10-14mm ballast A is slightly less than that for the track ballast sized ballast A. This is anticipated as the particles of 10-14mm ballast A are statistically stronger than the larger particles of ballast A used in the track.

The settlement and stiffness profiles for ballasts A, B and C are similar, where the stiffness increases and the change in sleeper level reduces with increasing number of tamps. Ballast D, however, has a different profile such that tamping has little or no effect on the sleeper level before each tamp. It was also found that ballast D has the highest degree of ballast breakage, where the total breakage for ballast underneath the sleeper for ballast D is at least 6 times higher than for any other ballast. This is consistent with the ballast index tests (WAV, LAA, and MDA) where ballast D was found to be the weakest of all. The petrographic analysis (Large, 2003) also revealed ballast D to be of the poorest quality, where some of the feldspars in the samples were markedly soft and were altered to clay minerals. The total ballast breakage for ballast underneath the sleeper for ballast B is similar to that for ballast C and is slightly lower than that for ballast A, which contradicts the large oedometer test results, where ballast A was comparable with ballast B, and ballast C was the best performing ballast. It is thought that ballast B did not rearrange as much as ballasts A and C during tamping (i.e. the gap underneath the sleeper was too small for particles to rearrange significantly), thus exhibiting a lower amount of degradation because of the fewer new contacts created after tamping.

The box test results seem to correlate very well with WAV, LAA, and MDA, which is thought to be due to the rearrangement of particles in the box test caused by the simulated tamping. It was noted that the box test results do not correlate well with the ACV. This was anticipated, as the ACV test uses 10-14mm ballast particles instead of track ballast sized particles. However, the box test results also do not correlate well with the total breakage values, or ACVs for the oedometer tests on

specification ballast. This could be due to the fact that ballast particles in the oedometer tests were not subjected to the significant rearrangement caused by simulated tamping and the oedometer tests were conducted in the dry condition, whereas the box tests were performed under wet conditions. The box test results do not correlate well with the weighted tensile strength σ_{ow} of specification ballast particles. This could be due to the fact that the initial voids ratio of the ballast in the box was not considered. It was shown that the box test results correlate well with the relative strength index R_s , which considers the effect of the voids ratio of the ballast in addition to the tensile strength of ballast particles.

Chapter 6

Numerical Modelling

6.1 Introduction

Previous research has had some success in simulating the behaviour of sand in single particle crushing tests, one-dimensional compression tests (Robertson, 2000; McDowell & Harireche, 2002), and triaxial tests (Robertson, 2000; Cheng et al., 2003) using PFC^{3D}. This chapter presents an investigation of the application of PFC^{3D} to simulate ballast behaviour, especially the behaviour of ballast in the box test.

One of the main advantages of using PFC^{3D} to simulate the box test is that it allows the study of the heterogeneous stresses of ballast in the box, which can be used to compare local ballast stresses with the tensile strengths of ballast particles. However, it is noted that in order to investigate the heterogeneous stresses of ballast in the box appropriately, it is vital to simulate the correct ballast behaviour, during loading and unloading. This has led to the main aim of this chapter which is to investigate different methods of simulating ballast behaviour.

It is noted that the use of elastic spherical balls in PFC^{3D} to simulate ballast behaviour is inadequate, especially if the gradual build up of residual horizontal stress is to be simulated. The existence of residual horizontal stress for soil, which has been one-dimensionally normally compressed and unloaded, is well documented in geotechnical literature for both clay and granular materials (e.g. Wood, 1990).

Past research (Norman & Selig, 1983) on ballast box tests has shown a build up of residual horizontal stress with the number of cyclic load applications, as shown in Figure 6.1. This behaviour has been presumed to be caused by interlocking of ballast particles. The use of elastic spherical balls in PFC^{3D} should not reproduce horizontal residual stress because there is no interlocking of particles. Therefore, elastic spherical balls have to be bonded together to form an irregular shape to produce interlocking of asperities.

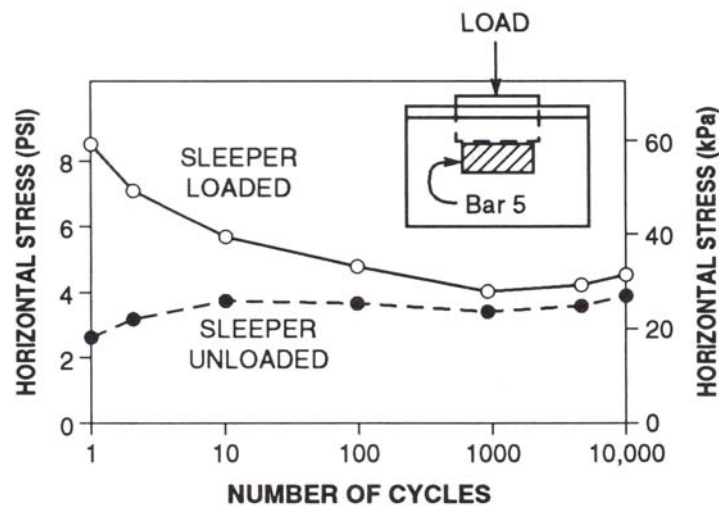


Figure 6.1. Effect of repeated load on horizontal stress (Norman & Selig, 1983).

The main drawback of using PFC^{3D} to simulate ballast behaviour is the high computational time required. Though the use of bonded elastic spherical balls to produce irregular shaped particles is more realistic, the use of elastic spherical balls is more practical because of lower computational time (computational time increases with an increase in the number of balls in an assembly). Since the computational time is the main constraint, it is sensible to simulate a smaller and simplified test to investigate different methods of simulating ballast behaviour. Consequently, a preliminary study was performed to simulate an oedometer test on an aggregate of elastic spherical balls and an aggregate of bonded elastic spherical balls or agglomerates.

Following McDowell & Harireche (2002a), single particle crushing tests were simulated to obtain agglomerates with average strength and distribution of strengths similar to particles of a typical ballast. These agglomerates were then used in a

simulated oedometer test, and the test was compared with a laboratory oedometer test on a typical ballast. Even though it is more realistic to simulate an aggregate of agglomerates in the box test, it is not practical to do so because of the high computational time required. Hence, a box test was simulated using elastic spherical balls and angular uncrushable agglomerates or clumps (a clump is a cluster of overlapping balls, and may be defined as a single entity). This means there are no significant changes in computational time as there is no increase in the number of entities in the assembly. The box simulated was of the size used in the laboratory and the aggregate was subjected to cyclic load. The resilient and permanent deformation were investigated and compared with those for a real box test.

6.2 Preliminary oedometer test simulations

This preliminary test attempts to simulate the Aggregate Crushing Value (ACV) test, which is described in section 2.2.3. The principle of the ACV test is the same as the oedometer test, where a sample of aggregate is compressed one-dimensionally in a steel mould. Three types of aggregate were investigated: 13-ball agglomerates, spherical balls with linear elastic contacts, and spherical balls with Hertzian contacts. Simulations of oedometer tests using more realistic agglomerates derived from simulations of single particle crushing tests, are presented later.

6.2.1 Test description

The oedometer was a cube of side 133mm. PFC^{3D} provides a general command to generate a random assembly of balls within a specified space. Balls generated by this command are not permitted to overlap. If a selected ball location would result in an overlap, PFC^{3D} will make 20,000 (default) attempts to position a ball in a new co-ordinate that would not result in an overlap. If a co-ordinate that would not result in an overlap cannot be found after 20,000 attempts, the ball will not be generated. Thus, in order to generate a dense assembly, it is necessary to generate smaller balls within a specified region to increase the probability of locating a co-ordinate that

would not result in an overlap, and then expand the balls to a final size. Therefore, smaller balls were generated within the oedometer and then expanded to a final diameter of 22mm. The expanded balls were cycled to equilibrium to avoid high contact forces with the coefficient of friction set to zero to make rearrangement easier.

For the oedometer test with agglomerates, the expanded balls were replaced by agglomerates of approximately the same size. This was done, following Robertson (2000), by first creating a linked list storing the co-ordinates of the centres of the expanded balls. The balls were then deleted and randomly rotated agglomerates were then created, with the centres of each agglomerate at the co-ordinates in the list. The assembly of agglomerates was again cycled to equilibrium to avoid high contact forces with the bond strength set to a high value ($F_c^n = F_c^s = 1 \times 10^{16}$ N, where F_c^n and F_c^s are normal and shear bond strengths, respectively) to avoid breakage. Since the preliminary oedometer test with agglomerates was to examine the effect of having bonded balls in an assembly, a hexagonal closed packed agglomerate of 13 balls with a bounding diameter of approximately 22mm was used to represent each ballast particle, as shown in Figure 6.2. The number of agglomerates in the oedometer was obtained through trial and error to maintain low contact forces after cycling to equilibrium prior to loading.

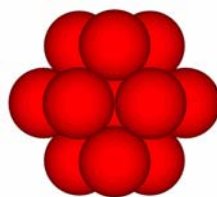


Figure 6.2. A hexagonal closed packed agglomerate with 13 balls.

The ball stiffnesses were calculated by the equation given by Itasca Consulting Group, Inc. (1999), which relates the Young's modulus of the material E_c to the radius of the balls R and the stiffness:

$$k_n = k_s = 4RE_c \quad (6.1)$$

The Young's modulus of granite ($E_c=70\text{GPa}$) was used. The bond strengths were calculated using equations given by Itasca Consulting Group, Inc. (1999) as:

$$\begin{aligned} F_c^n &= 4R^2\sigma_c \\ F_c^s &= 4R^2\tau_c \end{aligned} \tag{6.2}$$

where σ_c and τ_c are material tensile and shear strengths. The shear and tensile strengths were both arbitrarily chosen to be 16MPa. The shear strength was set to be equal to the tensile strength because the bonding material should fracture under the same stress in pure tension and pure shear, if it contains a wide distribution of flaws (McDowell & Harireche, 2002a). Using equations 6.1 and 6.2, the ball normal and shear stiffnesses for the 13-ball agglomerates were both set to $1.04\times 10^9 \text{ Nm}^{-1}$, and the normal and shear bond strengths were both $8.76\times 10^2 \text{ N}$. For the spherical balls with the linear elastic contact model, the normal and shear stiffnesses of the balls were both set to $3.11\times 10^9 \text{ Nm}^{-1}$. For the spherical balls with the Hertzian contact model, the Poisson ratio ν was arbitrarily chosen to be 0.2 and the corresponding shear modulus G is $3\times 10^{10} \text{ Pa}$, which was calculated using the equation:

$$G = \frac{E_c}{2(1+\nu)} \tag{6.3}$$

The density of the balls was set to 2600kgm^{-3} , which is a typical value for granite. The coefficients of friction for the balls and the walls were arbitrarily set to 0.5 and 0, respectively. The stiffnesses of the walls were arbitrarily chosen to be the same as the balls.

The initial assembly was not in a compacted form, especially for the assembly with agglomerates because the size of the agglomerate is smaller than the size of the ball used to allocate the space for the agglomerate. Thus, the initial assembly was compacted by applying a repeated load to the bottom wall; with high gravitational acceleration ($9.81\times 10^2 \text{ ms}^{-2}$) applied to the particles. This procedure was thought to be able to reduce the computational time compared to compaction by either applying

vibratory compaction at the bottom wall, or allowing the assembly to settle under high gravitational acceleration. To apply this repeated load to the bottom wall, the servomechanism discussed in section 2.4.4 was modified. The required stress in the original servomechanism is programmed in such a way that it increases and then decreases in an incremental fashion to follow a sinusoidal curve. Ten load cycles with maximum load of 3 times the self-weight (under gravitational acceleration of $9.81 \times 10^2 \text{ ms}^{-2}$) of the assembly and a frequency of 200Hz were applied to the assembly. The force and the rate of compaction were arbitrarily chosen. During the compaction process, the bond strength was set to a high value ($F_c^n = F_c^s = 1 \times 10^{16} \text{ N}$) to avoid breakage and the coefficient of friction was set to zero to ease compaction. Following compaction, the high gravitational acceleration applied to the particles was reduced to 9.81 ms^{-2} and the ball properties were reset to the final values. The compacted assembly was cycled to equilibrium using the SOLVE command, which limits the ratio of mean unbalanced force to mean contact force, or the ratio of maximum unbalanced force to maximum contact force to a default value of 0.01 (Itasca Consulting Group, Inc., 1999). The top wall was relocated at the highest point of the assembly prior to loading. Figures 6.3 and 6.4 show the oedometer with 260 agglomerates and 200 spherical balls, respectively, prior to loading.

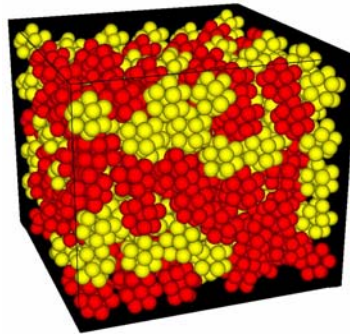


Figure 6.3. Oedometer test on 13-ball agglomerates prior to loading.

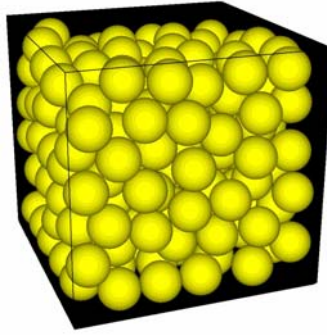


Figure 6.4. Oedometer test on spherical balls prior to loading.

6.2.2 One-dimensional compression of agglomerates

The compacted assembly of agglomerates in the oedometer was compressed using different displacement rates to identify the effect of displacement rate on the normal compression line. Four platen velocities were investigated: 0.2ms^{-1} , 0.4ms^{-1} , 0.8ms^{-1} and 1.6ms^{-1} . Figure 6.5 shows a plot of volume V normalised by initial volume V_o against the logarithm of vertical stress on the top wall σ_{top} , for four different displacement rates. It can be seen that the normal compression line deviates to the right as the displacement rate increases and the normal compression line for the displacement rate of 1.6ms^{-1} is significantly different to those for the other three displacement rates. Figure 6.6 shows a plot of volume V normalised by initial volume V_o against the logarithm of mean vertical stress σ_{mean} , which is taken to be the average of the vertical stress on the top and the bottom walls, for the four different displacement rates. The normal compression line in Figure 6.6 still deviates to the right with increasing displacement rate, but it seems to deviate less than in Figure 6.5. The difference between these two figures suggests that the stresses on the top and bottom walls are different. Figure 6.7 shows a plot of average vertical stress on the top and bottom walls, for stress levels corresponding to 24→25% strain, against displacement rate. It is obvious in this plot that the difference in vertical stress between the top and the bottom walls increases with increasing displacement rate. This means that for high displacement rates, the stresses in the assembly are not uniformly distributed at any time during the test and the results will depend on the difference in vertical stress. For example, for the displacement rate of 1.6ms^{-1} , the vertical stress on the top wall is 3.5MPa or 85%

higher than the vertical stress on the bottom wall. However, for a displacement rate of 0.2ms^{-1} , the vertical stress on the top wall is only 0.5MPa or 14% higher than the vertical stress on the bottom wall.

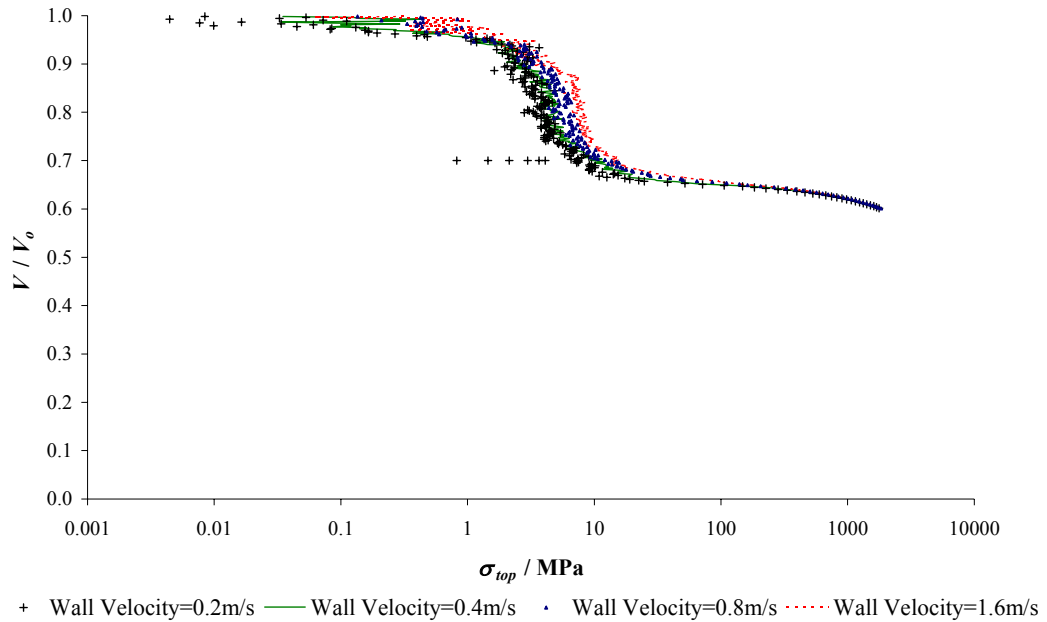


Figure 6.5. V/V_0 against logarithm of vertical stress on the top wall for oedometer test using agglomerates (each agglomerate represent a soil particle).

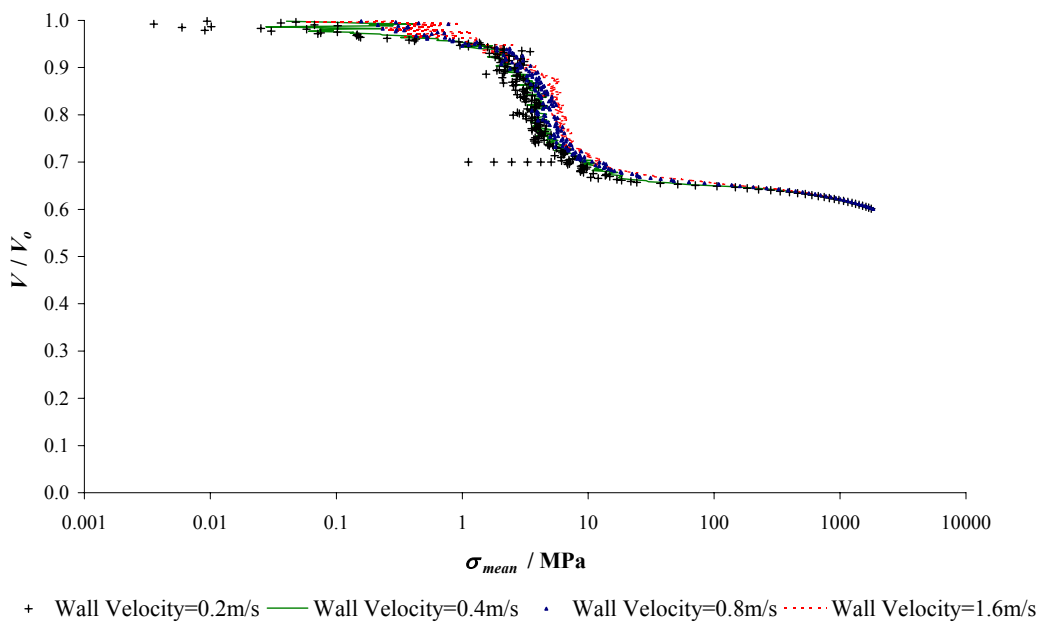


Figure 6.6. V/V_0 against logarithm of mean vertical stress for oedometer test using agglomerates.

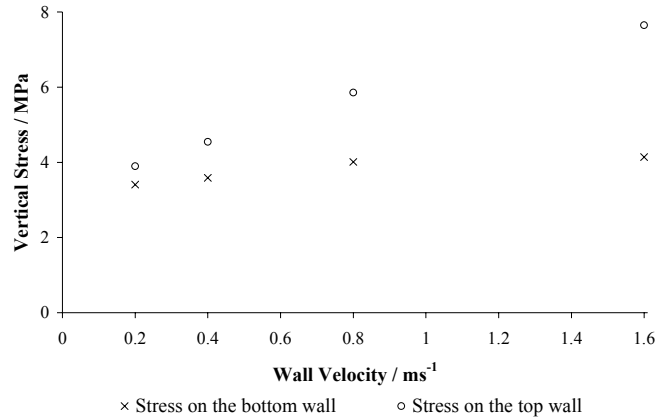


Figure 6.7. Average vertical stress on the top and the bottom walls for different displacement rates.

The PFC^{3D} manual (Itasca Consulting Group, Inc., 1999) provides a microcrack monitoring and display package that records bond breaking events in a linked list. When a bond breaks, a data block that stores the breakage event is created and added to the linked list. This allows the number of broken bonds to be monitored during the simulation. Figure 6.8 shows a plot of the total number of bonds against the logarithm of mean vertical stress σ_{mean} for the sample which has been loaded with a displacement rate of 0.2ms^{-1} . It can be seen that this plot is similar to the one-dimensional compression plot as shown in Figures 6.5 and 6.6, where the change of curvature is directly related to the rate of bond breakage. This implies that the point of maximum curvature on a plot of voids ratio against log of vertical stress is a suitable definition of yield.

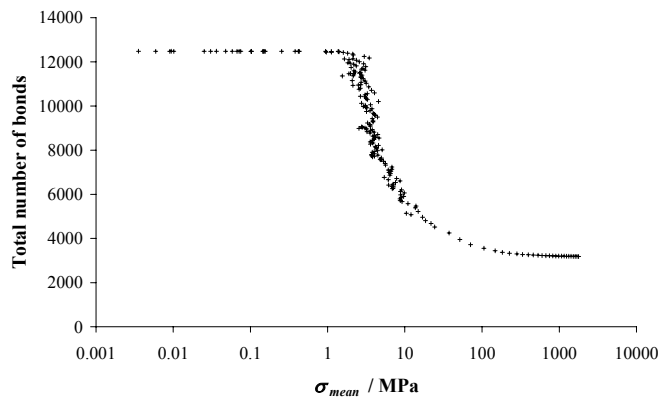


Figure 6.8. Total number of bonds against logarithm of mean vertical stress for sample loaded with a displacement rate of 0.2ms^{-1} .

6.2.3 One-dimensional compression of spherical balls

One-dimensional compression of elastic spherical balls was conducted for comparison with the one-dimensional compression of agglomerates. Two tests were conducted using this compacted assembly: one with the linear contact model and the other with the Hertzian contact model.

Since the difference in vertical stress between the top and the bottom walls was small for loading an assembly of agglomerates with a displacement rate of 0.2ms^{-1} , it was anticipated that the difference in vertical stress should also be negligible for loading an assembly of spherical balls at a displacement rate of 0.2ms^{-1} . Thus, both tests were loaded at a displacement rate of 0.2ms^{-1} . Figure 6.9 shows the compression curve for loading and unloading balls with linear contacts and Hertzian contacts, plotted in a $V/V_o - \log\sigma_{mean}$ space. Clearly, balls with the linear contact model behave in an elastic manner. The balls with the Hertzian contact model do seem to have some rearrangement at the early stage of loading, so that the compression curve is similar to that for an assembly of agglomerates as shown in Figure 6.6, in the sense that the platen force fluctuates as particles rearrange. However, the unloading curve appears to be elastic, so there has been only a small amount of permanent deformation at the end of the load-unload cycle.

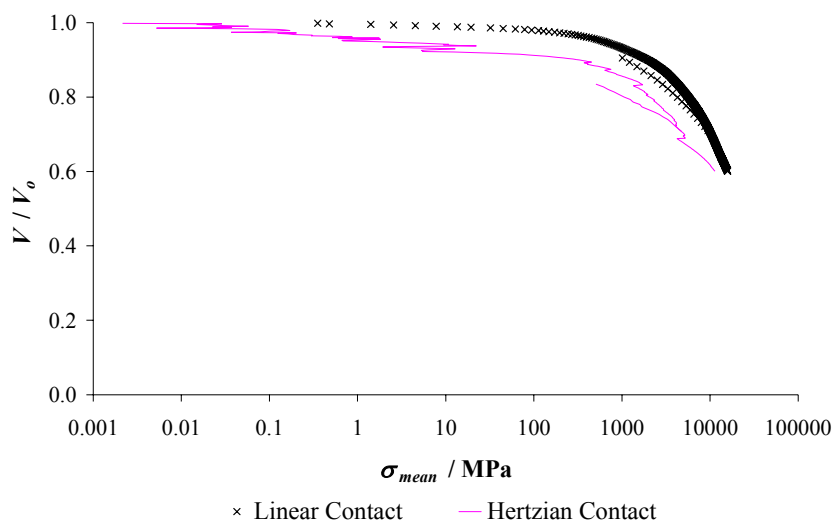


Figure 6.9. V/V_o against logarithm of mean vertical stress for oedometer test using balls (each ball represents a soil particle).

6.2.4 Discussion

The shape of the linear-elastic loading curve in $V/V_o - \log \sigma_{mean}$ space is similar to that for the agglomerates in Figure 6.6 and this poses the question as to whether the definition of ‘yield’, as the point of maximum curvature is suitable when there is no yield in Figure 6.9. However, the unloading curve in Figure 6.6, and the onset of breakage in Figure 6.8 are consistent with the proposed definition. This is consistent with observations by McDowell & Harireche (2002b). It can also be seen that the curvature of the plot changes again at about 35% volumetric strain, as shown in Figures 6.5 and 6.6. It can be seen in Figure 6.8 that there is no further bond breakage at this stage, which suggests that most of the agglomerates in the assembly have already broken and the assembly mainly consists of individual spherical balls or “strings” of balls (i.e. balls bonded by one or two bonds only). Any remaining agglomerates may be protected by the individual balls, and if an agglomerate fractures, the voids may be too small for the fragments to fill. This is consistent with data from one-dimensional compression tests on dense silica Leighton Buzzard sand by McDowell (2002). He found that the rate of crushing with increasing stress reduces considerably at high stresses and explained this as being due to the large particles being well protected by many neighbours, and because the smallest particles (balls) are unbreakable.

6.3 *Single particle crushing test simulations*

Preliminary oedometer test simulations have shown that ballast is best simulated as an aggregate of crushable balls, such that the ballast will undergo degradation if induced tensile stresses are sufficiently high. In order to simulate ballast degradation correctly, it is important to simulate crushable balls with the average strength and distribution of strengths of real ballast. McDowell & Harireche (2002a) were successful in simulating crushable agglomerates with the average strength and distribution of strengths of silica sand particles using PFC^{3D}. They were also able to simulate the size effect on strength for silica sand correctly. For these reasons, the

approach used by McDowell & Harireche (2002a) was used to produce crushable balls with the average strength and distribution of strengths of ballast A, by simulating single ballast particle crushing tests between flat platens. Table 6.1 shows the result of the laboratory single ballast particle crushing tests on ballast A.

| Nominal size / mm | Weibull modulus / m | 37% tensile strength σ_o / MPa |
|-------------------|-----------------------|---------------------------------------|
| 24 | 2.82 | 31.4 |
| 44 | 3.45 | 20.7 |

Table 6.1. Single particle crushing tests result for ballast A.

It should be noted that some of the initial sample of ballast A in storage was used to make a pavement by some sub-contractor without the consent of the author! Thus, more ballast A was sourced from the supplier, which resulted in 2 sets of test results for ballast A. The strengths simulated here are using the first set of strengths for ballast A (because the simulations were performed before the ballast went missing), and the results presented in Chapter 3 are for the second batch of ballast A.

6.3.1 Test description

Thirty tests were conducted on each agglomerate type to give a statistical representation of the sample strength and distribution of strengths. Each test was conducted on a hexagonal close packed (HCP) agglomerate, and 13.5% balls were removed initially at random to replicate a dense random packing, and some balls were then randomly removed (0-25%) to simulate flaws, and then each agglomerate was given a random rotation. Two types of agglomerate were used for this simulation: an agglomerate containing initially 135 balls (giving agglomerate diameters of 24mm and 48mm depending on the ball size) and an agglomerate containing initially 1477 balls (giving an agglomerate diameter of 48mm). Each agglomerate was bonded together with contact bonds. McDowell & Harireche (2002a) noticed that HCP packing gives a regular and maximum possible agglomerate density (74%), which results in an opposite size effect on strength to

that observed for real materials. Thus, they attempted to simulate a correct size effect by using agglomerates that have a dense random packing where balls in this configuration occupy 64% of the total volume. They achieved this by removing 13.5% $[1 - (64/74)]$ balls at random initially to partly replicate a dense random packing and introduce flaws, before removing an additional 0-25% balls. McDowell & Harireche (2002a) found that removing 13.5% balls initially was inadequate to simulate the size effect on strength for silica sand, and increased the percentage of balls removed initially to increase the size effect. The same methodology will be used here, where removing 13.5% balls initially at random will be used first, and altered if the size effect for ballast A is not reproduced.

Each agglomerate was stabilised under gravity for 50,000 timesteps before compression. In order to reduce computational time, a gravitational field of $9.81 \times 10^5 \text{ ms}^{-2}$ was applied so that the agglomerate stabilised in an acceptable number of timesteps. To prevent the agglomerate from shattering during this process, the bond strength was temporarily set to a very high value. Once the agglomerate had stabilised, the gravitational field was reduced gradually to 9.81 ms^{-2} and the bond strength reduced to the desired value. Following stabilisation under gravity, the top platen was located at the highest point of the agglomerate, and then moved downwards at a constant velocity to compress the agglomerate. It was noted that there were non-uniform locked-in forces within the agglomerate after stabilising the agglomerate under gravity, and removing the gravity did not reset the locked-in forces to zero. This behaviour was not expected because all the ball contacts were elastic (i.e. linear contact model), which should restore the agglomerate initial state or geometry when gravity is reduced. This behaviour is not understood and requires further research.

Figure 6.10 shows a typical result for a force-strain plot for a 48mm diameter agglomerate initially containing 1477 balls, subjected to random rotation, then removal of some balls (e.g. 356 balls in this case), followed by stabilisation under gravity and then loading (note: strain was calculated by dividing the platen displacement by the initial distance between the loading platens). Figure 6.10 also presents three different platen velocities used to compress the same agglomerate and

it can be seen that a platen velocity of 0.08ms^{-1} can be applied, without significantly affecting the results. Thus, all tests, including the agglomerate initially containing 135 balls, were conducted with a platen velocity of 0.08ms^{-1} , and to a strain of 12%. The strength of each agglomerate was determined by dividing the failure force (peak force) by the square of the particle size (i.e. distance between the loading platens) at failure ($\sigma_f = F_f / d_f^2$) for that agglomerate.

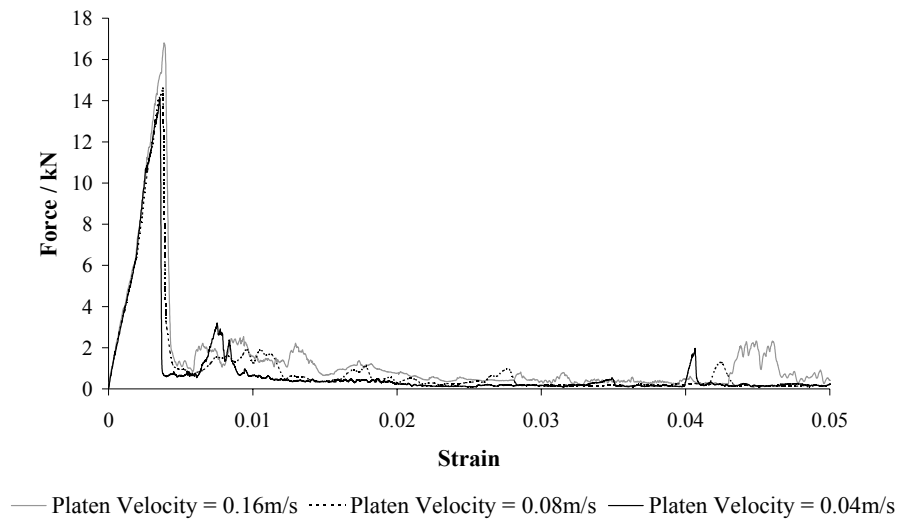
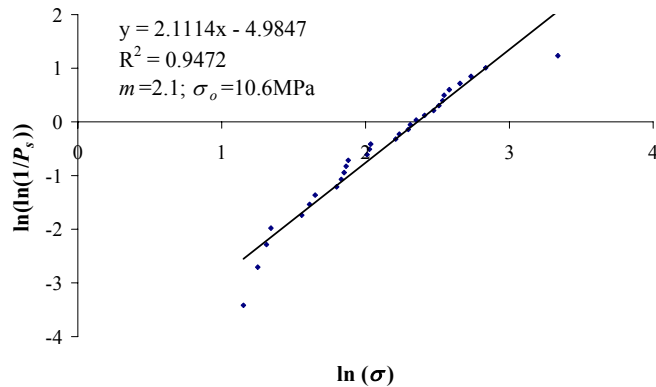


Figure 6.10. Typical force-strain plot for 48mm diameter agglomerate initially containing 1477 balls for different platen velocities.

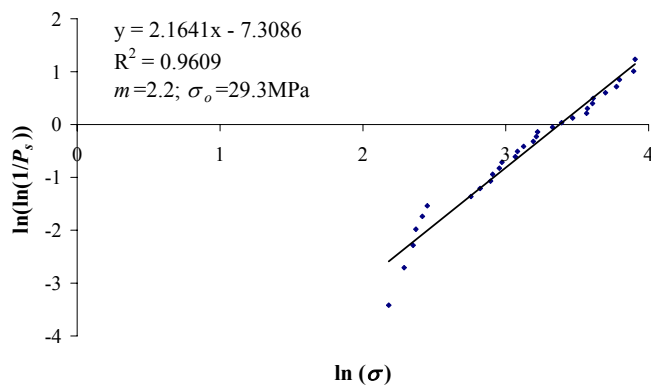
6.3.2 Results

The initial stiffnesses and bond strengths were estimated using equations 6.1 and 6.2. The normal and shear stiffnesses were both $4.97 \times 10^8 \text{Nm}^{-1}$, and the normal and shear bond strengths were both set to $2.61 \times 10^2 \text{N}$ (using a Young's modulus of 70GPa, and tensile strength of 20.7MPa respectively). These parameters were used to simulate the 24mm diameter agglomerate initially comprising 135 balls of diameter 3.55 mm, subjected to an initial random removal of 13.5% balls, then removal of some balls (0-25%) and then random rotation, followed by stabilisation under gravity and then loading. Figure 6.11 (a) shows the Weibull probability plot (described in section 3.3.1) for 30 tests on the 135-ball agglomerates of diameter 24mm simulated with the initial parameters. It can be seen that the 37% tensile strength σ_o (10.6MPa) is

lower than that presented in Table 6.1 for ballast A of nominal size of 24mm (31.4MPa). Thus, in order to reproduce σ_o of ballast A, the bond strength and ball and platen stiffnesses were scaled by $f = 31.4/10.6 = 2.96$ and the tests were repeated. This gives $\sigma_o=29.3$ MPa (Figure 6.11 (b)). For both of these tests, the seed of the random number generator was constant so that the same geometries and flaws could be tested with different bond strengths and stiffnesses.



(a)



(b)

Figure 6.11. Weibull probability plot for 24 mm diameter agglomerate initially containing 135 balls with stiffnesses and bond strength: (a) unscaled, $f=1$; (b) scaled $f=2.96$.

The size effect was investigated by simulating a 48mm diameter agglomerate initially containing 1477 balls of diameter 3.55 mm, in the same way as the 135-ball agglomerates of 24mm diameter. The parameters used were the same as the scaled ($f = 2.96$) parameters for the 135-ball agglomerates of 24mm diameter. Figure 6.12 shows the Weibull probability plot for 30 tests on the 1477-ball agglomerates of diameter 48mm simulated with the scaled parameters. It can be seen that the 37%

tensile strength σ_o (22.4MPa) is comparable to the σ_o presented in Table 6.1 for ballast A of nominal size of 44mm (20.7MPa). Thus, the use of initially removing 13.5% balls and then removal of some balls (0-25%) randomly is adequate to simulate the size effect for ballast A.

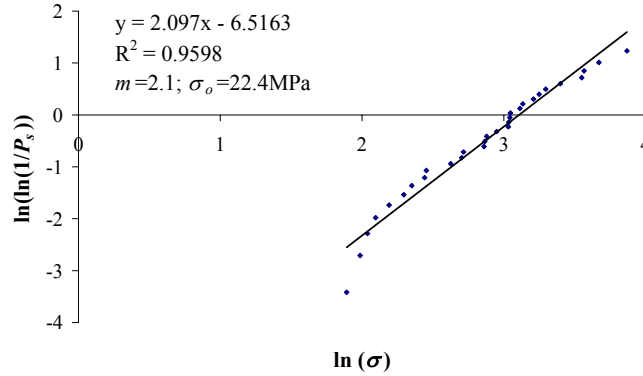
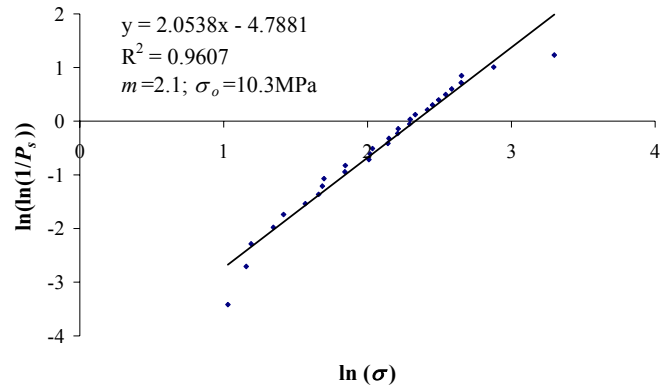
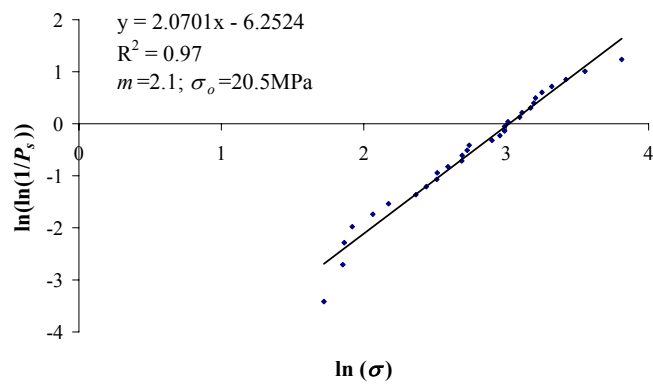


Figure 6.12. Weibull probability plot for 48 mm diameter agglomerate initially containing 1477 balls ($f=2.96$).

In order to reduce computational time for simulating oedometer tests with agglomerates, 135-ball agglomerates of 48mm diameter were used instead of the 1477-ball agglomerates of 48mm diameter. Thus, 30 samples of 48mm diameter agglomerates initially comprising 135 balls of diameter 7.10 mm, subjected to an initial random removal of 13.5% balls, then removal of some balls (0-25%) and then random rotation, followed by stabilisation under gravity and then loading, were simulated. The normal and shear stiffnesses were both $9.95 \times 10^8 \text{ Nm}^{-1}$ (calculated from equation 6.1), and the normal and shear bond strengths were both set to $1.04 \times 10^3 \text{ N}$ (calculated from equation 6.2). Figure 6.13 (a) shows the result with the unscaled parameters. It can be seen that the 37% tensile strength σ_o (10.3MPa) is lower than that presented in Table 6.1 for ballast A of nominal size of 44mm (20.7MPa). Thus, the bond strength and ball and platen stiffnesses were scaled by $f = 20.7/10.3 = 2.01$ and the tests were repeated. This gives a σ_o of 20.5MPa (Figure 6.13 (b)). This agglomerate was used to simulate the oedometer tests presented in section 6.4.



(a)



(b)

Figure 6.13. Weibull probability plot for 48 mm diameter agglomerate initially containing 135 balls with stiffnesses and bond strength: (a) unscaled, $f=1$; (b) scaled $f=2.01$.

6.3.3 Discussion

It was noted in some cases that it was not possible to observe a diametral fracture of the agglomerate. Hazzard et al. (2000) found that the stress waves emanating from cracks were capable of inducing more cracks, and high levels of damping inhibit the formation of large clusters or a chain reaction of cracking. For example, they found that by using a damping coefficient of 0.015 (chosen to represent granite sample with faults) for the simulation of the compression of brittle rock using PFC^{2D}, the peak strength was reduced by up to 15% and the number of cracks increased in discrete jumps compared to model runs with high damping (coefficient of damping = 0.7). PFC^{2D} and PFC^{3D} provide local non-viscous damping to dissipate energy by damping the unbalanced force in the system (Itasca Consulting Group, Inc., 1999).

The damping coefficient is a constant that specifies the magnitude of damping. An attempt was made to make the fracture process more realistic by reducing the damping within the agglomerate. Figure 6.14 shows a force-strain plot for a 24mm diameter agglomerate initially comprising 135 balls of diameter 3.55 mm, subjected to an initial random removal of 13.5% balls, then random rotation and removal of some balls (0-25%), followed by stabilisation under gravity and then loading. The normal and shear stiffnesses were both $4.97 \times 10^8 \text{ Nm}^{-1}$, and the normal and shear bond strengths were both set to $2.61 \times 10^2 \text{ N}$. Figure 6.14 presents the results for two different damping coefficients used to compress the same agglomerate. It can be seen that the agglomerate that was compressed with a damping coefficient of 0.015 failed at a lower force and in a more catastrophic manner compared to the one with a damping coefficient of 0.7. Figure 6.15 shows a plot of the number of broken bonds against strain. It can be seen that the agglomerate that was compressed with a damping coefficient of 0.015 failed by fast fracture i.e. the agglomerate that was compressed with a low damping coefficient failed in a more realistic manner where failure occurred quickly and catastrophically. However, it was noticed in some cases using a low damping coefficient was still not enough to cause diametral fracture of the agglomerate.

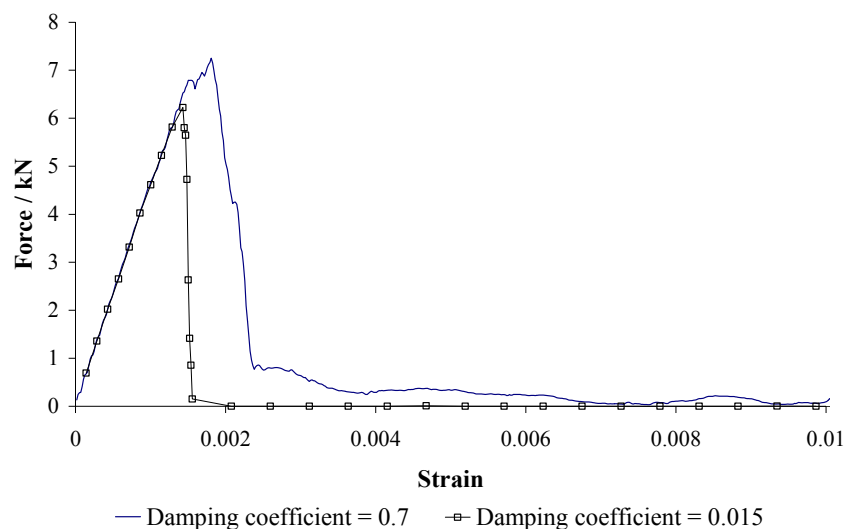


Figure 6.14. Force-strain plot for a 24mm diameter agglomerate initially containing 135 balls for different damping coefficients.

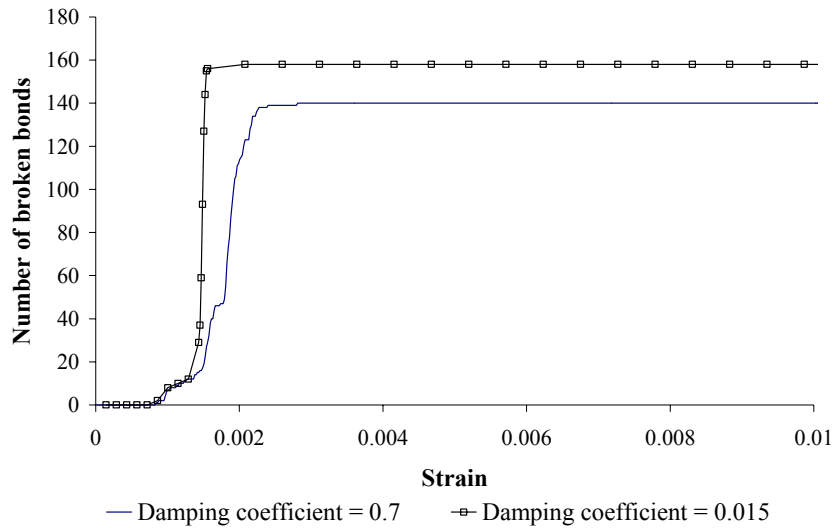


Figure 6.15. Number of broken bonds against strain for the compression of a 24mm diameter agglomerate initially containing 135 balls with different damping coefficients.

6.4 Oedometer test simulations

The purpose of the oedometer test simulation is to attempt to simulate the oedometer test conducted in the laboratory (Chapter 4), using crushable particles with the distribution of strengths of ballast A, as described in the previous section.

6.4.1 Test description

The dimensions of the oedometer were 270mm long \times 270mm wide \times 150mm deep. Smaller balls were generated within the oedometer and then expanded to a final diameter of 48mm. The expanded balls were cycled to equilibrium and then replaced by agglomerates of approximately the same size. The agglomerate used in this test was the 48mm diameter agglomerate initially comprising 135 balls of diameter 7.10 mm described in the previous section. Each agglomerate was subjected to an initial random removal of 13.5% balls, then removal of some balls (0-25%) and then random rotation. The number of agglomerates in the oedometer

was obtained through trial and error to maintain low contact forces after cycling to equilibrium prior to loading.

The properties of the agglomerates were the same as the scaled properties of the 135-ball agglomerates of 48mm diameter in the previous section. The ball normal and shear stiffnesses were both $2.0 \times 10^9 \text{ Nm}^{-1}$, and the normal and shear bond strengths were both set to $2.1 \times 10^3 \text{ N}$. The coefficients of friction for the balls and the walls were set to 0.5 and 0, respectively. The stiffnesses of the walls were chosen to be the same as for the balls.

After the agglomerates were created, the sample was cycled for 30,000 timesteps to avoid high concentrations of contact force. During this period, the bond strengths were set to a high value ($F_c^n = F_c^s = 1 \times 10^{16} \text{ N}$) to avoid breakage and the coefficient of friction was set to zero to make rearrangement easier. The ball properties were then reset to the final values and the assembly was cycled to equilibrium using the SOLVE command. Due to the high computational time required (nominally 135-ball agglomerates instead of the 13-ball agglomerates used in section 6.2), this assembly was not compacted. The rate of loading was chosen to be 0.1 ms^{-1} because the difference in vertical stress between the top and the bottom wall for this loading rate was small. For example, the average vertical stress on the top wall was only 0.15MPa or 8% higher than the vertical stress on the bottom wall, for stress levels corresponding to 40→41% strain (on the normal compression line). The sample was loaded to a vertical stress of 21MPa and this test took approximately 3 weeks on an 800MHz computer with 128Mb RAM to complete. Figure 6.16 shows the oedometer with 113 agglomerates prior to loading.

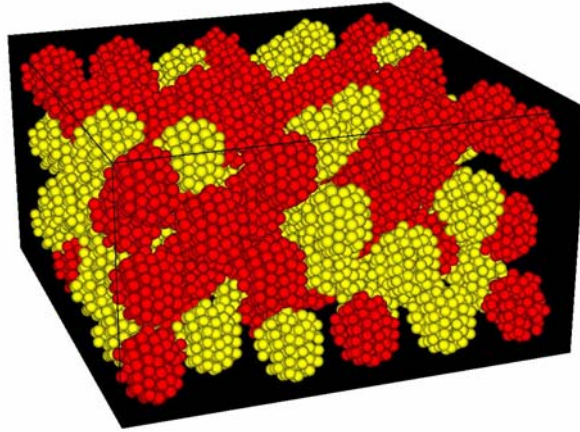


Figure 6.16. Oedometer test on 48 mm agglomerates initially containing 135 balls prior to loading.

6.4.2 Results

Figure 6.17 shows a plot of volume V normalised by initial volume V_0 against the logarithm of vertical stress σ (mean vertical stress) for the oedometer test simulation on 135-ball agglomerates of 48mm diameter, and the laboratory oedometer test on 37.5-50mm ballast A. The oedometer test simulation on 135-ball agglomerates had more initial strain because the sample was not compacted, whilst the oedometer test on 37.5-50mm ballast A was compacted to maximum density. Yielding for the agglomerates appears to occur at around 30% strain and the yield stress is lower than for the oedometer test on 37.5-50mm ballast A. This is anticipated as the agglomerates in the sample were not compacted. In addition, the agglomerates were reasonably spherical, which leads to columns of strong force in the agglomerates and yielding at a lower than expected yield stress. For example, if compacted angular agglomerates were used, the average stress on each agglomerate would be lower because the load would be transmitted by more force columns. It can be seen that for the oedometer test simulation on 135-ball agglomerates, the compressibility is higher than the oedometer test on 37.5-50mm ballast A at stresses just after yielding, but lower at high stress levels. McDowell & Harireche (2002b) showed that agglomerates fracture at stresses just after yielding, and because each agglomerate is porous and internal voids become external voids when the agglomerate fractures, this gives a high compressibility. At high stress levels, however, most of the

agglomerates have already fractured and the smallest fragments (balls) are unbreakable. Figure 6.18 shows a plot of total number of bonds against the logarithm of mean vertical stress σ_{mean} for the oedometer test simulation on 135-ball agglomerates of 48mm diameter. It is obvious in this plot that yielding coincides with the onset of agglomerate fracture.

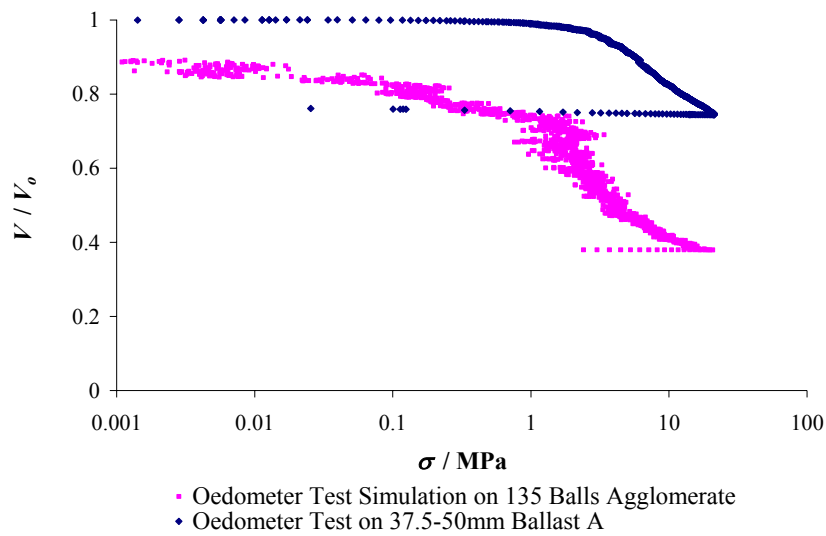


Figure 6.17. V/V_0 against logarithm of vertical stress for oedometer test using 135-ball agglomerates of 48mm diameter and the laboratory oedometer test on 37.5-50mm ballast A.

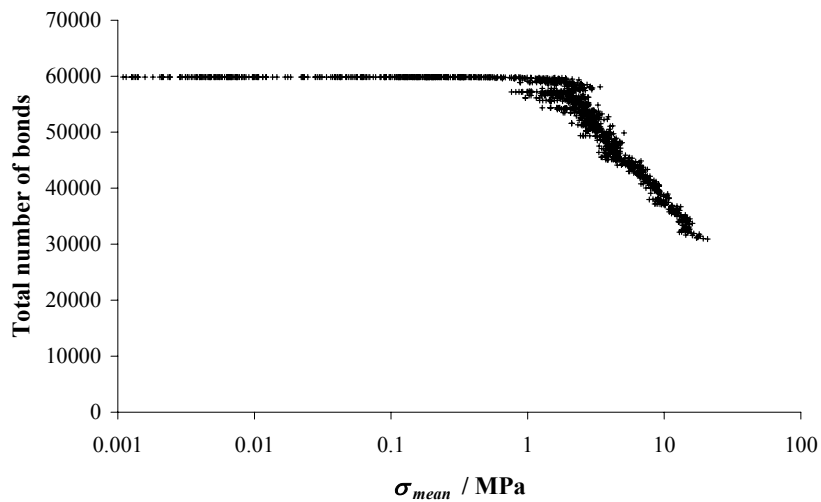


Figure 6.18. Total number of bonds against logarithm of mean vertical stress σ_{mean} for the oedometer test simulation on 135-ball agglomerates of 48mm diameter.

Figure 6.19 shows a plot of mean K_o , which is the ratio of mean horizontal stress (on all 4 vertical walls) to mean vertical stress, against vertical strain for loading and unloading in the oedometer test simulation on 135-ball agglomerates. It can be seen that K_o gradually evolves to a constant value of approximately 0.5 beyond yield at 30% strain. The increase in K_o during unloading is presented in Figure 6.20, which is a plot of K_o against overconsolidation ratio OCR for different unloading wall velocities. It can be seen that the result of unloading the sample with a wall velocity of 0.1ms^{-1} differs from the results with the two other wall velocities and the increase in K_o for all the unloading speeds is not as high as anticipated.

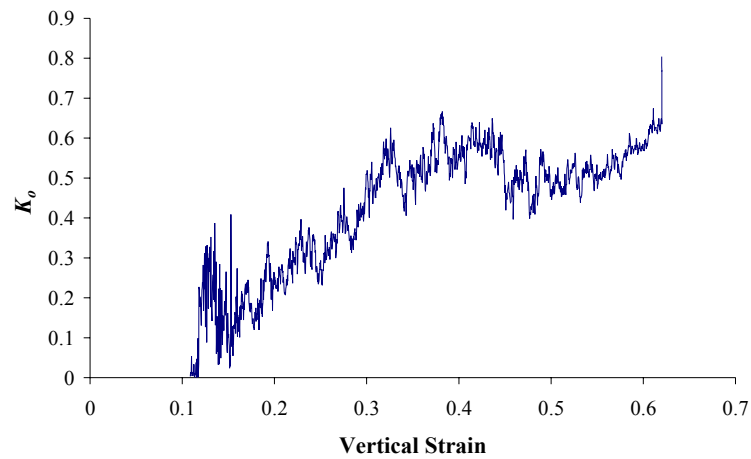


Figure 6.19. Mean K_o against vertical strain for oedometer test on 135-ball agglomerates of 48 mm diameter.

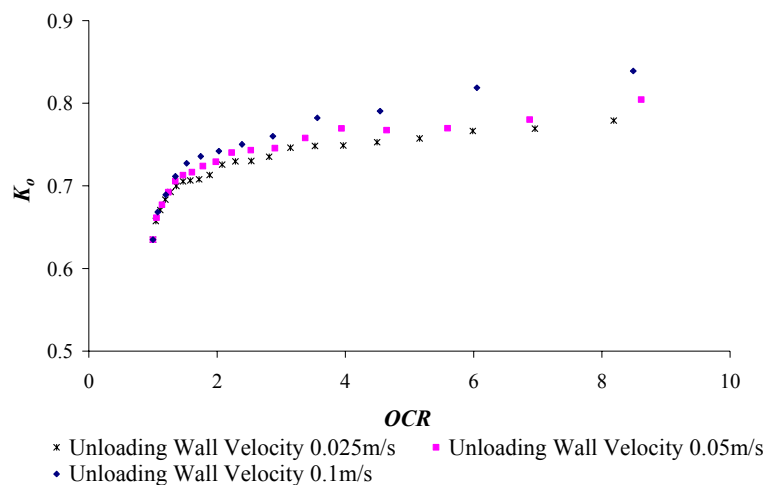


Figure 6.20. K_o against OCR for oedometer test on 135-ball agglomerates of 48 mm diameter.

6.4.3 Discussion

It was noted that the stress in the loaded sample could relax and approach zero stress rapidly. For example, a further 10,000 timesteps were permitted after halting the wall movements when the mean vertical stress in the sample reached 21MPa. Figure 6.21 shows a plot of mean vertical stress σ_{mean} against number of timesteps. It can be seen that the mean vertical stress in the sample dropped very quickly within 10,000 timesteps or 1.25×10^{-3} seconds. This must be because the sample was not in a quasi-static state, with large unbalanced forces within the sample, leading to further bond breakage and rearrangement in the sample. This observation suggests that the small increase in K_o during unloading in Figure 6.20 is apparent because the sample is not in a quasi-static state and the contact forces in the sample are still changing. This observation also suggests that the sample is not in equilibrium, even though the difference in the vertical stress on the top and bottom walls is small.

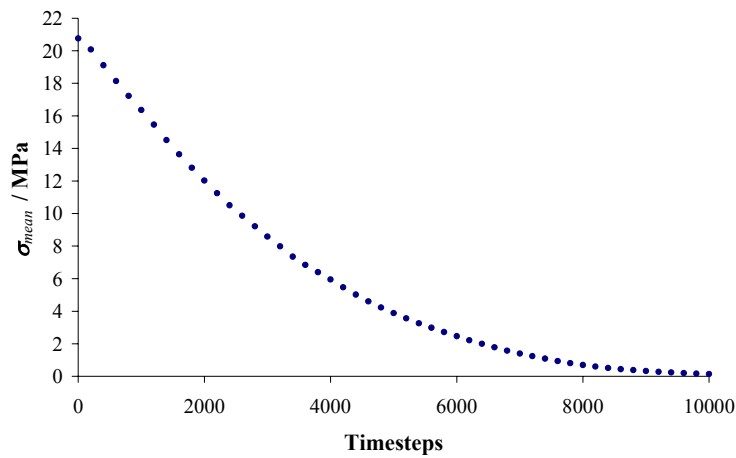


Figure 6.21. Mean vertical stress σ_{mean} against number of timesteps.

In order to obtain a sample in a quasi-static state, after reaching a mean vertical stress of 21MPa, the sample was further cycled by maintaining the vertical stress at 21MPa until the ratio of mean unbalanced force to mean contact force R_{mean} became equal to 0.001. Figure 6.22 shows a plot of number of broken bonds against the number of timesteps. It can be seen that the total number of broken bonds increases by approximately 10% when the ratio of mean unbalanced force to mean contact force R_{mean} attained a value of 0.001. The rate of increase in bond breakage at this

ratio is very small, so the sample can be considered in a quasi-static state. It should be noted that the vertical strain had only increased by 1% for the sample forces to arrive at this ratio, so the one-dimensional compression line in Figure 6.17 would not change significantly.

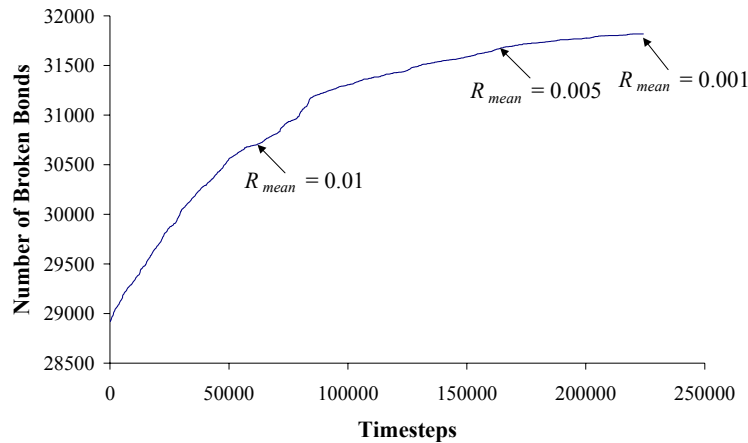


Figure 6.22. Number of broken bonds against number of timesteps.

The sample that was cycled to a ratio of mean unbalanced force to mean contact force R_{mean} of 0.001 was unloaded by maintaining this ratio at 0.001 at all stages (e.g. unload sample to a certain OCR and cycle to a ratio of 0.001 whilst maintaining the vertical stress). Figure 6.23 shows a plot of K_o against OCR for the sample unloaded by maintaining this ratio at 0.001. It can be seen that there is no increase in K_o , and in fact, the sample was not physically unloaded because the depth of the sample at an OCR of 10 is 0.1mm smaller than the depth before unloading. It was noted that there were a further 5 bonds which broke during unloading, which is negligible compared to the total number of bonds broken. However, this could trigger further rearrangement in the sample and the use of contact bonds may enhance this effect because contact bonds allow rolling of balls relative to one another without breaking the contact bond. A contact bond provides no resistance to rolling because a contact bond acts only at a point and not over an area of finite size, and so cannot resist moment (Itasca Consulting Group, Inc., 1999). Figure 6.24 illustrates a contact bond that allows rolling of ball A relative to ball B without slipping, thus without breaking the contact bond. It is noted that this event only occurs for balls that are free to roll; additional contact bonds provided by surrounding balls will prevent a ball from

rolling (Figure 6.25). Therefore, it is likely that the compressed sample which has many fractured agglomerates will result in balls having a single bond, permitting rolling and further rearrangement.

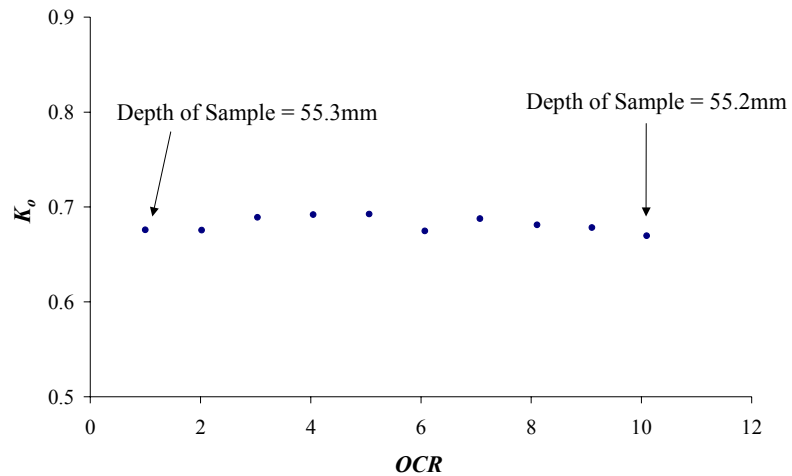


Figure 6.23. K_o against OCR for the sample unloaded by maintaining $R_{mean} \approx 0.001$.

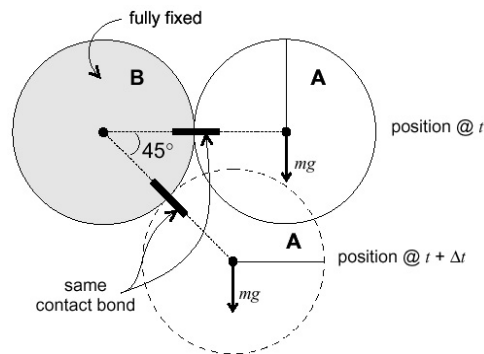


Figure 6.24. Rolling without slip at a contact bond (Itasca Consulting Group, Inc., 1999).

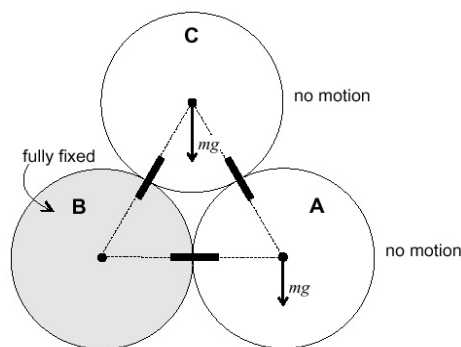


Figure 6.25. Constraint provided by surrounding balls which prevent rolling at a contact bond (Itasca Consulting Group, Inc., 1999).

6.5 Box test simulations

Due to the high computational time required to simulate the box test with the 135-ball agglomerates, balls or clumps need to be used to represent ballast particles in the box. Since it was noted that breakage in the box test was minimal (Chapter 5), balls and clumps, both of which are uncrushable, will be used to represent ballast particles. This section presents the simulation of box tests with spherical balls and clumps.

6.5.1 Test description

The size of the box and the sleeper in this simulation are equal to the size of the box and sleeper in the laboratory: 700×300×450mm and 250×300×150mm respectively. The diameter of the balls is 36.25mm (i.e. the weighted size of the specification ballast, which was computed by combining the nominal size of 37.5-50mm and 25-37.5mm using 40% and 60% weightings respectively), which leads to a normal and shear stiffnesses of $5.08 \times 10^9 \text{ Nm}^{-1}$ (equation 6.1). The stiffnesses of the walls and sleeper were chosen to be the same as for the balls. Since the Young's modulus of stiff rubber is approximately 2,000 times smaller than that of steel (Ashby & Jones, 1980), the stiffnesses of the base were chosen to be 2,000 times smaller than that of the walls, namely $2.54 \times 10^6 \text{ Nm}^{-1}$. The ball, wall, and base friction coefficients were set to 0.5 and the gravitational field was set to 9.81 ms^{-2} .

As for the oedometer test, smaller balls were generated within the box and then expanded to a final diameter of 36.25mm. The expanded balls were cycled for 5000 cycles to avoid high contact forces, and for the test with clumps, replaced by clumps of approximately the same size. Since one of the criteria for ballast selection is that particles should be equidimensional, an 8-ball cubic clump was used to represent each ballast particle in the box as shown in Figure 6.26. A wall was located at the top of the box to confine the particles initially. This wall was removed after the particles were generated by gradually moving it away from the box, so that particles would not escape from the box.

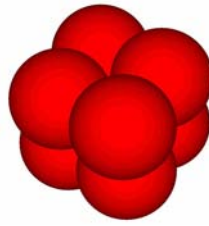


Figure 6.26. An 8-ball cubic clump.

The assembly was compacted by applying a high gravitational acceleration ($9.81 \times 10^3 \text{ ms}^{-2}$) for 50,000 timesteps. After compaction, the gravitational field was reduced gradually to 9.81 ms^{-2} . In order to apply the servomechanism as described in section 2.4.4, which requires particles to be in contact with the wall, the assembly in the box was initially loaded by moving the sleeper towards the assembly to give a load equivalent to the self-weight of the sleeper in the laboratory (34kg). Once the target stress was achieved on the bottom of the sleeper, the SOLVE command was used to reduce the unbalanced forces. The default value of the ratio of mean unbalanced force to mean contact force, or the ratio of maximum unbalanced force to maximum contact force of 0.01 was used. It was shown earlier that by limiting the ratio of mean unbalanced force to mean contact force to 0.001, this had a small effect on the values of K_o obtained on unloading in oedometer tests. However, use of a tighter tolerance on this ratio greatly increases computational time, and so here the default SOLVE command has been used. The modified servomechanism described in section 6.2.1 was used to apply repeated load to the assembly. The assembly was loaded with a sinusoidal load pulse with minimum load of 3kN and maximum load of 40kN, at a frequency of 3Hz. Figures 6.27 and 6.28 show the box with 1769 spherical balls and 1769 clumps, respectively, prior to loading.

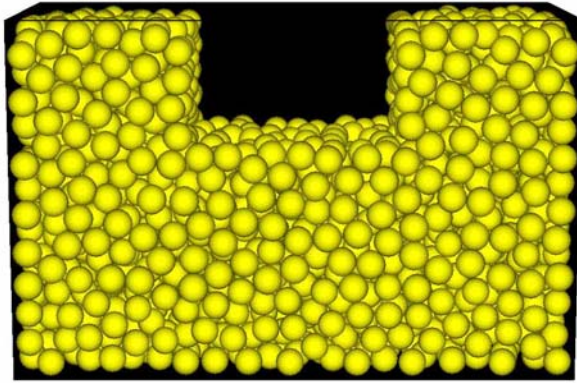


Figure 6.27. Box test on spherical balls prior to loading.

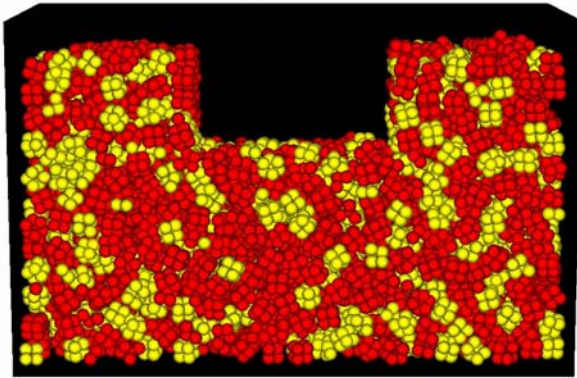


Figure 6.28. Box test on 8-ball cubic clumps prior to loading.

6.5.2 Results

Figure 6.29 shows a plot of load against deformation for the first cycle of the box test on spherical balls and 8-ball cubic clumps. It can be seen that the assembly with the 8-ball cubic clumps is stiffer on loading than the assembly with the spherical balls. The clumps gave a higher resilient stiffness, and less permanent deformation is produced. This difference must be due to the additional resistance provided by the irregular or non-spherical shape of the clumps. It can also be seen that the load-deformation plot for the assembly with the spherical balls differs from that of real ballast subjected to repeated load, in the sense that further deformation occurs after achieving maximum load. This could be due to the spherical shape of the balls which allows the assembly to flow at high stresses.

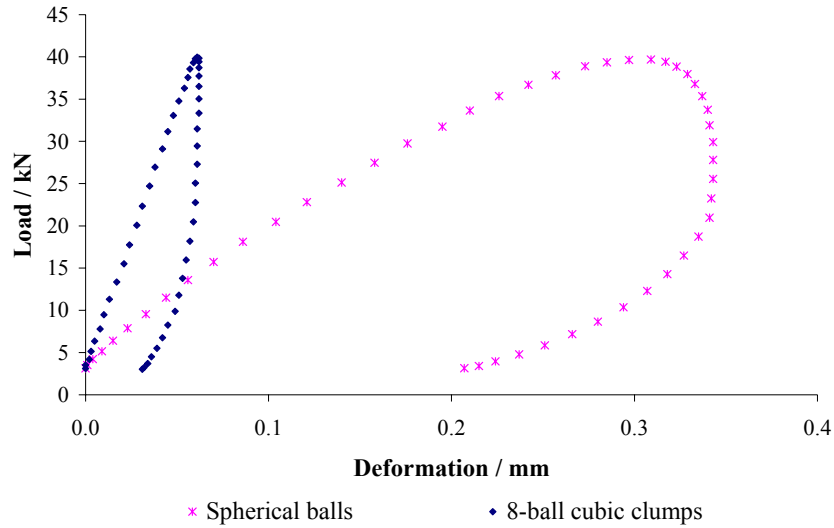


Figure 6.29. Load against deformation for the box test on spherical balls and 8-ball cubic clumps.

6.5.3 Discussion

It is noted that the stiffnesses of the assembly with the spherical balls and 8-ball cubic clumps in the box were very high compared to those described in the real box tests in Chapter 5, even though the normal and shear stiffnesses of the balls were supposed to correspond to the Young's modulus of the material (equation 6.1). Ball stiffnesses are derived from an elastic beam joining the centre of 2 balls in contact. For example, the normal stiffness at the contact K^n is derived as:

$$\sigma = E_c \varepsilon$$

$$\frac{F}{A} = E_c \frac{\Delta l}{l}$$

$$K^n = \frac{F}{\Delta l} = E_c \frac{A}{l}$$

$$K^n \propto A$$

where σ is the applied stress, ε is the strain, E_c is the Young's modulus, F is the applied force, A is the beam cross-sectional area, Δl is the displacement of the elastic

beam, and l is the length of the elastic beam (i.e. the addition of the radii of the 2 balls in contact). Equation 6.1 is derived by assuming that A is equal to πR^2 , where R is the average radius of the 2 balls in contact. It is noted that contact stiffnesses should ideally be a function of the overlap U^n or the actual contact area between the 2 balls in contact; a Hertzian contact model would therefore be more appropriate. This means that equation 6.1 gives an overestimate of the ball stiffnesses. Thus, both assemblies are stiffer than expected, but the stiffnesses of the balls and walls can easily be reduced.

It is noted that contact forces in the assembly in the box are not uniformly distributed (e.g. contact forces for particles underneath the sleeper are higher than contact forces for particles near the base of the box), as shown in Figure 6.30. As discussed earlier, the particle-particle contact stiffness should be a function of the overlap of the balls in contact. Since, the overlap of the balls in contact is a function of the normal contact force (section 2.4.2), the actual ball stiffnesses should vary throughout the box because of the non-uniformity of the contact forces in the assembly. The Hertzian contact model should therefore be more suitable in simulating the box test. This would permit an evaluation of the heterogeneous stresses within the box, and a comparison between these stresses and the ballast particle tensile strengths to see whether fracture is likely. This is a matter for further research.

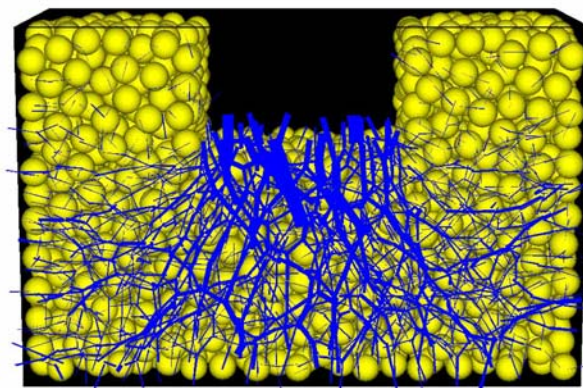


Figure 6.30. Non-uniform distribution of contact forces in the assembly in the box (contact forces are shown as lines with thickness proportional to the magnitude of the contact force).

6.6 Conclusions

The average strength and distribution of strengths for real ballast particles was successfully simulated using the McDowell & Harireche (2002a) approach, even though it was noted that some agglomerates did not exhibit a fast fracture. The use of a low damping coefficient is considered more realistic because it was found to lead to fast fracture of the agglomerates. However, the use of a low damping coefficient still cannot guarantee diametral fracture of the agglomerate. Permanent non-uniform locked-in forces were found within the agglomerate after stabilising under gravity. This behaviour is not understood and requires further examination.

The normal compression line of crushable agglomerates resembles that of real ballast. The normal compression of uncrushable spherical balls does not match experimental data because the loading and unloading curves almost coincide. The yield stress of the oedometer test on crushable agglomerates was found to be lower than in the laboratory oedometer test, even though the average strength and distribution of strengths of the agglomerates were similar to the real ballast particles, because the shape of the agglomerates differ from the shape of real ballast particles and lead to columns of strong force. The yield stress for the oedometer test on crushable agglomerates was also found to coincide with the onset of bond breakage. The sample of crushable agglomerates was found to be more compressible at stresses just after yielding than the laboratory sample, but less compressible at high stress levels. This must be due to the fact that each agglomerate is porous, so that internal voids become external voids when agglomerates fracture after yield, but at high stress levels the aggregate consists mostly of balls which cannot fracture- so the aggregate becomes much less compressible than the real laboratory sample.

The normal compression line of crushable agglomerates was found to be different at high displacement rates because of the large differences in stress on the top and bottom walls. Minimising the difference in vertical stress was found to produce an acceptable normal compression line, in the sense that small displacement rates did not affect it. However, this practice does not ensure a quasi-static sample, and further bond breakage and rearrangement is possible if the sample is cycled (i.e. the

constitutive equations are solved repeatedly) at constant stress level. This observation explains the apparent increase in K_o observed if the sample was unloaded immediately after loading because the sample was not in a quasi-static state and the contact forces in the sample were still changing, and the increase in K_o was larger for faster unloading rates. However, it was found that unloading a quasi-static sample did not give an increase in K_o on unloading because of further compression which arose during unloading. This is thought to be due to the use of contact bonds, which allow rolling of one ball relative to another without breaking the contact bond, giving further rearrangement during unloading. This requires further research.

The box test on an assembly of spherical balls is not realistic because further deformation was observed after maximum load or during unloading, which is not evident in real ballast subjected to repeated load. The box test on an assembly of 8-ball cubic clumps, however, resembles that of real ballast subjected to repeated load. The assembly of 8-ball cubic clumps was found to give less permanent deformation than the assembly of spherical balls, which should be due to the additional shearing resistance provided by the non-spherical shape of the clumps. It was noted that the equation for the calculation of ball stiffnesses recommended by Itasca Consulting Group, Inc. (1999) gave an overestimate of the aggregate stiffnesses in the box because the ball-ball contact stiffness should ideally be a function of the overlap of the balls. The Hertzian contact model may be more suitable in simulating the variability in contact stiffnesses within the box because of the varying ball contact forces throughout the box. This would permit an evaluation of the heterogeneous stresses within the box, and a comparison between these stresses and the ballast particle tensile strengths to see whether fracture is likely.

Chapter 7

Implications of this Research for Engineering

Practice

It has been clearly shown that the strength of railway ballast displays a size effect, such that smaller ballast is statistically stronger. This has been shown by the 37% tensile strengths σ_o of ballast particles, and the total breakage factors B_t in the oedometer and the box tests. It has also been shown that different ballasts have different size effects, which explains the poor correlation of the ACV test (on 10-14mm ballast) and the total breakage factor B_t in the box test on specification ballast (25-50mm ballast). This is consistent with the removal of the ACV test in the new (2005) specification (RT/CE/S/006 Issue 3, 2000). The size effect observed in railway ballast highlights the importance of testing ballast of the size used in the trackbed and considering the size effect on ballast strength when conducting tests that use small ballast to predict the performance of large ballast.

It was shown that the WAV, LAA and MDA show good correlations with the degradation of ballast in the box test. This is considered to be because the WAV, LAA and MDA tests full scale ballast as in the box test, and these tests cause extensive rearrangement, as does the simulated tamping in the box test. The tamping disturbs and rearranges ballast in the box, especially the highly stressed ballast underneath the sleeper, exposing new contacts and asperities of ballast particles to further abrasion during traffic loading. However, Wright (1983) showed that WAV does not correlate with the degradation of ballast subjected to real tamping (i.e. with a tamping machine), as shown in Table 7.1, which lists the WAVs and tamping

results for different ballasts. The tamping result is the mass of ballast passing the 14mm sieve per sleeper for ballast subjected to 10 tamping cycles. Thus, the WAV test does not account for particles subjected to the “squeezing” force of the tamping machine and further work is required to conclude the usefulness of WAV, LAA and MDA to predict degradation of ballast subjected to both real tamping in the field and traffic loading.

| Ballast | WAV / % | Mass (kg) passing 14mm per sleeper |
|-----------|---------|------------------------------------|
| Granite | 4.5 | 39.0 |
| Quarzite | 5.5 | 24.8 |
| Limestone | 6.2 | 18.0 |

Table 7.1. WAV and degradation under tamping for different ballasts (Wright, 1983).

The single particle crushing test provides a quantitative analysis of the tensile strength of ballast particles and the size effect on strength for different ballasts. The tensile strength of a ballast particle was shown to be a fundamental parameter in evaluating the strength of aggregates in the oedometer and box since this affects the relative strength index R_s . It is noted that the result of the single particle crushing test does not just indicate the strength at which bulk fracture occurs; it also provides an indication of the strength of asperities, and this is more relevant for aggregate subjected to low stress levels by traffic. Besides the tensile strength of ballast particles, the water absorption test is also considered to be a fundamental test as it has been shown that the strength of some ballasts decreases significantly under wet conditions. Thus, the single particle crushing test and water absorption test are considered as fundamental tests that can be used to evaluate the performance of different ballasts.

The large oedometer test is a simple test to evaluate the crushing resistance of an aggregate. It was noted that more information on aggregate degradation is obtained if ACV and total breakage factors B_t values are both used. For example, for large ballast particles tested in an oedometer, the ACV alone gives information on the mass of fines generated but nothing about the total amount of breakage. As opposed

to ACV, B_t only gives information on the total amount of breakage but nothing on the mass of fines present, which is important when evaluating the permeability of the ballast. Thus, better evaluation of ballast performance will be achieved if both ACV and B_t values are available. The large oedometer test results were shown to correlate well with the relative strength index R_s , which is a function of the 37% tensile strength σ_o of ballast particles and the initial voids ratio e_i of the aggregate (for the same relative density). For the same relative density, the difference in initial voids ratio e_i of different ballasts must be due to the difference in particle shape. Thus, the large oedometer test also gives a simple evaluation of the effect of particle shape on the strength of aggregate which is not offered by the single particle crushing test or the water absorption test. However, there are several drawbacks in using the large oedometer test. The stress levels in the large oedometer test are much higher than those caused by traffic, and the large oedometer test only simulates a confined ballast sample with no extensive rearrangement of ballast particles and no lateral movement. It was shown that the rearrangement of ballast particles during simulated tamping varies with the type of ballast. This may lead to a false indication of ballast degradation in the field i.e. for 2 ballast materials that have equal amount of degradation in the large oedometer test, the one that rearranges more during tamping would have a greater amount of degradation in the field. Measuring degradation of ballast with no lateral strain may also give a false indication of the performance of different ballasts, because the stability of ballast in trackbed (i.e. extent of lateral flow of ballast) is also very important. Nevertheless, the large oedometer test is easy to conduct and can be used to evaluate degradation of a confined ballast sample underneath the sleeper with no tamping and no lateral strain (i.e. trackbed with a well compacted shoulder ballast - see Figure 2.2).

Petrographic analysis was found to be useful to predict qualitatively the results of ballast tests and provide rational explanations of test results, which is consistent with observations by Watters et al. (1987) and Boucher & Selig (1987). Petrographic analysis (Large, 2003) found that ballast D has the worst quality of all 6 ballasts investigated because some of the feldspars were altered at low temperature to soft and fine clay minerals. This is consistent with all the physical tests where ballast D was shown to be a weak ballast compared to other ballasts. The presence of clay

minerals in ballast D also explains the high water absorption of ballast D (Table 4.11). Petrographic analysis also found that ballast C has the best quality because it has the fewest altered materials (i.e. alteration tends to produce weaker minerals) and has a fine grain structure (i.e. fine grain minerals have a lower potential for cleavage fracture). This is consistent with all the physical tests where ballast C was shown to perform as well, if not better, compared with other ballasts, even though it has a large amount of flaky ballast particles. Petrographic analysis also found that all the 6 ballasts investigated have the same weathering potential. For example, all six ballasts do not have sulfides and olivine which would accelerate the chemical weathering of both ballast rock and the derived fines, but do have feldspars, which when broken down to fines, will weather rapidly to clay minerals (Watters et al., 1987).

The box test provides the most extensive information compared to other tests investigated in this research, because the settlement and stiffness can each be determined as a function of the number of wheel loads, in addition to the amount of degradation. The settlement and stiffness plots of the 2 samples of ballast A were shown to be repeatable (see Figures 5.8 and 5.9). This indicates a minimum variation in settlement and stiffness for the same loading and boundary conditions. However, it is noted that the sleeper levels for the 2 box tests on ballast A can be significantly different (see Figure 5.36), because of different initial sleeper levels and sleeper levels after tamping. This observation suggests that for a ballast material subjected to similar traffic loads, degrees of tamping and boundary conditions, differential settlement is a function of the initial sleeper levels and sleeper levels after tamping. This emphasizes the importance of minimising the difference in initial sleeper levels and sleeper levels after tamping in order to minimise differential settlement. This process may cause problems because it requires alteration of the tamping effort or degree of tamping, which may affect the amount of settlement after tamping. It was noted that it is difficult to tamp 10-14mm ballast properly in the box which must be due to the relatively small size of the ballast compared with the width of the sleeper. This means that ballast that has significantly degraded cannot be tamped efficiently and must be cleaned or replaced.

To summarise, the implications for engineering practise that can be drawn from this research are:

- Tests should be on ballast of the size used in the trackbed.
- The size effect on ballast strength must be considered when conducting scaled tests.
- WAV, LAA and MDA simulate the particle mechanics of ballast subjected to simulated tamping in the box test (i.e. the rearrangement effect), but cannot simulate the damage caused by the impact and squeezing of the tamping tines.
- The single particle crushing test and water absorption test are considered to be fundamental tests which may be used to indicate the performance of different ballasts in the field.
- The large oedometer test measures the crushing resistance of a confined ballast sample. However, the stress levels are much higher than those caused by traffic. The stress levels may be similar to those produced by tamping, but tamping causes extensive rearrangement, so the use of the oedometer test is questionable. Nevertheless, it is a simple test and can be used to provide a simple evaluation of the effect of particle shape on the degradation of the aggregate.
- A better evaluation of ballast performance will be achieved if both ACV and B_t values are determined.
- The petrographic analysis is useful for predicting qualitatively the results of ballast tests and providing rational explanations of test results.
- It is important to minimise the differences in initial sleeper levels and sleeper levels after tamping in order to minimise differential settlement. However, it

is noted that this process may cause problems because it requires alteration of the tamping effort or degree of tamping, which may affect the amount of settlement after tamping.

- Ballast that has degraded significantly may be difficult to tamp efficiently because the size of the ballast underneath the sleeper is relatively small compared to the width of the sleeper. Such ballast will need to be clean or replaced.
- The amount of degradation of an aggregate is better correlated with the relative strength index R_s , which is a function of the 37% tensile strength σ_o of ballast particles and the initial voids ratio e_i of the aggregate (for the same relative density), than with the 37% tensile strength σ_o of ballast particles only.

Chapter 8

Conclusions and Suggestions for Further Research

8.1 Conclusions

The main aims of the research reported in this thesis were as follows:

- To identify ballast testing methods which provide results reflecting the field performance of different ballast materials.
- To apply the mechanics of crushable soils to ballast in order to gain an understanding of ballast degradation.
- To use the discrete element program PFC^{3D} (Itasca Consulting Group, Inc., 1999) to simulate ballast as an aggregate of crushable or uncrushable balls, in order to study stresses in ballast and the micro mechanics of degradation.

The following specific objectives have been achieved in order to meet these aims:

- 1) A literature review has been performed to study the behaviour of ballast, ballast testing methods, mechanics of crushable soils, and application of discrete element modelling using PFC^{3D} in simulating soil behaviour.
- 2) Six types of ballast that are widely used in the United Kingdom and represent a range of physical properties have been selected for this research.
- 3) Current ballast tests as specified in the Railtrack Line Specification (RT/CE/S006 Issue 3, 2000) have been conducted on the six ballasts.

- 4) A particle crusher, which can measure force as a function of displacement, has been modified for compressing a single ballast particle between two flat platens.
- 5) Single ballast particles have been crushed between flat platens to measure, indirectly, the tensile strength, and the Weibull modulus and average or 37% tensile strength has been calculated as a function of size for six types of ballast.
- 6) A large oedometer has been designed and manufactured to test ballast particles of the size used in the trackbed.
- 7) Oedometer tests have been conducted on ballast to determine ballast degradation upon loading to a stress level equivalent to that in the ACV test, for six types of ballast.
- 8) A box has been designed and manufactured to simulate loading conditions by traffic and tamping in the trackbed in a simplified and controlled manner.
- 9) Box tests on ballast have been conducted to determine ballast degradation under typical stresses induced in the trackbed, for four types of ballast.
- 10) Petrographic analysis has given a qualitative assessment of ballast performance and provides rational explanations of the laboratory test results.
- 11) Test results have been correlated, and good ballast testing methods and engineering practises have been proposed.
- 12) The single particle crushing test, oedometer test, and box test have been simulated using PFC^{3D}.

The conclusions that can be drawn from this research are:

- The strength of ballast has been traditionally measured by abrasion tests, or the ACV test, both of which were considered as inappropriate because of the inaccurate simulation of the particle mechanics of ballast underneath the railway track during traffic loading and the inappropriate ballast size used for the test respectively.
- It is necessary to have ballast testing methods which assess the quality of different ballast materials scientifically and provide results reflecting the field performance of different ballast materials.

- It was found in the single particle crushing tests that there is a size effect on the strength of ballast, where smaller ballast particles are statistically stronger, and the size effect is material dependent.
- The size effect on the strength of ballast was not as high as expected because ballast particles that survived the grinding process during production are statistically stronger.
- Weibull (1951) statistics that applies the integration of some function of stress over the particle area (rather than volume) may be more appropriate to analyse the size effect on strength in ballast.
- It was found that the relative performance of small ballast particles cannot be used to predict the relative performance of large ballast particles because the size effect on the strength of ballast is material dependent. Thus, the traditional ACV test is not appropriate and it is important to test ballast of the size used in the trackbed.
- Ballasts that are less “flaky” seemed to undergo less breakage and wet ballast appeared to be weaker than dry ballast. The degree of strength reduction appears to be a function of the water absorption of the ballast.
- The values of total breakage and scaled ACV (ACV_d) in the large oedometer tests are best correlated with the relative strength index R_s , which considers both the 37% tensile strength σ_o of ballast particles and the initial grading e_i of the sample.
- The box test is a repeatable test, where settlements, stiffnesses and particle size distributions can be reproduced.
- The simulated tamping process is considered as appropriate because it was able to improve the ballast performance in the sense that there was a decrease

in settlement and an increase in stiffness after each tamp, which is likely to represent the early life of the ballast in the field.

- The simulated tamping process was noted to simulate only the rearrangement of ballast underneath the sleeper during tamping using the tamping machine, but not the “squeezing” force.
- The increase in ballast stiffness in the box test with tamping and traffic loading was achieved by ‘squeezing’ additional ballast towards the bottom of the sleeper, compaction of the lower layer of the ballast in the box not disturbed by tamping, and a progressive increase in ballast density within the box.
- The settlement and stiffness profiles for the box test on 10-14mm ballast are similar to those on track ballast sized ballast, even though there is slightly less breakage, due to the statistically stronger 10-14mm ballast.
- It is more difficult to tamp 10-14mm ballast properly (i.e. difficult to fill the gap underneath the sleeper with small ballast). Thus, ballast that has degraded significantly cannot be tamped efficiently and must be cleaned or replaced.
- The settlement and stiffness profiles for the box tests on ballasts A, B and C were shown to be similar, where the settlement reduces and stiffness increases with increasing number of tamps, whilst the profiles for ballast D were shown to be different, such that tamping had little or no effect on the sleeper level before each tamp, and the stiffness was approximately constant.
- Ballast D had the highest degree of ballast breakage in the box, where the total breakage for the ballast underneath the sleeper is at least 6 times higher than any of the other ballasts. This is consistent with all the other ballast tests where ballast D was found to be as weak, if not weaker, compared with other ballasts.

- The petrographic analysis revealed the incompetence of ballast D, where it was noted that some of the feldspars in the samples were markedly soft and were altered to clay minerals. The presence of clay minerals in ballast D also explained the high water absorption of ballast D.
- The box test results correlate well with WAV, LAA and MDA values. This is considered to be due to the rearrangement of particles which also occurs for the ballast subjected to the simulated tamping in the box.
- The box test results do not correlate with the traditional ACV, which was anticipated because the ACV test uses 10-14mm ballast particles instead of track ballast sized particles.
- The box test results do not correlate well with the oedometer test results on specification ballast. This could be due to the fact that ballast particles in the oedometer tests were not subjected to extensive rearrangement and the oedometer tests were conducted in a dry condition.
- The box test results correlate well with the relative strength index R_s which accounts for both particle strength and packing.
- The single particle crushing test was successfully simulated in PFC^{3D} by compressing an agglomerate between two walls, and the average strength and distribution of strengths for real ballast particles were reproduced.
- The use of a low damping coefficient is more realistic because agglomerates fail by fast fracture.
- Ballast is best simulated using agglomerates of bonded balls, such that agglomerates will fracture if the induced tensile stresses are sufficiently high.
- The normal compression line of crushable agglomerates was shown to be different under high displacement rates. Minimising the difference in vertical

stresses on the top and bottom walls during loading produced an acceptable normal compression line.

- Minimising the difference in vertical stresses on the top and bottom walls during loading did not ensure a quasi-static sample, and the slight increase in K_o for a sample that was unloaded immediately after loading was a result of this.
- Unloading a quasi-static sample did not give an increase in K_o , and further compression resulted during unloading.
- The use of contact bonds was thought to cause further rearrangement during unloading because it allows rolling of balls relative to one another without breaking the contact bond.
- Simulation of the box test on an assembly of 8-ball cubic clumps resembles that of real soil subjected to repeated load. The assembly was also found to give less permanent deformation than the assembly of spherical balls, which should be due to the additional resistance provided by the non-spherical shape of the clumps.
- Ball stiffness should ideally be a function of the degree of overlap of balls or the contact force of the balls in contact. The Hertzian contact model, which calculates the contact stiffness based on the contact force of the balls in contact, would be more suitable in simulating the box test because the contact forces vary throughout the box.

8.2 Suggestions for further research

One of the most important aspects of track ballast geometry that the box test is not able to simulate is the lateral flow of ballast. This is an important ballast characteristic that needs further research because ballast settlement, stiffness and

degradation must also depend on ballast stability in addition to the applied load and the strength of the aggregate. Ballast stability should be a function of the shape, angularity and tensile strengths of the ballast particles and asperities. Thus, conducting a “box” test without the front wall (i.e. the longer sides of the box) and characterising ballast stability using the relative strength index R_s , may be a useful starting point.

Further box tests that vary the applied load and subgrade stiffness should be conducted to identify critical loads for different subgrade stiffnesses. For a given subgrade stiffness, a critical load is a load above which there is a rapid increase in the rate of settlement and ballast degradation (Raymond & Bathurst, 1987). Thus, conducting more box tests with different applied loads and subgrade stiffnesses, and correlating the critical loads with values of relative strength index R_s , may also prove to be useful.

The use of contact bonds in PFC^{3D} for the crushable agglomerates was shown to allow rolling of balls at contacts without breaking of the contact bonds. Thus, a parallel bond, which can also resist moment is considered to be a better alternative for simulating crushable agglomerates. The Hertzian contact model is a more realistic contact model for use in the box test but is incompatible with the use of any type of bonding. In addition, it is noted that higher computational time is required when using the Hertzian contact model, compared with the linear-elastic model. It may be useful to use a linear contact model which can approximate the Hertzian contact model, for different loading conditions (i.e. different stiffnesses could be used at different levels of contact force). More clump shapes should be investigated in order to find a shape that best represents ballast particles for future simulations. This will facilitate the examination of stresses within the ballast and whether such stresses are likely to cause extensive degradation.

References

Alva-Hurtado, J. E. (1980). *A methodology to predict the elastic and inelastic behaviour of railroad ballast*. Ph.D. dissertation, University of Massachusetts, Amherst, Massachusetts.

Ashby, M. F. & Jones, D. R. H. (1980). *Engineering materials 1*. Oxford: Pergamon Press.

Boucher, D. L. & Selig, E. T. (1987). Application of petrographic analysis to ballast performance evaluation. *Transportation Research Record* **1131**, pp. 15-25.

British Standard: BS 812 (1951). Clause 27. *Methods for determination of wet attrition value (WAV)*.

British Standard: BS 812-103.1 (1985). *Methods for determination of particle size distribution- Sieve tests*.

British Standard: BS 812-105.1 (1989). *Methods for determination of particle shape- Flakiness index*.

British Standard: BS 812-105.2 (1990). *Methods for determination of particle shape- Elongation index of coarse aggregate*.

British Standard: BS 812-110 (1990). *Methods for determination of aggregate crushing value (ACV)*.

British Standard: BS EN 1097-1 (1996). *Tests for mechanical and physical properties of aggregates- Determination of the resistance to wear (micro-Deval)*.

British Standard: BS EN 1097-2 (1998). *Tests for mechanical and physical properties of aggregates- Methods for the determination of resistance to fragmentation*.

British Standard: BS EN 13450 (2002). *Aggregates for railway ballast*.

British Standard: BS EN 933-1 (1997). *Determination of particle size distributions- Sieving method*.

British Standard: BS EN 933-3 (1997). *Determination of particle shape- Flakiness index*.

Brown, S. F. (1996). Soil mechanics in pavement engineering. *Géotechnique* **46**, No. 3, pp. 383-426.

Brown, S. F. & Hyde, A. F. L. (1975). Significance of cyclic confining stress in repeated-load triaxial testing of granular material. *Transportation Research Record* **537**. Transportation Research Board, Washington, DC, pp. 45-51.

Cheng, Y. P., Nakata, Y. & M. D. Bolton (2003). *Géotechnique* **53**, No. 7, pp. 633-641.

Cundall, P. A. & Hart, R. (1992). "Numerical Modelling of Discontinua," *J. Engr. Comp.*, **9**, pp. 101-113.

Cundall, P. A. & Strack, O. D. L. (1979). A discrete numerical model for granular assemblies. *Géotechnique* **29**, No. 1, pp. 47-65.

Davidge, R. W. (1979). *Mechanical behaviour of ceramics*. Cambridge University Press.

Draft Network Rail Code of Practice (2003). Draft 1d RT/CE/C/039. *Formation Treatments*.

Fukumoto, T. (1992). Particle breakage characteristics in granular soils. *Soils and Foundation* **32**, No. 1, pp. 26-40.

Griffith, A. A. (1920). The phenomena of rupture and flow in solids. *Phil. Trans. R. Soc. Lond.* **A221**, 163-198.

Gur, Y., Shklarsky, E. & Livneh, M. (1967). Effect of coarse-fraction flakiness on the strength of graded materials. *Proceedings of the 3rd Asian Regional Conference on Soil Mechanics and Foundation Engineering*, September 1967.

Han, X & Selig, T. (1997). Effects of fouling on ballast settlement. *6th International Heavy Haul Conference*. St Louis; Int. Heavy Haul Association; Spornet Vol. 1, pp. 257-268.

Hardin, B.O. (1985). Crushing of soil particles. *Journal of Geotechnical Engineering*., ASCE. Vol **111**, No. 10, pp. 1177-1192.

Hazzard, J. F., Young, R. P. & Maxwell, S. C. (2000). Micromechanical modelling of cracking and failure in brittle rocks. *Journal of Geophysical Research*. Vol. 105, No. B7, pp. 16,683-16,697.

Hicks, R. G. & Monismith, C. L. (1971). Factors influencing the resilient response of granular materials. *Highway Research Record* **345**, Highway Research Board, Washington, DC, pp. 15-31.

Hveem, F. N. & Carmany, R. M. (1948). The factors underlying the rational design of pavements. *Proc. Highway Research Board* **28**, Washington, DC, pp. 101-136.

Hveem, F. N. (1955). Pavement deflections and fatigue failures. *Highway Research Board Bulletin*, No. 114, Washington, DC, pp. 43-87.

Itasca Consulting Group, Inc. (1999). *Particle flow code in 3 dimensions*.

Knutson, R. M. (1976). *Factors influencing the repeated load behaviour of railway ballast*. PhD Dissertation, University of Illinois at Urbana-Champaign.

Large, D. (2003). *Petrographic description of railway ballast samples*. University of Nottingham (confidential report).

Lee, D. M. (1992). *The angles of friction of granular fills*. Ph.D. dissertation, University of Cambridge.

Lekarp, F., Isacsson, U., & Dawson, A. (2000a). "State of the art. I: Resilient response of unbound aggregates." *J. Transp. Engrg.*, ASCE. Vol **126**, No. 1, pp. 66-75.

Lekarp, F., Isacsson, U., & Dawson, A. (2000b). "State of the art. II: Permanent strain response of unbound aggregates." *J. Transp. Engrg.*, ASCE. Vol **126**, No. 1, pp. 76-83.

McDowell, G. R. & Amon, A. (2000). The applicability of Weibull statistics to the fracture of soil particles. *Soils and Foundations* **40**, No. 5, pp. 133-141.

McDowell, G. R. & Bolton, M. D. (1998). On the micromechanics of crushable aggregates. *Géotechnique* **48**, No. 5, pp. 667-679.

McDowell, G. R., Bolton, M. D. & Robertson, D. (1996). The fractal crushing of granular materials. *J. Mech. Phys. Solids* **44**, No. 12, pp. 2079-2102.

McDowell, G. R. & Harireche, O. (2002a). Discrete element modelling of soil particle fracture. *Géotechnique* **52**, No. 2, pp. 131-135.

McDowell, G. R. & Harireche, O. (2002b). Discrete element modelling of yielding and normal compression of sand. *Geotechnique* **52**, No. 4, pp. 299-304.

McDowell, G. R. (2002). On the yielding and plastic compression of sand. *Soils and Foundations* **42**, No. 1, pp. 139-145.

McDowell, G. R. (2001). Statistics of soil particle strength. *Geotechnique* **51**, No.10, pp. 897-900.

McDowell, G. R., Lim, W.L., & Collop, A.C. (2003). Measuring the strength of railway ballast. *Ground Engineering* **36**, No.1, pp. 25-28.

Nakata, Y., Hyde, A.F.L., Hyodo, M., & Murata, H. (2001). A probabilistic approach to sand particle crushing in the triaxial test. *Geotechnique* **49**, No.5, pp. 567-583.

Nakata, Y., Kato, Y., Hyodo, M., Hyde, A.F.L., & Murata, H. (1999). One-dimensional compression behaviour of uniformly graded sand related to single particle crushing strength. *Soils and Foundations* **41**, No. 2, pp. 39-51.

Norman, G. M. & Selig, E. T. (1983). Ballast performance evaluation with box tests. *American Railway Engineering Association, Bulletin* 692, Proceedings Vol. **84**, pp. 207-239.

Oda, M. (1977). Co-ordination number and its relation to shear strength of granular material. *Soils and Foundation* **17**, No. 2, pp. 29-42.

Pappin, J. W. & Brown, S. F. (1980). Resilient stress-strain behaviour of a crushed rock. *Proc. Int. Symp. Soils under cyclic and transient loading*, Swansea Vol. 1, pp. 169-177.

Railtrack Line Specification (2000). RT/CE/S/006 Issue 3. *Track Ballast*.

Raymond, G. P. & Bathurst, R. J. (1987). Performance of large-scale model single tie-ballast systems. *Transportation Research Record* **1131**, pp. 7-14.

Robertson, D. (2000). *Numerical simulations of crushable aggregates*. Ph.D. dissertation, University of Cambridge.

Sammis, C. (1996). Fractal fragmentation and frictional stability. *Proceedings of the IUTAM symposium on mechanics of granular and porous materials* (eds N. A. Fleck and A. C. F. Cocks). Kluwer.

Seed, H. B., Chan, C. K. & Lee, C. E. (1962). Resilience characteristics subgrade soils and their relation to fatigue failures. *Proc. Int. Conf. Structural Design of Asphalt Pavements*, Ann Arbor, Michigan, pp. 611-636.

Selig, E. T. & Boucher, D. L. (1990). Abrasion tests for railroad ballast. *Geotechnical Testing Journal*, GTJODJ, Vol. **13**, No. 4, pp. 301-311.

Selig, E. T. & Roner, C. J. (1987). Effects of particle characteristics on behaviour of granular material. *Transportation Research Record* **1131**, pp. 1-6.

Selig, E. T. & Waters, J. M. (1994). *Track geotechnology and substructure management*. Thomas Telford. London.

Selig, E. T., Parsons, B. K. & Cole, B. E. (1993). Drainage of Railway Ballast. *Proceedings of the 5th International Heavy Haul Conference*, Beijing, China pp. 200-206.

Sharpe, P., Collop, A.C., & Dawson, A.R. (1998). Applying engineering principles to optimise trackbed performance. *Proceedings of Infrastructure Issues: International Railtech Congress '98*, IMechE Seminar Publication 1998-23, pp. 29-38.

Shenton, M. J. (1974). Deformation of railway ballast under repeated loading conditions. *British Railways Research and Development Division*.

Shipway, P. H. & Hutchings, I. M. (1993). Fracture of brittle spheres under compression and impact loading. I. Elastic stress distributions. *Phil. Mag. A* **67**, No. 6, pp. 1389-1404.

Watters, B. R., Klassen, M. J., & Clifton, A. W. (1987). Evaluation of ballast materials using petrographic criteria. *Transportation Research Record* **1131**, pp. 45-58.

Weibull, W. (1951). A statistical distribution function of wide applicability. *J. Appl. Mech.* **18**, pp. 293-297.

Wood, D. M. (1990). *Soil behaviour and critical state soil mechanics*. Cambridge University press.

Wright, S. E. (1983). Damage caused to ballast by mechanical maintenance techniques. *British Rail Research Technical Memorandum* TM TD 15, May 1983.

Appendix

Mineralogy of Railway Ballast Samples (Large, 2003)

Ballast A

Two samples were selected in ballast A: one of grey granodiorite (A1) and one of red granodiorite (A2). A2 is an alteration product of A1 and is more abundant than A1. The relative proportions of A1 and A2 are approximately 30% to 70% respectively.

Sample: A1

Rock type:
Granodiorite

Composition (based on visual estimate):

| | |
|-----------------|-----|
| Plagioclase | 30% |
| Quartz | 25% |
| Alkali feldspar | 20% |
| Hornblende | 10% |
| Biotite | 5% |
| Opagues | 5% |
| Chlorite | <5% |
| Accessories | <5% |
| Sphene | |
| Tourmaline | |
| Epidote | |
| White mica | |

Sample: A2

Rock type:
Altered granodiorite

Composition (based on visual estimate):

| | |
|-----------------|------------------------------------|
| Plagioclase | 30% (mainly altered to white mica) |
| Quartz | 25% |
| Alkali feldspar | 20% |
| Chlorite | 15% |
| Opagues | 5% |
| Hornblende | <5% |
| Accessories | <5% |
| Sphene | |
| Tourmaline | |
| Epidote | |

Ballast B

Two samples were selected in ballast B: one of white granite (B1) and one of slightly reddish granite (B2). Macroscopically these samples appeared to display different degrees of alteration with B2 being more altered than B1. The relative proportions of B1 and B2 are approximately 60% and 40% respectively.

Sample: B1

Rock type:
Granite

Composition (based on visual estimate):

| | |
|-----------------|-----|
| Plagioclase | 35% |
| Quartz | 30% |
| Alkali feldspar | 20% |
| Biotite | 7% |
| Chlorite | 3% |
| Accessories | 5% |
| White mica | |
| Apatite | |
| Zircon | |
| Opagues | |

Sample: B2

Rock type:
Granite

Composition (based on visual estimate):

| | |
|-----------------|-----|
| Plagioclase | 35% |
| Quartz | 30% |
| Alkali feldspar | 20% |
| Biotite | 1% |
| Chlorite | 6% |
| Accessories | 5% |
| White mica | |
| Apatite | |
| Zircon | |
| Opagues | |

Ballast C

Only one sample of rock was selected in ballast C: a grey granodiorite (C1).

Sample: C1

Rock type:
Granodiorite

Composition (based on visual estimate):

| | |
|--------------------|-----|
| Plagioclase | 40% |
| Quartz | 25% |
| Amphibole | 25% |
| Augite | 5% |
| Accessories | 5% |
| Potassium feldspar | |
| White mica/clay | |
| Biotite | |
| Apatite | |
| Opagues | |

Ballast D

Three samples were selected based on the degree of alteration observed. The least altered is D3 and the most altered is D2. The relative proportions of the slightly altered granodiorite (D1, D3) and the most altered granodiorite (D2) are approximately 45% and 55% respectively.

Sample: D1

Rock type:
Granodiorite (Altered)

Composition (based on visual estimate):

Primary Composition

| | |
|-------------|---------------------------------------|
| Plagioclase | 50% (mainly altered to clay and mica) |
| Quartz | 30% |
| Hornblende | 10% |
| Biotite | 5% (mainly altered to chlorite) |
| Augite | <5% |
| Opauques | <5% |
| Accessories | <5% |
| Epidote | |
| Chlorite | |
| Calcite | |

Sample: D2

Rock type:
Granodiorite (Highly altered)

Composition (based on visual estimate):

Primary Composition

| | |
|-------------|---------------------------------------|
| Plagioclase | 50% |
| Quartz | 30% |
| Hornblende | 10% (Altered to epidote and chlorite) |
| Biotite | 5% (Altered to epidote and chlorite) |
| Opauques | <5% |
| Accessories | <5% |
| Calcite | |

Sample: D3

Rock type:
Granodiorite

Composition (based on visual estimate):

Primary Composition

| | |
|-------------|-----|
| Plagioclase | 50% |
| Quartz | 30% |
| Hornblende | 10% |
| Biotite | 5% |
| Augite | <5% |
| Opauques | <5% |
| Accessories | <5% |
| Chlorite | |

Ballast E

Only one sample of rock was selected in ballast E: a red porphyritic felsite (E1).

Sample: E1

Rock type:
Porphyritic Felsite

Composition (based on visual estimate):

| | |
|-----------------|----------------------------------|
| Phenocrysts | 5% |
| Plagioclase | |
| Groundmass | 95% |
| Plagioclase | 80% (altered to fine white mica) |
| Quartz | 5% |
| Alkali Feldspar | 5% |
| Biotite | 5% |
| Apatite | <5% |
| Opaques | <5% |

Ballast F

Ballast F displays the greatest diversity and consists of metasediments, pyroclastics and granodiorite in various stages of alteration. Samples F1, F4 and F6 are granodiorite in various stages of alteration. The metasediment (F3) and pyroclastic tuffs (F2, F5) are from the surrounding country rock into which the granodiorite was intruded. The relative proportions of metasediments (F3), pyroclastics (F2, F5) and granodiorite (F1, F4, F6) are approximately 20%, 25% and 55% respectively.

Sample: F1

Rock type:
Granodiorite (highly altered oxidised)

Composition (based on visual estimate):

| | |
|----------------------|-----|
| Original composition | |
| Feldspar | 50% |
| Ferromagnesian | 15% |
| Accessories | 5% |
| Apatite | |
| Zircon | |
| Alkali Feldspar | |

| | |
|------------------------|-----|
| Current composition | |
| White mica (muscovite) | 30% |
| Hematite | 35% |
| Quartz | 30% |
| Accessories | 5% |

Sample: F2

Rock type:
Metamorphosed Pyroclastic Breccia (Tuff)

Composition (based on visual estimate):

| | |
|--|-----|
| Clasts | 70% |
| Porphyritic Andesite with feldspar phenocrysts | |
| Trachyte | |
| Matrix | 30% |
| Epidote | |
| Chlorite | |
| Hematite | |
| Plagioclase | |

Sample: F3

Rock type:
Metamorphosed siltstone

Composition (based on visual estimate):

| | |
|------------|-----|
| Quartz | 90% |
| Others | 10% |
| Epidote | |
| Chlorite | |
| White mica | |

Sample: F4

Rock type:
Epidotised Granodiorite

Composition (based on visual estimate):

| | |
|----------------------|-----|
| Original composition | |
| Plagioclase | 60% |
| Quartz | 35% |
| Accessories | 5% |
| Ferromagnesian | |
| Apatite | |

| | |
|---------------------|-----|
| Current composition | |
| Epidote | 50% |
| Calcite | 10% |
| Quartz | 35% |
| Accessories | 5% |
| Chlorite | |
| Hematite | |
| Apatite | |

Sample: F5

Rock type:
Metamorphosed Pyroclastic breccia (Tuff)

Composition (based on visual estimate):

| | |
|--|-----|
| Clasts | 85% |
| Porphyritic Andesite with feldspar phenocrysts | |
| Trachyte | |
| Epidote | |
| Chlorite | |
| Matrix | 15% |
| Epidote | |
| Chlorite | |
| Hematite | |

Sample: F6

Rock type:
Granodiorite

Composition (based on visual estimate):

| | |
|-----------------------|-----|
| Quartz | 25% |
| Alkali feldspar | 20% |
| Plagioclase unaltered | 5% |
| Plagioclase altered | 25% |
| Epidote | |
| White mica | |
| Chlorite | |
| Hornblende | 20% |
| Accessories | 5% |
| Opauques | |
| Apatite | |